STRUCTURES, ENERGETICS AND REACTIONS OF HYDROCARBONS ON NICKEL

Thesis by

Jonathan Edward Mueller

In Partial Fulfillment of the Requirements for the degree of

Doctor of Philosophy

CALIFORNIA INSTITUTE OF TECHNOLOGY

Pasadena, California

2010

(Defended May 4, 2010)

To Papa

"…as thy days, so shall thy strength be."

Deuteronomy 33:25

A c k n o w l e d g e m e n t s

My graduate studies have been enriched by the presence of people God has brought into my life. Many individuals have contributed to the completion of this thesis and many more have impacted me during my time in graduate school. It is my pleasure to acknowledge a few of these who have been a part of my life and studies these past few years at Caltech.

I joined Professor Goddard's research group with no previous research experience in atomistic simulations; nevertheless, he gave me the opportunity to try something new. As my adviser, he has been supportive of my work and given me a great deal of freedom in my studies. I have learned much from his many chemical intuitions and improbable conjectures, and am especially grateful for his patience along the way. He and the other members of my thesis committee, Professors Bercaw, Heath and Wang, have made me a better scientist by challenging me to both think and communicate clearly.

Many of the members of the Material and Process Simulation Center have been my friends, collaborators, officemates, mentors and colleagues over the past several years. Adri was a source of guidance and invaluable assistance for the work presented in this thesis and other projects also. Mario managed several industrial projects I was involved in with great enthusiasm. John talked me into joining the MSC and has encouraged me to take advantage of new opportunities ever since. Mu-Jeng has been a good friend and classmate from the start.

For three months during the Fall of 2009, Timo Jacob afforded me the opportunity of visiting his theoretical electrochemistry group at the Universität Ulm in Ulm, Germany.

The members of the Institut für Elektrochemie welcomed me warmly and helped make my stay academically productive and enjoyable.

I am grateful for the many friends I have had over the past five years in Pasadena. The people of Trinity Baptist Church in Pasadena have been a large part of my life during this time. In particular, Amos, Genti, Jeremie, Sarah, Tania, and Tim have been good friends. Dwayne & Malana, and Joe & Elsa have been there during some of the hard times along the way. Long distance prayer times with Dan have been a regular blessing.

My family has been a continual source of love and encouragement. My great uncles and aunts, John & Ella and Fred & Char, have frequently welcomed me into their California homes. The faithful prayers of my grandfathers have been a labor of their love. My sister and brothers, Johanna, Daniel and Peter, have often reminded me to take time to enjoy life along the way. My parents, Rodney & Linnea, have shown their unconditional love and support for me through it all. Thanks be unto God for his unspeakable gift!

Finally, I thank God for his faithfulness through these years, and for the grace, mercy and love he has shown me through Christ Jesus. πιστος ο καλων υμας, ος και ποιησει.

A b s t r a c t

To better understand and improve reactive processes on nickel surfaces such as the catalytic steam reforming of hydrocarbons, the decomposition of hydrocarbons at fuel cell anodes, and the growth of carbon nanotubes, we have performed atomistic studies of hydrocarbon adsorption and decomposition on low index nickel surfaces and nickel catalyst nanoparticles. Quantum mechanics (QM) calculations utilizing the PBE flavor of density functional theory (DFT) were performed on all CH_x and C_2H_y species to determine their structures and energies on Ni(111). In good agreement with experiments, we find that CH_{ad} is the most stable form of CH_x on Ni(111). It is a stable intermediate in both methane dehydrogenation and CO methanation, while $CH_{2,ad}$ is only stable during methanation. We also find that nickel surface atoms play an important catalytic role in C-H bond formation and cleavage. For the C_2H_y species we find a low surface coverage decomposition pathway proceeding through $CHCH_{ad}$, the most stable intermediate, and a high surface coverage pathway which proceeds through $CCH_{3,ad}$, the next most stable intermediate. Our enthalpies along these pathways are consistent with experimental observations.

To extend our study to larger systems and longer time scales, we have developed the ReaxFF reactive force field to describe hydrocarbon decomposition and reformation on nickel catalyst surfaces. The ReaxFF parameters were fit to geometries and energy surfaces from DFT calculations involving a large number of reaction pathways and equations of state for nickel, nickel carbides, and various hydrocarbon species chemisorbed on Ni(111), Ni(110) and Ni(100). The resulting ReaxFF description was validated against additional DFT data to demonstrate its accuracy, and used to perform reaction dynamics (RD) simulations on methyl decomposition for comparison with experiment. Finally ReaxFF RD

simulations were applied to the chemisorption and decomposition of six different hydrocarbons (methane, acetylene, ethylene, benzene, cyclohexane and propylene) on a 468 atom nickel nanoparticle. These simulations realistically model hydrocarbon feedstock decomposition and provide reaction pathways relevant to this part of the carbon nanotube growth process. They show that C-C π bonds provide a low barrier pathway for chemisorption, and that the low energy of subsurface C is an important driving force in breaking C-C bonds.

Table of Contents

STRUCTURES, ENERGETICS AND REACTIONS
OF HYDROCARBONS ON NICKEL

P r e f a c e

This thesis contains four chapters corresponding to four papers I co-authored with Adri C. T. van Duin and William A. Goddard III. Three of these (Chapters 1, 3 and 4) have already been published in the *Journal of Physical Chemistry C*, and we plan to submit the fourth paper for publication soon. My contributions to these papers include performing and analyzing all calculations in Chapters 1, 2 and 4. My contributions to Chapter 3 include providing a significant portion of the DFT training data, and performing and analyzing the calculations used for the force field validation. Adri van Duin is primarily responsible for the force field optimization presented in Chapter 3, and several others contributed to the training data. I am primarily responsible for writing and preparing all four manuscripts for publication.

Introduction

The four chapters in this thesis can all be classified as atomistic studies of hydrocarbon chemistry on nickel catalyst surfaces. The first two chapters are detailed density functional theory (DFT) studies of CH_x and C_2H_y species reacting on and with the Ni(111) surface. The final two chapters present the development, validation and application of a ReaxFF reactive force field for modeling hydrocarbon chemistry on nickel surfaces. Each chapter is self-contained, and can be read either by itself or in conjunction with the other chapters.

Chapter 1 is a DFT study of the chemistry of all single carbon hydrocarbon (CH_x) species chemisorbed on Ni(111). Because the binding of all CH_x species at each of four high symmetry sites (fcc, hcp, bridge, and on-top) on Ni(111) is considered, this study provides a systematic understanding of C interacting with the Ni(111) under a range of coordinations and hybridization states. Furthermore, reaction pathways and barriers for converting between the CH_x species provide an initial exploration of the nature and reactivity of C-H bonds in the presence of the Ni(111) surface. These reaction pathways are compared with experimental results.

Chapter 2 contains a similar DFT study of C_2H_y species chemisorbed onto Ni(111). The lowest energy structure for each of the nine plausible adsorbates is considered in detail, with special attention being paid to the energetic cost of breaking the C-C bond in each C_2H_y species to form separated CH_x and CH_{y-x} adsorbates. Thus, the focus is primarily on the stability and reactivity of C-C bonds on Ni(111).

To study larger hydrocarbon species on nickel, we developed a ReaxFF reactive force field describing hydrocarbon chemistry on nickel, which we present in Chapter 3. To do this we optimized of the ReaxFF parameters against a large set of DFT training data, which

includes the results presented in Chapters 1 and 2. The resulting ReaxFF reactive forcefield description of hydrocarbons in the presence of nickel catalysts surfaces is validated by making comparisons with both experimental and DFT data.

In Chapter 4 we apply the ReaxFF reactive force field developed in Chapter 3 to the chemisorption and decomposition of six hydrocarbon species on a 468 atom nickel nanoparticle. Temperature programmed reactive dynamics (RD), in which the temperature is increased at a constant rate from 500 K to 2500 K, are used to explore the chemisorption and decomposition of hydrocarbons on a nickel nanoparticle catalyst. The hydrocarbon species considered (acetylene, benzene, cyclohexane, ethylene, methane and propylene) were selected to provide a diverse sample of hydrocarbon species. The size of the nanoparticle (21 Å diameter) is similar to the size of catalysts used experimentally for carbon nanotube growth. Thus, our RD simulations provide a glimpse into the atomistic details of a system large enough to conduct experiments on.

C h a p t e r 1

STRUCTURES, ENERGETICS, AND REACTION BARRIERS FOR CH_X BOUND TO NICKEL (111)[1]

To provide a basis for understanding and improving such reactive processes on nickel surfaces as the catalytic steam reforming of hydrocarbons, the decomposition of hydrocarbons at fuel cell anodes, and the growth of carbon nanotubes, we report quantum mechanics (QM) calculations (PBE flavor of density functional theory, DFT) of the structures, binding energies, and reaction barriers for all CH_x species on the Ni(111) surface using periodically infinite slabs. We find that all CH_x species prefer binding to μ_3 (three-fold) sites leading to bond energies ranging from 42.7 kcal/mol for CH_3 to 148.9 kcal/mol for CH (the number of Ni-C bonds is not well defined). We find reaction barriers of 18.3 kcal/mol for $CH_{3,ad} \rightarrow CH_{2,ad} + H_{ad}$ (with ΔE = +1.3 kcal/mol), 8.2 kcal/mol for $CH_{2,ad} \rightarrow CH_{ad} + H_{ad}$ (with ΔE = -10.2 kcal/mol) and 32.3 kcal/mol for $CH_{ad} \rightarrow C_{ad} + H_{ad}$ (with ΔE = 11.6 kcal/mol). Thus CH_{ad} is the stable form of CH_x on the surface. These results are in good agreement with the experimental data for the thermodynamic stability of small hydrocarbon species following dissociation of methane on Ni(111) and with the intermediates isolated during the reverse methanation process.

1. Introduction

The chemistry of hydrocarbons reacting on nickel is of interest for a number of scientific and technological reasons. Nickel is the primary catalyst in the steam reforming process [1] for converting methane (CH_4) and water into synthesis gas (carbon monoxide

---

[1] Reproduced with permission from Jonathan E. Mueller, Adri C. T. van Duin and William A. Goddard, III, "Structures, Energetics, and Reaction Barriers for CH_x Bound to the Nickel (111) Surface" *J. Phys. Chem. C*, **2009**, *113* (47), 20290-20306. Copyright 2009 American Chemical Society.

plus dihydrogen) which is then used in such important industrial processes as the Haber-Bosch synthesis of ammonia and the Fischer-Tropsch formation of higher hydrocarbons [2]. In addition, nickel has been used to catalyze the formation and growth of carbon nanotubes from hydrocarbon feedstock [3].

The role of nickel as the catalyst of choice for industrial steam reformation motivated a number of experimental and theoretical studies of CH_4 adsorption and decomposition on various nickel surfaces. Since the dissociative chemisorption of CH_4 unto the catalyst is the rate limiting step, the focus has been on the energetics and activation barrier for this chemisorption process on various nickel surfaces. Early experiments demonstrated that the Ni(111) surface is the least reactive of the low index surfaces [4]; however, as the most stable surface, most subsequent studies were for this surface.

High-resolution electron energy loss spectroscopy (HREELS) experiments have identified the stable species formed from the dissociative chemisorption of CH_4 on Ni(111) as a function of temperature [5, 6]. These studies show that above 150 K methyl ($CH_{3,ad}$) loses two H atoms to form methylidine (CH_{ad}), which dimerizes above 250 K to form chemisorbed acetylene, $(CH{=}CH)_{ad}$. The effect of additional heating depends on the surface coverage. If the surface coverage of $(CH{=}CH)_{ad}$ is at least 0.24 monolayers (ML), the $(CH{=}CH)_{ad}$ molecules join together to form four-, six-, and eight-membered rings. However, for surface coverages below 0.05 ML, dehydrogenation of $(CH{=}CH)_{ad}$ occurs before the $(CH{=}CH)_{ad}$ molecules can diffuse to react with each other to form ring structures. Another study [7] used static secondary ion mass spectrometry (SIMS) to detect $CH_{3,ad}$, methylene ($CH_{2,ad}$), and CH_{ad} intermediates in the Fischer-Tropsch synthesis of CH_4 and water from carbon monoxide and hydrogen gas catalyzed on Ni(111). The presence of

all three CH_x intermediates on the Ni(111) surface provides evidence for a sequential hydrogenation mechanism in which no single hydrogenation step dominates the overall reaction rate.

Several theoretical studies have reported relative stabilities of CH_x species on Ni(111) [8-16]. All studies agree qualitatively that the strength of the bond formed to the surface decreases as the number of H substituents is increased; however, quantitative results from previous studies often disagree significantly. Thus, binding energies have been reported

- from 134 kcal/mol [9] to 176 kcal/mol [8] for C_{ad} at a μ_3 fcc site (we find 154.8 kcal/mol for a μ_3 hcp sites),
- from 69 kcal/mol [17] to 165 kcal/mol [8] for CH_{ad} at a μ_3 fcc site (we find 148.9 kcal/mol for a μ_3 hcp site),
- from 62 kcal/mol [17] to 104 kcal/mol [8, 9] for $CH_{2,ad}$ at a μ_3 fcc site (we find 89.3 kcal/mol for a μ_3 fcc site), and
- from 15 kcal/mol [9] to 49 kcal/mol [13] for $CH_{3,ad}$ at a μ_3 fcc site (we find 42.7 kcal/mol for a μ_3 fcc site).

Various studies also disagree as to which site is most energetically favorable. (See Figure 1 for a description of binding sites). Two DFT cluster studies [8, 9] predict that $CH_{3,ad}$ prefers the on-top site to the fcc site by ~10 kcal/mol, while CI calculations on an embedded Ni cluster [16] predict that the fcc site is preferred by 5 kcal/mol. These differences in binding energies lead to rather different predictions for the energetics of reactions involving these species. Watwe [14] and Au [8] both predict that $CH_{3,ad} \rightarrow CH_{2,ad} + H_{ad}$ is slightly exothermic (ΔE = -0.7 and -3.5 kcal/mol respectively), while Siegbahn [13] and Michaelides [11] predict that it is endothermic (ΔE = +8.0 kcal/mol and +11.4 kcal/mol

respectively); we predict a slightly endothermic reaction ($\Delta E = +2.4$). The reaction energies and barriers for breaking the two remaining C-H bonds show similar inconsistencies between studies. Nevertheless, the calculated vibrational states of these species [10, 12, 15-16, 18] match experimental spectroscopic measurements [6].

Here we report binding energies and heats of formation for $CH_{3,ad}$, $CH_{2,ad}$, CH_{ad}, C_{ad}, and H_{ad} on the Ni(111) surface obtained from DFT calculations on periodically infinite slabs. We also report the pathway and barriers for interconversion between these species as calculated using the nudged elastic band (NEB) method. The theoretical methods and computational details are discussed in section 2, with the results in section 3. The binding of each adsorbate at each possible surface site is presented before the transition states for reactions involving these species as products and reactants. Section 4 compares these results with experimental observations of the species resulting from chemisorption of CH_4 on the Ni(111) surface and of intermediate species in the conversion of CO and H_2 to CH_4, as well as with previous theoretical results.

2. Theoretical Methods

2.1. DFT methods

All of our periodic DFT calculations utilize the generalized gradient approximation (GGA) for exchange correlation energy developed by Perdew, Burke and Ernzerhof (PBE) [19]. The 18 core electrons ($1s$, $2s$, $2p$, $3s$, $3p$) of Ni were replaced with an angular momentum projected norm conserving pseudopotential and the 1s electrons of C were also replaced with such a pseudopotential.

We used a double zeta plus polarization basis set as implemented in the SeqQuest[20] periodic DFT code where the contraction coefficients were optimized for a five layer fcc Ni

slab, and diamond C. For the d basis functions on Ni and C, we included only the 5 true d orbitals (excluding the $3s$ combination of Cartesian Gaussians).

All geometry optimization calculations allowed spin polarization with the net spin projection optimized. We did not require that the net spin projection be maintained in comparing energies of reactants and products. Instead, we assumed that the deeper layers of a realistic nickel crystal surface would act as a 'spin bath' to balance the optimum spin at a surface site without altering the intensive spin properties of the crystal. For the NEB pathways we used the lowest spin state for the reactant (hydrogenated species) along the entire pathway.

We found that the energies of various spin projections led to a smooth minimum centered about the optimum spin projection. We chose to restrict the net spin projection to the nearest half integral M_s spin projection to simplify analysis of the wavefunction. We did this by finding the M_s value for which the energy values of the M_s states ½ M_s higher and ½ M_s lower both yield higher energies. The energies of these three states were typically within 2 kcal/mol of each other, so we expect our energy to be within 1 kcal/mol of the bottom of the M_s energy well. The importance of using the optimum spin in all calculations can be seen by comparing the cases of C and H binding to μ_3 fcc sites with and without using the lowest energy spin polarization of each system. We find that:

- Assuming the the bare Ni slab to have a closed shell singlet spin state increases the energy (compared to the optimum spin state with 12 unpaired spins per 16 Ni atoms) by 31.8 kcal/mol.

- Assuming the system with C bonded to the slab to have a closed shell singlet state increases the energy (compared to the optimum state with 10 unpaired spins per 16 Ni atoms) by 23.5 kcal/mol.
- Thus, assuming a closed shell singlet state overestimates the binding energy of C by 8.3 kcal/mol.

Similarly, the closed shell singlet state assumption gives rise to an energy of H chemisorbed to the slab which is 30.3 kcal/mol higher than the optimal spin state, leading to an overestimation of 1.5 kcal/mol in the binding energy of H.

While this approach leads to reliable energies and structures, it can provide misleading comparisons between the spin states of different systems. For example we find that the lowest energy spin state for the bare Ni slab and also for CH_3 bonded at an fcc site is M_s = 12/2. This result suggests that that there is no net change in the spin of the slab by binding CH_3. However fitting the energies associated with M_s = 11/2, 12/2 and 13/2 to a parabola leads to an optimum predicted spin of 12.38/2 (henceforth reported as "12.38") for the bare Ni slab and 11.54 for the CH_3 bonded system, a reduction of the spin by 0.84. Thus we use such estimates, rather than the spin of our lowest energy calculation, to compare the optimum spin of various systems.

One issue with DFT calculations is the accuracy expected from various functionals (known as flavors of DFT). Unfortunately there are few cases for which accurate experimental rate parameters are available for a well defined step of the reaction. One surface reaction for which PBE, B3LYP, and experiment are all available is the activation of propane by the vanadyl oxygen of supported V_2O_5 [21]. Here B3LYP leads to a barrier of 23.0 kcal/mol while PBE leads to a barrier of 27.3 kcal/mol, both of which are close to

the experimental value of 27.0 kcal/mol. This suggests that PBE barriers for surface reactions might be accurate within a few kcal/mol.

2.2. Band calculations

All calculations used a $p(2\times 2)$ two-dimensionally periodic unit cell with periodic sides of a = b = 4.98 Å each, and angles of α = β = 90º and γ =120º. These parameters correspond to the experimental lattice constants for bulk nickel. We used c = 21.00 Å for the third cell parameter leading to a minimum vacuum region of 6 angstroms between the top of the adsorbent molecule in one periodic unit cell and the bottom of the slab in the next unit cell up.

A slab consisting of four layers of Ni atoms was used for all calculations. We tested the binding energies of C and CH for slabs with two to nine layers and found reasonable convergence for four layers (Figure 2). The Ni atoms comprising the bottom three layers were fixed at the experimental Ni lattice distance (2.49 Å) [22] with only the Ni atoms in the top layer allowed to relax. We tested this restriction by allowing the second layer of Ni atoms to also relax, and found that the binding energy for C at an fcc site improves by only 0.09 kcal/mol.

A grid of 0.091 Å was used for numerical integration in real space. For a two dimensionally periodic slab (rather than a three-dimensional periodic crystal), we consider band states in two dimensions. The reciprocal space associated with the band states was described with a 5×5 k-point grid Each of these parameters was found to yield an energy convergence of less than 1.0 kcal/mol.

Unconstrained geometry minimization was attempted for each chemisorbed species at four sites (for description of sites see Figure 1): μ_3 fcc, μ_3 hcp, μ_2 bridge, and μ_1 on-top .

The μ_3 fcc and μ_3 hcp sites were stable (i.e. were local potential energy minima) for all adsorbed species. For the cases where binding at a μ_2 site was not stable, the NEB procedure was used to find the transition state (TS) between the fcc and hcp sites. In cases where the μ_1 site was not stable the Ni atom in the top layer at the on-top site and the central atom of the adsorbed species were constrained to remain along a vector perpendicular to the bottom surface proceeding out of a fixed atom directly below them in the bottom layer.

The NEB procedure was also used to calculate energy barriers for reactions. All calculations used consistent parameters (grids, convergence criteria [23], number of layers, etc.). A post analysis code was used to analyze the local charge and spin properties of each system [24].

2.3. Analysis

2.3.1. Energies of Formation

Both energies of formation (ΔE_{form}) and atomization energies (ΔE_{atom}) are useful in comparing energetics of various systems.

Experimental energies of formation use as their reference energy the ground state under standard conditions of temperature and pressure. Thus, for the systems quoted here the energy per atom in fcc Ni, graphite, and H_2 is taken as zero. For DFT calculations it is useful instead to refer to these systems at their optimum structures, which ignores the zero-point energy (ZPE) and heat capacity of the vibrational modes. Since the energy for bulk Ni (experimental lattice constant) with our pseudopotential and basis is E_{Niref} = -93.63925709 Ryd, we subtract this number times the number of Ni atoms to get the cohesive energy, 116.0 kcal/mol. The total energy for a four layer slab with 16 Ni atoms is

-1497.811422 Ryd leading to a total surface energy of $E_{slab} - 16\ E_{Niref}$ = 130.7 kcal/mol or 16.3 kcal/mol per surface atom.

It is more accurate to use diamond than graphite as a reference for C in our DFT calculations because the bonding in diamond is more similar to that of CH_4 and the chemisorbed species. Furthermore, DFT methods are not especially accurate for graphite because of the importance of dispersion interactions between the graphene sheets, which are not well described by DFT. Our calculated energy of diamond (experimental structure) is E_{diaC} = -11.39428812 Ryd. Since the experimental energy of diamond is 0.45 kcal/mol higher than that of graphite [25], we set E_{Cref} = 11.39428812 + 0.45 kcal/mol = -11.3957223633 Ryd.

To be consistent with the energy for H_2 we calculated it with SeqQuest using the same periodic cell as in our slab calculations. Using the optimized bond distance we obtain E_{Href} = -2.3311760070 Ryd.

For any other calculation with N_{Ni} Ni atoms, N_C C atoms, and N_H H atoms we convert the DFT energy to a total energy of formation by subtracting $N_{Ni}\ E_{Cref}$, $N_C\ E_{Cref}$, and $N_H\ E_{Href}$. This is the general procedure; however, since every calculation uses exactly the same Ni slab we just subtract the total energy of the Ni slab to obtain energies of formation (ΔE_{form}).

2.3.2. Atomization energies

A second reference energy convention for DFT calculations is the atomization energy (ΔE_{atom}), which is the energy to break every bond to form every atom in its ground state. Normally this would be Ni in its ^{3}F state, C in its ^{3}P state, and H in its ^{2}S state. However,

since the slab is common to all atoms we instead reference Ni to the relaxed slab energy in quoting atomization energies.

The problem with atomization energies is that the DFT calculations of the separate atomic states, which tend to be open shell systems are usually not as accurate as for the bulk systems and chemisorption calculations in which most electrons are spin paired. This inaccuracy leads to systematic errors proportional to the number of C and H atoms.

For the atomic reference states, we placed a single atom in the same periodic unit cell used for the slab calculations. For C we did a spatially unrestricted calculation with unpaired $2p_x$ and $2p_y$ orbitals, allowing the $2s$ to mix with the $2p_z$ orbital.

The atomization energy for a configuration is obtained by taking the energy of the configuration of interest and subtracting the reference state energy of each type of atom in the cell times the number of atoms of its type.

2.3.3. Adiabatic Bond and Snap Bond Energies

In analyzing the energetic contributions of geometric factors in bonding we find it useful to quote both the adiabatic bond energy (E_{bond}, which is the bond energy relative to the relaxed fragments), and the snap bond energy (E_{snap}, which is the bond energy relative to the unrelaxed fragments). Thus, the adiabatic bond energy for A-B is the energy difference between the optimized A-B bonded species and the separated A and B fragments both geometrically relaxed. The snap bond energy for A-B is the energy difference between the optimized A-B system, and the separated (but not relaxed) A and B fragments. Thus, there is no geometric relaxation of either the surface or the adsorbate from their geometries when bonded together in calculating the reference states for a snap bond energy. The spin projections of the separated A and B are taken at the values they would normally have after

geometric relaxation unless otherwise noted. Thus, the slab energy is always calculated using the relaxed spin projection of $M_s = 12/2$.

2.4. Vibrations

To obtain zero-point energy (ZPE) and finite temperature (298.15 K) corrections for reliable comparison with experiment, we performed DFT calculations on each CH_x species, C and H bonded to a μ_3 fcc site on a nine atom Ni cluster (six surface Ni atoms and three in the second layer). The calculations were performed with the Jaguar 7.0 [26] program's implementation of the DFT-B3LYP functional, which utilizes the Becke three-parameter functional (B3) [27] combined with the correlation function developed by Lee, Yang and Par (LYP)[28]. Vibrational frequencies typically do not depend strongly on the method and model used [29] so the use of another model and DFT method is appropriate. The positions of the Ni atoms were fixed at their respective positions from our slab calculations and the adsorbate was allowed to relax. The normal modes for the adsorbate were then used to calculate ZPE and 298.15K finite temperature corrections to the energy. Calculations of CH_4, CH_3, CH_2, CH and H_2 in the gas phase were used to compute the ZPE and 298.15K adiabatic bond energies and reaction enthalpies (ΔH) for these species based on rotational and vibrational modes, as well as the translational and PV contributions to the finite temperature correction. Surface species were assumed to be stationary and infinitely dilute, so that surface diffusion and site entropy are neglected.

3. Results

3.1. Ni(111) fcc slab (Figure 1)

Using the experimental cell parameters we calculate an optimum spin projection for bulk Ni (12 atoms per cell) to be ¾ unpaired electrons per Ni (9 unpaired spins per cell).

Fitting the energies for the M_s = 8/2, M_s = 9/2 and M_s = 10/2 spin polarization states to a parabola leads to an optimum spin polarization of 8.57 or 0.71 unpaired spins per Ni. This result agrees roughly with the experimental magnetization of bulk Ni of 0.61 [30]. Assuming a closed shell configuration for bulk Ni increases the energy of the 12 Ni atom unit cell by 21.5 kcal/mol or 1.8 kcal/mol per Ni.

For the bare Ni(111) surface we consider a four layer periodically infinite slab with four atoms per layer per unit cell (a $p(2\times 2)$ surface cell). We find a net spin polarization of 12 unpaired electrons for the 16 atoms in the unit cell leading to ¾ unpaired electron per slab Ni. The optimum spin is 12.38 unpaired spins or 0.77 unpaired spins per Ni. This optimum spin leads to a modest increase of 0.06 spins per Ni or 0.12 per surface atom from the bulk value, indicating the (111) surface has only a small effect on the magnetization. This negligible difference between the bulk and slab magnetism for Ni(111) agrees with previous Green's function calculations [31] (0.64 for bulk and 0.64 for six-layer slab) and tight-binding [32] calculations (0.59 for bulk and five-layer slab, 0.62 for three-layer slab). Assuming a closed shell configuration for the nickel slab increases the energy by 31.8 kcal/mol per cell or 2.0 kcal/mol per Ni atom.

The spin populations are 0.74 unpaired spins for surface atoms and 0.76 unpaired spins for central layers, indicating a very modest change in spin associated with the surface. The spin on all atoms is primarily confined to the d orbitals with 0.02 spin associated with the s orbitals of each atom.

We calculate that the four-layer bare Ni(111) fcc slab has a total surface energy of 130.7 kcal/mol per unit cell (2 surfaces with 4 atoms on each) or 16.3 kcal/mol per surface atom compared to the energy of bulk nickel. This value gives a surface energy of 2.11 J/m^2,

in reasonable agreement with experimental results (2.38 J/m^2, 2.45 J/m^2) [33, 34] and with other calculations (2.02 J/m^2, 2.01 J/m^2)[35, 36]. We find that the separation between the top layer and the second layer remains effectively fixed at the bulk value of 2.03 Å and that the energy decreases by a mere 0.1 kcal/mol when the slab structure is relaxed (the distance between atoms in the same layer remains fixed at the bulk value of 2.49 Å),

3.2. Adsorbed Species (Table 1)

3.2.1. H on Ni(111) (Figure 3)

We find that the most stable site for H_{ad} is the fcc site with a binding energy of E_{bond} = 65.7 kcal/mol leading to ΔH = -13.5 kcal/mol at 0K (relative to H_2 gas and ignoring the ZPE corrections). Correcting for ZPE leads to ΔH = -12.6 kcal/mol at 0K. Correcting for a finite temperature of 298.15 K leads to ΔH = -13.5 kcal/mol. Our results are in good agreement with flash desorption experiments (E_{bond} = 65 kcal/mol (estimated D_e); ΔH = -11.5 kcal/mol) [37].

Previous theoretical studies report binding energies of E_{bond} = 57.8 kcal/mol [9] from DFT(LDA) calculations on a Ni_{13} cluster, E_{bond} = 60.0 kcal/mol [38] from DFT (PW91) with plane-waves on a three-layer periodic slab, and E_{bond} = 64.6 kcal/mol [10] from DFT (PW91) periodic calculations with plane-waves on a five layer slab.

3.2.1.1. H at μ_3 fcc site

We calculate a snap bond energy of E_{snap} = 65.9 kcal/mol, indicating that binding H strains the Ni slab by 0.2 kcal/mol. We find a bond distance of $R_{H\text{-}Ni}$ = 1.72 Å to each of the three nearest surface Ni atoms. The net charge on the H atom is 0.21, and the three Ni atoms bonded to it each have a charge of -0.09, resulting in a dipole moment normal to the surface. There is no net spin on the H, while the same three Ni atoms bonded to it each

have a spin density of 0.67, 0.07 less than in the bare slab. Thus the lowest energy total spin projection for the slab is still $M_s = 12/2$, with a small amount of spin transfer among the Ni atoms to accommodate H binding to the slab. We find that the optimum spin of the slab is 11.77 unpaired spins, indicating that binding H decreases the spin of the slab by 0.59. For a covalent bond to a localized orbital on the surface, we would expect a decrease of 1.0. So a decrease of 0.59 indicates fairly localized bonding between H and the Ni orbitals. In fact, the reduction of the slab spin involves primarily the d_{z^2} orbitals of the three Ni atoms around the site, with the spin on each of these orbitals reduced by 0.07.

3.2.1.2. H at μ_3 hcp site

We calculate the binding energy to an hcp site to be 65.4 kcal/mol, 0.3 kcal/mol less than to an fcc site. Nevertheless, the H-Ni bond distances of $R_{H\text{-}Ni} = 1.72$ Å remain the same with similar charges and spin densities on all atoms.

3.2.1.3. H at μ_2 bridge site

We find that binding at a μ_2 bridge site is the saddle point on the NEB path between binding to adjacent fcc and hcp sites. The bond energy is 62.6 kcal/mol and the H-Ni bond distance of $R_{H\text{-}Ni} = 1.64$ Å between H and the two Ni atoms coordinating with it is 0.08Å shorter than for H binding at a μ_3 site (1.72 Å to three coordinating Ni atoms). Thus the barrier for H migration across the Ni(111) surface is 3.1 kcal/mol (neglecting ZPE and finite temperature corrections).

Upon binding, the slab spin is reduced by 0.59 to 11.79, reflecting a degree of covalent bonding on par with the bonding at μ_3 sites, as we might expect from the similar bond energies. Again, the reduction in spin is primarily associated with d_{z^2} orbitals on the two Ni atoms forming bonds with H, which each lose 0.11 in spin density.

3.2.1.4. H at μ_1 on-top site

Constraining H to an on-top site leads to a bond energy of E_{bond} = 52.7 kcal/mol, with a H-Ni bond distance of $R_{H\text{-}Ni}$ = 1.48 Å, a normal H-Ni single bond distance. Here the charge on the H is only 0.09 while the charge on the Ni bonded to H is -0.28, indicating polarization of the surface. Once again, the reduction of spin is associated with the d_{z^2} orbital of the Ni atom bonding with H. This orbital loses the majority of its spin (0.22 before and 0.07 after) in bonding to H, leading to an optimum spin for the slab of 11.93, which reflects a net reduction of 0.44 from the bare surface.

3.2.2. CH_3 on Ni(111) (Figure 4)

Methyl (CH_3) has energy minima for binding at both μ_1 and μ_3 sites, with the μ_3 fcc site being the most energetically favorable. The μ_2 site is a saddle point along the lowest energy pathway for migration between adjacent μ_3 sites, and is lower in energy than binding to a μ_1 site.

3.2.2.1. CH_3 at μ_3 fcc site

As with H, the fcc site is the most favorable binding location for CH_3, leading to an adiabatic bond energy of E_{bond} = 42.7 kcal/mol. The bound CH_3 has H-C-H bond angles of 107º and C-H distances of $R_{C\text{-}H}$ = 1.11Å, whereas in the gas phase the H-C-H bond angles are wider (120º for planar methyl) and the C-H bonds shorter ($R_{C\text{-}H}$ = 1.09Å, which is a normal C-H bond length). The H-C-H bond angles indicate sp^3 hybridization of C allowing an sp^3 orbital to point directly into the surface and bind to a partially occupied Ni interstitial orbital [39] in the μ_3 site. Keeping the CH_3 fixed at the chemisorbed structure leads to a snap bond energy of E_{snap} = 53.9 kcal/mol, 11.2 kcal/mol higher than E_{bond}. Of

this energy difference 10.6 kcal/mol is due to strain in CH_3 associated with changing the C hybridization from sp^2 to sp^3. The remaining 0.6 kcal/mol results from strain in the Ni slab.

The lowest energy integral value for the spin is still $M_s = 12/2$; however, we calculate an optimal spin of 11.54, which is 0.84 less than the bare Ni slab. This reduction in optimal spin indicates that CH_3 makes a covalent bond to a localized slab orbital. Most of the spin reduction in the slab is associated with the d_{xz} and d_{yz} orbitals on three surface Ni atoms bound to CH_3, which each have their spin reduced by between 0.11 and 0.08. This reduction of spin in the d orbitals rather than the s orbitals suggests that linear combinations of d orbitals lead to the molecular orbital at the fcc interstitial site (as in the interstitial electron model[39]) that bonds to the sp^3 orbital of CH_3. An alternative interpretation is that the C sp^3 orbital bonds with an interstitial orbital formed primarily from s electrons, but that the spin reduction is passed off to nearby d orbitals. A large drop in the center of the s band associated the three Ni atoms involved in bonding (-4.19 eV to -5.19 eV) supports this latter interpretation. The covalent nature of the bonding is also evident in the near absence of spin on the adsorbate atoms (0.00 for all three H atoms and 0.05 for C).

Particularly interesting is the eclipsed orientation of the C-H bonds at the surface. They overlap the Ni atoms (H-Ni distance of $R_{H\text{-}Ni}$ = 2.09 Å) indicating an agostic interaction in which the polarized C-H bond (charges of -0.56 for C and 0.20 for each H) is partially stabilized by the surface Ni atoms (which have no net charge). The staggered configuration is 7.8 kcal/mol higher in energy, indicating that each agostic interaction is worth 2.6 kcal/mol.

An alternative interpretation is that there are repulsive Pauli repulsions between the C-H bonds and the metal band orbitals that are stronger in the staggered configuration. In the staggered configuration the H-Ni distances (R_{H-Ni} = 2.49 Å, 2.51Å and 2.55 Å) increase by ~ 0.40 Å (with six long Ni-H bonds instead of three short ones) as the C moves slightly out of the center of the fcc site toward one of the Ni atoms. The C-H distances decrease to 1.10 Å, a typical C-H single bond length, indicating normal C-H bonds.

3.2.2.2. CH_3 at μ_3 hcp site

Binding at an hcp site is similar, except that methyl sits 0.01 Å farther away from the surface, leading to an adiabatic bond energy of E_{bond} = 42.3 kcal/mol, which is 0.4 kcal/mol weaker than binding at an fcc site. The preference for the fcc site can be understood in terms of the interstitial electron model [39], in which the s (or possibly d) electrons in nickel (d^9s^1) form interstitial bonding orbitals, which—along with localized bonds involving the d orbitals—are responsible for bonding between metal atoms and anything bonded to the metal. Because Ni prefers an fcc structure over an hcp structure, we expect that a better bond can be formed with an interstitial orbital at an fcc site than at an hcp site. Because the C sp^3 orbital binding to a Ni μ_3 site points toward the interstitial orbital in the μ_3 site rather than toward the d orbitals on particular Ni atoms, we expect it to bind with an interstitial orbital and hence prefer the fcc site.

3.2.2.3. CH_3 at μ_2 bridge site

The lowest energy pathway for CH_3 migration between adjacent μ_3 sites leads to a TS at the μ_2 bridge site. Our NEB calculation of this TS for CH_3 gives a bond energy at a bridge site of E_{bond} = 39.3 kcal/mol, leading to a surface migration barrier of 3.4 kcal/mol (neglecting ZPE and finite temperature corrections). The snap bond energy is E_{snap} = 50.5

kcal/mol, indicating a total strain of 11.2 kcal/mol. Most of this strain (10.0 kcal/mol) is the result of rehybridizing CH_3 to give an approximately tetrahedral geometry, as in the cases of CH_3 binding at μ_3 sites.

Over the course of the migration one of the H atoms remains anchored above one of the Ni atoms bounding the intermediate bridge site, (with $R_{C\text{-}Ni}$ changing from 2.09 Å to 2.07 Å to 2.10 Å), so that the net motion of the CH_3 is a cartwheel in which one H remains over one Ni as the other two rotate over the bridge site. The C sp^3 orbital bonds to a Ni d_{z^2} orbital at the μ_2 saddle point with a Ni-C bond distance of 2.07 Å. This covalent bond is reflected in the reduction of the spin of the d_{z^2} orbital on the relevant Ni. The Ni-C-H bond angles at the saddle point are 100º, 101º and 134º which average to the value of 112º, the value for the μ_3 sites. The methyl H-C-H angles are 106º, 106º and 110º which average to the value of 107º, the same value as for binding at μ_3 sites. These angles indicate that the sp^3 hybridization of C is maintained over the course of the migration.

3.2.2.4. CH_3 at μ_1 on-top site

Methyl is stable binding at the μ_1 on-top site but the bond energy (E_{bond} = 37.2 kcal/mol) is 5.5 kcal/mol weaker than for the μ_3 fcc site. The C-Ni bond distance (R_{CNi} = 1.97 Å) is close to the normal value for a C-Ni covalent bond (the C-Ni bond distance in $NiCH_3$ is 1.88 Å). At the μ_1 site, the CH_3 prefers the staggered configuration with respect to the nearest Ni atoms. The H-Ni distances range from 2.94 Å to 3.08 Å, which we consider as too long for an agostic interaction. In this case the staggered geometry is expected because it leads to weaker Pauli repulsions between the C-H and surface bonds.

The snap bond energy is 45.7 kcal/mol, with 6.9 kcal/mol coming from strain in CH_3 and 1.5 kcal/mol from strain in the Ni slab. The C-H bond distances are all $R_{C\text{-}H}$ = 1.10 Å

and the H-C-H angles are all 110 º, indicating sp^3 hybridization and normal C-H bonds. The adsorbate is highly polarized with a negative charge of -0.51 on C and positive charges of +0.17 on each H. There is only a small negative charge (-0.10) on the Ni atom bonded to C, but the spin density on that Ni atom is reduced by 0.30 to 0.46 leaving the C with almost no net spin density, 0.02. We calculate an optimal spin of 11.80 for the slab, which is 0.58 less than the bare slab. The d_{z^2} orbital on the Ni bonded to CH_3 is associated with the reduction in spin, suggesting that it is the orbital primarily involved in forming the σ covalent bond to CH_3.

3.2.2.5. CH_3 summary

In binding to all four simple sites on Ni(111), CH_3 is sp^3 hybridized with bonding that can be explained in terms of the C sp^3 dangling bond orbital forming a bond to either the d_{z^2} orbital of a particular Ni atom or with the interstitial orbital at a μ_3 site. Agostic interactions between H and Ni are also important in stabilizing CH_3 binding at μ_2 and μ_3 sites. Thus, the CH_3 binding energy to a μ_3 fcc site on Ni(111) of 42.7 kcal/mol includes a Ni-C bond worth 35.1 kcal/mol, and 7.6 kcal/mol of additional stabilization from agostic Ni-H interactions. Because binding at the on-top site does not involve agostic interactions, the binding energy is only 37.2 kcal/mol. A μ_2 bridge site is intermediate between these since it is stabilized by a single agostic interaction.

An alternative explanation of the eclipsed structure for CH_3 at the μ_3 site is that binding in the μ_3 site leads to strong Pauli repulsions due to interactions with the surface. This explanation would imply that substituting C-H bonds with C-CH_3 bonds would dramatically increase this repulsion, leading to stabilization at the μ_1 site. Indeed, we find

that CH_2CH_3, $CH(CH_3)_2$, and $C(CH_3)_3$ all prefer the μ_1 site by increasing amounts, (0.3 kcal/mol for CH_2CH_3, 8.4 kcal/mol for $CH(CH_3)_2$, and 10.3 kcal/mol for $C(CH_3)_3$.

3.2.3. CH on Ni(111) (Figure 5)

Methylidyne (CH) binding to Ni(111) is stable only for binding at three-fold μ_3 sites, with the hcp site more stable than the fcc site. The μ_2 site is a saddle point on the lowest energy pathway between adjacent μ_3 sites.

3.2.3.1. CH at μ_3 hcp site

The hcp site is preferred by 0.9 kcal/mol over an fcc site, with a binding energy of E_{bond} = 148.9 kcal/mol.

There is some question regarding the selection of the reference state of CH in computing the snap bond energy. The ground state of CH is the $^2\Pi$ state but this state has only one unpaired spin. The $^4\Sigma^-$ excited state of CH is calculated to be 6.3 kcal/mol higher in energy, but has three unpaired spins available for bonding. The decrease of the optimum spin polarization of the slab from 12.38 to 10.06 upon binding the CH suggests that $^4\Sigma^-$ is the appropriate reference state. This reference state leads to a snap bond energy of E_{snap} = 157.2 kcal/mol, 8.3 kcal/mol stronger than the adiabatic bond energy. Of this energy difference, 1.4 kcal/mol is from Ni slab strain and 6.9 kcal/mol is promotion of the C orbitals to the quartet state, which corresponds with the C-H bond length decreasing from $R_{C\text{-}H,\ gas}$ = 1.14 Å to $R_{C\text{-}H,\ ad}$ = 1.10 Å.

The symmetry of the Ni-C bond distances (all 1.85 Å) and Ni-C-H angles (all 126º) is consistent with either of two bonding configurations. One model is in terms of a C *sp* hybridized orbital forming a σ bond to an interstitial orbital and the remaining *p* orbitals forming two π bonds to d_{z^2} orbitals on surrounding Ni atoms. In this case, resonance in the

π system would result in equivalent bonds to all three Ni atoms to give the observed symmetry. The other possibility is that C is sp^3 hybridized and forms three equivalent σ bonds to the three Ni atoms surrounding the μ_3 site. The absence of spin on the adsorbate and the decrease in spin on each of the three Ni atoms surrounding the site from 0.74 to 0.21 is consistent with either scenario, as is the reduction in spin of the Ni atoms being primarily associated with their d_{z^2} orbitals.

3.2.3.2. CH at μ_3 fcc site

Binding to an fcc site shows similar trends with a binding energy of E_{bond} = 148.0 kcal/mol, and symmetric C-Ni bond distances of $R_{C\text{-}Ni}$ = 1.86, Ni-C-H angles of 126º, and Ni-C-Ni angles of 85º. The slightly longer C-Ni bond distances correspond with the small, 0.9 kcal/mol, decrease in binding energy. Because of the important role that Ni d orbitals play in the bonding, we can rationalize this slight preference for binding to an hcp site over an fcc site by assuming that the bonding takes place via three σ bonds to the three Ni atoms around the μ_3 site. The idea is that for the hcp geometry the three C-Ni σ bonds make C-Ni-Ni_{hcp} angles of 93º to the Ni-Ni bonds between the first (top) and second (hcp) layers of Ni atoms in the slab. Similar angles in the fcc geometry are 163º. Thus, the d orbitals of a Ni atom on the surface would be more easily directed toward the sp^3 orbitals of CH at a μ_3 hcp site, than those of a CH at a μ_3 fcc site, because d orbital lobes prefer 90º orientations with each other. This preference for μ_3 hcp sites provides a contrast with the case of CH_3 which binds to an interstitial orbital at a μ_3 site and thus prefers μ_3 fcc sites over μ_3 hcp sites.

3.2.3.3. CH at μ_2 bridge site

The lowest energy pathway between μ_3 sites crosses a bridge site where CH binds to the surface with a binding energy of E_{bond} = 139.4 kcal/mol, leading to a barrier of 9.5 kcal/mol.

The energy for exciting CH to the quartet state and constraining the C-H bond distance to $R_{C-H,ad}$ = 1.10 Å in CH as it binds to the surface is 6.9 kcal/mol, and the strain on the Ni slab is worth 3.7 kcal/mol giving a snap bond energy of E_{snap} = 150.0 kcal/mol. The C-Ni bond distances with the Ni atoms bounding the μ_2 site are R_{C-Ni} = 1.80 Å, indicating strong C-Ni bonds.

The covalent nature of the bonding is evident in the absence of spin on the adsorbate and the reduction of the optimal spin of the slab from 12.38 to 10.42. This reduction of spin is primarily reflected in loss of spin from the s and d orbitals of the two Ni atoms forming bonds with C. While all of the d orbitals are affected, the d_{z^2} orbitals show the largest reduction in spin (0.20 each).

The symmetric nature of the transition state (equal C-Ni bond distances: R_{C-Ni} = 1.80 Å, and H-C-Ni angles: 132º) could be consistent with either sp or sp^2 hybridization. The sp case seems less likely because it would involve a σ bond with a bridge site—i.e. the space between surface Ni atoms. The sp^2 case would lead to two σ bonds to Ni atoms leaving a π bond with the two interstitial sites adjacent to the bridge site. This orbital configuration is consistent with sp^3 hybridization at μ_3 sites, so that migration between adjacent sites simply converts the sp^3 orbital bond to the Ni-C bond being broken into a p orbital parallel to the surface at the TS, and an sp^3 orbital bonding to the new Ni-C σ bond at the new μ_3 site.

3.2.3.4. CH at μ_1 on-top site

Constraining CH to an on-top site, leads to an adiabatic bond energy of E_{bond} = 99.5 kcal/mol. The short C-Ni distance, $R_{C\text{-}Ni}$ = 1.66 Å, indicates a strong bond. The snap bond energy is E_{snap} = 108.4 kcal/mol, since exciting CH to the quartet state and compressing the C-H bond distance from $R_{C\text{-}H,\ gas}$ = 1.14 Å to $R_{C\text{-}H,\ ad}$ = 1.09 Å costs 6.9 kcal/mol, and the strain on the Ni slab is worth 2.0 kcal/mol.

The geometry requires *sp* hybridization in order for C to form a σ bond to the surface Ni atom and an sp σ bond to H. This orbital configuration leaves two *p* orbitals parallel to the surface for π bonding. The bonding leaves 0.20 spins on C suggesting that the π bonding is incomplete. The optimal spin for the slab of 10.92 is higher than in the case of "complete" bonding to higher coordination sites (10.24 & 10.06 for μ_3 sites). The reduction in the spin of the slab that we see is particularly associated with the Ni atom bonding to C, which has a total spin of 0.22. The d_{z^2} orbital makes the largest contribution to bonding (0.17), followed by d_{xz} and d_{yz}. Unlike most of the other cases of Ni bonding to C, there is a negative charge of -0.14 associated with this Ni atom.

3.2.3.5. CH summary

In the case of CH_3, C was sp^3 hybridization for binding at any of the four high symmetry sites. This consistency in hybridization is the case because there is only one unpaired electron on CH_3 which allows for only a single bond to be formed to the Ni(111) surface. By contrast, the three unpaired electrons in CH can form up to three bonds with the Ni(111) surface leaving C free to adopt *sp*, sp^2 or sp^3 hybridization. The geometry at an on-top site is consistent with *sp* hybridization, because there is only one Ni with which to form a σ bond. Similarly, because there are two Ni atoms available for σ bonding at a μ_2

site, sp^2 hybridization is most plausible. The availability of interstitial electron density at a μ_3 site allows the CH to form either one σ bond and two π bonds (sp hybridization) or three equivalent σ bonds (sp^3 hybridization). Either is consistent with our results; however, sp^3 hybridization seems more likely.

Simplistically we could consider the Ni-C bonding as three bonds worth ~50 kcal/mol each for μ_3 sites, two bonds worth ~70 kcal/mol each for a μ_2 bridge site, and one bond worth ~100 kcal/mol for a μ_1 site. We might further partition the bond energy in the latter two cases into ~50 kcal/mol for a σ bond, ~40 kcal/mol for a π bond perpendicular to a bridging site, and ~25 kcal/mol for each π bond above an on-top site. Assuming sp^3 hybridization at μ_3 sites is then compatible with considering the bonding in terms of three σ bonds each worth ~50 kcal/mol. Alternatively, assuming *sp* hybridization at a μ_3 sites leads to two π bonds each worth ~50 kcal/mol.

3.2.4 C on Ni(111) (Figure 6)

Like CH, C is stable binding at μ_3 sites, but not μ_2 or μ_1 sites. The μ_2 site is lower in energy than the μ_1 site, and is a saddle point between adjacent μ_3 sites.

3.2.4.1. C at μ_3 hcp site

Binding to a μ_3 hcp site is most favorable, with a binding energy of E_{bond} = 154.8 kcal/mol and C-Ni bond distances of $R_{C\text{-}Ni}$ = 1.78 Å. In computing the snap bond energy we take the reference state for C as the ground state, the ^{3}P state. There is an the excited ^{5}S state, 82.6 kcal/mol higher in energy that could make up to four covalent bonds, but the strength of Ni-C single bonds is not sufficient for such a promotion. We calculate a snap bond energy of E_{snap} = 156.4 kcal/mol indicating a Ni surface strain of 1.6 kcal/mol.

The absence of a net spin on C is consistent with a model in which there is a doubly occupied $2s$ lone pair with the two unpaired spins in p_x and p_y orbitals parallel to the surface forming two π bonds with the surface.

The covalent bonds with the slab reduce the slab's optimal spin from 12.38 to 9.87 in binding C, suggesting the formation of at least 2½ bonds to the surface. This reduction in spin primarily affects the three Ni atoms surrounding the μ_3 site, which are reduced by 0.61 each. All of their d orbitals are affected, but the d_{z^2} orbitals have the largest decrease in spin (0.20 each). This decrease in spin of greater than 2.00 suggests some back bonding from the surface into the empty p_z orbital (i.e. some promotion toward the ^{5}S state). However, the nearly neutral charge of C, -0.03, indicates very little net electron charge transfer.

3.2.4.2. C at μ_3 fcc site

Binding to an fcc site is 1.6 kcal/mol less stable than to an hcp site with a binding energy of E_{bond} = 154.8 kcal/mol, but with the same C-Ni bond distances, $R_{C\text{-}Ni}$ = 1.78 Å, and similar Ni-C-Ni angles of 91º. As in the case of CH, the preference for binding to an hcp site over an fcc site might involve the preference for C-Ni-Ni_{hcp} bond angles of 89º (which is the case for hcp sites) compared with the analogous angles of 158º in the case of binding to an fcc site.

3.2.4.3. C at μ_2 bridge site

The lowest energy pathway for C to migrate between μ_3 sites is to cross a bridge site. The binding energy to this site is E_{bond} = 143.1 kcal/mol, leading to a surface migration barrier of 11.7 kcal/mol. The snap bond energy is E_{snap} = 147.6 kcal/mol, indicating a strain

on the Ni slab worth 4.5 kcal/mol in this TS. The C-Ni bond distances are all $R_{C\text{-}Ni}$ = 1.72 Å, and the Ni-C-Ni angles are all 103º.

As in the case of binding at a μ_3 site, there is no spin left on C after bonding, suggesting two bonds to the surface with a lone pair of electrons pointing away from the surface. The geometry of the site suggests sp^2 hybridization with the non-bonding electron pair pointing away from the surface while two of the remaining sp^2 orbitals each bond with a surface Ni atom. However, the optimal spin of the slab, 10.04, suggests a covalent bond order greater than 2. Again, the additional bonding could be due to back bonding into the empty p orbital parallel to the surface; however, the negative charge on C of -0.10 is not consistent with this interpretation.

3.2.4.4. C at μ_1 on-top site

Constraining C to be at a μ_1 on-top site leads to a bond energy of E_{bond} = 103.6 kcal/mol and a C-Ni distance of $R_{C\text{-}Ni}$ = 1.64 Å. We expect C to be sp hybridized with one sp orbital forming a σ bond with the Ni atom at the on-top site, and the other housing an unpaired electron. The remaining two valence electrons then form two π bonds to the surface. However, this electronic configuration is not consistent with the absence of spin on C. The reduction of the optimal spin of the slab by 1.42 supports a covalent bond order of two or less. The d orbitals on the Ni binding to C, and especially the d_{z^2}, d_{xz} and d_{yz} orbitals are involved in this reduction in spin.

3.2.4.5. C summary

The bond energies for C and CH to the surface are similar with all bonds being ~5 kcal/mol stronger for C than CH. About half of this difference is explained by ~3 kcal/mol worth of strain in the C-H bond distance for the CH case. The remainder of this difference,

~2 kcal/mol, is apparently due to stronger bonding of C to the surface. This difference in bonding is reflected in the shorter Ni-C bond distances for C versus CH respectively at the μ_1 sites (1.64 Å and 1.66Å reflecting an energy difference of 0.3 kcal/mol), at μ_2 sites (1.72 Å and 1.80 Å reflecting an energy difference of 0.8 kcal/mol each) and at μ_3 sites (1.78 Å and 1.85 Å reflecting an energy difference of 1.0 kcal/mol each). The trends in the optimal spins of the slab are consistent with these distance and energy trends.

Starting with CH bonded to the surface and removing H would lead to an unpaired electron on C in an orbital pointing away from the surface. Thus we might expect C to exhibit similar bonding to CH. The only difference would be an unpaired electron pointing away from the surface instead of H. The similar bond energies and bond distances for C and CH at the various sites support this description. Alternatively, an electron pair on C pointing away from the surface might result in no net spin on C, while weakening the bonding to the surface by one bond order. In this case we might expect the bonding to bear some resemblance to CH_2 binding to the surface. However, the absence of unpaired spin density on atomic C bonded to the surface, as well as the larger reduction of net spin on the slab for binding to C than for binding to CH, indicates that a third option must be available. Apparently the unpaired electron in the C is able to pair with unpaired spin in the slab, reducing the net spin of the system.

3.2.5. CH_2 on Ni(111) (Figure 7)

Methylene (CH_2) is stable binding at both μ_3 and μ_2 sites. A μ_3 fcc site is the most favorable binding location with a μ_2 site serving as the TS along the lowest energy pathway between adjacent μ_3 sites.

3.2.5.1. CH_2 at μ_3 fcc site

Binding at a μ_3 fcc site is most favorable with an adiabatic bond energy of E_{bond} = 89.3 kcal/mol. Binding to the μ_3 fcc site leads the C to rehybridize from sp^2 in the gas phase ($R_{C\text{-}H,\ gas}$ = 1.08 Å and H-C-H = 134º) to sp^3 ($R_{C\text{-}H}$ = 1.10 Å and 1.14Å with H-C-H = 104º) at an energetic cost of 9.9 kcal/mol. The snap bond energy of E_{snap} = 100.0 kcal/mol indicates a strain on the Ni slab worth 2.3 kcal/mol.

With two H atoms bonding to two sp^3 orbitals, there remain two singly occupied orbitals to bind to the surface. At a μ_3 fcc site the electrons in these orbitals form σ bonds ($R_{C\text{-}Ni}$ = 1.94 Å) with two of the three Ni atoms at the corners of the μ_3 site (the third Ni-C distance is $R_{C\text{-}Ni}$ = 2.02 Å). One of the H atoms sits above the third Ni atom of the μ_3 site resulting in a favorable agostic interaction, while the other H points away from the surface (at an angle of 43º with respect to a vector normal to the surface).

The optimal spin of the Ni surface is reduced by 1.50, to 10.88, consistent with forming two bonds to CH_2. The two Ni atoms closest to C, have their spins reduced by 0.35 (mostly in their d_{z^2}, d_{xz} and d_{yz} orbitals) evidencing their role in the covalent bonding.

The H coordinating with the third Ni atom around the μ_3 site has a positive charge, 0.20, resulting in a favorable agostic interaction with the Ni atom. This agostic interaction is evidenced in the Ni-H distance of $R_{H\text{-}Ni}$ = 1.85 Å and the increased C-H bond length of $R_{C\text{-}H}$ = 1.14 Å. The H-Ni distance suggests an agostic interaction significantly stronger than for CH_3 (where $R_{H\text{-}Ni}$ = 2.09 Å with an interaction energy of 2.6 kcal/mol), but still much longer than a normal H-Ni bond, which has a bond length of $R_{H\text{-}Ni}$ = 1.48 Å. Unlike the other Ni atoms in the surface, the Ni atom involved in the agostic interaction has a small negative charge, -0.06, which is consistent with the agostic interaction.

3.2.5.2. CH_2 at μ_3 hcp site

Binding at an hcp site is similar, except that the interaction is 0.7 kcal/mol weaker with a bond energy of E_{bond} = 88.6 kcal/mol and a snap bond of E_{snap} = 99.4 kcal/mol. The bond distances and angles are almost exactly the same. Because C forms σ bonds to individual Ni atoms, rather than interstitial orbitals, we might expect a slight preference for the hcp site as is the case for CH and C. The C-Ni-Ni_{hcp} angles (~110º & ~ 167º for the fcc site, and ~ 95º & ~140º for the hcp site) are consistent with this reasoning, although they predict a weaker preference than for the other cases.

The key difference between CH_2 and either C or CH binding to μ_3 sites, is the agostic interaction in the case of CH_2. This interaction can be viewed as an electrostatic interaction between Ni and H, or as a three-body bond involving C, H and Ni, in which interstitial electron density might make an important contribution. This possible role of interstitial electron density could explain the preference here for fcc over hcp sites.

3.2.5.3. CH_2 at μ_2 bridge site

Methylene also forms a stable bond to a bridge site with a bond energy of E_{bond} = 83.9 kcal/mol. Because the H-C-H angle (109º) is not strained as much as for fcc or hcp sites (104º) the energy cost to promote the C atom in CH_2 from sp^2 (134º) to sp^3 (109º) is only 6.5 kcal/mol resulting in a snap bond energy of E_{snap} = 91.3 kcal/mol.

As in the case of binding at μ_3 sites the two singly occupied sp^3 orbitals form σ bonds with the two Ni atoms bounding the bridge site. As in previous cases the covalent nature of the bonding is evident in spin reduction on C (2.00 to 0.06) and the d_{z^2}, d_{xz} and d_{yz} orbitals on the Ni atoms in the bonds (0.74 to 0.44). An optimal spin of 11.04 for the slab results, which means there is a reduction of 1.34 due to binding CH_2.

Here the H atoms are too far away from Ni atoms for appreciable agostic interactions (R_{HNi} = 2.55, 2.50 Å). The absence of stabilizing agostic interactions explains why the bonding is weaker than at μ_3 sites.

3.2.5.4. CH_2 at μ_1 on-top site

Constraining CH_2 to bind at an on-top site leads to an H-C-H angle of 113º (compared with 134º in the gas phase), which has an energy cost of 4.5 kcal/mol. The sp^2 lobe not bonded to one of the H atoms forms a σ bond to the Ni atom at the on-top site, while the p orbital parallel to the surface forms a weak π bond with the surface. This geometry gives a binding energy of E_{bond} = 66.0 kcal/mol, and a C-Ni bond length of $R_{C\text{-}Ni}$ = 1.78 Å. The snap bond energy of E_{snap} = 71.1 kcal/mol indicates a strain on the Ni slab worth 0.6 kcal/mol.

The covalent nature of the bonding is evident in the reduction of spin on C to 0.26 from 2.00 in the gas phase and in the reduction of the optimal slab spin from 12.38 to 11.62. Again, this reduction of spin involves primarily the d_{z^2}, d_{xz} and d_{yz} orbitals on the Ni atom

The bond distance and energy for CH_2 to a μ_1 site (E_{bond} ~70 kcal/mol and $R_{C\text{-}Ni}$ ~1.80 Å) can be compared to CH at the same site (E_{bond} ~ 100 kcal/mol and $R_{C\text{-}Ni}$ ~1.65 Å), indicating that the second π bond is worth ~30 kcal/mol, and decreases the C-Ni bond distance by 0.15 Å.

3.2.5.5. CH_2 summary

Methylene uses sp^3 orbitals to form two σ bonds with Ni d orbitals at both μ_2 and μ_3 sites. The superior binding at the fcc site results from favorable Ni-H agostic interactions. At a μ_1 site a sp^2 orbital forms a σ bond with the d_{z^2} orbital of an underlying Ni atom

while the leftover p orbital participates in a π bond with d_{xz} and d_{yz} orbitals on the same Ni atom.

3.2.6. Summary and General Discussion of CH_x Binding on Ni(111)

The key features of the binding of CH_x species at the four high symmetry sites on Ni(111) can be explained by making two assumptions about the orbital properties of Ni.

First, each Ni atom prefers to form only a single σ bond with an adsorbed molecule. This preference comes about because the $3d$ orbitals on Ni, important in σ bonds with individual Ni atoms, are highly localized compared to the $4s$ orbital. As a result they form good σ bonds with orbitals pointed directly toward them, but do not overlap well with the more diffuse orbitals involved in forming π bonds. For CH_x species the result is that π bonds centered over particular Ni atoms are weak, and result in energetically unfavorable structures. Thus, binding at on-top sites is only stable for species that want to form a single bond to the surface (i.e. CH_3), and binding at bridge sites is only stable for species that form exactly two bonds to the surface (i.e. CH_2).

Second, the electrons from the Ni $4s$ (or possibly $3d$) orbitals combine to form interstitial orbitals, located in tetrahedral interstitial sites in the bulk and at μ_3 sites on the surface. These interstitial orbitals have a slight preference for fcc sites over hcp sites. Interstitial orbitals allow for more diffuse bonding at μ_3 sites than d orbitals allow at μ_1 sites, resulting in stronger bonds at μ_3 sites for cases in which the orbital configuration of the adsorbate is unable to match the geometrical constraints of on-top site binding. This preference is evident in the case of H binding at μ_1 and μ_3 sites. At a μ_1 site the weaker overlap of the H $1s$ orbital with the Ni atomic orbitals leads to a bond which is 13.0 kcal/mol weaker than for the bond to an interstitial orbital at a μ_3 site. These interstitial

orbitals are also capable of forming strong π bonds with *p* orbitals parallel to them, as is evident from the strong binding of C and CH at μ_2 sites.

Finally, by considering the number of each type of bond that each species forms to the surface, we can explain the approximate binding energies of C and the various CH_x species at all four sites. We assume that a σ bond to either a surface atom or an interstitial site is worth ~50 kcal/mol, a π bond across a bridge site is worth ~40 kcal/mol, and π bond to a Ni atom is worth ~25 kcal/mol. These assumptions then predict that C and CH should have the same binding trends: ~ 150 kcal/mol from three σ bonds at μ_3 sites, ~140 kcal/mol from two σ bond and one strong π bond at μ_2 sites, and ~100 kcal/mol from one σ bond and two weak π bonds at μ_1 sites. For CH_2 they lead to ~100 kcal/mol from two σ bonds at both μ_3 and μ_2 sites, and ~75 kcal/mol from one σ bond and one weak π bond at μ_1 sites. Finally, CH_3 binds at all sites with a single σ bond worth ~50 kcal/mol. Thus, we can explain the snap bond energies within 6 kcal/mol for all but one case, CH_2 binding at a μ_2 site. Other factors covered in the detailed discussion above, such as agostic interactions and steric effects, are required to explain the binding energies in greater detail. Nevertheless, this simple model with three types of bonds being the only factors considered provide a rationalization of the basic trends.

3.2.7. Discussion of Surface Diffusion Barriers

In all cases μ_3 sites are the preferred binding sites and the lowest energy pathway between μ_3 sites has a TS at a μ_2 site. Ignoring ZPE and finite temperature effects the diffusion barriers are: 11.7 kcal/mol for C, 9.5 kcal/mol for CH, 5.4 kcal/mol for CH_2, 3.4 kcal/mol for CH_3, and 3.1 kcal/mol for H. The obvious trend is that species bonding more strongly to the surface have larger diffusion barrier energies.

In all cases the binding to on-top sites is much weaker, making them unlikely to play a significant role in migration under low coverage conditions

3.3. Reactions & Transition States (Table 2)

3.3.1. $CH_3 \rightarrow CH_2 + H$ on Ni(111) (Figure 8)

The TS for dissociating $CH_{3,ad}$ on Ni(111) to form $CH_{2,ad} + H_{ad}$ has an energy of $E_{barrier}$ = 18.4 kcal/mol above the ground state of the reactant. This barrier leads to a product state lying 8.2 kcal/mol in energy above the reactant with $CH_{2,ad}$ bonded at an fcc site and H_{ad} at the nearby hcp site sharing a single common Ni surface atom. Allowing the products to further separate and move to their individually preferred binding sites, lowers the energy of the final product so that the reaction is endothermic by only $E_{reaction}$ = 1.3 kcal/mol.

At the TS the leaving H atom sits near an on-top site, forming a bond with the Ni atom below. The H-Ni bond distance is $R_{H\text{-}Ni}$ = 1.50 Å, which is similar to the bond distance of $R_{H\text{-}Ni}$ = 1.48 Å for H binding at an on-top site. There is also a positive charge of 0.13 on H and a negative charge of -0.20 on Ni, suggesting a favorable electrostatic interaction.

The C-H bond being broken is stretched to $R_{C\text{-}H}$ = 1.80 Å at the TS, well beyond the length of a typical C-H single bond (1.10 Å), suggesting that the C-H bond is already broken at the TS. Thus, as the C-H bond breaks, the leaving H atom forms a bond with a Ni atom at one of the corners of the μ_3 fcc site, and then moves to a neighboring μ_3 site. The new H-Ni bond stabilizes the dehydrogenation pathway, showing exactly how this process is catalyzed on Ni(111).

In the reactant C is sp^3 hybridized, binding to three H atoms, with the fourth orbital forming a bond to the Ni interstitial orbital directly below the μ_3 site. In the product, CH_2,

C is also sp^3 hybridized, with two orbitals forming bonds to the two H atoms and the other two bonding with d orbitals on two of the Ni atoms at the corners of the μ_3 site.

The H-C-H angle involving the two H atoms maintaining their bonds to C remains constant over the course of the reaction (107º in the reactant, 106º in the TS, and 105º in the product), indicating sp^3 hybridization throughout the whole reaction. Thus, the reaction pathway requires one sp^3 orbital to exchange its bond to the leaving H atom for a bond to a Ni atom. Simultaneously, the sp^3 orbital binding to the interstitial site in the reactant transfers its bond to a particular Ni. The other two sp^3 orbitals maintain their bonds with the H atoms not dissociating from C.

One of the remaining H atoms maintains its agostic interaction with Ni at the transition state. This interaction is evident in the H-Ni distance ($R_{H\text{-}Ni}$ = 2.09 Å in the reactant, 2.10 Å at the transition state and 1.94 Å in the product). The other H loses its agostic interaction as the H-Ni distance increases steadily from 2.09 Å to 2.54 Å over the course of the reaction. The distance of $R_{H\text{-}Ni}$ = 2.32 Å at the TS indicates that the agostic interaction has already decreased significantly.

We calculate that the optimal spin of the slab decreases over the course of the reaction from 11.54 for the initial product to 10.41 for the final product. This decrease in spin is due to forming new H-Ni and C-Ni covalent bonds. The optimal spin for the slab at the TS lies part way between these at 11.02, suggesting partial formation of these new bonds.

The d orbitals on the Ni atom inserting into the C-H bond are involved in bonding both C and H at the TS, leading to a large spin reduction of 0.35 on the inserting Ni atom. The d_{xz} and d_{yz} orbitals play the largest role among the Ni orbitals in bonding, followed by

d_{z^2}. This participation is reasonable since H is beyond the on-top site at the TS (and thus more in line with the d_{xz} and d_{yz} orbitals than the d_{z^2} orbital), while the CH_2 seeks additional bonding from these same orbitals during the reaction

The Ni atoms at the other corners of the μ_3 site remain involved in bonding with C, as reflected in spin reductions associated with their d_{xz} and d_{yz} orbitals.

3.3.2 CH_2 → CH + H on Ni(111) (Figures 9 & 10)

The next step in the decomposition of $CH_{3,ad}$ is $CH_{2,ad}$ → CH_{ad} + H_{ad}. The lowest energy pathway for this process has a reaction barrier of $E_{barrier}$ = 8.2 kcal/mol relative to the ground state of $CH_{2,ad}$. This process leads directly to CH_{ad} at an fcc site and H_{ad} at the hcp site sharing a single common surface Ni atom. The co-adsorbed products (on a $p(2\times 2)$ periodically infinite slab) are 6.5 kcal/mol lower in energy than the reactant, while the final products (allowed to dissociate further) are an additional 3.7 kcal/mol lower in energy, giving an overall reaction energy of $E_{reaction}$ = -10.2 kcal/mol.

Once again the TS has the leaving H near an on-top site with a Ni-H bond distance of $R_{H\text{-}Ni}$ = 1.49 Å. The C-H distance at the TS is $R_{C\text{-}H}$ = 1.69 Å and indicates a broken C-H bond. As before, Ni(111) stabilizes this dehydrogenation step by providing a Ni atom to bond the H as the C-H bond breaks

Over the course of this reaction we find that the optimal spin of the slab reduces from 10.88 to 9.75, with 10.23 at the TS. This reduction of spin over the course of the reaction is consistent with a partially formed H-Ni bond and stronger C-Ni bonding at the TS. Again, the d_{xz} and d_{yz} orbitals on the Ni atom being inserted into the C-H bond show the largest reduction in spin (0.38), reflecting their significance in stabilizing both C and H as they break their bond.

The reactant has C sp^3 hybridization, however the bonding in the product may be sp^3 or sp hybridized. If the product, CH, has an sp^3 hybridized C, then the reaction simply involves transferring an sp^3 orbital from binding with H to forming another σ bond with d orbitals on the third Ni around the μ_3 site. If the product is sp hybridized then the only bond C strictly retains over the course of the reaction is a σ bond to the remaining H. The σ bond with the other H is broken in exchange for a π bond to the Ni surface. The two σ bonds to particular Ni atoms are transformed into a σ bond with interstitial electron density in the μ_3 site and a second π bond to the Ni surface.

3.3.3 CH → C + H on Ni(111) (Figure 11)

The final step in the dehydrogenation of $CH_{3,ad}$ on Ni(111) converts CH_{ad} to C_{ad} and H_{ad}. The lowest energy pathway has a TS which is $E_{barrier}$ = 32.8 kcal/mol higher in energy than the reactant. The immediate product has C_{ad} and H_{ad} bound at adjacent μ_3 hcp sites that share a common Ni surface atom. The products thus co-adsorbed in the same unit cell of a $p(2\times 2)$ periodically infinite slab are 19.3 kcal/mol higher in energy than the reactant. When the products are allowed to further dissociate and find their preferred individual binding sites the overall reaction energy decreases to $E_{reaction}$ = 11.6 kcal/mol.

The endothermicity of the reaction is evident in the smaller decrease in the optimal spin, (from 10.06 to 9.35 for a net decrease of 0.71) than in the previous reactions (each had a decrease of 1.13 overall). The smaller amount of spin reduction associated with this reaction means that there is less covalent bonding with the Ni surface being exchanged for the C-H bond being broken than in the dehydrogenation steps already considered. We find that the optimal spin at the TS is 9.65. The reduction of spin that we do see results from a weakly forming H-Ni covalent bond ($R_{H\text{-}Ni}$ = 1.63 Å). The spin on all the d orbitals on the

Ni atom inserting into the bond is strongly affected, as the total spin on the same Ni atom decreases from 0.76 in a bare slab to 0.13 at this TS.

The shorter C-H distance (R_{C-H} = 1.55 Å, which is still too long for a weak single bond) at the TS is not what we might expect based on the endothermicity of the reaction. The TS of an endothermic reaction typically resembles the product more than the reactant, which would suggest a longer C-H distance in this case. Instead, the shorter C-H distance at the TS indicates that the Ni atom over which the bond cleavage takes place plays less of a role in stabilizing the reaction pathway and TS than in the previous reactions. There are two reasons for this reduced role. First, C cannot form more bonds to Ni than CH is able to, so removing the final H does not allow for a significant increase in C-Ni bonding as was the case in the previous reactions. Second, the Ni atom inserting into the C-H bond is already involved in bonding with C, either a σ bond with a C sp^3 orbital or contributions to π bonding and σ bonding with an interstitial orbital. Already being involved in bonding to C makes the Ni atom being inserted into the C-H bond less reactive.

3.3.4. Summary and Discussion of Reactions

The adsorbed species studied here have been observed by chemisorption and decomposition of CH_4 on Ni(111). In addition they serve as intermediates in the reverse process of methane formation from CO and H_2. Figure 12 summarizes the energetics and barriers for the various processes of chemisorption of CH_4 to form in sequence $CH_{3,ad}$, $CH_{2,ad}$, CH_{ad}, and C_{ad} where in each case we assume that the resulting H atoms are adsorbed at low coverage.

The energies of formation for the relevant species are for gas phase CH_4: -32.0 kcal/mol, for $CH_{3,ad} + H_{ad}$: -31.8 kcal/mol, for $CH_{2,ad} + 2\ H_{ad}$: -30.5 kcal/mol, for $CH_{ad} + 3\ H_{ad}$: -40.6 kcal/mol , and for Cad + 4 H_{ad}: -29.0 kcal/mol.

3.3.4.1. Dehydrogenation of CH_4

The experimental barrier for chemisorption of CH_4 to form $CH_{3,ad} + H_{ad}$ is 17.7 kcal/mol [2], and we find that the subsequent barrier to form $CH_{2ad} + H_{ad}$ from $CH_{3,ad}$ is 18.4 kcal/mol. The barrier for $CH_{2,ad} \rightarrow CH_{ad} + H_{ad}$ is 8.3 kcal/mol while the barrier for $CH_{ad} \rightarrow C_{ad} + H_{ad}$ is 32.8 kcal/mol. As a result the $CH_{2,ad}$ intermediate is not observed following the gas phase chemistroption of CH_4 on Ni(111) while CH_{ad} is quite prominent.

Figure 12 shows that for low coverage, CH_{ad} is the lowest energy state. Nevertheless, the barrier between $CH_{3,ad}$ and $CH_{2,ad}$ makes $CH_{3,ad}$ kinetically stable on Ni(111) at low temperatures following the chemisorption of CH_4. Once formed, $CH_{2,ad}$ is also kinetically stable at low temperatures; however, because the barrier to convert $CH_{2,ad}$ into CH_{ad} lies 8.8 kcal/mol below the barrier to convert CH_{3ad} into $CH_{2,ad}$ the $CH_{2,ad}$ species may form with enough excess energy to overcome the reaction barrier for its subsequent decomposition to form CH_{ad}. In any case, the thermal conditions required to overcome the initial barrier are more than sufficient for any $CH_{2,ad}$ formed to be almost immediately converted into CH_{ad}.

Further decomposing CH_{ad} into C_{ad} and H_{ad} has a much higher barrier of 32.8 kcal/mol, which lies 24.1 kcal/mol above gas phase CH_4. In addition the overall reaction energy is endothermic by 11.7 kcal/mol. Thus, this final step requires a significantly higher temperature to take place than the earlier stages of CH_3 decomposition.

3.3.4.2. Hydrogenation of C_{ad}

The first step of the reverse (hydrogenation) reaction (C_{ad} + Had → CH_{ad}) has a barrier of 21.1 kcal/mol, while the subsequent steps have barriers of 18.4 kcal/mol (CH_{ad} → $CH_{2,ad}$), and 17.0 kcal/mol ($CH_{2,ad}$ → $CH_{3,ad}$). The final barrier for desorption of CH_4 is 17.6 kcal/mol (experimental value for chemisorption [2] modified by our reaction energy). Because the barriers for the sequential hydrogenation steps are similar (there is a 4.1 kcal/mol range for the four reactions we consider), we expect that none will be the sole rate determining step so that all three CH_x species will exist as stable intermediates in the methanation process.

3.3.4.3. Role of Hydrogen

The strong binding of H to Ni(111) is an important factor in the overall energetics of both the forward and reverse processes on Ni, so that at low coverage the changes in energetics balance the changes in C-Ni bond orders for both hydrogenation and dehydrogenation making both feasible. Since the energy for chemisorbing unto the Ni(111) surface is -13.5 kcal/mol per H, H_{ad} is the favored state of H at low temperature.

At higher temperatures H_{ad} atoms combine to form $H_{2,gas}$. The pressure of H_2 gas can then be used to drive methanation forward or backward, with high pressures favoring hydrogenation and low pressures dehydrogenation.

4. Comparison with Previous Studies

4.1. Comparison with Experiment

4.1.1. Binding Energies with ZPE and Finite Temperature Corrections (Table 3)

To facilitate comparison of our binding energies with energies from experiments we use a nine atom Ni cluster model (six atoms in the top layer, and three in a second layer) to calculate frequencies for each species adsorbed to a μ_3 site.

Because experimental data is presently available for comparison the case of H binding is of particular importance. We find that the ZPE correction for H is 4.1 kcal/mol and the finite temperature correction at 298.15 K is 2.7 kcal/mol, leading to effective binding energies of $E_{bond,\ 0K}$ = 61.6 kcal/mol at 0 K and $E_{bond,\ 298K}$ = 63.0 kcal/mol at 298.15 K. Taking into account the ZPE for H_2 of 6.4 kcal/mol and the 298.15 K temperature correction of 8.5 kcal/mol, the heats of formation for H_{ad} are ΔH_{0K} = -12.6 kcal/mol and $\Delta H_{298.15\ K}$ = -13.5 kcal/mol. This result is in good agreement with the experimental value of -11.5 kcal/mol [37].

In all cases the ZPE correction decreases the binding energy of a species because adsorption introduces three additional vibrational modes associated with the motion of the adsorbate relative to the surface in exchange for the three lost transitional degrees of freedom (At 0 K there is no contribution from either rotations or translations). At finite temperature translational degrees of freedom become more important as the temperature increases; however, we assume adsorbed molecules to be fixed at low coverage so that translational contributions are not included for them. Thus the values we report are for the case most favorable to the adsorbed phase.

In the case of reaction enthalpies we find that in all cases the ZPE and finite temperature corrections favor the species with a large number of separate species on the surface (in Table 4 this corresponds to the products in all reactions). However, again, we are not including surface diffusion and coverage effects, and assume an ideal gas at standard state for gas phase species. In general, increased pressure in the gas phase favors the formation of surface species, while increased surface coverage favors hydrogenation reactions as well as the creation of gas phase species.

4.1.2. Relative Stabilities

Experimental studies have identified the most stable hydrocarbon species on Ni(111). Surface science experiments [6] used HREELS to identify methyl as the stable hydrocarbon product directly following CH_4 chemisorption on Ni(111), concluding that CH_3 binds to a μ_3 site with 3v symmetry. This result agrees with our calculations which find binding to a μ_3 fcc site with C_{3v} symmetry to be most favorable. HREELS experiments also show that CH_{ad} binds most favorably to three-fold sites in a symmetric structure [6], in agreement with our calculations.

In experiments on the chemisorption of CH_4 on Ni(111), CH_{ad} is observed but not $CH_{2,ad}$. The absence of $CH_{2,ad}$ agrees with our calculations, which suggest that $CH_{2,ad}$ immediately further decomposes to produce CH_{ad} because $CH_{2,ad}$ is less stable than either $CH_{3,ad}$ or CH_{ad}. Even more importantly, the barrier to form CH_{ad} from $CH_{2,ad}$ is much lower than the barrier to form $CH_{2,ad}$ from $CH_{3,ad}$.

In the Fischer-Tropsch synthesis producing CH_4 from CO and H_2, $CH_{3,ad}$, $CH_{2,ad}$ and CH_{ad} intermediates were all observed using SIMS.[7] The authors used these results as evidence against a previously proposed model which made $C_{ad} + H_{ad} \rightarrow CH_{ad}$ the rate-

determining step in the methanation process [40]. Their results suggested that all three CH_x fragments adsorbed on Ni(111) have similar stabilities, and are all present on the surface in a mechanism of sequential hydrogenation. More specifically, their experiments show that the $CH_{2,ad}$ population is stable up to 411 K, the $CH_{3,ad}$ population up to 443 K, and the CH_{ad} population up to at least 483 K. This is consistent with our findings in that $CH_{2,ad}$ is the least stable CH_x species on Ni(111) and that CH_{ad} is the most stable. Furthermore, if we assume that three body collisions (e.g. $C_{ad} + H_{ad} + H_{ad} \rightarrow CH_{2,ad}$) do not play an important role in the hydrogenation process, and that the excess energy which a newly formed product has from overcoming the previous hydrogenation barrier is dissipated to the surface before it collides with another H_{ad} (so that the energy from overcoming the previous barrier is usually not available for the next hydrogenation step), then our barriers for the reactions of interest all fall within a 4.1 kcal/mol range. These barriers are: 21.1 kcal/mol for $C_{ad} + H_{ad} \rightarrow CH_{ad}$, 18.4 kcal/mol for $CH_{ad} + H_{ad} \rightarrow CH_{2,ad}$, and 17.0 kcal/mol for $CH_{2,ad} + H_{ad} \rightarrow CH_{3,ad}$. Thus, it is reasonable that none of these steps is rate-determining by itself.

Finally, the high temperature of 700K [41] required to decompose CH_{ad} into C_{ad} and H_{ad} supports the high barrier predicted in our calculations, 32.8 kcal/mol.

4.2. Comparison with Previous Theory

Our results are in agreement with most of the major qualitative trends in previous theoretical studies. Our binding energies (see Table 5), reaction energies, and barriers (see Table 6) generally lie in the middle of the wide range of binding energies previously predicted.

The most relevant comparison for our calculations is with previous periodic calculations. Our results are in excellent agreement with those of Henkelman et al. [10] who used a $p(3\times3)$ slab with 5 layers with a plane wave basis set. For binding H at an fcc site they found E_{bond} = 64.5 kcal/mol compared to our value of 65.7 kcal/mol. For binding CH_3 to an fcc site they found E_{bond} = 41.5 kcal/mol compared to our value of 42.7 kcal/mol. They found a barrier for methyl diffusion of 3.9 kcal/mol compared to our value of 3.4 kcal/mol.

Michaelides et al. [11, 38, 42] used PW91 with a plane wave basis set on a three-layer $p(2\times2)$ periodic slab. They found that the fcc site is preferred for H, CH_2 and CH_3, with a binding energy for H of E_{bond} = 60.0 kcal/mol (we find 65.7 kcal/mol), a binding energy for CH_2 of E_{bond} = 75.2 kcal/mol (we find 89.3 kcal/mol), and a binding energy for CH_3 of E_{bond} = 34.1 kcal/mol (we find 42.7 kcal/mol). Although these differences between binding energies show similar trends, they find smaller binding energies than we do, probably because of the use of a three-layer slab model, which underestimates binding energies (see Figure 1). For $CH_{3,ad} \rightarrow CH_{2,ad} + H_{ad}$ they find a barrier of 24.7 kcal/mol (we find 18.4 kcal/mol). This higher barrier is likely related to their much higher (+11.4 kcal/mol) reaction energy (we find +1.4 kcal/mol).

Watwe et al. [14] carried out closed shell PBE calculations with a plane wave basis set on a 2x2 unit cell with a two-layer periodic slab for the entire dissociation pathway. Their reaction energies and barrier for the three steps of CH_3 dissociation are all within 2.1 kcal/mol of the values we find. They find $CH_{3,\,ad} \rightarrow CH_{2,\,ad} + H_{ad}$ to be exothermic with an overall reaction energy of -0.7 kcal/mol (we find an endothermic reaction energy of 1.4 kcal/mol) and a barrier of 16.3 kcal/mol (we find 18.4 kcal/mol). For $CH_{2,\,ad} \rightarrow CH_{ad} + H_{ad}$

they find a reaction energy of -10.3 kcal/mol (we find -10.2 kcal/mol) and a barrier of 6.7 kcal/mol (we find 8.3 kcal/mol). For $CH_{ad} \rightarrow C_{ad} + H_{ad}$ they find a reaction energy of 12.7 kcal/mol (we find 13.3 kcal/mol) and a barrier of 6.7 kcal/mol (we find 8.3 kcal/mol). Finally, they find that the dissociation of H_2 on Ni(111) is exothermic, with a chemisorption energy of -20.6 kcal/mol (we find -26.9 kcal/mol). If we had neglected spin polarization (as they do) we would have found -30.0 kcal/mol. The experimental value of -23.0 kcal/mol, must be corrected for ZPE and finite temperature effects to compare to these computed numbers, leading to -24.3 kcal/mol in good agreement with our value of -26.9 kcal/mol.

4.3. Comparison with Previous Kinetic Models.

The reaction energetics described in this paper find their significance mainly in the context of larger reaction networks. Simple kinetic models of CO methanation and CH_4 decomposition to carbon (two relevant processes involving such reaction networks) have been developed utilizing parameters (e.g. reaction energies and barrier heights) from both experiment and theory [14, 43, 44]. The simplest of these reaction schemes must consider parameters for at least eight to ten reactions. Here we have considered three such reactions. The development of such a kinetic model is beyond the scope of this paper; nevertheless, the results presented here could appropriately be combined with additional results to produce kinetic models of relevant chemical processes.

5. Summary

Where data are available for comparison to experiment our results for the binding energies and barriers are in agreement with the experimental values. This agreement suggests that these relatively simple calculations with four layers of Ni atoms and a

$p(2\times 2)$ unit cell are sufficient for both binding enthalpies and for barriers obtained with the NEB method.

We find that Ni catalyzes these reactions by inserting a Ni atom into the C-H bond being broken, and stabilizes the leaving H atom with a localized Ni-H bond. The Ni atom simultaneously forms a covalent bond to the C orbital being vacated by the H atom, stabilizing the remaining CH_x fragment. Nickel is able to catalyze both dehydrogenation and methanation reactions because the energies for H and the various CH_x fragments adsorbing unto Ni(111) balance the energy of the C-H bond being broken (to within 10.2 kcal/mol). The strength of the H bond to the surface (65.7 kcal/mol, which is a bit stronger than an H-H bond per H, 52.2 kcal/mol) as well as the nearly proportional nature of the bond order/ bond strength relationship for the hydrocarbon species make this possible. In the dissociation of $CH_{3,ad}$ on Ni(111), our barriers indicate that $CH_{2,ad}$ would not be stable at the temperature needed to break the first C-H bond in $CH_{3,ad}$, whereas CH_{ad} is stable. In the reverse process of methanation, $CH_{2,ad}$ is expected to be a stable intermediate along with CH_{ad} and $CH_{3,ab}$. These predications are in good agreement with experiment.

Tables

Bound Species	Binding Site	Calc. M_s	Opt. M_s	$\mathbf{E_{bond}}$	E_{snap}	CH_x Strain	Slab Strain	ΔE_{atom}	$\mathbf{\Delta E_{form}}$
Ni Slab	none	12/2	12.38	0.0	0.0	0.0	NA	0.0	0.0
H	**fcc**	**12/2**	**11.77**	**65.7**	**65.9**	**0.0**	**0.2**	**-65.7**	**-13.5**
H	hcp	12/2	11.78	65.4	65.7	0.0	0.3	-65.4	-13.2
H	bridge	12/2	11.79	62.6	62.8	0.0	0.2	-62.6	-10.4
H	on-top	12/2	11.93	52.7	52.8	0.0	0.1	-52.7	-0.5
C	fcc	10/2	9.87	153.2	155.0	0.0	1.8	-153.2	26.4
C	**hcp**	**10/2**	**9.82**	**154.8**	**156.4**	**0.0**	**1.6**	**-154.8**	**24.8**
C	bridge	10/2	10.04	143.1	147.6	0.0	4.5	-143.1	36.6
C	on-top	11/2	10.96	103.6	104.2	0.0	0.6	-103.6	76.0
CH	fcc	10/2	10.24	148.0	152.1	2.9	1.1	-231.2	0.6
CH	**hcp**	**10/2**	**10.06**	**148.9**	**153.3**	**2.9**	**1.4**	**-232.1**	**-0.3**
CH	bridge	10/2	10.42	139.4	146.1	3.0	3.7	-222.6	9.2
CH	on-top	11/2	10.92	99.5	104.5	3.0	2.0	-182.7	49.1
CH_2	**fcc**	**11/2**	**10.88**	**89.3**	**100.0**	**9.9**	**0.8**	**-287.6**	**-3.6**
CH_2	hcp	11/2	10.77	88.6	99.4	9.8	1.1	-286.9	-2.9
CH_2	bridge	12/2	11.04	83.9	91.3	6.5	1.0	-282.2	1.8
CH_2	on-top	12/2	11.62	66.0	71.1	4.5	0.6	-264.3	19.7
CH_3	**fcc**	**12/2**	**11.54**	**42.7**	**53.9**	**10.6**	**0.5**	**-354.7**	**-18.4**
CH_3	hcp	12/2	11.60	42.3	53.6	10.5	0.7	-354.2	-18.0
CH_3	bridge	12/2	11.69	39.3	50.5	10.0	1.2	-351.2	-15.0
CH_3	on-top	12/2	11.80	37.2	45.7	6.9	1.5	-349.2	-12.9

Table 1: Summary of Hydrocarbon Binding Data on Ni(111). "Calc. M_s" corresponds to the half-integer spin state with the lowest energy, which is the spin used in the optimum geometry and energy calculations presented here. "Opt. M_s" is the optimum spin state (in number of unpaired electrons) predicted by a parabolic fit of the energies of the lowest three half-integer spin calculations. **"E_{bond}"** is the adiabatic bond energy (difference between the geometry relaxed energy of the complex and the sum of the geometry relaxed energies of the slab and the adsorbent infinitely separated from each other). "E_{snap}" is the bond energy for which the separated adsorbent geometry and the slab geometry remain the same as in the complex. "CH_x strain" is the energy released by relaxing the geometry of the adsorbate after breaking its bond to the surface by moving it infinitely far away. "Slab strain" is the energy released by relaxing the slab geometry after moving the adsorbate that was bonding to it infinitely far away. "ΔE_{atom}" is the atomization energy not including the energy for forming the Ni(111) slab. **"ΔE_{form}"** is the energy of formation with respect to standard states: H_2 gas, graphite (adjusted to our computational reference of diamond corrected using the 0.45 kcal/mol experimental value of diamond relative to graphite) and the bare Ni(111) slab. All energies are in kcal/mol.

Adsorbed Species	Binding Site(s)	Calc. Spin	Opt. Spin	E_{bond}	$\mathbf{\Delta E_{reaction}}$	ΔE_{atom}	$\mathbf{\Delta E_{form}}$	$\mathbf{\Delta E_{meth}}$
CH_3	fcc	12/2	11.54	42.7	0.0	-354.7	-18.4	0.1
CH_2---H	**fcc, top (TS)**	12/2	11.02	24.4	**18.4**	-336.3	**0.0**	**18.5**
CH_2 + H	fcc, hcp	12/2	10.41	34.5	8.2	-346.4	-10.2	8.3
CH_2, H	fcc, fcc	NA	NA	41.4	1.3	-353.3	-17.0	1.4
CH_2	fcc	11/2	10.88	89.3	0.0	-287.6	-3.6	1.5
CH---H	**fcc, top (TS)**	11/2	10.23	81.0	**8.3**	-279.4	**4.7**	**9.7**
CH + H	fcc, hcp	11/2	9.75	95.8	-6.5	-294.1	-10.1	-5.0
CH, H	hcp, fcc	NA	NA	99.5	-10.2	-297.8	-13.7	-8.7
CH	hcp	10/2	10.06	148.9	0.0	-232.1	-0.3	-8.7
C---H	**hcp, brdg (TS)**	10/2	9.65	116.2	**32.8**	-199.4	**32.5**	**24.1**
C + H	hcp, hcp	10/2	9.35	129.6	19.3	-212.8	19.0	10.6
C, H	hcp, fcc	NA	NA	137.2	11.6	-220.4	11.4	2.9

Table 2: Summary of Dehydration Reaction Energetics on Ni (111). For each reaction the reactant is listed followed by the transition state (TS), the products complexed on the surface within the $p(2\times 2)$ unit cell, and the products completely separated on the surface. "Calc. spin" corresponds to the half-integer spin state with the lowest energy for the reactant, which is the spin used in the optimum geometry and energy calculations of all NEB images presented here. "Opt. spin" is the optimum state spin predicted by a parabolic fit of the energies of the lowest three half-integer spin calculations. "E_{bond}" is the adiabatic bond energy (difference between the geometry relaxed energy of the complex and the sum of the geometry relaxed energies of the slab and the adsorbent(s) infinitely separated from each other). **"$\Delta E_{reaction}$"** is the energy relative to the reactants. "ΔE_{atom}" is the atomization energy not including the energy for forming the Ni(111) slab. **"ΔE_{form}"** is the energy of formation with respect to standard states: H_2 gas, graphite (adjusted to our computational reference of diamond corrected using the 0.45 kcal/mol experimental value of diamond relative to graphite) and the bare Ni(111) slab. **"ΔE_{meth}"** is the energy of formation relative to CH_4 gas, H bonded to the Ni(111) surface at an fcc site and the bare Ni(111) slab. All energies are in kcal/mol.

	site	$\mathbf{E_{bond}}$ $\mathbf{D_e}$	Gas ZPE	Ad ZPE	Net ZPE	$\mathbf{E_{bond}}$ **0 K**	Gas 298.15 K	Ad 298.15 K	Net 298.15 K	$\mathbf{E_{bond}}$ **298.15 K**
H	fcc	**65.7**	0.0	4.1	4.1	**61.6**	1.4	4.2	2.7	**63.0**
C	hcp	**154.8**	0.0	1.6	1.6	**153.2**	1.4	1.7	0.3	**154.6**
CH	hcp	**148.9**	4.0	8.7	3.7	**145.2**	6.1	8.7	2.6	**146.4**
CH_2	fcc	**89.3**	10.9	13.9	3.0	**86.3**	13.3	15.4	2.1	**87.2**
CH_3	fcc	**42.7**	18.7	22.0	3.3	**39.5**	21.3	23.5	2.2	**40.5**

Table 3: ZPE and Finite Temperature Corrected Binding Energies of CH_x Species to most stable sites on Ni(111). "$\mathbf{E_{bond}}$ $\mathbf{D_e}$" is the binding energy obtained directly from our periodic PBE calculations on a four layer, $p(2\times2)$ Ni(111) slab. "Gas ZPE" is the zero-point energy (ZPE) of the adsorbate in the gas phase. "Ad ZPE" is the ZPE of the adsorbate adsorbed at a μ_3 site on Ni(111). "Net ZPE" is the effective ZPE on the binding energy. "**$\mathbf{E_{bond}}$ 0 K"** is the effective binding energy at 0 K, obtained by correcting $E_{bond,\ De}$ for ZPE energies. "Gas 298.15 K" is the finite temperature correction for the adsorbate in the gas phase at 298.15 K. "Ad 298.15 K" is the finite temperature correction for the adsorbate adsorbed at an fcc site on Ni(111) at 298.15 K. "Net 298.15 K" is the effective finite temperature correction for the binding energy at 298.15 K. **"$\mathbf{E_{bond}}$ 298.15K"** is the effective binding energy at 298.15 K obtained by correcting $E_{bond,\ De}$ for the ZPE and the finite temperature correction at 298.15 K. Both ZPE and finite temperature corrections were obtained from B3LYP calculations on a Ni_9 cluster. All values are in kcal/mol. The finite temperature corrections reported here include the translational and PV contributions to the enthalpy for the gas phase species (1.481 kcal/mol), which were not included in the values reported in the original paper.

Reaction	ΔH_{De}	ΔH_{0K}	$\Delta H_{298.15K}$
$\frac{1}{2}\ H_{2,\ gas} \rightarrow H_{ad}$	-13.5	-12.6	-13.5
$CH_{4,\ gas} \rightarrow CH_{3,\ ad} + H_{ad}$	0.1	-2.1	-2.9
$CH_{3,\ ad} \rightarrow CH_{2,\ ad} + H_{ad}$	1.3	-2.5	-2.6
$CH_{2,\ ad} \rightarrow CH_{ad} + H_{ad}$	-10.2	-12.3	-12.7
$CH_{ad} \rightarrow C_{ad} + H_{ad}$	11.6	9.6	8.9

Table 4: ZPE and Finite Temperature Corrected Enthalpies for Dehydrogenation Enthalpies on Ni(111). "$\mathbf{\Delta H_{De}}$" = $\Delta E_{reaction}$ is the reaction energy obtained directly from our periodic PBE calculations on four layer, $p(2\times2)$ Ni(111) slab. **"$\mathbf{\Delta H_{0K}}$"** is the reaction enthalpy at 0 K (including ZPE corrections obtained from B3LYP calculations on a Ni_9 cluster). **"$\mathbf{\Delta H_{298.15K}}$"** is the reaction enthalpy at 298.15 K (including finite temperature corrections obtained from B3LYP calculations on a Ni_9 cluster). All values are in kcal/mol. The finite temperature corrections reported here include the translational and PV contributions to the enthalpy for the gas phase species (1.481 kcal/mol), which were not included in the values reported in the original paper.

Reference		Present	Henkelman [10]	Michaelides [11, 38]	Burghgraef [9, 45]	Yang [16, 17]
Method		DFT (PBE)	DFT(PW91)	DFT (PW91)	DFT (LDA)	CI + embedding
Model		(2x2) 4 L Slab	(3x3) 5L Slab	(2x2) 3L Slab	Ni_{13} Cluster	Ni_{62} Cluster
H	top	52.7	—	—	56	44.7
H	bridge	62.6	—	—	60	59.3
H	fcc	65.7	64.5	60.0	65	61.8
H	hcp	65.4	—	58.6	—	61.3
C	top	103.6	—	—	90	—
C	bridge	143.1	—	—	114	—
C	fcc	153.2	—	—	142	—
C	hcp	154.8	—	—	—	—
CH	top	99.5	—	—	83	39.0
CH	bridge	139.4	—	—	104	66.9
CH	fcc	148.0	—	—	128	69.2
CH	hcp	148.9	—	—	—	72.2
CH_2	top	66.0	—	54.4	72	36.4
CH_2	bridge	83.9	—	72.4	68	62.7
CH_2	fcc	89.3	—	75.2	90	62.3
CH_2	hcp	88.6	—	74.3	—	67.1
CH_3	top	37.2	—	28.6	43	33.9
CH_3	bridge	39.3	—	31.6	36	35.5
CH_3	fcc	42.7	41.5	34.1	34	38.7
CH_3	hcp	42.3	—	33.7	—	38.7

Table 5: Comparison of Theoretical Results for Binding of CH_x Species to Ni(111). Comparison of binding energies for various methods and models for CH_x species binding at high symmetry sites on Ni(111). All values are in kcal/mol.

Reference		Present	Watwe [14]	Michaelides [11, 38]	Au [8]	Siegbahn [13]
Method		DFT (PBE)	DFT (RPBE)	DFT (PW91)	DFT (VWN)	CAS-SCF
Model		(2x2) 4L Slab	(2x2) 2L Slab	(2x2) 3L Slab	Ni_7 Cluster	Ni_3 Cluster
$H_{2,gas} \rightarrow H_{ad} + H_{ad}$	$\Delta E_{reaction}$[a]	-27.0	-20.6	-17.3	—	—
$CH_{4,gas} \rightarrow CH_{3,ad} + H_{ad}$	$\Delta E_{reaction}$	0.1	9.8	—	-5.5	—
$CH_{3,ad} \rightarrow CH_{2,ad} + H_{ad}$	$\Delta E_{reaction}$	1.4	-0.7	11.4	-3.5	8
	$E_{barrier}$	18.4	16.3	24.4	18.9	—
$CH_{2,ad} \rightarrow CH_{ad} + H_{ad}$	$\Delta E_{reaction}$	-10.2	-10.3	—	-15.2	7
	$E_{barrier}$	8.3	6.7	—	16.6	—
$CH_{ad} \rightarrow C_{ad} + H_{ad}$	$\Delta E_{reaction}$	13.3	12.7	—	5.5	-12
	$E_{barrier}$	32.8	33.2	—	27.4	—

a. The experimental value is 23 kcal/mol after accounting for ZPE and finite temperature corrections [37].

Table 6: Comparison of Theoretical Results for Reactions Among CH_x Species on Ni(111). Comparison of reaction energies and barriers given by various computational methods and models for reactions involved in CH_4 decomposition on Ni(111). All values are in kcal/mol.

Figures

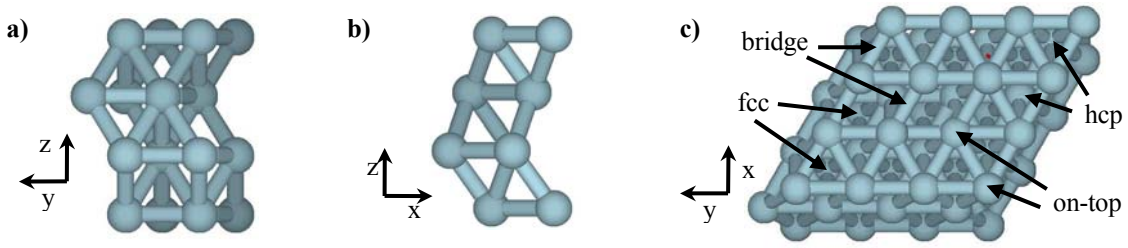

Figure 1: Three views of the periodic Ni(111) slab used to model the Ni(111) surface: side views of a single unit cell **a)** along the x direction, and **b)** along the y direction; **c)** a top view (along the z direction) of four $p(2\times 2)$ unit cells. Examples of high symmetry binding sites are labeled. One-fold (i.e. μ_1 on-top) sites lie directly above a single surface atom. Two-fold (i.e. μ_2 bridge) sites lie halfway between two adjacent surface atoms. Three-fold sites (μ_3 hcp or μ_3 fcc) lie equidistant from three nearest neighbor surface atoms. If there is an atom directly below the three-fold site in the first subsurface layer, the site is a μ_3 hcp site. If instead there is an atom directly below the three-fold site in the second subsurface layer, the site is a μ_3 fcc site.

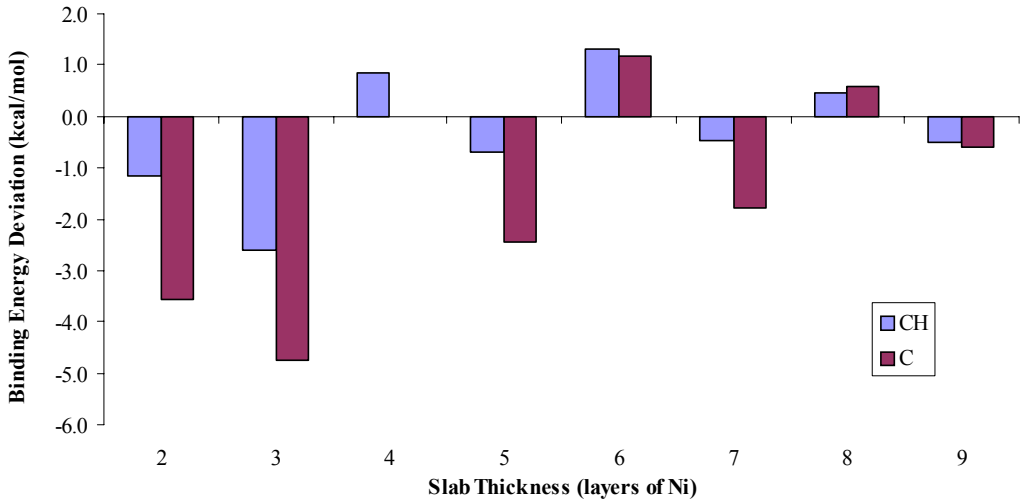

Figure 2: Deviation in binding energy (relative to average of bond energy to eight and nine layer slabs) for C and CH bonded to fcc site of Ni(111) slabs with two to nine layers of Ni atoms. The positions of C or CH and the Ni atoms in the first layer were allowed to relax. Nickel atoms below the top layer where fixed in their experimental bulk positions. From these results we concluded that calculations using the four layer slab are reliable.

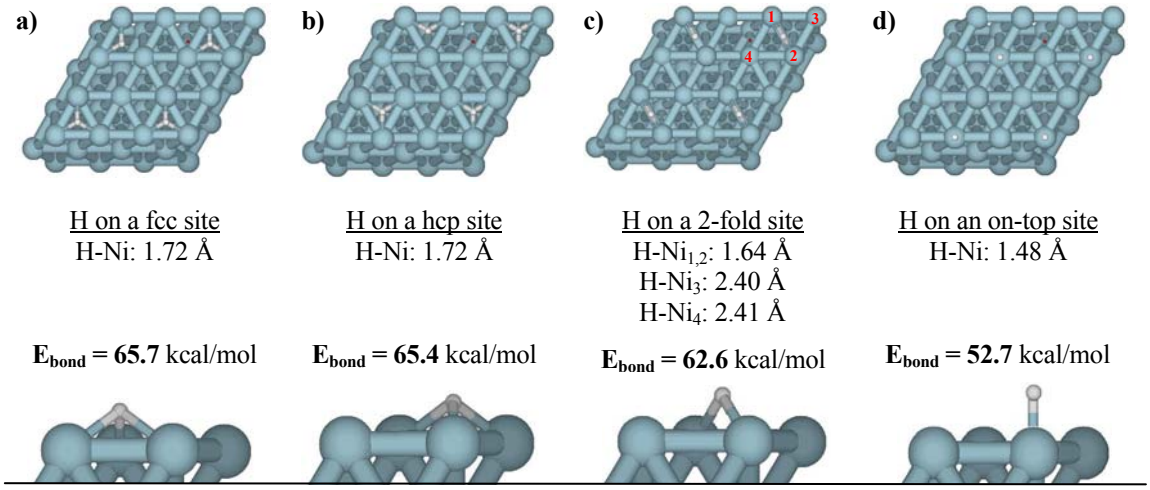

Figure 3: Adiabatic bond energies and geometries for H binding to **a)** μ_3 fcc site, **b)** μ_3 hcp site, **c)** μ_2 bridge site and **d)** μ_1 on-top site on Ni(111).

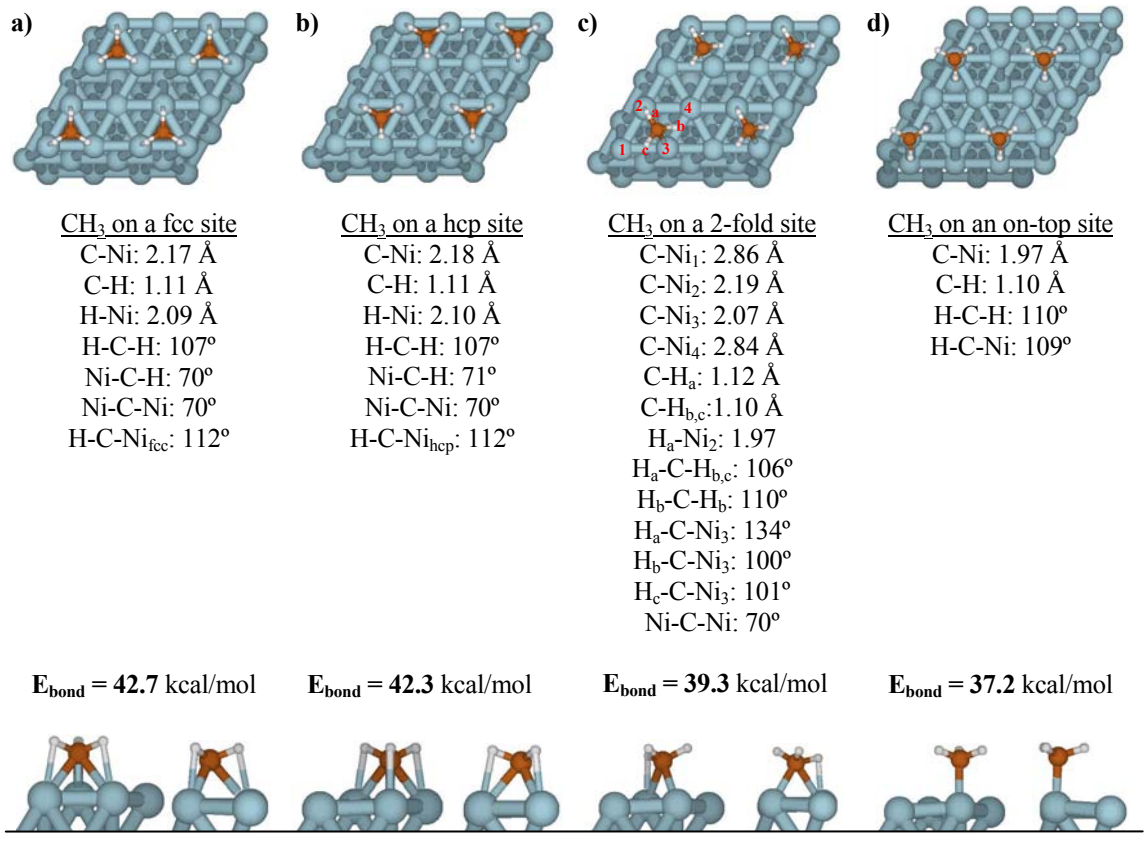

Figure 4: Adiabatic bond energies and geometries for CH_3 binding to **a)** μ_3 fcc site, **b)** μ_3 hcp site, **c)** μ_2 bridge site and **d)** μ_1 on-top site on Ni(111).

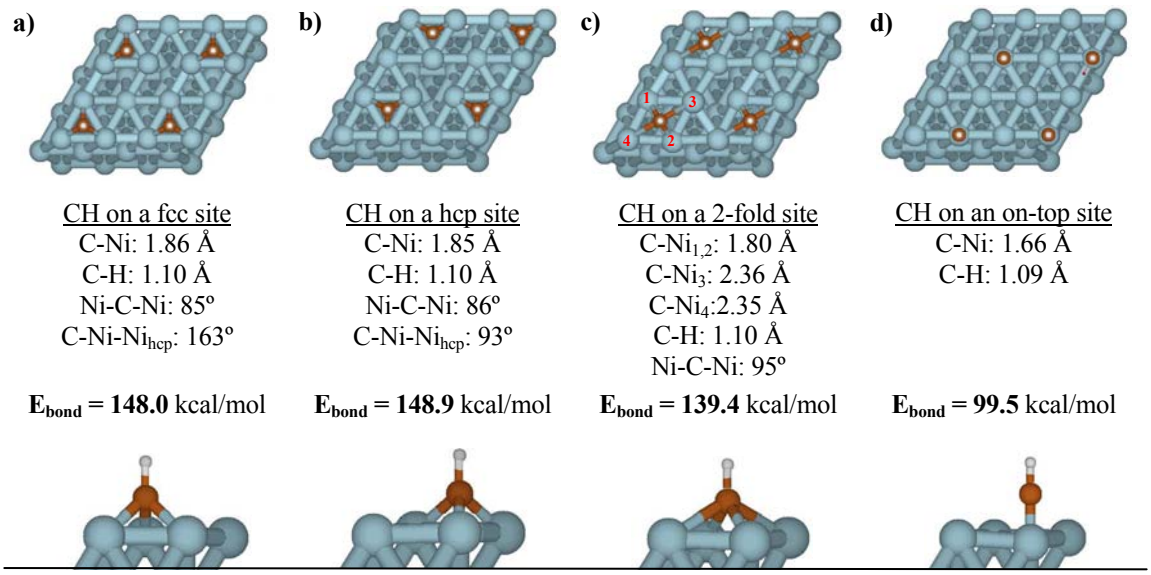

Figure 5: Adiabatic bond energies and geometries for CH binding to **a)** μ_3 fcc site, **b)** μ_3 hcp site, **c)** μ_2 bridge site and **d)** μ_1 on-top site on Ni(111).

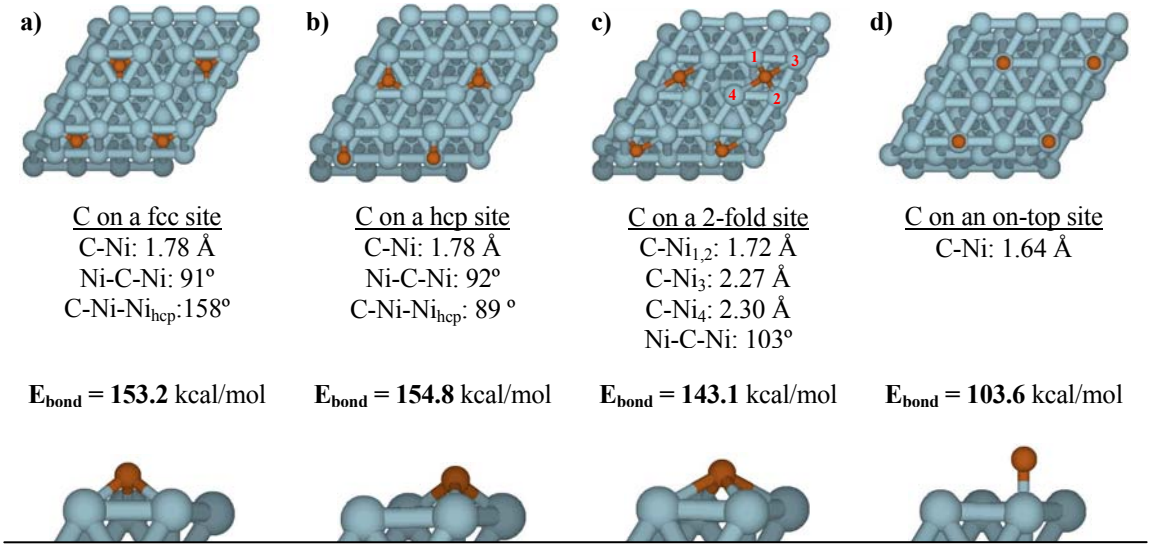

Figure 6: Adiabatic bond energies and geometries for C binding to **a)** μ_3 fcc site, **b)** μ_3 hcp site, **c)** μ_2 bridge site and **d)** μ_1 on-top site on Ni(111).

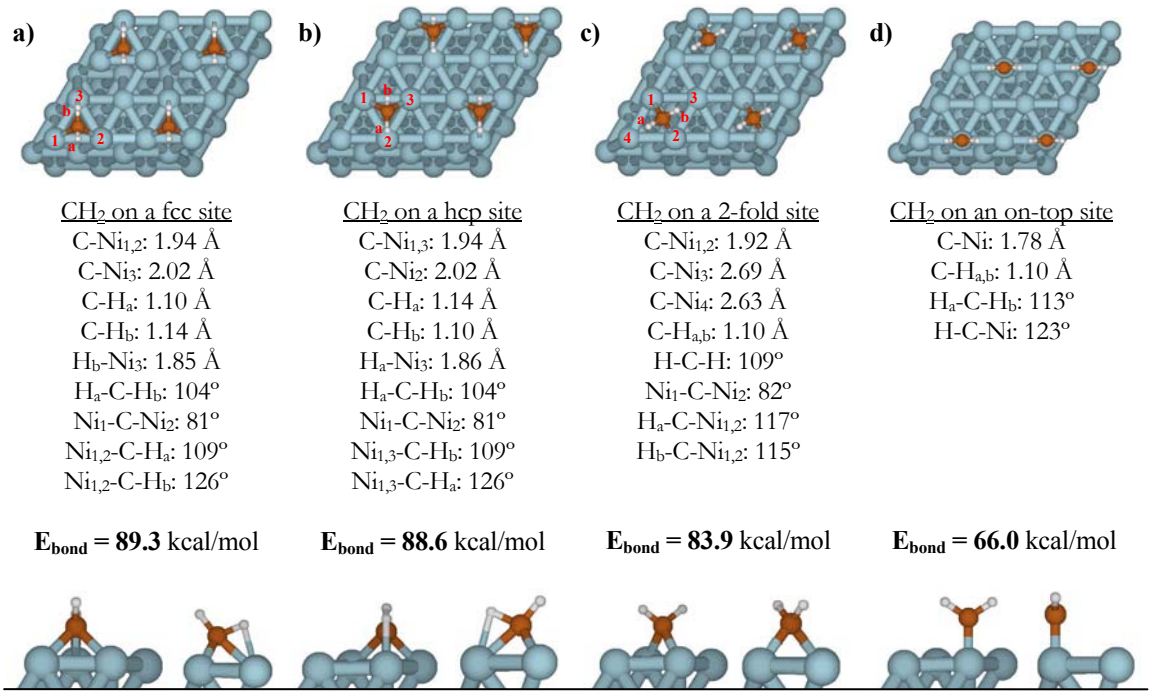

Figure 7: Adiabatic bond energies and geometries for CH_2 binding to **a)** μ_3 fcc site, **b)** μ_3 hcp site, **c)** μ_2 bridge site and **d)** μ_1 on-top site on Ni(111).

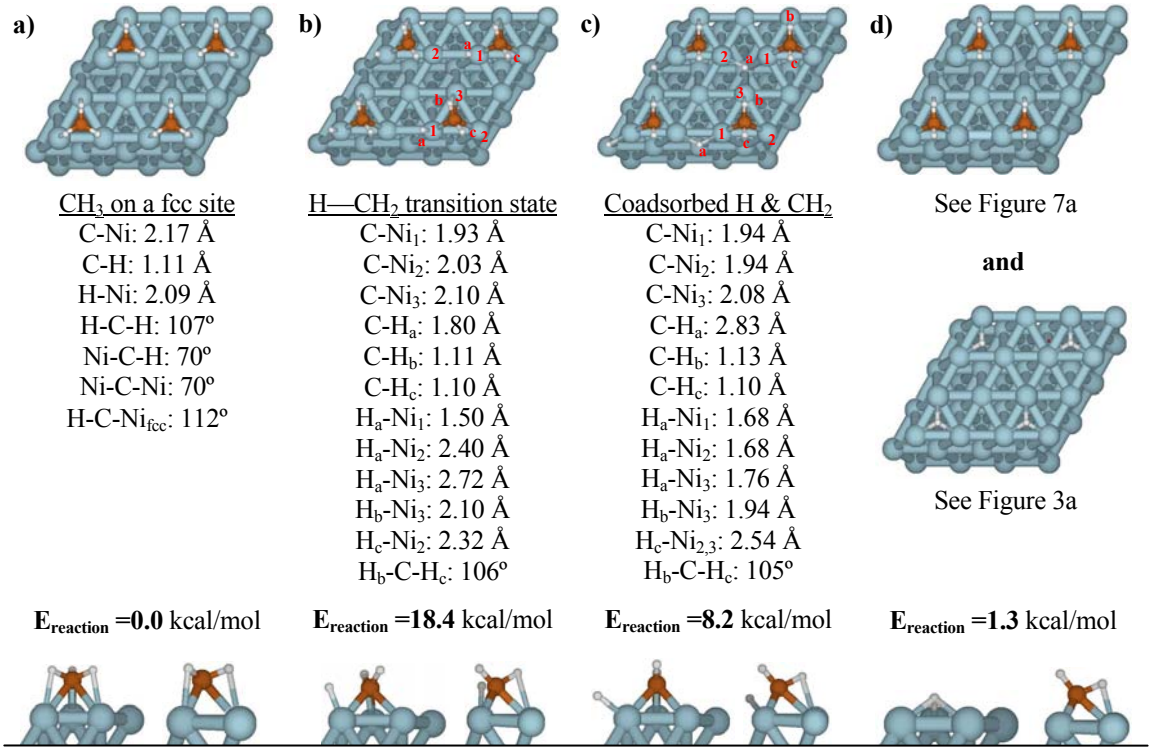

Figure 8: Energies and geometries for **a)** reactants, **b)** TS, **c)** coadsorbed products, and **d)** separated products from NEB pathway for $CH_{3,ad} \rightarrow CH_{2,ad} + H_{ad}$ on Ni(111).

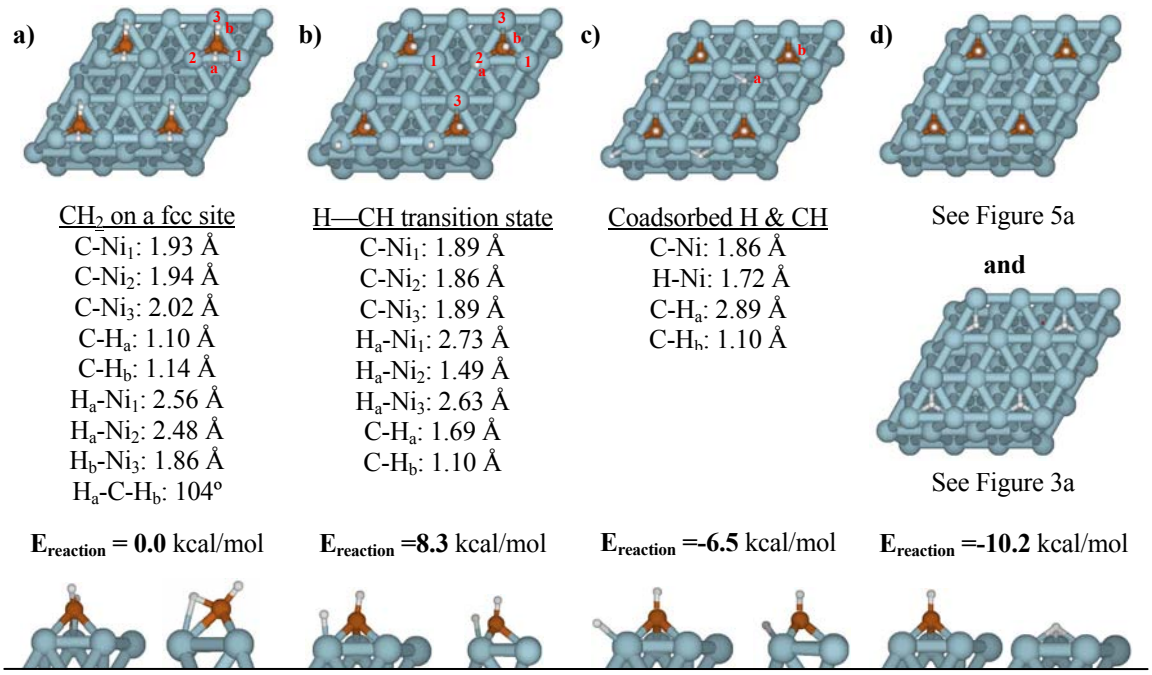

Figure 9: Energies and geometries for **a)** reactants, **b)** TS, **c)** coadsorbed products, and **d)** separated products from NEB pathway for $CH_{2,ad} \rightarrow CH_{ad} + H_{ad}$ on Ni(111).

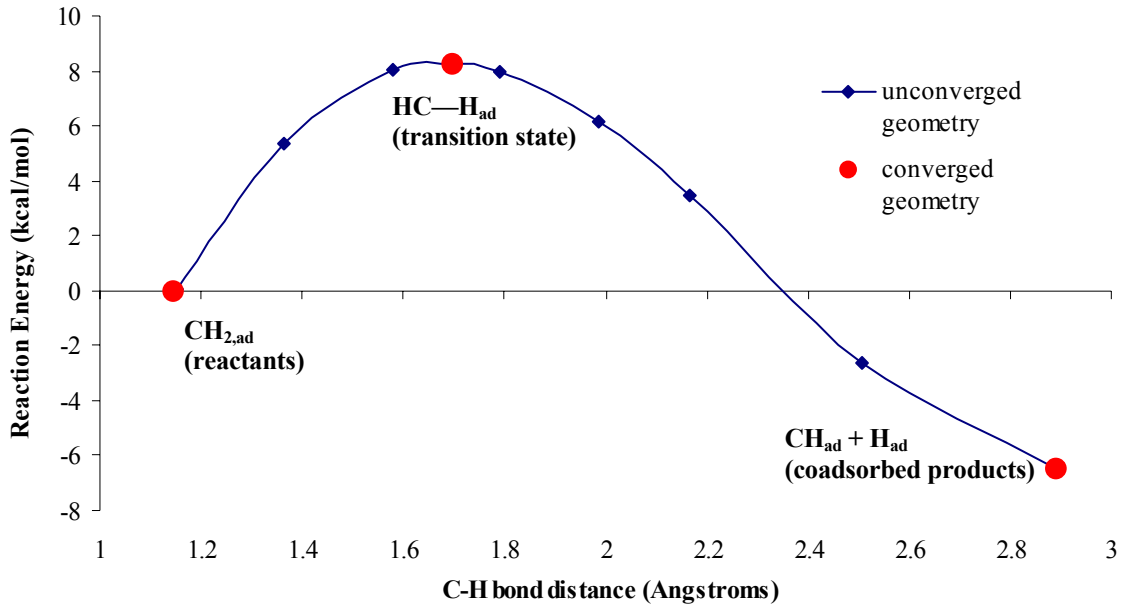

Figure 10: NEB pathway for dissociation of $CH_{2,ad}$ to form CH_{ad} and H_{ad} on Ni(111).

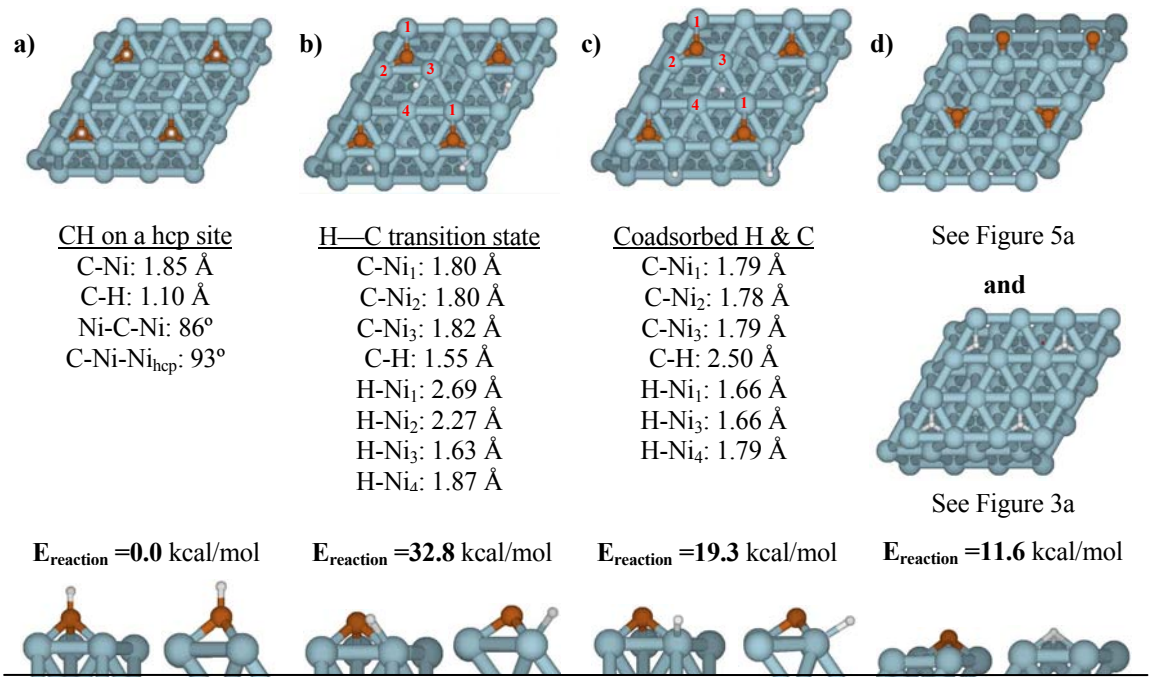

Figure 11: Energies and geometries for **a)** reactants, **b)** TS, **c)** coadsorbed products, and **d)** separated products from NEB pathway for CH_{ad} → C_{ad} + H_{ad} on Ni(111).

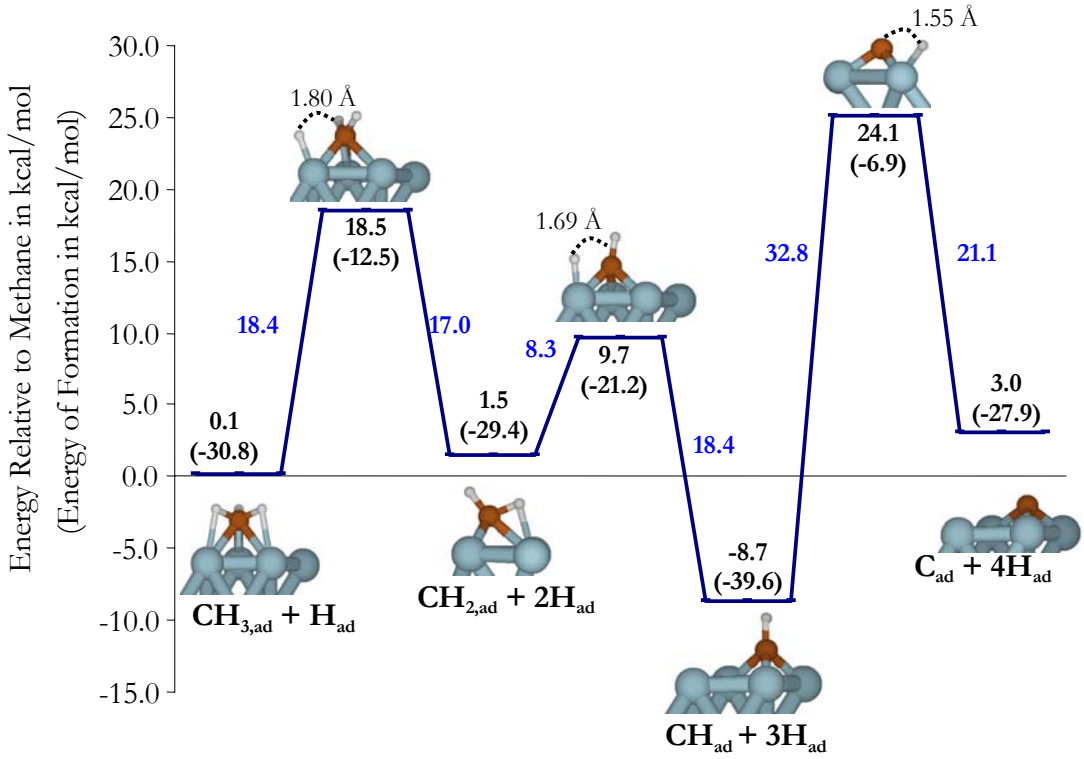

Figure 12: Energy pathway for CH_4 decomposition on Ni(111).

References

1. Rostrup-Nielsen, J. R. Catalytic Steam Reforming, in *Catalysis, Science and Technology*, J.R. Anderson and M. Boudar, Eds. 1984, Springer: Berlin; 1-117.
2. Egeberg, R. C.; Ullman, S.; Alstrup, I.; Mullins, C. B.; Chorkendorff, I. Dissociation of CH_4 on Ni(111) and Ru(0001). *Surf. Sci.* **2002**, *497* (1-3), 183-193.
3. Paillet, M.; Jourdain, V.; Phoncharal, P.; Sauvajol, J.-L.; Zahab, A. Versatile Synthesis of Individual Single-Walled Carbon Nanotubes from Nickel Nanoparticles for the Study of their Physical Properties. *J. Phys. Chem. B* **2004**, *108* (44), 17112-17118.
4. Beebe, T. P.; Goodman, D. W.; Kay, B. D.; Yates, J. D. Kinetics of the Activated Dissociative Adsorption of Methane on the Low Index Planes of Nickel Single Crystal Surfaces. *J. Chem. Phys.* **1987**, *87* (4), 2305-2315.
5. Yang, Q.Y.; Ceyer, S.T. The Stability and Chemistry of Methyl Radicals Adsorbed on Ni(111). *J. Vac. Sci. Technol. A* **1988**. *6* (3), 851-852.
6. Yang, Q.Y.; Maynard, K. J.; Johnson, A. D.; Ceyer, S. T. The Structure and Chemistry of CH_3 and CH Radicals Adsorbed on Ni(111). *J. Chem. Phys.* **1995**, *102* (19), 7734-7749.
7. Kaminsky, M. P. Winograd, N.; Geoffroy, G. L.; Vannice, M. A. Direct SIMS Observation of Methylidyne, Methylene, and Methyl Intermediates on a Ni(111) Methanation Catalyst. *J. Am. Chem. Soc.* **1986**, *108* (6), 1315-1316.
8. Au, C. T.; Liao, M. S.; Ng, C. F. A Detailed Theoretical Treatment of the Partial Oxidation of Methane to Syngas on Transition and Coinage Metal (M) Catalysts (M = Ni, Pd, Pt, Cu). *J. Phys. Chem. A* **1998**, *102* (22), 3959-3969.
9. Burghgraef, H.; Jansen, A. P. J.; van Santen, R.A. Methane Activation and Dehydrogenation on Nickel and Cobalt: a Computational Study. *Surf. Sci.* **1995**, *324* (2-3), 345-356.
10. Henkelman, G.; Arnaldsson, A.; Jonsson, H. Theoretical Calculations of CH_4 and H_2 Associative Desorption from Ni(111): Could Subsurface Hydrogen Play an Important Role? *J. Chem. Phys.* **2006**, *124* (4), 044706.
11. Michaelides A.; Hu, P. A First Principles Study of CH_3 Dehydrogenation on Ni(111). *J. Chem. Phys.* **2000**, *112* (18), 8120-8125.
12. Schule, J.; Siegbahn, P.; Wahlgren, U. A Theoretical Study of Methyl Chemisorption on Ni(111). *J. Chem. Phys*. **1988**, *89* (11), 6982-6988.
13. Siegbahn, P. E. M.; Panas, I. A Theoretical Study of CH_x Chemisorption on the Ni(100) and Ni(111) Surfaces. *Surf. Sci.* **1990**, *240* (1-3), 37-49.
14. Watwe, R. M; Bengaard, H. S.; Rostrup-Nielsen, J. R.; Dumesic, J. A.; Nørskov, J. K. Theoretical Studies of Stability and Reactivity of CH_x Species on Ni(111). *J. Catal.* **2000**, *189* (1), 16-30.
15. Wonchoba, S.E.; Truhlar, D. G. Embedded Diatomics-in-Molecules Potential Energy Function for Methyl Radical and Methane on Nickel Surfaces. *J. Phys. Chem. B* **1998**, *102* (35), 6842-6860.
16. Yang, H.; Whitten, J.L. Ab initio Chemisorption Studies of CH_3 on Ni(111). *J. Am. Chem. Soc.* **1991**, *113* (17), 6442-6449.

17. Yang, H.; Whitten, J. L. Chemisorption of Atomic H and Atomic CH_x Fragments on Ni(111). *Surf. Sci.* **1991**, *255* (1-2), 193-207.
18. Burghgraef, H.; Jansen, A. P. J.; van Santen, R. A. Theoretical Investigation of CH_4 Decomposition on Ni: Electronic Structure Calculations and Dynamics. *Faraday Discuss.* **1993**, 96, 337-347.
19. Perdew, J. P.; Burke, K.; Ernzerhof, M. Generalized Gradient Approximation Made Simple. *Phys. Rev. Lett.* **1996**, *77* (18), 3865-3868.
20. Schultz, P. A. *SeqQuest*, Sandia National Labs, Albuquerque, NM http://dft.sandia.gov/Quest/.
21. Cheng, M.-J.; Chenoweth, K.; Oxgaard, J.; van Duin, A. C. T.; Goddard, W. A. Single-site Vanadyl Activation, Functionalization, and Reoxidation Reaction Mechanism for Propane Oxidative Dehydrogenation on the Cubic V_4O_{10} Cluster. *J. Phys. Chem. C* **2007**, *111* (13), 5115-5127.
22. Our calculated value for the energy minimized Ni-Ni distance in the bulk fcc structure is 4.50 Å; nevertheless, the computed energy difference per Ni atom between the experimental and calculated lattice constants is less than 0.1 kcal/mol, so using the experimental value is appropriate.
23. An scf convergence criteria half as strict was required to procure energy convergence for H binding to hcp and bridge sites.
24. Edwards, A. *Post analysis code for SeqQuest*, http://dft.sandia.gov/Quest/SeqQ_Dev_Guides.html.
25. D.R. Lide, ed. *CRC Handbook of Chemistry and Physics*, 81st ed.; CRC Press: Boca Raton, FL, 2000.
26. *Jaguar 7.0*. 2007, Schrodinger Inc.
27. Becke, A. D. Density-Functional Thermochemistry. III. The Role of Exact Exchange. *J. Chem. Phys.* **1993**, *98* (7), 5648-5652.
28. Lee, C. T.; Yang, W. T.; Parr, R. G.; Development of the Colle-Salvetti Correlation-Energy Formula into a Funtional of the Electron Density. *Phys. Rev. B* **1988**, *37* (2), 785-789.
29. Wong, M. W. Vibrational Frequency Prediction Using Density Functional Theory. *Chem Phys. Lett.* **1996**, *256* (4-5), 391-399.
30. Apsel, S. E.; Emmert, J. W.; Deng, J.; Bloomfield, L. A. Surface-Enhanced Magnetism in Nickel Clusters. *Phys. Rev. Lett.* **1996**, *76* (9), 1441-1444.
31. Alden, M.; Mirbt, S.; Skriver, H. L.; Rosengaard, N. M.; Johansson, B. Surface Magnetism in Iron, Cobalt, and Nickel. *Phys. Rev. B* **1992**, *46* (10), 6303-6312.
32. Lui, F.; Press, M. R.; Khanna, S. N.; Jena, P. Magnetism and Local Order: ab initio Tight-Binding Theory. *Phys Rev. B* **1989**, *39* (10), 6914-6924.
33. de Boer, F. R. B. R. *Cohesion in Metals*. North-Holland: Amersterdam,1988.
34. Tyson, W. R.; Miller, W. A . Surface Free-Energies of Solid Metals: Estimation from Liquid Surface-Tension Measurements. *Surf. Sci.* **1977**, *62* (1), 267-276.
35. Hong, S.; Shin, Y.-H.; Ihm, J. *Jpn. J. Appl. Phys*. **2002**, *41*, 6142.

36. Kalibaeva, G.; Vuilleumier, R.; Meloni, S.; Alavi, A.; Ciccotti, G.; Rosei, R. Ab Initio Simulation of Carbon Clustering on an Ni(111) Surface: A Model of the Poisoning of Nickel-Based Catalysts. *J. Phys. Chem. B* **2006**, *110* (8), 3638-3646.
37. Christmann, K.; Behm, R. J.; Ertl, G.; van Hove, M. A.; Weinberg, W. H. Chemisorption Geometry of Hydrogen on Ni(111): Order and Disorder. *J. Chem. Phys.* **1979**, *70* (9), 4168-4184.
38. Michaelides, A.; Hu, P. A Density Functional Theory Study of CH_2 and H Adsorption on Ni(111). *J. Chem. Phys.* **2000**, *112* (13), 6006-60014.
39. Kua, J.; Goddard, W. A. Chemisorption of Organics on Platinum. 1. The Interstitial Electron Model. *J. Phys. Chem. B* **1998**, *102* (47), 9481-9491.
40. Hayes, R. E.; Thomas, W. J.; Hayes, K. E. Surface Intermediates in the Nickel Catalyzed Methanation of Carbon-Monoxide as Revealed by Computer Enhanced Multiple Reflectance Infrared-Spectroscopy. *Appl. Catal.* **1983**, *6* (1), 53-59.
41. Ceyer, S. T.; Lee, M. B.; Yang, Q. Y.; Beckerle, J. D.; Johnson, A. D. The Mechanism for the Dissociation of Methane on a Nickel Catalyst, in *Methane Conversion*, Biddy, M.; Chang, C.; Howe, R.; Yurchak, S. Eds. Elsevier Science Publishers: Amsterdam, 1988; 51-66.
42. Michaelides A.; Hu, P. Methyl Chemisorption on Ni(111) and C-H-M Multicentre Bonding: A Density Functional Theory Study. *Surf. Sci.* **1999**, *437* (3), 362-376.
43. Alstrup, I. On the Kinetics of CO Methanation on Nickel Surfaces. *J. Catal.* **1995**, *151* (1), 216-225.
44. Alstrup, I.; Tavares, M. T. The Kinetics of Carbon Formation from CH_4 + H_2 on a Silica-Supported Nickel-Catalyst. *J. Catal.* **1992**, *135* (1), 147-155.
45. Burghgraef, H.; Jansen, A. P. H.; van Santen, R. J. Electronic-Structure Calculations and Dynamics of the Chemisorption of Methane on a Ni(111) Surface. *Chem. Phys.* **1993**, *177* (2), 407-420.

Chapter 2

STRUCTURES AND ENERGETICS FOR C_2H_Y SPECIES ON NICKEL (111)

To elucidate the catalytic effects of nickel surfaces on hydrocarbons in reforming catalysts, fuel cell anodes and the synthesis of carbon nanotubes, we have performed quantum mechanics (QM) calculations, using the PBE flavor of density functional theory (DFT), to compute the binding energies and structures for all C_2H_y species on a periodically infinite Ni(111) surface. We find that CH_2CH_3, $CHCH_3$ and CCH_3 adsorb to the nickel surface using only their terminal C for bonding with binding energies of 32.5 kcal/mol, 82.7 kcal/mol and 130.8 kcal/mol respectively. In each of the remaining six C_2H_y species, both C atoms are able to form bonds to the surface. We find that three of these (CH_2CH_2, $CHCH_2$ and CCH_2) adsorb most favorably at a fcc-top site with the methyene C located at an on-top site and the other C at an adjacent fcc site. The bond energies for these species are 19.7 kcal/mol, 63.2 kcal/mol, and 93.6 kcal/mol respectively. The final three species (CHCH, CCH and C_2) all prefer binding at fcc-hcp sites, where the C atoms sit in a pair of adjacent fcc and hcp sites, with binding energies of 57.7 kcal/mol, 120.4 kcal/mol and 162.8 kcal/mol. We find that $CHCH_{ad}$ is the most stable species along the decomposition pathway of CH_3CH_3 on Ni(111) (ΔH_{eth} = -18.6), and that CCH_3 is its closest competitor (ΔH_{eth} = -18.2). Our enthalpies are consistent with the experimental observation of a low coverage pathway with $CHCH_{ad}$ as the key intermediate and a high coverage decomposition pathway involving the $CCH_{3,ad}$ intermediate.

The QM results reported here were used as training data in the development of a ReaxFF reactive force field describing hydrocarbon reactions on nickel surfaces [1]. Reactive dynamics studying the chemisorption and decomposition of six different hydrocarbon species on a Ni_{468} nanoparticle catalysts using this ReaxFF description were also recently reported [2].

1. Introduction

The catalytic capabilities of nickel surfaces in hydrocarbon chemistry are of interest for both scientific and technological reasons. Nickel is the primary catalyst in the steam reforming process for converting methane and water into synthesis gas [3] and also catalyzes the reverse Fischer-Tropsch reaction for producing hydrocarbons in which it typically selects for methane production [4]. More recently nickel has also been used extensively to catalyze the formation and growth of carbon nanotubes from hydrocarbon feedstock [5].

The simplest set of hydrocarbon molecules containing C-C bonds are the C_2H_y species. Thus, these hydrocarbons are of particular interest in efforts to better understand the chemistry of C-C bonds on nickel surfaces more generally. The adsorption and decomposition of ethylene and acetylene on nickel surfaces has been widely studied experimentally [6-19] and computationally [20-25]. These studies aimed at identifying the chemisorbed structures of these molecules on nickel surfaces and the chemical pathways along which they decompose. Nevertheless, this is the first QM study of the complete set of plausible C_2H_y species adsorbed on Ni(111) to be published.

Here we report binding energies and heats of formation for all C_2H_y species on Ni(111) obtained from periodic DFT (PBE) calculations. The theoretical methods and

computational details are discussed in the next section. The presentation of the binding of each C_2H_y adsorbate at its lowest energy site on Ni(111) is followed by a discussion of the implications of our results for possible reaction pathways for ethane (CH_3CH_3), CH_2CH_2 and CHCH decomposition on Ni(111). Finally, comparison is made with experimental observations and previous theoretical results.

One motivation for carrying out these calculations was to provide training data for the development of the ReaxFF reactive force field to describe hydrocarbon chemistry on nickel catalyst surfaces and clusters. The development of this ReaxFF description was published recently [1], along with an application of it to the chemisorption and decomposition of six different hydrocarbon species on Ni_{468} nanoparticles [2]. The sequence of intermediates observed in those reactive dynamics simulations is consistent with both the particular energies and general energetic trends observed here.

2. Theoretical Methods

2.1. DFT Calculations

All of our periodic DFT calculations utilize the spin polarized PBE [26] flavor of DFT as implemented in SeqQuest [27], with the pseudopotentials and basis set reported previously [28]. Strict spin conservation rules were not taken into account. Instead, the ground state spin projection was found to the nearest half integral M_s spin projection, which yields an energy within 1 kcal/mol of the bottom of the M_s energy well. For purposes of analysis the optimal value of M_s was estimated using a three point harmonic fit, and a post analysis code was utilized to analyze the local charge and spin properties of each system [29].

We use a four layer slab to model the Ni(111) surface in a $p\left(2\times\sqrt{7}\right)$ cell with six Ni atoms in each layer. The Ni atoms comprising the bottom three layers were fixed at the experimental nickel lattice distance (2.49 Å) [30]; only the Ni atoms in the top layer were allowed to relax. Thus, the dimensions for a unit cell in our 2-D periodic system are 4.98 Å and 6.59 Å with an angle of 100.9º between them. The vertical dimension normal to the periodicity was 21 Å resulting in a minimum vacuum region of 6 Å both above and below the slab and adsorbent molecule. A numerical grid spacing of 0.091 Å and 4×4 k-point sampling, which show energy convergence within 1 kcal/mol, were used. Unconstrained geometry minimization was used to relax all structures, starting from the most plausible low energy structures for each species. Only the lowest energy structures are reported here.

2.2. Energy Analysis

2.2.1. Energies of Formation

Experimental energies of formation typically use as their reference energies the ground states of elements at standard temperature and pressure. Thus, for the systems quoted here the energy per atom in fcc nickel, graphite, and H_2 gas at standard temperature and pressure would be taken as zero. For DFT calculations it is useful instead to refer to these systems at their optimum structures, which ignores the zero-point energy (ZPE) and heat capacity. In our DFT calculations it is more accurate to use diamond than graphite as the reference for C because the bonding in diamond is more similar to the bonding in the chemisorbed C_2H_y species than the bonding in graphite is. Furthermore, DFT methods are not especially accurate for graphite because of the importance of dispersion interactions between the graphene sheets, which are not well described by DFT. Since the experimental energy of diamond is 0.45 kcal/mol higher than that of graphite [31], we adjust our diamond

reference energy (E_{diaC}) for C by subtracting 0.45 kcal/mol and report results relative to graphite. To be consistent with the energy for H_2 we calculate E_{H_2} with SeqQuest using the same periodic cell as in our slab calculations. Finally, because every calculation uses exactly the same Ni slab we just subtract the total energy of the Ni slab to obtain energies of formation (ΔE_{form}), rather than referencing the Ni atoms in the slab to the energy of Ni atoms in bulk fcc nickel. Thus, for a system with N_C C atoms and N_H H atoms on the Ni(111) slab the energy of formation can be written:

$$\Delta E_{form} = E_{system} - E_{slab} - N_C\,(E_{diaC}\text{-}0.45) - N_H\,(E_{H_2}/2) \qquad \textbf{(1)}$$

2.2.2. Bond Energies

Both the adiabatic bond energy (E_{bond}) and the snap bond energy (E_{snap}) are useful for analyzing the energetic contributions of various geometric factors to bonding. The adiabatic bond energy (E_{bond}) for a bonded complex A-B is the energy difference between the optimized A-B species and the separated and geometrically relaxed A and B fragments. In contrast, the snap bond energy (E_{snap}) for A-B is the energy difference between the optimized A-B system, and the separated, but not relaxed, A and B fragments. Thus, there is no geometric relaxation of either the surface or the adsorbate from their geometries when bonded together in calculating the reference states for a snap bond energy. For our purposes, in calculating the snap bond energy the separated fragments are calculated using the ground spin projection states for their relaxed geometries unless noted otherwise. Thus, the energy of the separated unrelaxed adsorbate is calculated using the optimal spin for its relaxed geometry, while the energy of the unrelaxed slab is calculated using $M_s = 17/2$.

2.2.3. Enthalpies of Formation

To obtain zero-point energy (ZPE) and finite temperature (298.15 K) corrections for reliable comparison with experiment, we performed DFT calculations on each C_2H_y species bonded to either a nine or ten atom Ni cluster (either six or seven surface Ni atoms and three in the second layer). The calculations were performed with the Jaguar 7.0 [32] program's implementation of the DFT-B3LYP functional, which utilizes the Becke three-parameter functional (B3) [33] combined with the correlation function developed by Lee, Yang and Par (LYP) [34]. Vibrational frequencies typically do not depend strongly on the method and model used [35] so the use of another model and DFT method is appropriate. The positions of the Ni atoms were fixed at their respective positions from our slab calculations and the adsorbate was allowed to relax. The normal modes for the adsorbate were then used to calculate ZPE and 298.15 K finite temperature corrections to the energy. Similar calculations of the gas phase adsorbates were used to compute the ZPE and 298.15 K adiabatic adsorption energies for each of these species based on rotational and vibrational modes, as well as the translational and PV contributions to the enthalpy at finite temperature. Furthermore, ZPE and 298.15 K corrections were used to compute enthalpies of formation (ΔH_{form}) relative to diamond and H_2 gas. The ZPE and 298.15 K correction for diamond was obtained from Biograf [36] using the Dreiding force field [37]. Finally, enthalpies (ΔH_{eth}) referenced to CH_3CH_3 gas and H_{ad} on Ni(111) were calculated to elucidate the energetics for hydrocarbon decomposition on Ni(111). We assume infinitely dilute surface coverage and no surface diffusion, so that only vibrational and rotational contributions to the enthalpies are included for surface species.

3. Results

3.1. Adsorbed Species (Tables 1 and 2)

3.1.1. CH_2CH_3 (Figure 1)

We find that ethyl (CH_2CH_3) binds most favorably at a μ_1 on-top site, with a binding energy of E_{bond} = 32.5 kcal/mol. Binding at an fcc site is 0.3 kcal/mol less stable. This preference stands in contrast to the case of $CH_{3,ad}$, for which we found that the fcc site was preferred over an on-top site by 5.5 kcal/mol [28]. Favorable three-center, agostic interactions, involving C, H and Ni, and worth 7.8 kcal/mol, were a critical component in stabilizing $CH_{3,ad}$ binding at an fcc site. However, when a methyl group is substituted for a H atom, the result is a repulsive steric interaction between the methyl group and the surface, rather than a favorable agostic interaction. Thus, CH_2CH_3 prefers binding at an on-top site where the methyl-surface steric interaction is minimized.

The angles (108º, 112º, 104º, 117º) between the four substituents (H, H, C, and Ni) on methylene C suggest sp^3 hybridization. The C-H distances involving this C atom are typical C-H single bond distances (R_{C-H} = 1.10 Å), and the C-C bond distance (R_{C-C} = 1.52 Å) is a typical C-C single bond distance (1.54 Å is the C-C bond distance we find for ethane). Adsorbing CH_2CH_3 at an on-top site results in stretching the C-C bond by 0.06 Å from its gas phase value of 1.48 Å, and rehybridizing the methylene C to sp^3 from its sp^2 orbital configuration in the gas phase. As a result of these geometric modifications CH_2CH_3 is strained by 6.5 kcal/mol when chemisorbed at an on-top site on Ni(111).

The single σ bond formed to the Ni atom at the on-top site with one of these sp^3 orbitals has a bond distance of R_{C-Ni} = 1.99 Å, almost identical to the single bond distance observed when CH_3 adsorbs at an on-top site (1.97 Å). The covalent nature of the C-Ni bond is

evident in the reduction of spin density on the Ni atom participating in the bond from 0.71 to 0.32, with about half of this reduction being associated with the d_{z^2} orbital. The C-Ni bond pulls the participating Ni atom out off the surface plane by 0.2 Å at a cost of 2.3 kcal/mol on the Ni(111) slab. Because we do not expect any other significant surface adsorbate interactions, we attribute all of the snap bond energy (E_{snap} = 41.2 kcal/mol) to the C-Ni σ bond, which suggests that a C-Ni σ bond is worth about 40 kcal/mol for C-Ni bond distances around 2.0 Å.

3.1.2. $CHCH_3$ (Figure 2)

Similar to CH_2, ethylidene ($CHCH_3$) binds most strongly at a μ_3 fcc site with a binding energy of E_{bond} = 82.7 kcal/mol, which is 4.0 kcal/mol stronger than the bond formed at a μ_2 bridge site. Binding at the fcc site requires rehybridization of the methylidyne C from sp^2 in the gas phase (H-C-CH_3 angle is 135º) to sp^3 when adsorbed at an fcc site (H-C-CH_3 angle is 102º). This allows the methylidyne C to form a single C-C bond with a bond distance of R_{C-C} = 1.52 Å, a C-H bond with a bond distance of R_{C-H} = 1.10 Å, and a pair of C-Ni σ bonds with equal bond distances of R_{C-Ni} = 1.95 Å. The covalent nature of these C-Ni bonds is evident in the reduction of the spin (from 0.71 to.0.35) associated with each of the Ni atoms involved. Again, the primary role of the Ni d_{z^2} orbitals in the C-Ni σ bonds is reflected in their large contribution to the overall decrease in spin density.

In addition to the C-Ni bonds, there is an agostic interaction between the H on the methylidyne C and the Ni atom below it. This favorable interaction is evident in both the H-NI distance of R_{H-Ni} = 1.72 Å (the same H-Ni bond distance as for H binding at an fcc site! [28]) and elongated C-H bond (R_{H-Ni} = 1.17 Å). Based on these distances we expect this H-Ni interaction to be significantly stronger than in the case of CH_3 (H-Ni distances of

2.09 Å and C-H distances of 1.11 Å resulting in 2.7 kcal/mol per C-H-Ni interaction) and somewhat stronger than the case of CH_2 (H-Ni distances of 1.85 Å and C-H distances of 1.14 Å). Thus, this interaction is responsible for binding at an fcc site being more favorable than binding at a bridge site. These adjustments in the structure of $CHCH_3$ result in 14.0 kcal/mol in strain along with 1.1 kcal/mol in strain to the Ni(111) slab upon adsorption of $CHCH_3$, yielding a snap bond energy of E_{snap} = 97.8 kcal/mol. The C-Ni σ bonds here resemble those in CH_2 binding at a bridge site, which are worth 45 kcal/mol each and have similar C-Ni bond distances (R_{C-Ni} = 1.92 Å for CH_2 binding and R_{C-Ni} = 1.95 Å here). Thus, we might consider the snap bond energy (E_{snap} = 97.8) in terms of two C-Ni σ bonds, each worth 44 kcal/mol, plus an H-Ni agostic interaction worth 10 kcal/mol.

3.1.3. CCH_3 (Figure 3)

The final species, in which only one of the two C atoms bonds to the surface, is ethylidyne (CCH_3), for which we find a binding energy of 130.8 kcal/mol. The methyl C exhibits sp^3 hybridization (H-C-H angles of 110º and C-C-H angles of 111º) as expected with typical C-H single bond distances (R_{C-H} = 1.10 Å). The C-C bond distance (R_{C-C} = 1.49) is shorter than a typical C-C single bond, but longer than the distance we find in the gas phase (R_{C-C} = 1.45 Å), which is midway between typical single and double C-C bond distances. In the gas phase, two of the H atoms are equivalent with C-H bond distances of 1.11 Å and C-C-H angles of 118º, while the third H sits 1.12 Å away from C at a C-C-H angle of 94º, suggesting sp^2 hybridization. Adjusting the hybridization to adsorb to the Ni(111) surface costs 5.5 kcal/mol. As in the case of CH, the $^4\Sigma^-$ excited state is relevant to computing the snap bond energy rather than the $^2\Pi$ ground state, which lies 24.1 kcal/mol

lower in energy. Breaking the spin pairing costs 19.0 kcal/mol at optimal geometry for chemisorption, resulting in a net snap bond energy of E_{snap} = 156.7 kcal/mol.

We can consider the bonding to the surface either in terms of three equivalent σ bonds, each worth 52 kcal/mol, one to each of the three Ni atoms surrounding the fcc site or in terms of a σ bond to the interstitial orbital at the fcc site and two π bonds to d orbitals on the Ni atoms surrounding the fcc site. In the first case, we assume sp^3 hybridization for the terminal C atom, while in the latter case we assume sp hybridization. The same two possibilities were also available in the case of CH_{ad} binding at three-fold sites on Ni(111); however, migration of CH_{ad} across bridge sites was more consistent with sp^3 hybridization. Thus, we expect to find sp^3 hybridization in the case of $CCH_{3,ad}$. The covalent nature of the C-Ni bonding is reflected in the reduction of spin density on each of the three Ni atoms surrounding the fcc site by 0.45, with the d_{z^2} orbitals making the largest contribution.

3.1.4. CH_2CH_2 (Figure 4)

We find that ethylene (CH_2CH_2) is most stable binding at a fcc-top site with a binding energy of E_{bond} = 19.7 kcal/mol. Adsorption at a fcc-top site, with one C atom at an on-top site directly above a Ni atom and the other C atom sitting above an adjacent fcc three-fold site, is 2.2 kcal/mol more stable than binding at an on-top site in which the C-C bond is centered over a single Ni surface atom, and 4.2 kcal/mol more stable than binding at a double-top site, where the C atoms sit directly above adjacent Ni atom.

For binding at a fcc-top site, we find that the C-Ni distance between the C atom at the on-top site and the Ni atom directly below it of $R_{C\text{-}Ni}$ = 1.99 Å is similar to the C-Ni σ bond distance for CH_3 binding at an on-top site (1.97 Å [26]). This suggests that this C uses one of its sp^3 orbitals to form a σ bond with the d_{z^2} orbital on the Ni atom below, as evidenced

by a decrease in the spin density of 0.35 on this Ni atom upon bonding, primarily associated with its d_{z^2} orbital. The distance of the other C atom from the Ni atoms surrounding the fcc site (R_{Ni-C} = 2.27, 2.27 & 2.20 Å) allows for the possibility of a weak σ bond to the interstitial orbital at the fcc site (compare with the case of CH_3 where we find 3 equal C-Ni bond distances of 2.17 Å [28]). Thus, on one hand, we might consider the C-Ni bonding in terms of two σ bonds.

On the other hand, the C-C bond distance of R_{C-C} = 1.44 Å suggests that the C sp^3 orbitals involved in these σ bonds retain additional p character so that they are able to participate in a partial C-C π bond, which is responsible for the intermediate C-C bond distance. So we might alternatively consider the C-Ni bonding in terms of a C-C π bond perpendicular to the surface forming a three-center bond with the d_{z^2} orbital of the Ni atom below it.

Two of the H atoms are close enough to Ni atoms (R_{H-Ni} = 2.04 Å) for favorable, three-center agostic interactions resulting in elongated C-H bonds (R_{C-H} = 1.11 Å). This situation is very similar to that observed in the case of CH_3 binding at a three-fold fcc site where we found similar H-Ni (2.09 Å) and C-H (1.11 Å) distances, which resulted in individual interactions worth 2.7 kcal/mol each [28]. So for CH_2CH_2 binding to a perpendicular-bridge site we expect agostic interactions to be responsible for 5 kcal/mol of the snap bond energy. Thus, without these agostic interactions, binding at a fcc-top site would be less stable than binding at either an on-top or double-top site, where there are no agostic interactions.

In order to form the best bond to the Ni(111) surface, the trigonal planar sp^2 hybridized orbitals must pucker, so that the H atoms can point somewhat away from the Ni(111)

surface. This puckering is evident in the smaller C-C-H and H-C-H angles (all reduced by ~ 5º) when CH_2CH_2 chemisorbs to the surface, and has an energy cost of 21.2 kcal/mol. Alternatively, we might think of this energy in terms of the orbitals on the C atoms being rehybridized from sp^2 to sp^3. In either case, the result is a snap bond energy of E_{snap} = 42.6 kcal/mol.

Assuming sp^3 hybridization, we might account for this energy as follows. In the case of CH_3 adsorbed at an on-top site, the C-Ni bond is worth 45 kcal/mol with a C-Ni bond distance of 1.97 Å [28]. This is the same bond distance that we find here for the C atom in $CH_2CH_{2,ad}$ absorbed at the on-top site, thus we expect this σ bond to also be worth 45 kcal/mol. The C atom above the fcc site has a similar configuration to CH_3 adsorbed at a μ_3 site, except for longer C-Ni bond distances as noted above, resulting in weaker bonding. Thus we might expect bonding worth ~35 kcal/mol instead of ~45 kcal/mol as in the case of $CH_{3,ad}$. Finally, the three-center, agostic interactions are worth a total of 5 kcal/mol as noted above, suggesting that the total bonding is worth 85 kcal/mol, twice what we find in our calculations. The presence of the C-C partial π bond must decreases the strength of the C-Ni σ bonds by drawing extra electron density into a C-C bond (remember the C-C bond distance suggested a bond order greater than one) and interacting repulsively with the surface when lying parallel to it. To arrive at the expected snap bond energy, we consider these interactions to have an energetic cost of 42 kcal/mol.

Alternatively, if we consider the Ni-C bonding in terms of a three center π bond with C-Ni distances of $R_{C\text{-}Ni}$ = 1.99 Å and $R_{C\text{-}Ni}$ = 2.20 Å, we find that this bonding must be worth 37 kcal/mol to account for the snap bond energy along with the H-Ni agostic interactions.

3.1.5. CCH_2 (Figure 5)

Like CH_2CH_2, vinylidene (CCH_2) prefers binding to a fcc-top site, where it has a binding energy of E_{bond} = 93.6 kcal/mol. The bare C atom sits in the three-fold site so that the H atoms on the other C atom are far away from the surface. This minimizes any H-Ni repulsions at the expense of the favorable agostic interactions observed in the case of CH_2CH_2, and results in typical C-H bond distances (R_{C-H} = 1.09 Å). The H-C-H and C-C-H bond angles (115º and 121º respectively) suggest sp^2 hybridization. Thus, the C atom in the 3-fold site has two sp^2 orbitals available to form σ bonds (R_{C-Ni} = 1.87 Å) with the Ni d_{z^2} orbitals it points toward. The covalent nature of these bonds is reflected in the 0.38 decrease in spin density on each of the Ni atoms, which is most strongly associated with their d_{z^2} orbitals. The C-C bond distance (R_{C-C} = 1.38 Å) is typical for a C-C double bond, suggesting that C p_z electrons form a C-C π bond. The π system is then able to form a partial bond with the Ni atom most directly below it with C-Ni bond distances of R_{C-Ni} = 1.93 Å and R_{C-Ni} = 2.20 Å. The covalent nature of this interaction is revealed in a decrease of 0.29 in the spin density of the Ni atom involved.

Slightly puckering the plane in which the bonding in CCH_2 takes place (115º + 121º + 121º = 357º), and stretching the C-C bond length by 0.09 Å to form the best bond to Ni(111) costs 9.8 kcal/mol and results in a snap bond energy of E_{snap} = 105.5 kcal/mol. The C-Ni σ bonds resemble those formed when CH_2 is chemisorbed at a μ_2 bridge site and have similar C-Ni distance (1.92Å for CH_2, and 1.87 Å for CCH_2). Thus, we expect these σ bonds to each be worth 45 kcal/mol. The three center C-Ni π bond involves shorter C-Ni bond distances (R_{C-Ni} = 1.93 Å and R_{C-Ni} = 2.20 Å) than in the case of $CH_2CH_{2,ad}$ (1.99 Å and 2.20 Å), suggesting a stronger bond; however, the shorted C-C bond distance (R_{C-C} =

1.38 Å compared with 1.44 Å) indicates that the π electrons are more involved in the C-C π bond and thus less able to contribute to C-Ni bonding, resulting in weaker C-Ni bonding than in the case of $CH_2CH_{2,ad}$. Thus, we can account for the snap bond energy if we consider the π bond contribution to the Ni-C bonding to be 15 kcal/mol.

3.1.6. $CHCH_2$ (Figure 6)

Like CH_2CH_2 and CCH_2, vinyl ($CHCH_2$) is most stable on Ni(111) binding at a fcc-top site, with a binding energy of E_{bond} = 63.2 kcal/mol. The methylene C sits above the top site, while the methylidyne C sits at a adjacent fcc site. The C-C bond distance (R_{C-C} = 1.42 Å) is partway between typical single and a double bond distances, suggesting a weak C-C π bond perpendicular to the surface. The H-C-H bond angle of 113º suggests partial rehybridization of the C atoms from sp^2 to sp^3. The methylidyne C forms a strong σ bond (R_{C-Ni} = 1.92 Å) to a surface Ni atom with the sp^2 orbital that houses the radical electron in the gas phase. This σ bond reduces the overall spin density on the Ni atom involved by 0.27, and is associated with the Ni d_{z^2} and d_{xz} orbitals. The p orbitals that participate in the gas phase C-C π bond form a three-center π bond to the Ni atom beneath the methylene C, with C-Ni bond distances of R_{C-Ni} = 2.09 Å and R_{C-Ni} = 2.03 Å. The covalent nature of this interaction results in decrease in spin density of 0.31 on the Ni atom involved, primarily associated with the d_{xz} and d_{yz} orbitals.

For $CHCH_2$ to form the strongest bond to the surface, the C-C bond is elongated upon adsorption from 1.31 Å in the gas phase to R_{C-C} = 1.42 Å, as is the C-H bond on the methylidyne C (from 1.10 Å in the gas phase to 1.14 Å when adsorbed). Finally C-C-H angle associated with this H is decreased from 137º to 113º. These latter changes are associated with a three-center, agostic interaction involving this H, the C it is bonded to,

and the Ni atom below it. Based on the H-Ni distance of $R_{H\text{-}Ni}$ = 1.85 Å, we expect an agostic interaction similar to that observed in the case of CH_2 binding at an fcc site (same H-Ni distance of 1.85 Å). The strain caused by these structural modifications results in a snap bond energy of 82.1 kcal/mol.

As in other cases, we expect that the C-Ni σ bond to be worth 45 kcal/mol. The π bond most closely resembles the π bond in CH_2CH_2, but has a shorter C-C bond distance, which should result in a weaker C-Ni bond. This comparison suggests that a bond energy of 32 kcal/mol for this π bond would be quite reasonable. Finally, the H-Ni agostic interaction is expected to be worth 5 kcal/mol, thus accounting for the remainder of the snap bond energy.

3.1.7. CHCH (Figure 7)

Acetylene (CHCH) binds most favorably at a fcc-hcp site, where the C atoms sit in adjacent three-fold (fcc and hcp) sites. We find the binding energy for this configuration to be E_{bond} = 57.5 kcal/mol. The C-C distance ($R_{C\text{-}C}$ = 1.40 Å) is much longer than the triple bond distance in the gas phase (1.21 Å) and even longer than the double bond in gas phase ethylene (1.34 Å), suggesting a bond order less than two. Reducing the C-C bond order requires rehybridization of the C atoms from sp in the gas phase to mostly sp^2 when bound to the surface. This change is primarily reflected in the C-C-H angles which are reduced from 180º in the gas phase to 123º upon bonding to the surface at a cost of 67.0 kcal/mol, resulting in a snap bond energy of E_{snap} = 127.0 kcal/mol.

The sp^2 hybridization of the C atoms suggests that two types of bonds are formed with the surface. First, each C atom has a sp^2 orbital pointing toward the slab, which forms a σ bond with the surface. These σ bonds primarily involve the d_{z^2} orbitals on Ni_{fcc} and Ni_{hcp}.

The covalent nature of this bonding is seen in the 0.23 and 0.24 spin reduction on the Ni_{fcc} and Ni_{hcp} atoms, which is primarily associated with their d_{z^2} orbitals. Consideration of the C_{hcp}-C_{fcc}-Ni_{fcc} and C_{fcc}-C_{hcp}-Ni_{hcp} angles (137º and 136º) and large spin reduction on the Ni_{fcc} and Ni_{hcp} atomic orbitals suggests that the interstitial orbitals in the fcc and hcp sites may also play a role in the C-Ni σ bonding. The d_{z^2}, d_{xz} and d_{xy} orbitals on the Ni_{br} atoms also participate in a four center bond with the C-C π system. The H-Ni distances ($R_{H\text{-}Ni}$ = 2.45, 2.46 Å) are too long for agostic interactions so that the C-H bond distances are not elongated ($R_{C\text{-}H}$ = 1.10 Å).

We might account for the snap bond energy of E_{snap} = 127.0 kcal/mol in terms of two C-Ni σ bonds worth 45 kcal/mol each and π bonding involving the C-C π system and the two Ni_{br} atoms. This multi-center bond is characterized by $R_{C\text{-}Ni}$ = 2.03 Å and $R_{C\text{-}C}$ = 1.40 Å distances and is worth 37 kcal/mol.

3.1.8. CCH (Figure 8)

Like CHCH, acetylide (CCH) binds most favorably to an fcc-hcp site. We find a binding energy of E_{bond} = 120.4 kcal/mol. The C-C distance is elongated from its typical triple bond length of 1.22 Å in the gas phase radical to a double bond length of $R_{C\text{-}C}$ = 1.36 Å when CCH adsorbs on Ni(111), and the C atoms are rehybridized from sp to sp^2. The energetic cost of these modification is 10.4 kcal/mol, resulting in a snap bond energy of E_{snap} = 133.8 kcal/mol.

The C-C-H bond angle (132º) has not been reduced all the way to 120º as we would expect for pure sp^2 hybridization, suggesting that the central C atom still has some sp character. Thus, we expect a strong C-C π bond parallel to the surface, with some additional bonding to the two nearby Ni atoms (as we saw in the case of CHCH), and a

much weaker (i.e. not much electron density) C-C π bond perpendicular to the surface, which also participates in C-Ni bonding to the interstitial orbitals in the three-fold sites. The combination of the two partial π bonds provide a full additional bond to the C-C bond order, explaining the typical C-C double bond distance that we find (R_{C-C} = 1.36 Å).

The π bond perpendicular to the surface is weak because most of the electron density which would typically be associated with it is tied up in sp^2 rather than p orbitals. On the central C atom one of these binds to H and the other forms a bond with the d_{z^2} orbital of a Ni atom on the surface (R_{C-Ni} = 2.10 Å). On the bare C one of these forms a strong bond to Ni (R_{C-Ni} = 1.84 Å), while the other points away from the surface. We would expect the lone electron in this orbital to result in net spin density on C; however, we do not observe this in our calculations. Analogous to the case of $CHCH_{ad}$, the snap bond energy can be considered in terms of two C-Ni σ bonds involving sp^2 orbitals, each worth 45 kcal/mol, and additional bonding involving the two Ni atoms forming a bridge site perpendicular to the C-C bond and the electrons in the C-C π bond, worth 44 kcal/mol.

3.1.9. C_2 (Figure 9)

As in the cases of CHCH and CCH, the preferred binding site for dicarbide (C_2) on Ni(111) is a μ-bridge site with the C atoms sitting in adjacent three-fold sites. The C-C bond distance increases slightly from 1.31 Å in the gas phase to R_{C-C} = 1.34 Å when chemisorbed, and corresponds to a double bond (the C-C bond distance in ethylene is 1.33 Å). Stretching the C-C bond to chemisorb to the surface costs only 0.4 kcal/mol so that the difference between snap bond energy (E_{snap} = 168.9 kcal/mol) and the binding energy (E_{bond} = 162.8 kcal/mol) is primarily due to the relatively large strain on the Ni slab worth 5.7 kcal/mol. The C-C bond distance suggests a C-C σ bond involving either sp or sp^2 orbitals

and π bonding parallel to the surface. If the bonding resembles the case of CHCH, we would expect sp^2 hybridization perpendicular to the surface with an sp^2 orbital from each C involved in the C-C σ bond, the pair pointing toward the surface forming a pair of σ bonds to the Ni surface, and the final pair pointing away from the surface each housing an unpaired electron resulting in a net spin on each C atom. On the other hand, if we have *sp* hybridization, the p_z orbitals perpendicular to the surface can form σ bonds to the surface, while the sp orbitals pointing away from the C-C bond to partially bond to *d* orbitals on the Ni_{fcc} and Ni_{hcp} surface atoms. The result should be no net spin on the C atoms, if the spin pairing in all C-Ni bonds is complete; however, we might expect the imperfect overlap of the *sp* orbitals with the surface to result in a small spin polarization on each C. This agrees with the observed spin on the C atoms of 0.14 for C_{fcc} and 0.16 for C_{hcp}. Thus we can rationalize the snap bond energy in terms of two σ bonds involving the C sp orbitals opposite the C-C σ bond, each worth 45 kcal/mol, and two bonds involving the two C-C π bonds and two nearby Ni atoms, each worth 42 kcal/mol. The bonding of a second C-C π bond to the surface in $C_{2,ad}$ explains why it binds so much more strongly than CCH_{ad}, which has bonding very similar to $CHCH_{ad}$. The *sp* hybridization in $C_{2,ad}$ allows the formation of two C-C π bond systems, which both bond to the surface, whereas the sp^2 hybridization of CCH_{ad} and $CHCH_{ad}$ only has a single C-C π system and a pair of sp^2 orbitals pointing away from the surface.

In the gas phase the triplet is 15.1 kcal/mol lower in energy than the singlet state. Interestingly the optimal spin of the slab is hardly changed (16.67 to 16.52) upon binding C_2. This is in contrast to much more significant decreases in the spin of the system for binding CCH (15.77) and CHCH (15.58).

3.2. Zero Point Energies and 298.15 K Finite Temperature Corrections

To facilitate comparison of our binding energies with experiments we have calculated the vibrational frequencies for the same species on either a Ni_9 cluster (six atoms in top layer and three in second layer), a Ni_{10} cluster (seven atoms in top layer and three in second layer), or one of two Ni_{12} cluster (eight atoms in top layer and four in second layer). The C-H bond distances in the adsorbates on the clusters are within 0.05 Å of the values we find on the slab, and the C-C bond distances are all within 0.09 Å. The C-Ni σ bond distances are all within 0.16 Å (except for CCH_{ad}, where one of the C-Ni σ bonds is stretched by 0.50 Å), and C-Ni π bond distances are within 0.30 Å (except for a C-Ni π bond distance which is 0.63 Å longer in $CHCH_{2,ad}$ and one that is 0.47 Å longer in $CH_2CH_{2,ad}$). From the vibrational frequencies we calculated the zero point energy (ZPE) correction and the additional finite temperature correction at 298.15 K associated with each adsorbate and reference species. These corrections have been utilized to obtain binding energies at 0 K (E_{bond} 0K) and 298.15 K (E_{bond} 298.15K) for direct comparison with results from future experimental studies. The finite temperature correction associated with the translational motion and PV contributions to the enthalpy were also included for gas phase species; however, surface species were assumed to be fixed at their respective surface sites and be at infinitely dilute surface coverage. These results are summarized in Table 3. Enthalpies at 0 K and 298.15 K have also been calculated relative to both diamond and H_2 gas, and also CH_3CH_3 gas and H_{ad} for easy analysis of the energetics along various decomposition and reforming pathways. These results are summarized in Table 4.

4. Discussion

4.1. Ethane Decomposition on Ni(111)

Because ethane (CH_3CH_3) is a saturated hydrocarbon, chemisorbing unto the Ni(111) surface requires breaking at least one bond, which leads to two fragments each having an electron with which to form a bond to the surface. Thus, it is possible that CH_3CH_3 might initially chemisorb as either $CH_{3,ad}$ + $CH_{3,ad}$ or as $CH_2CH_{3,ad}$ + H_{ad}. While breaking the C-C bond to chemisorb as $CH_{3,ad}$ + $CH_{3,ad}$ is only a few kcal/mol higher in energy (0.7 kcal/mol at 0 K, and 1.4 kcal/mol at 298.15 K) than breaking a C-H bond to form $CH_2CH_{3,ad}$ + H_{ad}, we expect that breaking the C-C bond has a much higher barrier than breaking one of the C-H bonds, so that the formation of $CH_{3,ad}$ directly from CH_3CH_3 is kinetically hindered. Thus, we expect CH_3CH_3 to chemisorb as $CH_2CH_{3,ad}$ + H_{ad}.

Once $CH_2CH_{3,ad}$ has chemisorbed to the surface, it can lose a H from either the methyl or methylene C, or else break in half to form $CH_{2,ad}$ + $CH_{3,ad}$. Breaking the C-C bond, which is exothermic -2.0 at 0 K and -1.2 kcal/mol at 298.15 K, is the least favorable reaction. The loss of a methylene H to form $CHCH_{3,ad}$ is much more energetically favorable (overall reaction enthalpy of -11.8 kcal/mol at 0 K, and -11.5 kcal/mol at 298.15 K). This species would most likely be further converted to $CCH_{3,ad}$, which is exothermic an additional -17.0 kcal/mol at 0 K and -17.3 kcal/mol at 298.15 K from $CHCH_{3,ad}$. The other favorable direct product from $CH_2CH_{3,ad}$ is $CH_2CH_{2,ad}$, which is exothermic -11.4 kcal/mol at 0 K and -12.0 kcal/mol at 298.15 K. Thus, considering only the enthalpies of stable intermediates suggests that chemisorbed CH_3CH_3 will lead primarily to $CH_2CH_{2,ad}$ and $CHCH_{3,ad}$. The latter will likely further breakdown and form $CCH_{3,ad}$.

Following chemisorption onto Ni(111), breaking the C-C bond in $CH_2CH_{2,ad}$ is endothermic 6.7 kcal/mol at 0 K and 8.3 kcal/mol at 298.15 K. On the other hand, breaking a C-H bond is exothermic -2.4 kcal/mol at 0 K and -2.1 kcal/mol at 298.15 K. If the resulting $CHCH_{2,ad}$ is able to transfer a H to form $CCH_{3,ad}$, the loss of the H is exothermic -17.5 kcal/mol at 0 K and -16.7 kcal/mol at 298.15 K from $CH_2CH_{2,ad}$; however, there is no single process leading directly to this low energy product. The C-C bond in any $CCH_{3,ad}$ that forms is unlikely to break because C_{ad} + $CH_{3,ad}$ is significantly endothermic (24.2 kcal/mol at 0 K, and 23.7 kcal/mol at 298.15 K). Instead, the loss of a H from $CCH_{3,ad}$, leads to a product ($CCH_{2,ad}$) which is only slightly endothermic (3.6 kcal/mol at 0 K, and 2.7 kcal/mol at 298.15 K). The loss of an additional H to form CCH_{ad} is then exothermic by -1.2 kcal/mol at 0 K and -1.0 at 298.15 K, suggesting that any $CCH_{2,ad}$ that forms will convert to CCH_{ad} relatively quickly.

As the most stable C_2H_3 species, we might expect $CCH_{3,ad}$ to be the primary C_2H_3 species formed in the decomposition of CH_3CH_3 on Ni(111). However, because it does not form directly from the most stable C_2H_4 species ($CH_2CH_{2,ad}$), its formation must compete with the formation of other species formed directly from its most prevalent precursor, $CHCH_{2,ad}$. Thus, the formation of $CHCH_{ad}$, which is lower in enthalpy by 2.4 kcal/mol at 0 K and 3.3 kcal/mol at 298.15 K, is expected to compete with the formation of $CCH_{3,ad}$ from $CHCH_{2,ad}$. At low surface coverage we expect the formation of $CHCH_{ad}$ to dominate; however, at high coverage not only does $CCH_{3,ad}$ take up less surface space than $CHCH_{ad}$, but also includes an extra H which would otherwise occupy another additional surface site. Thus, we expect high surface coverage to favor the decomposition pathway that proceeds via $CHCH_{2,ad}$ → $CCH_{3,ad}$ → $CCH_{2,ad}$ → CCH_{ad}.

$CHCH_{ad}$ is the lowest enthalpic point in the decomposition process; however entropy is capable of driving further decomposition. In contrast to previous species, breaking the C-C bond of $CHCH_{ad}$ is more favorable than breaking either C-H bond. Thus, forming CH_{ad} + CH_{ad} from $CHCH_{ad}$ is endothermic by 2.1 kcal/mol at 0 K and 2.8 kcal/mol at 298.15 K, while forming CCH_{ad} is endothermic by 4.8 kcal/mol at 0 K and 5.0 kcal/mol at 298.15 K. Similarly, for any CCH_{ad} formed, additional decomposition is endothermic and breaking the C-C bond (6.9 kcal/mol at 0 K, and 6.7 kcal/mol at 298.15 K) is slightly favored over breaking the C-H bond (10.2 kcal/mol at 0 K, and 10.0 kcal/mol at 298.15 K). Finally, any $C_{2,ad}$ that is formed can only immediately decompose by breaking into individual C atoms, a process which is endothermic by 6.3 kcal/mol at 0 K, and 5.6 kcal/mol at 298.15 K, if the C atoms remain as adatoms on the Ni(111) surface.

Thus, based only on the enthalpies of possible intermediates, we expect CH_3CH_3 decomposition to proceed on Ni(111) primarily as follows. Under low coverage conditions:

$CH_3CH_{3,gas} \rightarrow CH_2CH_{3,ad} \rightarrow CH_2CH_{2,ad} \rightarrow CHCH_{2,ad} \rightarrow CHCH_{ad} \rightarrow CH_{ad} \rightarrow C_{ad}$.

Under high coverage conditions:

$CH_3CH_{3,gas} \rightarrow CH_2CH_{3,ad} \rightarrow CH_2CH_{2,ad} \rightarrow CHCH_{2,ad} \rightarrow CCH_{3,ad} \rightarrow CCH_{2,ad} \rightarrow CCH_{ad} \rightarrow CH_{ad} + C_{ad} \rightarrow C_{ad}$.

Of course other pathways are expected to be involved so that other intermediates will likely be observed; however, we expect each of these to be the primary pathway at the appropriate surface coverage.

4.2. Comparison with Experiment

4.2.1. Summary of Experiments (Figure 10)

Ethylene (CH_2CH_2) adsorption and decomposition has been studied on Ni(111) [6], Ni(110) [11], and Ni(100) [14,16]. In order to form two σ bonds to the surface, CH_2CH_2 rehybridizes from sp^2 in the gas phase to sp^3 when adsorbed to Ni(111) [21], and photoelectron diffraction experiments conclude that it binds at adjacent on-top sites [6]. However, measurements by EELS reveal the presence of a second tilted structure at high coverage, in which two of the H atoms interact with the surface [17]. Between 200 K and 230 K $CH_2CH_{2,ad}$ dehydrogenates to form acetylene ($CHCH_{ad}$) on Ni(111) [17]. On the other hand, in the presence of steps partial dehydrogenation produces $CHCH_{2,ad}$, which decomposes into methylidyne (CH_{ad}) and H_{ad} below 390 K [17]. This is similar to the process observed on the (100) surface in which CH_2CH_2, after being adsorbed at 150 K, partially dehydrogenates between 170 K and 200 K to form $CHCH_{2,ad}$ which is then stable up to 230 K [18].

The decomposition of a high surface coverage of $CH_2CH_{2,ad}$ (0.40 ML) is reported to produce $CCH_{3,ad}$ as an intermediate [15, 19]. In these high coverage experiments part of the $CH_2CH_{2,ad}$ is strongly di-σ bonded below 165 K, while the other part is weakly hydrogen bonded. Between 165 K and 200 K the weakly bonded $CH_2CH_{2,ad}$ desorbs. Above 200 K the remaining strongly bound $CH_2CH_{2,ad}$ decomposes to form $CHCH_{ad}$ and $CCH_{3,ad}$. Above 240 K $CHCH_{ad}$ begins to break down into CCH_{ad}, and CH_{ad}. Around 300 K H_2 gas desorbs and $CCH_{3,ad}$ begins to decompose into CCH_{ad}. The further breakdown of CCH_{ad} and CH_{ad} to form atomic C_{ad} begins at 340 K, at which point CHCH has completely reacted away.

By 400 K the $CCH_{3,ad}$ has completely decomposed, leaving CCH_{ad} and CH_{ad}, which decompose into surface and bulk C and H_2 gas before the temperature reaches 600 K.

Acetylene has also been studied on both Ni(100) [14], and Ni(111) [15]. On the (111) surface it chemisorbs by forming both σ and π bonds. Experiment and theory both show that it binds at an fcc-hcp site on Ni(111) [6,21]. At least two decomposition pathways have been observed depending on the surface coverage. At low surface coverage, acetylene decomposes primarily into CH_{ad} fragments starting around 400 K, although CCH_{ad} and methylene ($CH_{2,ad}$) have also been reported. These species then dissociate into atomic C_{ad} and H_{ad} at around 500 K. The presence of steps facilitates dehydrogenation so that CHCH is immediately converted to $C_{2,ad}$ at temperatures as low as 150 K. By 180 K the $C_{2,ad}$ molecules have all broken up into C_{ad} atoms [17].

4.2.2. Detailed Comparison to Experiment (Table 5)

A photoelectron diffraction study identifies the fcc-hcp site as the preferred site for $CHCH_{ad}$ on Ni(111) and reports a C-C bond distance of 1.44 ± 0.15 Å and C-$Ni_{surface}$ distance of 1.36 ± 0.15 Å for the C at the fcc site and 1.37 ± 0.15 Å for the C at the hcp site [6]. We find the same binding site preference with distances of C-C (1.40 Å) and C-$Ni_{surface}$ (1.41 Å and 1.41 Å) distances in good agreement with experiment.

For $CH_2CH_{2,ad}$ photoelectron diffraction experiments observe binding at a double-top site [6]. We find that a perpendicular bridge site is 4.2 kcal/mol lower in energy than the double-top structure. For the double-top structure, the uncertainty in the experimental C-C bond distance (1.60 ± 0.18 Å) includes the C-C distance (1.45 Å) we find for the di-σ structure; however, the experimental C-Ni distances normal to the surface (1.90 ± 0.02 Å) are shorter than the distance we compute (2.07 Å). The longer C-Ni distances in our

calculations suggest that the binding energy we calculate for binding at a double-top site is too weak. This may explain why we find binding at a fcc-top site to be preferred.

While no direct experimental measurements of the relative energies of these adsorbed C_2H_y species have been reported, we can compare our energetics with the experimentally observed decomposition pathways [15]. The experimental observation that under low coverage conditions $CH_2CH_{2,ad}$ decomposes to form $CHCH_{ad}$, without producing a large concentration of the intermediate $CHCH_{2,ad}$ is consistent with our results, since $CH_2CH_{2,ad}$ → $CHCH_{2,ad}$ is 3.0 kcal/mol endothermic, while the next step ($CHCH_{2,ad}$ → $CHCH_{ad}$) is 14.3 kcal/mol exothermic. The observation of an alternative pathway involving $CCH_{3,ad}$ at high coverage is consistent with our finding that $CCH_{3,ad}$ is only 0.3 kcal/mol energetically less stable than CHCH in the decomposition process.

Considering only the energies of stable species suggests that when both $CCH_{3,ad}$ and $CHCH_{ad}$ are formed that $CCH_{3,ad}$ will begin to decompose first because $CCH_{2,ad}$ is only endothermic by 4.7 kcal/mol while CCH_{ad} and CH_{ad} are endothermic from $CHCH_{ad}$ by 7.5 and 6.2 kcal/mol respectively. Nevertheless, we can explain the experimental observation that $CCH_{3,ad}$ does not decompose significantly until 300 K, while $CHCH_{ad}$ decomposes starting at 240 K, by considering the structure of $CCH_{3,ad}$. Because the H atoms, and as a result the C-H bonds, are far away from the surface (~3.1 Å for the shortest H-Ni distance) we expect a large energy barrier to break the C-H bonds in $CCH_{3,ad}$. In contrast the shortest H-Ni distances in $CHCH_{ad}$ are ~2.45 Å, enabling a nearby Ni atom to better stabilize a H atom as its C-H bond is broken. The breakdown of $CCH_{3,ad}$ to CCH_{ad} without readily observing $CCH_{2,ad}$ can be partially explained by the relative energies of the two steps (4.7 kcal/mol for $CCH_{3,ad}$ → $CCH_{2,ad}$, and 2.4 kcal/mol for $CCH_{2,ad}$ → CCH_{ad}), and more fully

explained by taking into account the effect of the H-Ni distance on the reaction barriers ($R_{H\text{-}Ni}$ = ~2.8 Å in $CCH_{2,ad}$, and $R_{H\text{-}Ni}$ = ~3.1 Å in $CCH_{2,ad}$). The absence of $C_{2,ad}$ in the decomposition process on terraces is consistent with the 2.8 kcal/mol advantage of breaking the C-C bond in CCH_{ad} rather than the C-H bond. Finally, the need for temperatures well above 300 K to produce atomic C is consistent with the high energy we find for it (29.6 kcal/mol higher in energy than $CHCH_{ad}$).

4.3. Comparison with Previous Theory (Tables 6 and 7)

QM calculations have previously been reported for isolated parts of these reaction schemes. A number of theoretical papers have examined the chemisorption of CH_2CH_2 or CHCH on nickel surfaces [20-22]. Another paper examined the formation of a C-C bonding between a surface C and either CH_3, CH_2 or CH to form CCH_3, CCH_2 or CCH on nickel [23]. Finally, empirical bond-order conservation methods have been used to estimate energies for all relevant species [24, 25]. However, no comprehensive, first-principles study of all C_2H_y species has yet been published.

Our results are compared with other theoretical results in Table 6 and Table 7. There is much quantitative disagreement among these studies. As we found in our previous study of CH_x species on Ni(111) [28], there is reasonable agreement between our numbers and those obtained from DFT calculations on similar slab models (in this case reference [22]). However, cluster calculations [20-21, 23] and more approximate methods (e.g. the bond-order conservation approach [24]) give widely varying results.

An early Hartree-Fock study considered the binding of CH_2CH_2 and CHCH to small nickel clusters [20]. On a Ni_2 cluster binding energies of 136 kcal/mol and 108 kcal/mol were found for CH_2CH_2 and CHCH respectively, and the analogous binding energies to a Ni_{13} cluster were 216 kcal/mol and 156 kcal/mol (we find 19.7 and 57.5 kcal/mol for

CH_2CH_2 and CHCH respectively). The dissociation of CH_2CH_2 into two CH_2 fragments was found to be -35 kcal/mol exothermic (we find -15.3 kcal/mol), and the dissociation of CHCH into two CH fragments -16 kcal/mol exothermic (we find -6.2 kcal/mol). These numbers differ significantly from ours. Nevertheless, there is qualitative agreement that cleaving the C-C bond is unfavorable for both CH_2CH_2 and CHCH on Ni(111), with CH_2CH_2 being the more unfavorable case.

Shustorovich has performed an extensive study using the empirical bond-order conservation Morse-potential (BOC-MP) approach [24-25]. While this study considers most interesting species, the results are quantitatively quite different from QM results and often qualitatively different. For example, the BOC-MP predicts that the C-C bond in $CCH_{3,ad}$ breaks exothermically with a bond energy of -21 kcal/mol. On the other hand we find an energetically favorable C-C bond, with a bond energy of 26.3 kcal/mol, making this C-C bond the strongest C-C bond we observe for C_2H_y species adsorbed on Ni(111), rather than the weakest as Shustorovich predicts. Burghgraef et al. also predict a strong C-C bond from DFT, which is worth 16 or 51 kcal/mol depending on which model they use [23]. The experimental observation that $CCH_{3,ad}$ decomposes by way of CCH_{ad} rather than atomic C and CH_x species is evidence for a strong C-C bond in $CCH_{3,ad}$ [19].

The DFT study by Burghgraef et al. considered the formation of C-C bonds on Ni_7 and Ni_{13} clusters [15]. The formation of CCH from coadsorbed C and CH was found to be +15 kcal/mol endothermic on both Ni_7 and Ni_{13} clusters (we find +10.3 kcal/mol). The formation of CCH_2 from coadsorbed C and CH_2 was found to be -36 kcal/mol exothermic on the Ni_7 cluster, but only -3 kcal/mol on the Ni_{13} cluster (we find -22.9 kcal/mol). Finally, the formation of CCH_3 from coadsorbed C and CH_3 was found to be -51 kcal/mol

exothermic on the Ni_7 cluster, but only -16 kcal/mol on the Ni_{13} cluster (we find -26.3 kcal/mol). The energies of the separately adsorbed C and CH_x species were all found to be much higher in energy (72-124 kcal/mol) than the same coadsorbed species. Significant differences in the charge distribution in the separately adsorbed system compared to the coadsorbed system suggest that this is an artifact of their calculations. Thus, the more reliable reaction energies from their paper are those relative to the coadsorbed, rather than infinitely separated, reactants. In the case of CCH formation, where their models agree within 1 kcal/mol, our reaction energy is within 5 kcal/mol of their result. In the other cases our reaction energy lies between the reaction energies obtained on their two different cluster models.

Another DFT study considered CH_2CH_2 and CHCH on Ni_4 and Ni_{14} clusters using the LDA functional modified by an exchange correction from the Becke functional and a correlation correction from the Perdew functional [21]. It considered fcc-hcp and top-top sites for both adsorbates and found that CH_2CH_2 prefers the double-top site, with binding energies of -4 kcal/mol and 13 kcal/mol to the Ni_4 and Ni_{14} clusters respectively (we find 19.7 kcal/mol to an fcc-top site, and 15.5 kcal/mol to a double-top site), while CHCH prefers the fcc-hcp, with energies of 37 kcal/mol and 50 kcal/mol to the Ni_4 and Ni_{14} clusters respectively (we find 57.5 kcal/mol at the same site).

Finally, a DFT (PW91) study on both 3 and 6 layer periodic Ni(111) slabs found binding energies for CHCH of 68.2 kcal/mol and 68.8 kcal/mol respectively at fcc-hcp sites, which were found to be most stable [22]. These numbers agree very well with the reported experimental value of 67 kcal/mol [38]. We find the same binding site to be most stable, but a weaker binding (57.5 kcal/mol) energy in our calculations.

5. Summary

Our enthalpies of formation for C_2H_y species adsorbed on Ni(111) are in good agreement with the decomposition pathways observed in experiments. The similar enthalpies we find for $CHCH_{ad}$ and $CCH_{3,ad}$, making $CHCH_{ad}$ the most stable C_2H_y species by only 0.4 kcal/mol over $CCH_{3,ad}$ in C_2H_y decomposition on Ni(111), are consistent with the experimental observation of a low surface coverage decomposition pathway in which CHCH is the longest lived C_2H_y intermediate, and a high surface coverage pathway in which $CCH_{3,ad}$ becomes an important intermediate. Our structure for $CHCH_{ad}$ matches the experimental binding site along with the C-C and C-Ni distances. For $CH_2CH_{2,ad}$ we find binding at a fcc-top site to be 4.2 kcal/mol more stable than the experimentally observed double-top binding site.

On Ni(111) forming a C-C bond to form a $C_2H_{y,ad}$ species from $CH_{x,ad}$ and $CH_{y-x,ad}$ is exothermic except in the case of $CHCH_{3,ad}$ where it is endothermic by 0.2 kcal/mol. Thus the strength of the C-C bonds on Ni(111) ranges from -0.2 kcal/mol for $CHCH_{3,ad}$ to 26.3 kcal/mol for $CCH_{3,ad}$. The small, but favorable energy typically associated with a C-C bond on Ni(111) helps explain its ability to catalyze the formation, cleavage and reformation of C-C bonds under various reaction conditions, because controlling the entropy (which generally favors breaking C-C bonds) can be used to adjust whether or not the overall system favors making or breaking the C-C bonds of interest.

Tables

Bound Species	Binding Site	Calc. M_s	Opt. $2M_s$	ΔM_s	C_2H_y M_s	ΔE_{form}	E_{bond}	E_{snap}	C_2H_y Strain	Slab Strain
Ni Slab	—	17/2	16.67	0.0	0.0	**0.0**	**—**	—	—	—
CH_2CH_3	top	16/2	16.21	-0.46	-0.01	**-24.0**	**32.5**	41.2	6.5	2.3
$CHCH_3$	fcc	16/2	15.50	-1.17	0.04	**-16.8**	**82.7**	97.8	14.0	1.1
CH_2CH_2	fcc-top	17/2	16.66	-0.01	0.00	**-22.9**	**19.7**	42.6	21.2	1.7
CCH_3	hcp	15/2	15.04	-1.63	-0.02	**-18.2**	**130.8**	156.7	24.5	1.4
$CHCH_2$	fcc-top	16/2	16.00	-0.67	0.08	**-6.5**	**63.2**	82.1	17.0	1.9
CCH_2	fcc-top	16/2	15.89	-0.88	0.03	**-2.2**	**93.6**	105.5	9.8	2.2
CHCH	fcc-hcp	16/2	15.58	-1.09	0.06	**-7.3**	**57.5**	127.0	67.0	1.9
CCH	fcc-hcp	16/2	15.77	-0.90	0.11	**13.8**	**120.4**	133.8	10.4	2.9
CC	fcc-hcp	17/2	16.52	-0.15	0.31	**40.4**	**162.8**	168.9	0.4	5.7

Table 1: Summary of C_2H_y Binding Data on Ni (111). "Calc. M_s" corresponds to the half-integer spin state with the lowest energy, which is the spin used in the optimum geometry and energy calculations presented here. "Opt. $2M_s$" is the optimum state spin (in number of unpaired electrons) predicted by a parabolic fit of the energies of the lowest three half-integer spin calculations. "ΔM_s" is the change in spin of the slab upon adsorption of the C_2H_y fragment. "C_2H_y M_s" is the spin density on the adsorbate when adsorbed on Ni(111). **"ΔE_{form}"** is the energy of formation with respect to standard states: H_2 gas, graphite (adjusted to our computational reference of diamond corrected using the 0.45 kcal/mol experimental value of diamond relative to graphite) and the bare Ni(111) slab. **"E_{bond}"** is the adiabatic bond energy (difference between the geometry relaxed energy of the complex and the sum of the geometry relaxed energies of the slab and the adsorbent infinitely separated from each other). "E_{snap}" is the bond energy for which the separated adsorbent geometry and the slab geometry remain the same as in the complex. "C_2H_y strain" is the energy released by relaxing the geometry of the adsorbate after breaking its bond to the surface by moving it infinitely far away. "Slab strain" is the energy released by relaxing the slab geometry after moving the adsorbate that was bonding to it infinitely far away. All energies are in kcal/mol.

Bound Species	Binding Site	R_{C-Ni}, Bond	R_{C-Ni}, Bond	R_{C-Ni}, Bond	R_{C-Ni}, Bond	R_{C-C}	E_{C-C}	C_2H_y charge
CH_2CH_3	top	1.99, σ	—	—	—	1.52	3.7	0.00
$CHCH_3$	fcc	1.95, σ	1.95, σ	—	—	1.52	-0.2	-0.13
CH_2CH_2	fcc-top	1.99, $\pi^{\perp}$	2.20, $\pi^{\perp}$	—	—	1.44	15.3	+0.14
CCH_3	hcp	1.87, σ	1.87, σ	1.87, σ	—	1.49	26.3	-0.17
$CHCH_2$	fcc-top	1.92, σ	2.03, $\pi^{\perp}$	2.09, $\pi^{\perp}$	—	1.42	2.1	+0.04
CCH_2	fcc-top	1.87, σ	1.87, σ	2.03, $\pi^{\perp}$	2.09, $\pi^{\perp}$	1.38	23.0	-0.04
CHCH	fcc-hcp	1.99, σ	2.00, σ	2.03 (2), $\pi^{\parallel}$	2.03 (2), $\pi^{\parallel}$	1.40	6.2	-0.10
CCH	fcc-hcp	1.84, σ	2.10, σ	1.96 (2), $\pi^{\parallel}$	2.08 (2), $\pi^{\parallel}$	1.36	10.3	0.00
CC	fcc-hcp	1.90, σ	1.90, σ	2.01 (2), $\pi^{\perp}$, $\pi^{\parallel}$	2.02 (2), $\pi^{\perp}$, $\pi^{\parallel}$	1.34	8.8	+0.05

Table 2: Summary of C_2H_y Binding Data on Ni (111). "$R_{C-Ni,}$ Bond" list the C-Ni bond distances and bond type associated with the distance. "σ" refers to a C-Ni σ bond, "$\pi^{\perp}$" refers to a C-C π bond perpendicular to the bonding to the Ni(111) surface involved in multi-center bonding to the surface, and "$\pi^{\parallel}$" refers to a C-C π bond parallel to the Ni(111) surface involved in multi-center bonding to the surface. Equivalent distances involved in the same multi-center bond are denoted with "(2)" following the bond distance. "R_{C-C}" is the C-C bond distance in Å. "E_{C-C}" is the energy in kcal/mol gained by forming $CH_xCH_{y-x,ad}$ from $CH_{x,ad}$ and $CH_{y-x,ad}$ on Ni(111). "C_2H_y charge" is the net charge on the adsorbate when adsorbed on Ni(111).

	site	$\mathbf{E_{bond}}$ $\mathbf{D_e}$	Gas ZPE	Ad ZPE	$\mathbf{H_{bond}}$ **0 K**	Gas 298.15K	Ad 298.15K	$\mathbf{H_{bond}}$ **298.15 K**
CH_2CH_3	top	**32.5**	37.3	41.6	**28.2**	3.1	2.1	**29.1**
$CHCH_3$	fcc	**82.7**	29.7	32.0	**80.4**	2.8	2.4	**80.9**
CH_2CH_2	fcc-top	**19.7**	32.1	36.4	**15.3**	2.5	1.4	**16.5**
CCH_3	fcc	**130.8**	22.2	25.7	**127.2**	2.6	2.1	**127.7**
$CHCH_2$	fcc-top	**63.2**	23.0	26.9	**59.3**	2.5	1.6	**60.2**
CCH_2	fcc-top	**93.6**	14.9	20.5	**88.0**	2.7	1.1	**89.5**
CHCH	fcc-hcp	**57.5**	17.0	19.7	**54.8**	2.4	1.1	**56.1**
CCH	fcc-hcp	**120.4**	8.0	12.8	**115.6**	2.1	1.2	**116.5**
CC	fcc-hcp	**162.8**	2.4	5.8	**159.4**	2.1	0.8	**160.7**

Table 3: ZPE and Finite Temperature Corrected Binding Energies of C_2H_y Species to most stable sites on Ni(111). "$\mathbf{E_{bond}}$ $\mathbf{D_e}$" is the binding energy obtained directly from our periodic PBE calculations. "Gas ZPE" is the zero-point energy (ZPE) of the adsorbate in the gas phase. "Ad ZPE" is the ZPE of the adsorbate adsorbed on Ni(111). "**$\mathbf{H_{bond}}$ 0 K"** is the effective binding enthalpy at 0 K, obtained by correcting E_{bond} D_e for ZPE energies. "Gas 298.15 K" is the finite temperature correction for the adsorbate in the gas phase at 298.15 K. "Ad 298.15 K" is the finite temperature correction for the adsorbate adsorbed at an fcc site on Ni(111) at 298.15 K. **"$\mathbf{H_{bond}}$ 298.15K"** is the effective binding enthalpy at 298.15 K obtained by correcting E_{bond} D_e for the ZPE and the finite temperature correction at 298.15 K. Both ZPE and finite temperature corrections were obtained from B3LYP calculations on a Ni_9 (or Ni_{10}) cluster. All energy values are in kcal/mol.

	Diamond and H_2 References			Ethane & H_{ad} References		
	ΔH_{form} D_e	**ΔH_{form} 0 K**	**ΔH_{form} 298.15 K**	**ΔH_{eth} D_e**	**ΔH_{eth} 0 K**	**ΔH_{eth} 298.15 K**
$CH_{4,gas}$	-32.4	-21.9	-23.7	2.5	3.3	4.4
$CH_3CH_{3,gas}$	-42.9	-25.2	-29.1	0.0	0.0	0.0
$CH_{3,ad} + CH_{3,ad}$	-37.7	-22.8	-26.2	5.2	2.4	2.9
$CH_2CH_{3,ad}$	-26.6	-10.9	-14.1	2.9	1.0	1.5
$CH_{2,ad} + CH_{3,ad}$	-22.9	-12.9	-15.3	6.6	-0.3	0.3
$CHCH_{3,ad}$	-19.4	-10.1	-12.0	-3.4	-9.1	-10.0
$CH_{,ad} + CH_{3,ad}$	-19.6	-12.5	-14.5	-3.6	-12.5	-12.4
$CH_2CH_{2,gas}$	-3.7	5.7	3.9	12.3	5.7	5.9
$CH_2CH_{2,ad}$	-23.4	-9.6	-12.6	-7.4	-9.6	-10.6
$CH_{2,ad} + CH_{2,ad}$	-8.1	-2.9	-4.3	7.9	-2.9	-2.3
$CCH_{3,ad}$	-20.8	-14.5	-15.8	-18.2	-27.1	-27.2
$C_{ad} + CH_{3,ad}$	5.5	9.7	7.9	8.1	-2.9	-3.5
$CHCH_{2,ad}$	-6.9	0.5	-1.2	-4.4	-12.1	-12.6
$CH_{ad} + CH_{2,ad}$	-4.8	-2.6	-3.5	-2.2	-15.2	-15.0
$CCH_{2,ad}$	-2.6	1.7	0.5	-13.5	-23.5	-24.5
$C_{ad} + CH_{2,ad}$	20.3	19.6	18.9	9.4	-5.6	-6.1
$CHCH_{gas}$	49.8	50.5	50.6	38.9	23.3	25.6
$CHCH_{ad}$	-7.7	-4.3	-5.5	-18.6	-29.5	-30.5
$CH_{ad} + CH_{ad}$	-1.5	-2.2	-2.7	-12.4	-27.4	-27.7
CCH_{ad}	13.4	13.1	13.0	-11.0	-24.7	-25.5
$C_{ad} + CH_{ad}$	23.6	20.0	19.7	-0.7	-17.8	-18.9
CC_{gas}	202.7	195.3	197.2	164.9	144.9	145.1
CC_{ad}	39.9	35.9	36.5	2.1	-14.5	-15.6
$C_{ad} + C_{ad}$	48.8	42.2	42.1	11.0	-8.2	-10.0

Table 4: ZPE and Finite Temperature Corrected Enthalpies for C_2H_y on Ni(111). "ΔH_{from} D_e" is the enthalpy of formation relative to diamond, H_2 gas, and the Ni(111) slab obtained directly from periodic DFT(PBE) calculations. **"ΔH_{form} 0 K"** is the enthalpy of formation relative to diamond, H_2 gas, and the Ni(111) slab at 0 K, including ZPE corrections obtained from B3LYP calculations. **"ΔH_{form} 298.15 K"** is the enthalpy of formation relative to diamond C, H_2 gas, and the Ni(111) slab at 298.15 K, including ZPE and finite temperature corrections obtained from B3LYP calculations. **"ΔH_{eth} D_e"** is the enthalpy of formation relative to CH_3CH_3 gas, H_{ad} on Ni(111), and the Ni(111) slab obtained directly from periodic DFT(PBE) calculations. **"ΔH_{eth} 0 K"** is the enthalpy of formation relative to CH_3CH_3 gas, H_{ad} on Ni(111), and the Ni(111) slab at 0 K, including ZPE corrections obtained from B3LYP calculations. **"ΔH_{eth} 298.15 K"** is the enthalpy of formation relative to CH_3CH_3 gas, H_{ad} on Ni(111), and the Ni(111) slab at 298.15 K, including ZPE and finite temperature corrections obtained from B3LYP calculations. All enthalpies are in kcal/mol.

		Bao et al. [6]	Present
Adsorbate	Distance	Photoelectron Diffraction	QM DFT(PBE)
CHCH	C-C	1.44 ± 0.15 Å	1.40 Å
CHCH	C_{fcc}-$Ni_{surface}$	1.36 ± 0.04 Å	1.41 Å
CHCH	C_{hcp}-$Ni_{surface}$	1.37 ± 0.04 Å	1.41 Å
CH_2CH_2	C-C	1.60 ± 0.18 Å	1.45 Å
CH_2CH_2	C-$Ni_{surface}$	1.90 ± 0.02 Å	2.07 Å

Table 5: Bond distances in $CHCH_{ad}$ and $CH_2CH_{2,ad}$. Comparison of bond distances with experimental values. The experimental binding site for $CHCH_{ad}$ (fcc-hcp) is the same as lowest energy binding site from DFT calculations. Experiment observes top-top site for CH_2CH_2, so our values are for binding at a top-top site, not the fcc-top site for which we observe the strongest binding energy (4.2 kcal/mol stronger than top-top site).

	Present	Medlin [22]		Fahmi [21]		Shustorovich [24]	Anderson [20]	
Method	QM DFT(PBE)	QM DFT(PW91)		QM DFT (LDA)		empirical BOC-MP	QM MO study	
Model	4 L Slab	6 L	3L	Ni_{14}	Ni_4	—	Ni_{13}	Ni_2
CH_2CH_3	32.5	—	—	—	—	49	—	—
$CHCH_3$	82.7	—	—	—	—	85	—	—
CH_2CH_2	19.7	—	—	13	-4	15	13	-4
CCH_3	130.8	—	—	—	—	115	—	—
$CHCH_2$	63.2	—	—	—	—	55	—	—
CCH_2	93.6	—	—	—	—	87	—	—
CHCH[a]	57.5	68.8	68.2	50	37	18	50	37
CCH	120.4	—	—	—	—	84	—	—
CC	162.8	—	—	—	—	—	—	—

[a]Experimental energy is 67 kcal/mol [36].

Table 6: Comparison of Theoretical Results for Binding of C_2H_y Species to Ni(111). Comparison of binding energies for various methods and models for C_2H_y species binding at different sites on Ni(111). All energy values are in kcal/mol.

	Present	Burghgraef [23]		Shustorovich [24]	Anderson [20]
Method	QM DFT (PBE)	QM DFT (LDA)		empirical BOC-MP	QM MO study
Model	4 L, 2x2 Slab	Ni_{13}	Ni_7	—	Ni_2
$CH_2CH_{3,ad} \rightarrow CH_{2,ad} + CH_{3,ad}$	3.7	—	—	18	—
$CHCH_{3,ad} \rightarrow CH_{ad} + CH_{3,ad}$	-0.2	—	—	13	—
$CH_2CH_{2,ad} \rightarrow CH_{2,ad} + CH_{2,ad}$	15.3	—	—	21	35
$CCH_{3,ad} \rightarrow C_{ad} + CH_{3,ad}$	26.3	16	51	-21	—
$CHCH_{2,ad} \rightarrow CH_{ad} + CH_{2,ad}$	2.1	—	—	13	—
$CCH_{2,ad} \rightarrow C_{ad} + CH_{2,ad}$	23.0	3	36	-2	—
$CHCH_{ad} \rightarrow CH_{ad} + CH_{ad}$	6.2	—	—	16	16
$CCH_{ad} \rightarrow C_{ad} + CH_{ad}$	10.3	-15	-15	-25	—
$C_{2,ad} \rightarrow C_{ad} + C_{ad}$	8.8	—	—	—	—

Table 7: Comparison of Theoretical Results for C-C Cleavage Reactions in C_2H_y species on Ni(111). Comparison of reaction energies for C-C bond cleavages in C_2H_y decomposition on Ni(111). All energy values are in kcal/mol.

Figures

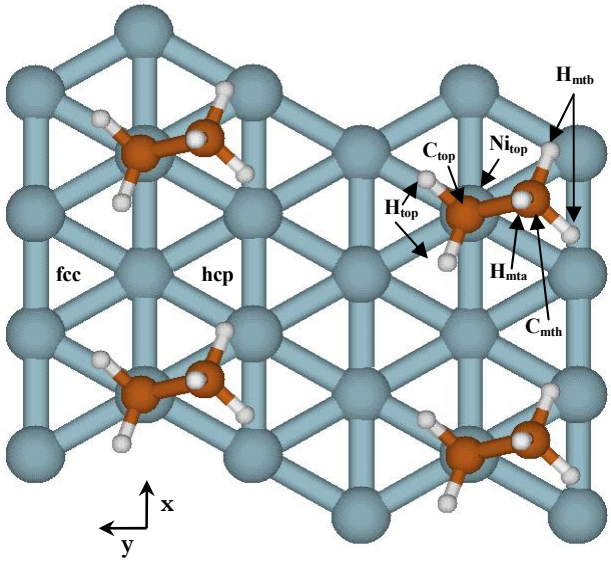

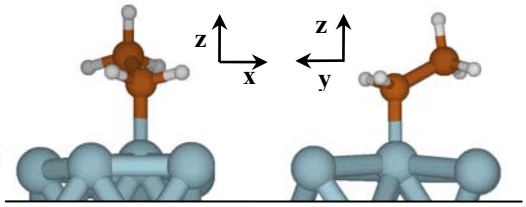

C_{top}-C_{mth}:	1.52 Å,	(σ)			
C_{top}-Ni_{top}:	1.99 Å,	(σ)			
C_{top}-H_{top} (2):	1.10 Å,	(σ)			
C_{mth}-H_{mta}:	1.10 Å,	(σ)			
C_{mth}-H_{mtb} (2):	1.10 Å,	(σ)			
Ni_{top}-C_{top}-H_{top} (2):	104º,		Ni_{top}-C_{top}-C_{mth}:	117º	
H_{top}-C_{top}-C_{mth} (2):	112º,		C_{top}-C_{mth}-H_{mtb}:	112º	
H_{mta}-C_{mth}-H_{mtb} (2):	107º,		H_{mtb}-C_{mth}-H_{mtb}:	107º	
C_{top}-C_{mth}-H_{mta} (2):	110º				
H_{top}-C_{top}-H_{top} (2):	108º				

Figure 1: Optimized structure for $CH_2CH_{3,ad}$ adsorbed at top site on four-layer Ni(111) slab (only top layer of Ni atoms is shown in 2×2 expansion of unit cell view in z direction). Bond distances and types (σ = σ bond, $\pi^{\parallel}$ = π bond parallel to surface, $\pi^{\perp}$ = π bond perpendicular to surface, σ^3 = three-center C-H-Ni bond, n.b. = no bond) for selected pairs of atoms are listed, followed by selected angles.

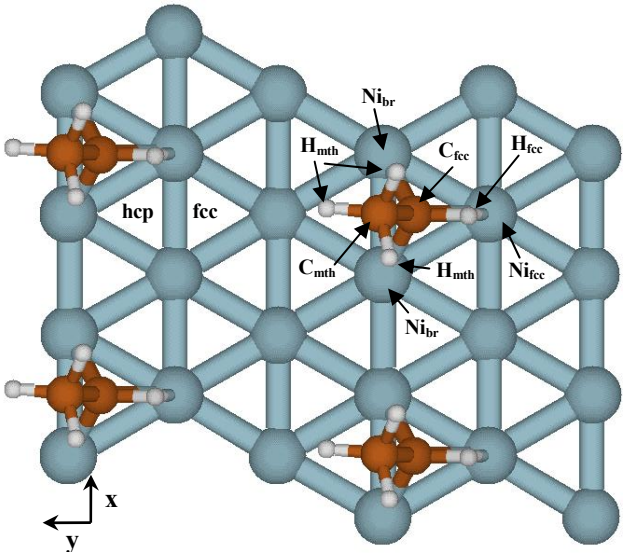

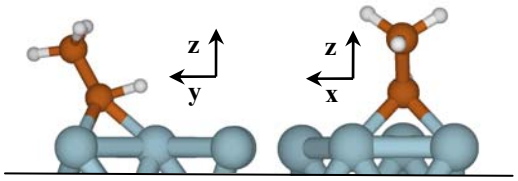

C_{fcc}-Ni_{fcc}:	2.05 Å,	(σ^3)			
C_{fcc}-Ni_{br} (2):	1.95 Å,	(σ)			
C_{fcc}-H_{fcc}:	1.17 Å,	(σ^3)			
H_{fcc}-Ni_{fcc}:	1.72 Å,	(σ^3)			
C_{fcc}-C_{mth}:	1.52 Å,	(σ)			
C_{mth}-H_{mth} (3):	1.10 Å,	(σ)			
Ni_{br}-C_{fcc}-H_{fcc} (2):	120º,		Ni_{fcc}-C_{fcc}-H_{fcc}:	57º	
Ni_{fcc}-C_{fcc}-Ni_{br} (2):	78º,		Ni_{br}-C_{fcc}-Ni_{br}:	80º	
Ni_{br}-C_{fcc}-C_{mth} (2):	117º,		Ni_{fcc}-C_{fcc}-C_{mth}:	159º	
C_{fcc}-C_{mth}-H_{mth} (3):	111º,		H_{fcc}-C_{fcc}-C_{mth}:	102º	
H_{mth}-C_{mth}-H_{mth} (3):	108º				

Figure 2: Optimized structure for $CHCH_{3,ad}$ adsorbed at a fcc site on a four-layer Ni(111) slab (only top layer of Ni atoms is shown in 2×2 expansion of unit cell view in z direction). Bond distances and types (σ = σ bond, $\pi^{\parallel}$ = π bond parallel to surface, $\pi^{\perp}$ = π bond perpendicular to surface, σ^3 = three-center C-H-Ni bond, n.b. = no bond) for selected pairs of atoms are listed, followed by selected angles.

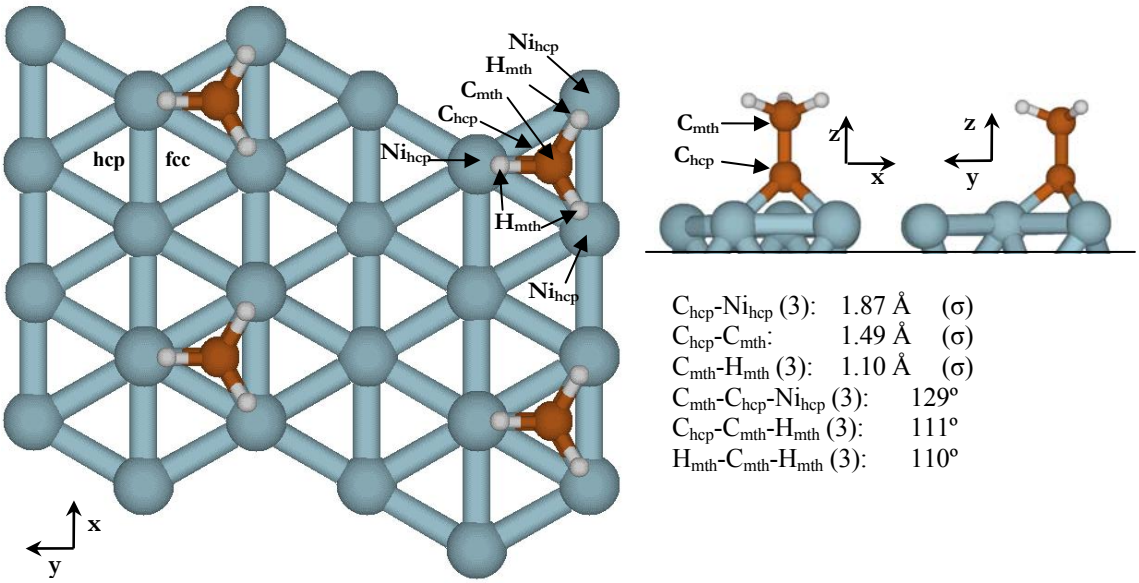

C_{hcp}-Ni_{hcp} (3):	1.87 Å	(σ)
C_{hcp}-C_{mth}:	1.49 Å	(σ)
C_{mth}-H_{mth} (3):	1.10 Å	(σ)
C_{mth}-C_{hcp}-Ni_{hcp} (3):	129º	
C_{hcp}-C_{mth}-H_{mth} (3):	111º	
H_{mth}-C_{mth}-H_{mth} (3):	110º	

Figure 3: Optimized structure for $CCH_{3,ad}$ adsorbed at a hcp site on a four-layer Ni(111) slab (only top layer of Ni atoms is shown in 2×2 expansion of unit cell view in z direction). Bond distances and types (σ = σ bond, $\pi^{\parallel}$ = π bond parallel to surface, $\pi^{\perp}$ = π bond perpendicular to surface, σ^3 = three-center C-H-Ni bond, n.b. = no bond) for selected pairs of atoms are listed, followed by selected angles.

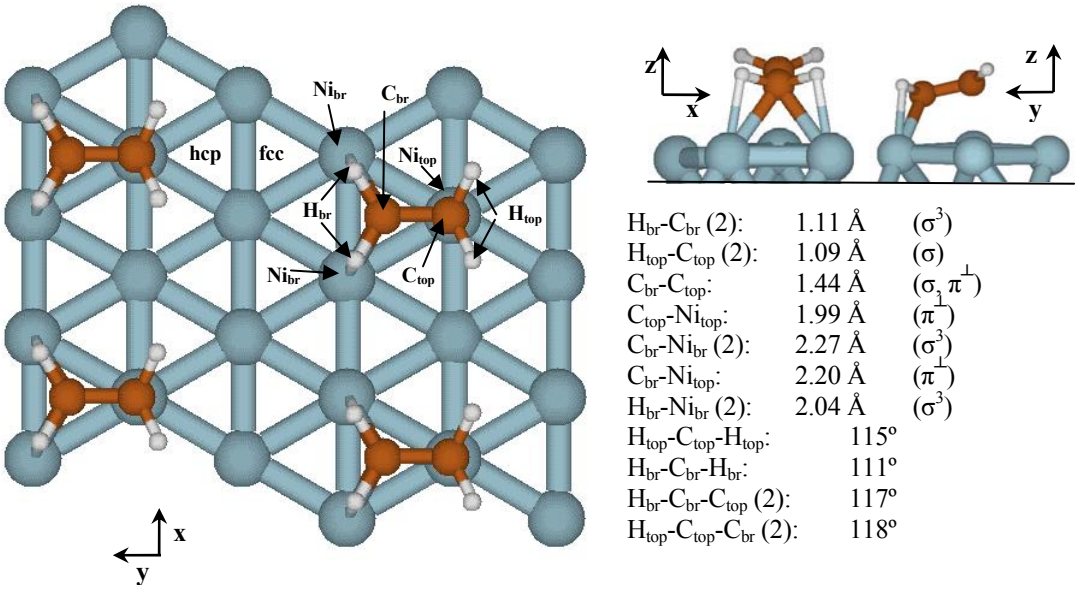

H_{br}-C_{br} (2):	1.11 Å	(σ^3)
H_{top}-C_{top} (2):	1.09 Å	(σ)
C_{br}-C_{top}:	1.44 Å	(σ, $\pi^{\perp}$)
C_{top}-Ni_{top}:	1.99 Å	($\pi^{\perp}$)
C_{br}-Ni_{br} (2):	2.27 Å	(σ^3)
C_{br}-Ni_{top}:	2.20 Å	($\pi^{\perp}$)
H_{br}-Ni_{br} (2):	2.04 Å	(σ^3)
H_{top}-C_{top}-H_{top}:	115º	
H_{br}-C_{br}-H_{br}:	111º	
H_{br}-C_{br}-C_{top} (2):	117º	
H_{top}-C_{top}-C_{br} (2):	118º	

Figure 4: Optimized structure for $CH_2CH_{2,ad}$ adsorbed at a fcc-top site on a four-layer Ni(111) slab (only top layer of Ni atoms is shown in 2×2 expansion of unit cell view in z direction). Bond distances and types (σ = σ bond, $\pi^{\parallel}$ = π bond parallel to surface, $\pi^{\perp}$ = π bond perpendicular to surface, σ^3 = three-center C-H-Ni bond, n.b. = no bond) for selected pairs of atoms are listed, followed by selected angles.

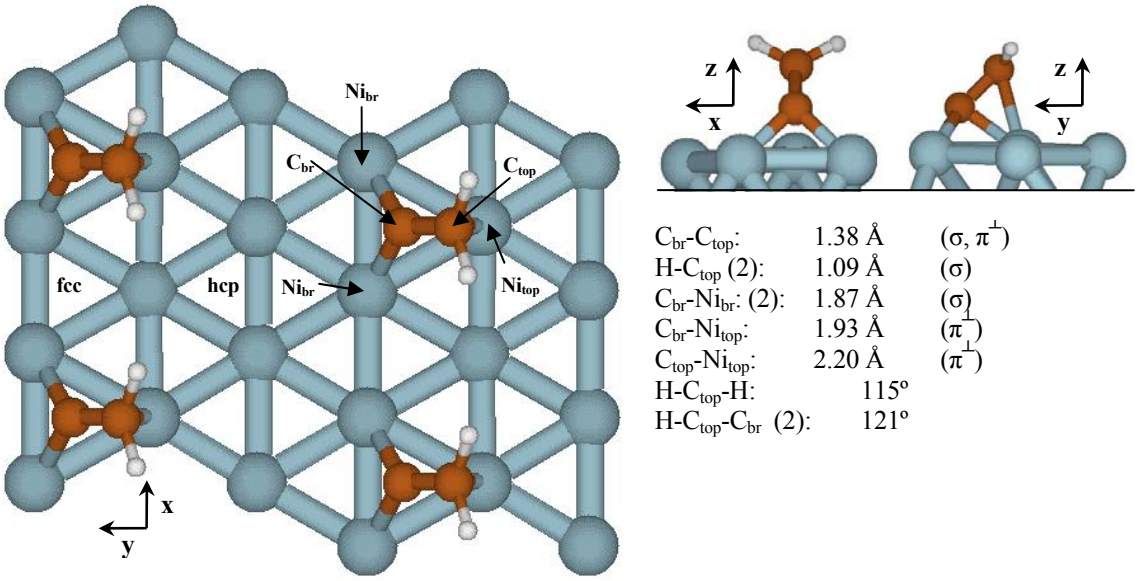

C_{br}-C_{top}:	1.38 Å	(σ, $\pi^{\perp}$)
H-C_{top} (2):	1.09 Å	(σ)
C_{br}-Ni_{br}: (2):	1.87 Å	(σ)
C_{br}-Ni_{top}:	1.93 Å	($\pi^{\perp}$)
C_{top}-Ni_{top}:	2.20 Å	($\pi^{\perp}$)
H-C_{top}-H:	115º	
H-C_{top}-C_{br} (2):	121º	

Figure 5: Optimized structure for $CCH_{2,ad}$ adsorbed at fcc-top site on a four-layer Ni(111) slab (only top layer of Ni atoms is shown in 2×2 expansion of unit cell view in z direction). Bond distances and types (σ = σ bond, $\pi^{\parallel}$ = π bond parallel to surface, $\pi^{\perp}$ = π bond perpendicular to surface, σ^3 = three-center C-H-Ni bond, n.b. = no bond) for selected pairs of atoms are listed, followed by selected angles.

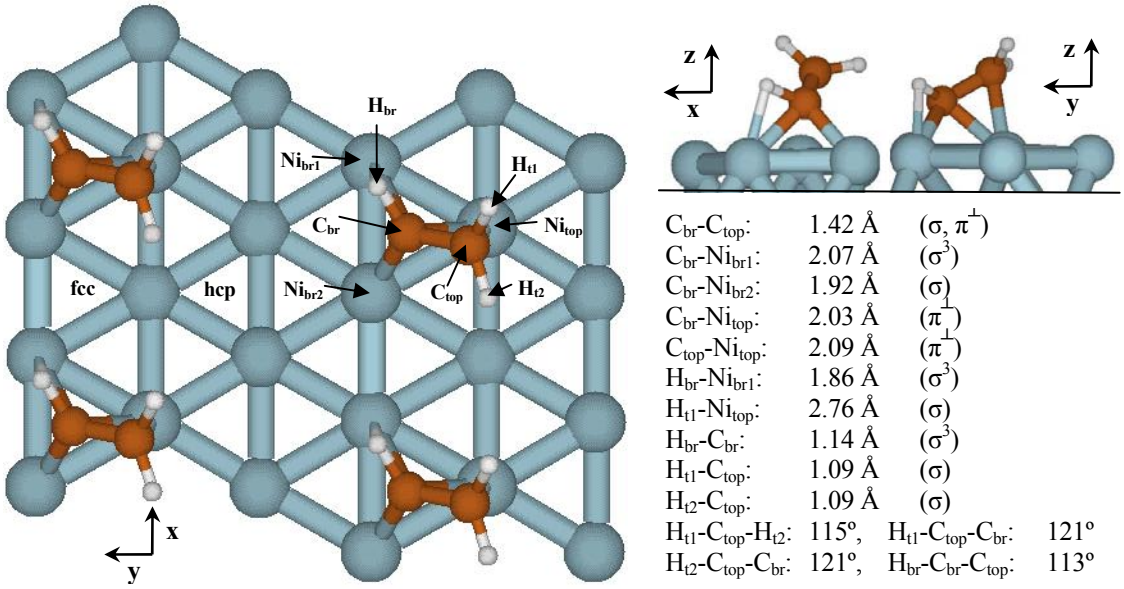

C_{br}-C_{top}:	1.42 Å	(σ, $\pi^{\perp}$)	
C_{br}-Ni_{br1}:	2.07 Å	(σ^3)	
C_{br}-Ni_{br2}:	1.92 Å	(σ)	
C_{br}-Ni_{top}:	2.03 Å	($\pi^{\perp}$)	
C_{top}-Ni_{top}:	2.09 Å	($\pi^{\perp}$)	
H_{br}-Ni_{br1}:	1.86 Å	(σ^3)	
H_{t1}-Ni_{top}:	2.76 Å	(σ)	
H_{br}-C_{br}:	1.14 Å	(σ^3)	
H_{t1}-C_{top}:	1.09 Å	(σ)	
H_{t2}-C_{top}:	1.09 Å	(σ)	
H_{t1}-C_{top}-H_{t2}:	115º,	H_{t1}-C_{top}-C_{br}:	121º
H_{t2}-C_{top}-C_{br}:	121º,	H_{br}-C_{br}-C_{top}:	113º

Figure 6: Optimized structure for $CHCH_2$ adsorbed at a fcc-top site on a four-layer Ni(111) slab (only top layer of Ni atoms is shown in 2×2 expansion of unit cell view in z direction). Bond distances and types (σ = σ bond, $\pi^{\parallel}$ = π bond parallel to surface, $\pi^{\perp}$ = π bond perpendicular to surface, σ^3 = three-center C-H-Ni bond, n.b. = no bond) for selected pairs of atoms are listed, followed by selected angles.

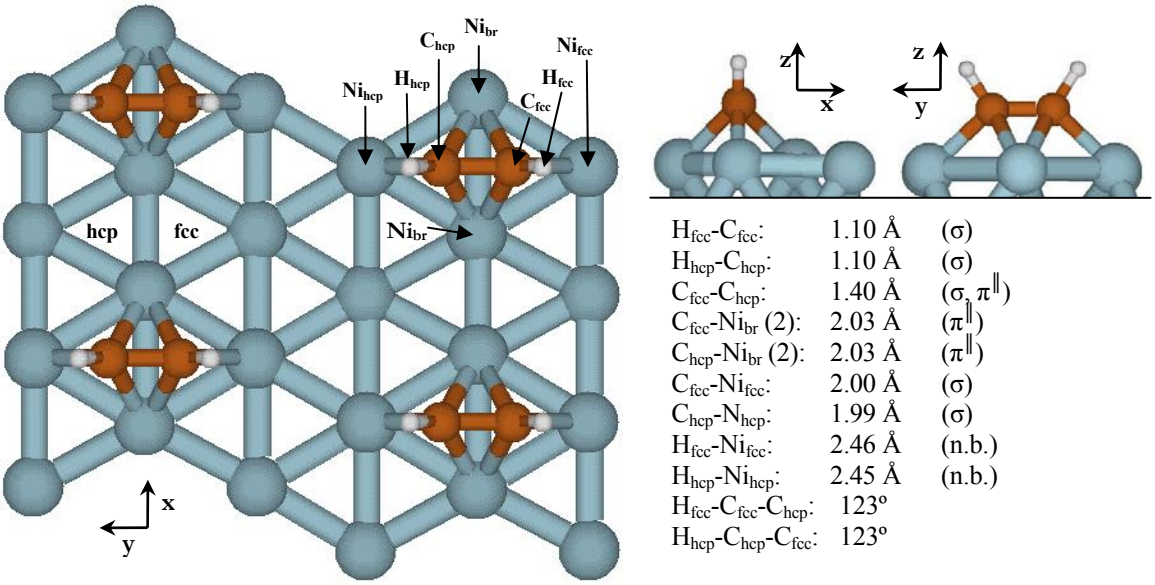

H_{fcc}-C_{fcc}:	1.10 Å	(σ)
H_{hcp}-C_{hcp}:	1.10 Å	(σ)
C_{fcc}-C_{hcp}:	1.40 Å	(σ, $\pi^{\parallel}$)
C_{fcc}-Ni_{br} (2):	2.03 Å	($\pi^{\parallel}$)
C_{hcp}-Ni_{br} (2):	2.03 Å	($\pi^{\parallel}$)
C_{fcc}-Ni_{fcc}:	2.00 Å	(σ)
C_{hcp}-N_{hcp}:	1.99 Å	(σ)
H_{fcc}-Ni_{fcc}:	2.46 Å	(n.b.)
H_{hcp}-Ni_{hcp}:	2.45 Å	(n.b.)
H_{fcc}-C_{fcc}-C_{hcp}:	123°	
H_{hcp}-C_{hcp}-C_{fcc}:	123°	

Figure 7: Optimized structure for $CHCH_{ad}$ adsorbed at a fcc-hcp site on a four-layer Ni(111) slab (only top layer of Ni atoms is shown in 2×2 expansion of unit cell view in z direction). Bond distances and types (σ = σ bond, $\pi^{\parallel}$ = π bond parallel to surface, $\pi^{\perp}$ = π bond perpendicular to surface, σ^3 = three-center C-H-Ni bond, n.b. = no bond) for selected pairs of atoms are listed, followed by selected angles.

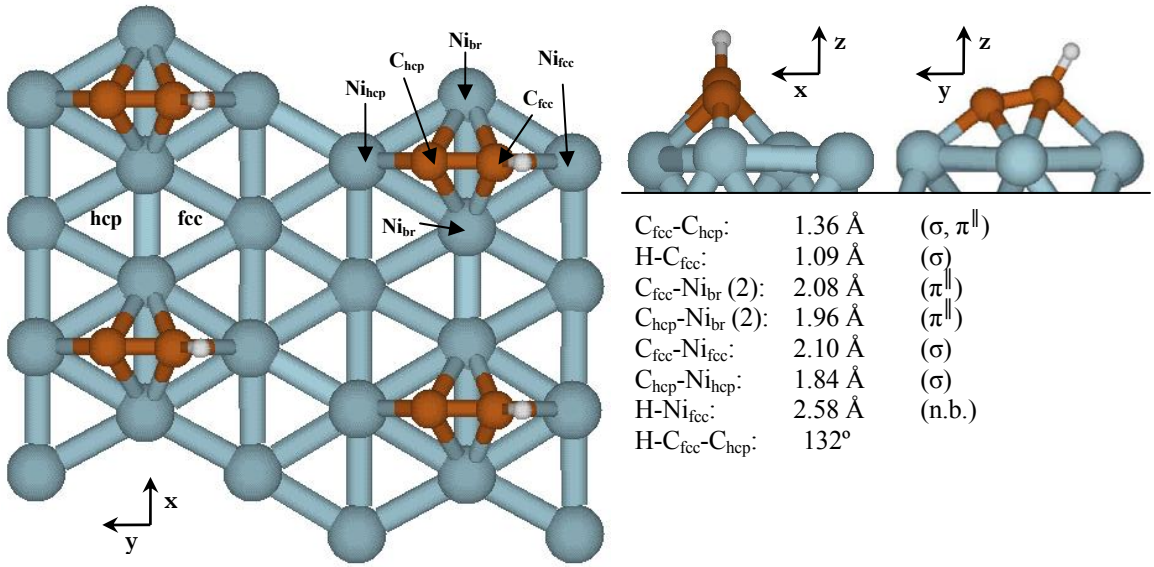

C_{fcc}-C_{hcp}:	1.36 Å	(σ, $\pi^{\parallel}$)
H-C_{fcc}:	1.09 Å	(σ)
C_{fcc}-Ni_{br} (2):	2.08 Å	($\pi^{\parallel}$)
C_{hcp}-Ni_{br} (2):	1.96 Å	($\pi^{\parallel}$)
C_{fcc}-Ni_{fcc}:	2.10 Å	(σ)
C_{hcp}-Ni_{hcp}:	1.84 Å	(σ)
H-Ni_{fcc}:	2.58 Å	(n.b.)
H-C_{fcc}-C_{hcp}:	132°	

Figure 8: Optimized structure for CCH_{ad} adsorbed at a fcc-hcp site on a four-layer Ni(111) slab (only top layer of Ni atoms is shown in 2×2 expansion of unit cell view in z direction). Bond distances and types (σ = σ bond, $\pi^{\parallel}$ = π bond parallel to surface, $\pi^{\perp}$ = π bond perpendicular to surface, σ^3 = three-center C-H-Ni bond, n.b. = no bond) for selected pairs of atoms are listed, followed by selected angles.

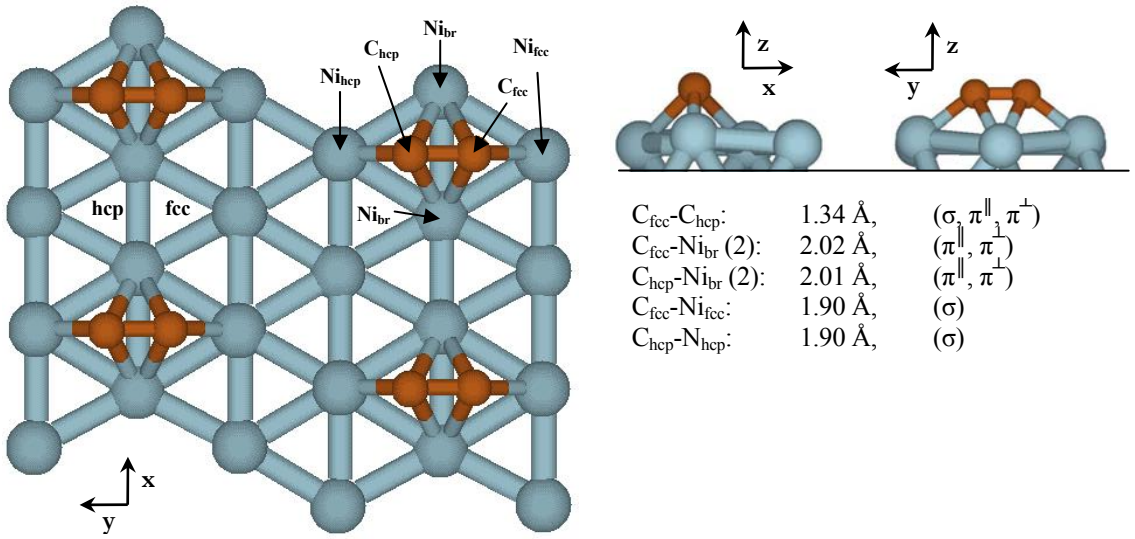

Figure 9: Optimized structure for CC adsorbed at a fcc-hcp site on a four-layer Ni(111) slab (only top layer of Ni atoms is shown in 2×2 expansion of unit cell view in z direction). Bond distances and types (σ = σ bond, $\pi^{\parallel}$ = π bond parallel to surface, $\pi^{\perp}$ = π bond perpendicular to surface, σ^{3} = three-center C-H-Ni bond, n.b. = no bond) for selected pairs of atoms are listed, followed by selected angles.

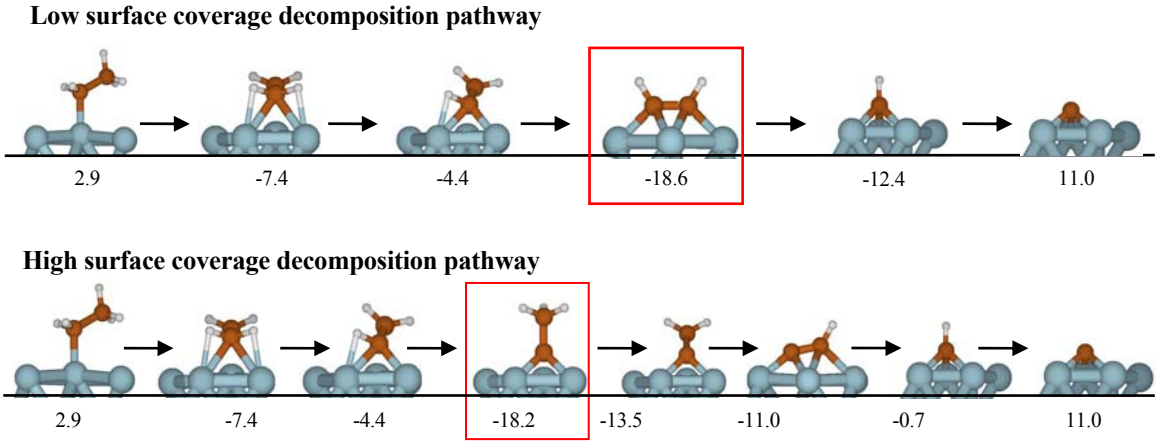

Figure 10: Expected decomposition pathways for ethane on Ni(111) based on energies of intermediates reported here. Energies of formation (D_e) relative to ethane reported in kcal/mol.

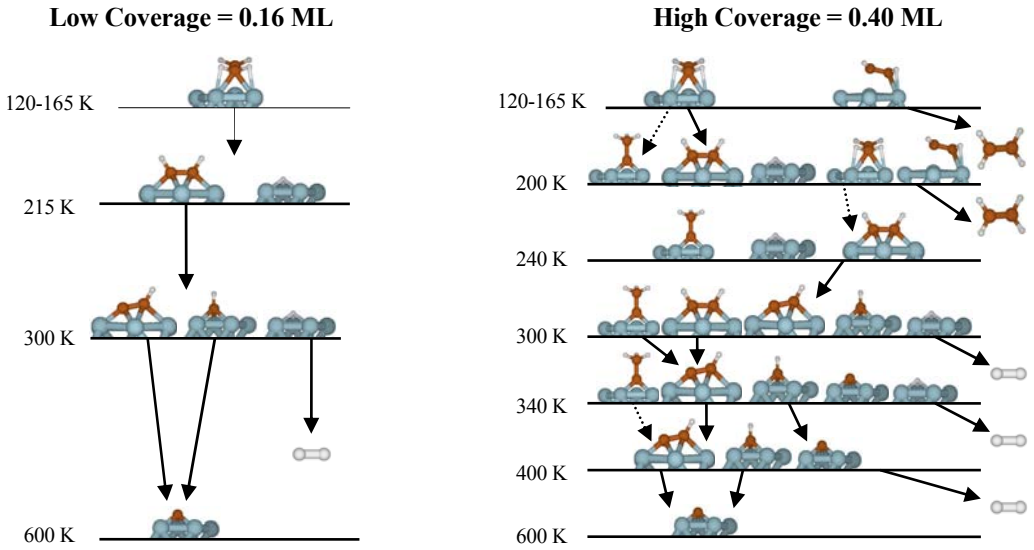

Figure 11: $CH_3CH_{3,gas}$ decomposition intermediates observed as a function of temperature in TPSSIMS in experiments on Ni(111) [15].

References

1. Mueller, J. E.; van Duin, A. C. T.; Goddard, W. A. Development and Validation of ReaxFF Reactive Force Field for Hydrocarbon Chemistry Catalyzed by Nickel. *J. Phys. Chem. C* **2010**, *114* (11), 4939-4949. (Chapter 3)
2. Mueller, J. E.; van Duin, A. C. T.; Goddard, W. A. Application of ReaxFF Reactive Dynamics to Reactive Dynamics of Hydrocarbon Chemisorption and Decomposition. *J. Phys. Chem. C* **2010**, *114* (12), 5675-5685. (Chapter 4)
3. Rostrup-Nielsen, J. R. Catalytic Steam Reforming, in *Catalysis, Science and Technology*, J.R. Anderson and M. Boudar, Eds. 1984, Springer: Berlin; 1-117.
4. Egeberg, R. C.; Ullman, S.; Alstrup, I.; Mullins, C. B.; Chorkendorff, I. Dissociation of CH_4 on Ni(111) and Ru(0001). *Surf. Sci.* **2002**, *497* (1-3), 183-193.
5. Paillet, M.; Jourdain, V.; Phoncharal, P.; Sauvajol, J.-L.; Zahab, A. Versatile Synthesis of Individual Single-Walled Carbon Nanotubes from Nickel Nanoparticles for the Study of their Physical Properties. *J. Phys. Chem. B* **2004**, *108* (44), 17112-17118.
6. Bao, S.; Hofmann, Ph.; Schindler, K.-M.; Fritzsche, V.; Bradshaw, A. M.; Woodruff, D. P.; Casado, D.; Asensio, M. C. The Local Geometry of Reactant and Product in a Surface Reaction: the Dehydrogenation of Adsorbed Ethylene on Ni(111). *Surf. Sci.* **1995**, *323 (1-2)*, 19-29.
7. Demuth, J. E. Conversion of Ethylene to Acetylene on Ni(111). *Surf. Sci.* **1978**, *76 (2)*, L603-L608.
8. Demuth, J. E. Molecular Geometries of Acetylene and Ethylene Chemisorbed on Cu, Ni, Pd, and Pt Surfaces. *IBM J. Res. Develop.* **1978**, *22 (3)*, 265-276.
9. Demuth, J. E. Structure of Chemisorbed Acetylene and Ethylene on Ni, Pd and Pt Surfaces. *Surf. Sci.* **1979**, *84 (2)*, 315-328.
10. Demuth J. E.; Eastman, D. E. Determination of the State of Hybridization of Unsaturated Hydrocarbons Chemisorbed on Nickel. P*hys. Rev. B* **1976**, *13 (4)*, 1523-1527.
11. Demuth J. E.; Eastman, D. E. Photoemission Observations of π-d Bonding and Surface-Reactions of Adsorbed Hydrocarbons on Ni(111). *Phys. Rev. Lett.* **1974**, *32 (20)*, 1123-1127.
12. Lehwald, S.; Erley, W.; Ibach, H.; Wagner, H. Dehydrogenation of Acetylene on a Stepped Nickel Surface. *Chem. Phys. Lett.* **1979**, *62 (2)*, 360-363.
13. Sham, T. K.; Carr, R. G. Carbon Near Edge X-Ray Absorption Fine-Structure (NEXAFS) Studies of Ethylene Adsorption on Ni(111) and Ni(110) Surfaces: Implication for Surface Morphology Insensitive Reactions. *J. Chem. Phys.* **1986**, *84(7)*, 4091-4095.
14. Zhu, X.-Y.; Castro, M. E.; Akhter, S.; White, M. E.; Houston, J. E. Static Secondary Ion Mass Spectroscopy Study of Ethylene and Acetylene on Ni: Coverage Dependence. *J. Vac. Sci. Technol. A* **1989**, *7 (3)*, 1991-1995.
15. Zhu, X.-Y.; White, J. M. Interaction of Ethylene and Acetylene with Ni(111): A SSIMS Study. *Surf. Sci.* **1989**, *214 (1-2)*, 240-256.

16. Casalone, G.; Cattania, M. G.; Simonetta, M.; Tescari, M. Chemisorption of Unsaturated-Hydrocarbons on Ni(100) Studied by Low-Energy Electron-Diffraction and Auger-Spectroscopy. *Surf. Sci.* **1977**, *62 (1)*, 321-325.
17. Lehwald, S.; Ibach, H. Decomposition of Hydrocarbons on Flat and Stepped Ni(111) Surfaces. *Surf. Sci.* **1979**, *89 (1-3)*, 425-445.
18. Zaera, F.; Hall, R. B. Low-Temperature Decomposition of Ethylene over Ni(100): Evidence for Vinyl Formation. *Surf. Sci.* **1987**, *180 (1)*, 1-18.
19. Zhu, X.-Y.; White, J. M. Evidence for Ethylidyne Formation on Ni(111). *Catal. Lett.* **1988**, *1*, 247-254.
20. Anderson, A. B. Structural and Orbital Analysis of Ethylene and Acetylene on Ni(111) Surfaces. *J. Chem. Phys.* **1976**, *65 (5)*, 1729-1734.
21. Fahmi, A.; van Santen, R. A. Density Functional Study of Acetylene and Ethylene Adsorption on Ni(111). *Surf. Sci.* **1997**, *371 (1)*, 53-62.
22. Medlin, J. W.; Allendorf, M. D. Theoretical Study of the Adsorption of Acetylene on the (111) Surfaces of Pd, Pt, Ni, and Rh. *J. Phys. Chem. B* **2003**, *107 (1)*, 217-223.
23. Burghgraef, H.; Jansen, A. P. J.; van Santen, R. A. Electronic-Structure Calculations and Dynamics of CC Coupling on Nickel and Cobalt. *J. Chem. Phys.* **1995**, *103 (15)*, 6562-6570.
24. Shustorovich, E. The Bond-Order Conservation Approach to Chemisorption and Heterogeneous Catalysis: Applications and Implications. Adv. Catal. **1990**, *37*, 101.
25. Shustorovich, E. Bond-Order Conservation Approach to Chemisorption of Polyatomic-Molecules: Effective Partitioning of 2-Center Bond-Energies. *Surf. Sci.* **1988**, *205 (1-2)*, 336-352.
26. Perdew, J. P.; Burke, K.; Ernzerhof, M. Generalized Gradient Approximation Made Simple. *Phys. Rev. Lett.* **1996**, *77 (18)*, 3865-3868.
27. Schultz, P. A. *SeqQuest*, Sandia National Labs, Albuquerque, NM http://dft.sandia.gov/Quest/.
28. Mueller, J. E.; van Duin, A.C.T.; Goddard, W.A. Structures, Energetics, and Reaction Barriers for CH_x Bound to Ni(111) Surfaces. *J. Phys. Chem. C* **2009**, *113* (47), 20290-20306. (Chapter 1)
29. Edwards, A. *Post analysis code for SeqQuest*, http://dft.sandia.gov/Quest/SeqQ_Dev_Guides.html.
30. Our calculated value for the energy minimized Ni-Ni distance in the bulk fcc structure is 4.50 Å; nevertheless, the computed energy difference per Ni atom between the experimental and calculated lattice constants is less than 0.1 kcal/mol, so using the experimental value is appropriate.
31. D.R. Lide, ed. *CRC Handbook of Chemistry and Physics*, 81st ed.; CRC Press: Boca Raton, FL, 2000.
32. *Jaguar 7.0*. 2007, Schrodinger Inc.
33. Becke, A. D. Density-Functional Thermochemistry. III. The Role of Exact Exchange. *J. Chem. Phys.* **1993**, *98 (7)*, 5648-5652.

34. Lee, C. T.; Yang, W. T.; Parr, R. G.; Development of the Colle-Salvetti Correlation-Energy Formula into a Functional of the Electron Density. *Phys. Rev. B* **1988**, *37 (2)*, 785-789.

35. Wong, M. W. Vibrational Frequency Prediction Using Density Functional Theory. *Chem Phys. Lett.* **1996**, *256 (4-5)*, 391-399.

36. *BIOGRAF 330*. 1993, Molecular Simulations Inc.

37. Mayo, S. L.; Olafson, B. D.; Goddard, W. A. Dreiding: A Generic Force-Field for Molecular Simulations. *J. Phys. Chem.* **1990**, *94 (26)*, 8897-8909.

38. Bond, G. C. *Catalysis by Metals*. **1962**, New York: Academic Press

Chapter 3

DEVELOPMENT AND VALIDATION OF REAXFF REACTIVE FORCE FIELD FOR HYDROCARBON CHEMISTRY CATALYZED BY NICKEL[1]

To enable the study of hydrocarbon reactions catalyzed by nickel surfaces and particles using reactive molecular dynamics on thousands of atoms as a function of temperature and pressure, we have developed the ReaxFF reactive force field to describe adsorption, decomposition, reformation, and desorption of hydrocarbons as they interact with the nickel surfaces. The ReaxFF parameters were determined by fitting to the geometries and energy surfaces from quantum mechanics (QM) calculations for a large number of reaction pathways for hydrocarbon molecules chemisorbed onto nickel (111), (110), and (100) surfaces, supplemented with QM equations of state for nickel and nickel carbides.

We demonstrate the validity and accuracy of applying ReaxFF reactive dynamics to hydrocarbon chemistry catalyzed by nickel particles and surfaces. First, ReaxFF is shown to reproduce the binding energies for small hydrocarbons on Ni(100) and Ni(110) obtained from QM calculations, which were not used to train the ReaxFF parameters. Good agreement is also shown between ReaxFF and important experimental values. Finally the accuracy and applicability of ReaxFF is demonstrated by performing ReaxFF reactive dynamics of methyl decomposition on three different nickel surfaces. Consistent with experiment, we observe the formation of chemisorbed methylidyne plus subsurface carbide following the dissociation of methyl on the (111), (100) and stepped (111) surfaces of

---

[1] Reproduced with permission from Jonathan E. Mueller, Adri C. T. van Duin and William A. Goddard, III, "Development and Validation of ReaxFF Reactive Force Field for Hydrocarbon Chemistry Catalyzed by Nickel" *J. Phys. Chem. C*, **2010**, *114* (11), 4939-4949. Copyright 2010 American Chemical Society.

nickel. We observe that the (111) surface is the least reactive, the (100) surface has the fastest reaction rates, and the stepped (111) surface has an intermediate reaction rate. These results highlight the importance of surface defects in accelerating reaction rates.

1. Introduction

The chemistry of hydrocarbons on nickel has been studied for several decades for scientific and technological reasons. Nickel is the primary catalyst in the steam reforming process [1] for converting methane and water into synthesis gas (carbon monoxide and hydrogen) which is then used in important industrial processes such as the Haber-Bosch synthesis of ammonia and the Fischer-Tropsch formation of higher hydrocarbons [2]. Recently nickel has also been used extensively to catalyze the formation and growth of carbon nanotubes from hydrocarbon feedstock.[3]

Nickel's role as the catalyst of choice employed in industrial steam reformation has motivated a number of experimental [2,4-9] and theoretical studies [10-13] of methane adsorption to various nickel surfaces. Because the dissociative chemisorption of methane unto nickel is the rate limiting step in the reformation process, much of the work on hydrocarbon chemistry on nickel surfaces has focused on the energetics and dynamics of methane sticking to various nickel surfaces, aiming to obtain an understanding of the physical nature of the activation barrier for this chemisorption process. Early experiments demonstrated that Ni(111) is the least reactive of the low index surfaces [14]; however, because of its high stability much of the subsequent research has focused on exploring reactions on this surface.

Besides the Ni(111) surface, several studies have also examined the reactivity of the Ni(100) [15-17] and Ni(211) [2,16,18-19] surfaces. The Ni(211) surface is of special

interest because it is the simplest surface that includes steps between Ni(111) terraces. Experimental studies have been conducted to test the effects of step defects on chemisorption unto the Ni(111) surface by using gold, sulfur, alkali metals or other atoms [20, 21] to selectively bind to and hence deactivate step sites. These studies confirm that the reactivity of a Ni(111) surface is enhanced by the presence of step defects. Both experimental and theoretical studies show that steps not only provide a low energy barrier for the chemisorption of methane unto nickel, but also catalyze the cleavage of additional carbon-hydrogen bonds and the formation of carbon-carbon bonds.

While much research has focused on the initial chemisorption process, other studies have examined the subsequent chemical processes that a methyl fragment undergoes once adsorbed [22-24]. Vibrational spectra from high-resolution electron energy loss spectroscopy (HREELS) have been used to identify the stable species formed from the chemisorption of methane unto Ni(111) as a function of temperature [23, 24]. These studies show that methyl (CH_3) loses two H atoms when the temperature reaches 150 K to form methylidyne (CH), which dimerizes at temperatures above 250 K to form acetylene (CHCH). The effect of additional heating depends on the surface coverage. If the surface is nearly saturated, the CHCH molecules join together to form four-, six- and eight-member rings. However, if the surface coverage is too low then dehydrogenation takes place before the CHCH molecules are able to diffuse and find each other to form ring structures. Another study used secondary ion mass spectroscopy (SIMS) to detect methyl, methylene and methylidyne intermediates in the Fischer-Tropsch synthesis of methane and water from carbon monoxide and hydrogen catalyzed on Ni(111) and concluded that a mechanism of sequential hydrogenation was responsible for methane production [22].

Atomistic simulations provide a useful tool for studying catalytic processes. In principle, quantum mechanics (QM) calculations (computing electron-electron interactions explicitly in the context of a background potential created by the nuclear charges) are capable of describing the forces on atoms along catalyzed reaction pathways in heterogeneous systems [25]. In particular, density functional theory (DFT) is widely used to explore catalytic systems (reference [26] is an example of how DFT can be used to study a related system); however, in many cases the complexity of the system requires system sizes and numbers of time steps well beyond the current practical limits of QM calculations to sufficiently characterize the process of interest. Because of this, traditional molecular dynamics (MD) simulations (in which inter-atomic interactions are the basic quantity computed) can be used to treat much larger systems and longer time scales than DFT calculations; however, because most of the classical force fields employed in traditional MD simulations use a simple harmonic-like bond description, traditional MD simulations are unable to correctly describe chemical reactions.

There are two approaches for bridging the gap between QM and traditional MD methods. One may either look for approximations to reduce the computational cost of handling electron-electron interactions explicitly, or else develop inter-atomic potentials which describe the results of electron-electron interactions implicitly. The former approach includes empirical tight binding (TB) methods, in which the number of electrons is reduced and the computation of at least some of the electron-electron interactions is simplified (reference [27] is an example of such a TB method applied to a related system). The conceptual advantage of a TB model is that the physics of electron-electron interactions is treated explicitly.

In contrast, the second approach utilizes chemical concepts (e.g. bond order, electronegativity and valency) to describe the effects of electron-electron interactions, which are thus described implicitly in inter-atomic interactions. Along these lines, reactive force field methods—capable of describing bond formation and cleavage in MD simulations—have been developed [28-30]. In particular, several of these have been applied to nickel (or other similar transition metals such as iron) and carbon in order to study carbon nanotube growth [31-37]. A key limitation to many of the reactive force fields developed so far has been that they are typically designed to treat a very specific chemical system and are not easily transferred or extended beyond that system.

Here, we describe the development and application of a highly-transferable reactive force field description for C/H/Ni systems, by deriving ReaxFF parameters for these atoms and their interactions. Some previously reported ReaxFF descriptions include hydrocarbons [38], silicon/silicon oxide [39], metals [40], metal oxides [41], and metal hydrides [42], indicating the transferability of the ReaxFF concept. ReaxFF RD simulations have proved useful in studying a variety of complex chemical systems [39, 43-45]. Several years ago we reported on the development of a ReaxFF description for all carbon materials and their interactions with cobalt, nickel and copper atoms (i.e. a C/Ni force field primarily describing C-C and C-Ni bonding) [46]. We have combined the C/Ni parameters from this ReaxFF description of C/Ni systems with the C/H parameters from ReaxFF description of hydrocarbons, and then extended the resulting force field to treat condensed nickel and nickel carbide phases, as well as the chemistry of hydrocarbon species on nickel surfaces. The result is a C/H/Ni ReaxFF force field with parameters describing C-C, C-H, C-Ni, H-

Ni and Ni-Ni bonding, which is thus capable of modeling a wide range of hydrocarbon reactions catalyzed by nickel surfaces, particles or atoms.

To validate our ReaxFF description for hydrocarbons and nickel we have performed reactive MD simulations of the decomposition of methyl radicals on three nickel surfaces: (100), (111), and (111) with a step. The influence of steps has been characterized both experimentally and theoretically, providing a basis for comparison with our results.

2. Theoretical Methods

2.1. QM Methods

Both periodic and cluster *ab initio* calculations were used to provide QM results against which to fit the ReaxFF parameters. Many of these QM results have been published previously [26, 38, 46].

As described elsewhere [26], all periodic QM calculations were performed with the SeqQuest periodic DFT code and utilized the spin-polarized PBE flavor of DFT and pseudopotentials [47]. Forces were relaxed within 0.0005 Rydbergs/Bohr. Reasonably converged grid spacing and numbers of k-points were used. An accelerated steepest descent (ASD) geometry minimization algorithm was used to relax all structures. A nudged elastic band (NEB) procedure was used to calculate energy barriers for reactions.

All non-periodic ab *initio* cluster calculations were taken from Nielson et al. [46]. These calculations were performed with the B3LYP flavor of DFT as implemented in the Jaguar 5.0 program package [48]. Nickel was described with the Wadt and Hay core-valence (relativistic) effective core potential [49-51] (treating the valence electrons explicitly) using the LACVP basis set with the valence double-ζ contraction of the basis functions, LACVP**. All electrons were used for all other elements using a modified

variant of Pople et al.'s 6-31G** basis set [52, 53], where the six d functions have been reduced to five. For the all-carbon training set the QM training set was composed from DFT/B3LYP/6-31G** calculations.

2.2. ReaxFF Reactive Force Field

ReaxFF uses the bond order/bond distance relationship introduced by Tersoff [30], and applied to carbon chemistry by Brenner to describe chemical reactivity [28]. Bond orders—summed from σ, π and ππ terms—are calculated instantaneously from interatomic distances as follows:

$$BO_{ij} = BO_{ij}^{\sigma} + BO_{ij}^{\pi} + BO_{ij}^{\pi\pi} = \exp\left[p_{bo1}\left(\frac{r_{ij}}{r_0^{\sigma}}\right)^{p_{bo2}}\right] + \exp\left[p_{bo3}\left(\frac{r_{ij}}{r_0^{\pi}}\right)^{p_{bo4}}\right] + \exp\left[p_{bo5}\left(\frac{r_{ij}}{r_0^{\pi\pi}}\right)^{p_{bo6}}\right] \quad \textbf{(1)}$$

Overcoordination and undercoordination energy penalties are then used to enforce the correct bond order. The total system energy is a sum of a several partial energy terms; these include energies related to: lone pairs, undercoordination, overcoordination, valence and torsion angles, conjugation, hydrogen bonding, and van der Waals and Coulomb interactions. Thus, the total energy can be expressed as:

$$E_{system} = E_{bond} + E_{lp} + E_{over} + E_{under} + E_{val} + E_{pen} + E_{coa} + E_{C_2} + E_{tors} + E_{H-bond} + E_{vdWaals} + E_{Couloumb} \quad \textbf{(2)}$$

Because Coulomb and van der Waals interactions are calculated between every pair of atoms, ReaxFF describes not only covalent bonds, but also ionic bonds and the whole range of intermediate interactions. Charge distributions are calculated based on geometry and connectivity using the electronegativity equalization method (EEM) [54]. Coulomb interactions are treated using a seventh order spline (Taper function) [39]. To keep ReaxFF

from erroneously predicting a strong triple bond in C_2, an additional partial energy contribution is utilized as reported previously [46].

The force field parameters were optimized to the QM data using the single-parameter search optimization technique described previously [55]. Because the geometries of optimum reaction pathways in ReaxFF will not necessarily be identical to the optimum reaction pathways obtained from DFT, we focus our training on the energetics (relative energies of resting states and barriers) of reactions rather than on the forces along each pathway (only the zero forces as stationary points are relevant). In all cases, differential energies were obtained by comparing calculations performed using the same basis sets and the same functional. The ReaxFF equations are provided in Appendix A, and parameters relevant to the C/H/Ni force field presented in Appendix B.

2.3. MD Simulations

The temperature programmed (NVT)-MD simulations were performed using a velocity Verlet approach with a time step of 0.25 fs. A Berendsen thermostat with a damping constant of 100 fs was used for temperature control. Each MD simulation was initiated from an energy minimized structure and was equilibrated to the simulation temperature by the thermostat prior to any reactive events being observed.

3. Results and Discussion

3.1. Force Field Development

To train the ReaxFF force field parameters to describe hydrocarbon reactions catalyzed on nickel particles we began with the parameters from the previously published ReaxFF force field description of the interactions between carbon and nickel atoms, which has been successfully applied to the early stages of nanotube growth as catalyzed by nickel atoms

[46], and from the previously published ReaxFF description of hydrocarbons [38]. To obtain an accurate description of nickel catalyst particles, ReaxFF parameters relevant to Ni-Ni bonding (see Table 1) were optimized to fit heats of formation for nickel at various densities in fcc, bcc, a15, simple cubic, and diamond crystal structures as calculated with QM. For an accurate description of nickel catalyzed hydrocarbon chemistry, the ReaxFF parameters relevant to C-Ni and H-Ni bonding (Tables 2-5) were optimized to fit an extensive set of binding energies for hydrocarbons at nickel surface, subsurface and bulk sites. Furthermore, because there are situations in which the catalyst particle is likely to form a nickel carbide, these same parameters were simultaneously optimized against heats of formation calculated from QM for Ni_3C, Ni_2C, and the B1, B2, B3 and B4 phases of NiC.

3.1.1. Hydrocarbon Interactions

The bond, angle and torsion parameters for C, H and C/H were determined by a fit to the previously published [38] hydrocarbon training set along with additional structures relative to CNT growth [46]. Because of the importance of the graphite-like structures for studying carbon nanotube growth, the atomization energy for graphite was corrected to give 180.2 kcal/mol matching our QM value of 180.7 kcal/mol. Thus a total of 773 data points were used to fit 68 relevant C/H parameters.

3.1.2. Nickel-Nickel Interactions

To ensure that ReaxFF appropriately treats nickel atoms in a range of chemical environments and configurations with different numbers of near neighbors we trained it to reproduce the energies for expansions and compressions of a variety of nickel crystal structures obtained from QM. Although most of these structures are not experimentally

realizable, it is important that ReaxFF is able to identify them as energetically unfavorable so that it avoids them in simulations by recognizing their high energy cost. ReaxFF predicts the equilibrium bcc crystal structure to be 0.41 kcal/mol higher in energy than the fcc structure in good agreement with our QM value of 0.85 kcal/mol. The a15 structure is 2.92 kcal/mol higher in energy than the fcc structure, agreeing with our QM result of 2.73 kcal/mol. The simple cubic crystal structure is significantly higher in energy, with ReaxFF giving an energy of 19.35 kcal/mol greater than the fcc structure, while QM gives 14.97 kcal/mol for this quantity. For high energy states such as the simple cubic lattice it is not essential that ReaxFF produces the energy exactly as long as it gives a sufficiently high energy to realize that the configuration is energetically unfavorable, because an energetically unfavorable structure is not something ReaxFF needs to know how to reproduce exactly, but merely to avoid. The diamond structure is even more unfavorable with QM showing it to be 30.22 kcal/mol higher than the fcc structure and ReaxFF giving a similarly large value of 35.25 kcal/mol. Figure 1 shows a comparison between relative energies for the expansion/compression curves of these crystal types obtained from ReaxFF and QM. The curves show good agreement between ReaxFF and QM, except for the diamond structure, which does not show a minimum in the region of interest. However, ReaxFF does reproduce both the unfavorable energy of the diamond structure relative to the other structures as well as the inner potential wall making diamond particularly unfavorable at typical nickel densities. This is an indication that additional training would be required before using ReaxFF to study low density nickel solid phases. Finally, it should also be noted that ReaxFF reproduces the cohesive energy of nickel (103.7 kcal/mol) in good agreement with experiment (102.4 kcal/mol) [56].

The energy versus cell volume data for the nickel fcc lattice can also be used to compute structural properties such as the lattice constant, the density and the bulk modulus. ReaxFF gives an equilibrium lattice spacing of 3.656 Å in good agreement with our QM result of 3.54 Å, and the experimental result of 3.524 Å [57]. This gives an equilibrium density of 7.98 g/cm^3 which is in reasonable agreement with the experimental value of 8.91 g/cm^3 [58]. Using the Birch-Murnaghan equation of state to fourth order [59], we obtain values for the bulk modulus of 148 GPa from the ReaxFF data and 142 GPa from the QM data. These are both in reasonable agreement with the experimental value of 180.26 GPa [58].

Finally, ReaxFF reproduces the surface energies per surface atom for the Ni(111) and Ni(100) surfaces as 15.2 kcal/mol and 18.59 kcal/mol respectively compared to 14.7 kcal/mol and 20.4 kcal/mol from QM. For both surfaces these surface energies are in good agreement with experimental and other theoretical results. For the (111) surface the experimental results are 18.4 kcal/mol [60], and 18.9 kcal/mol [61], while other results from theory are 15.4 kcal/mol [62] and 15.5 kcal/mol [63]. For the (100) surface the experimental value is 14.1 kcal/mol [64] and another theoretical result is 17.2 kcal/mol [62]. Overall, 78 data points were used to fit the 11 parameters listed in Table 1.

3.1.3. Hydrocarbon Interactions with Atomic Nickel

To validate the ReaxFF method for interactions between nickel atoms and many hydrocarbon species we used the metal hydrocarbon interactions previously computed from QM and used to train the ReaxFF parameters to study the early stages of carbon nanotube growth catalyzed by Ni atoms [46].

3.1.3.1. Nickel Carbides

The energies for expansions and compressions of several nickel carbide phases in Figure 2 show good agreement with corresponding QM calculations. Training with both stable and unstable carbide phases helps ensure that ReaxFF is able to recognize both favorable and unfavorable structures by energetically distinguishing between a variety of valence configurations.

3.1.3.2. Chemisorbed Hydrocarbons

To extend the ReaxFF method to treat interactions of hydrocarbons with nickel particles we have trained the ReaxFF parameters against an extensive set of energies and structures from QM involving the binding of a range of hydrocarbon species to nickel surface and bulk structures. Because we believe that it is important to characterize the ability of different metal surface sites to form one, two or three bonds with an adjacent hydrocarbon we have included the binding of H, C, CH, CH_2 and CH_3 to all high symmetry surface sites (fcc, hcp, bridge & on-top) on Ni(111). Figure 3a shows good agreement between ReaxFF and QM for heats of formation of these species bonded at these four sites.

Because C-H bond formation and cleavage is an important step in much of the hydrocarbon chemistry that is catalyzed by nickel particles it is important that the ReaxFF method is able to give the appropriate barriers for C-H bond formation and cleavage in different geometric configurations on nickel. Figure 3b shows the barriers for the chemisorption and complete dissociation of CH_4 into atomic C and adsorbed H atoms on Ni(111). Because these cases include C-H bonds pointed toward the surface ($CH_4 \rightarrow CH_{3,ad} + H_{ad}$), parallel to the surface ($CH_{3,ad} \rightarrow CH_{2,ad} + H_{ad}$ and $CH_{2,ad} \rightarrow CH_{ad} + H_{ad}$) and away from the surface ($CH_{ad} \rightarrow C_{ad} + H_{ad}$) they demonstrate that ReaxFF is able to describe all of

the basic kinds of C-H bond formation and cleavage that might take place in more complex reactions. Desorption of hydrogen from the surface as H_2 gas is also an important process for freeing surface sites and lowering the chemical potential of hydrogen on the surface. The ReaxFF parameters have also been optimized to accurately model this reaction.

Surface sites with coordination numbers not available on the (111) surface can play an important role in chemical reactions, especially when species capable of forming multiple bonds to the surface are involved. To verify that ReaxFF treats such interactions correctly, we trained it against the binding of C and CH to five coordination sites on Ni(100) and Ni(110). Comparison with QM data is in Figure 3c.

The stability of C-C bonds on nickel surfaces is important for studying both Fischer-Tropsch chemistry and the formation of carbon structures such as nanotubes on nickel catalyst particles. The binding of CC, CCH, CCH_2, CHCH, $CHCH_2$ and CH_2CH_2 provides a test set that covers the complete range of carbon-carbon bond types that can be formed parallel to the surface. Figure 3d shows the energetic comparison between ReaxFF and QM for these species.

Also of importance in describing the reactions of larger hydrocarbons on metal surfaces are steric interactions with the surface. To ensure that ReaxFF describes these effects correctly the binding energies for CH_x species with methyl groups substituted for one or more of the hydrogen substituents were used to train the force field parameters. ReaxFF correctly describes these steric effects as shown in Figure 3e.

For larger carbon structures C-C bonding on nickel surfaces is also important. Besides the many multi-carbon configurations found in the all carbon training set we trained ReaxFF to correctly describe the energies of C and CH chains on Ni(111). We have also

considered the case of a graphene sheet resting on the Ni(111) surface. It is particularly important that ReaxFF reproduces the appropriate energetic trends for these species so that it correctly describes the growth of carbon structures on nickel surfaces. Figure 4 compares energies from ReaxFF and QM data for this type of process.

3.1.3.3. Subsurface and Bulk Species

Subsurface and bulk carbon is believed to be important in catalyzing processes such as nanotube growth [65-67]. Figure 5a shows that ReaxFF correctly describes the energetics of carbon in both subsurface and bulk sites of nickel. Because carbon diffusion plays an important role in the vapor-liquid-solid (VLS) model, we included the migration barrier for interstitial carbon migration in nickel as shown in Figure 5b. Additionally, ReaxFF is capable of describing equations of state for several nickel carbide species and structures as described above.

Similarly, there are studies claiming that subsurface hydrogen can significantly alter the viable reactions hydrocarbons on nickel surfaces are able to undergo [68, 69], so we have also trained ReaxFF against a similar set of data for hydrogen in nickel subsurface and bulk sites. Figure 6 summarizes these results.

3.1.3.4. Charge Transfer

The EEM parameters (η, EEM hardness; χ, EEM electronegativity; and γ, EEM shielding parameter) for nickel were fit to Mulliken charge data from QM calculations on small clusters, with Ni in a variety of environments. For Ni bridging two CH_3 groups with single bonds the charge on Ni is 0.0639 in ReaxFF and 0.0964 with QM. If Ni is surrounded by four CH_3 groups in a tetrahedral configuration ReaxFF shows a charge of 0.1600 on Ni, similar to the value of 0.0700 from QM. When Ni forms a double bond to

CH_2 ReaxFF finds a charge of 0.0480 on Ni (the QM value is 0.0000). In the case of binding to hydrogen there is a negative charge on Ni. Thus, for Ni bridging between two H atoms, ReaxFF gives a charge of -0.0934 on Ni compared to -0.0589 in QM.

3.1.4. Training Summary for C/H/Ni Parameters

In all, there are 470 data points, which 85 ReaxFF parameters relevant to C/Ni, H/Ni, and C/H/Ni interactions were optimized against. These 85 parameters include 15 bond parameters (Table 2), 7 off-diagonal parameters (Table 3), 49 angle parameters (Table 4), and 9 torsion parameters (Table 5).

3.2. Force Field Validation

3.2.1. Explicit Comparison with Experiment

While, there is very little quantitative data from experiments for explicit comparison with our ReaxFF description of C/Ni, H/Ni and C/H/Ni interactions, the following cases (summarized in Table 6) are available for consideration:

1) The experimental activation energy for methane on Ni(111) is 17.7 kcal/mol [2], the QM result we trained ReaxFF against is 18.9 kcal/mol [11], and ReaxFF gives a result of 18.4 kcal/mol in excellent agreement with both.

2) The experimental reaction energy for ½ $H_{2,gas}$ → H_{ad} on Ni(111) is -12.5 kcal/mol (corrected to give values relative to D_e) [70, 26] [26, 70]. The QM result we trained ReaxFF against is -13.5 kcal/mol [26], and ReaxFF gives a result of -10.2 kcal/mol, which is in good agreement with both.

3) Surface science experiments (HREELS) [24] suggest that a three-fold site is the most stable binding site for both CH_3 and CH fragments on Ni(111). For CH_3, ReaxFF finds that binding to a three-fold (fcc) site is 4.5 kcal/mol more stable than binding to either a one-

fold (on-top) or two-fold (bridge) site. This value is in good agreement with the values obtained from the QM results ReaxFF was trained against (5.4 kcal/mol and 3.4 kcal/mol respectively). For CH ReaxFF finds that binding to a three-fold (hcp) site is 10.7 kcal/mol lower in energy than binding to a two-fold (bridge) site and 48.1 kcal/mol lower in energy than binding to a one-fold (on-top) site. Again, the ReaxFF ordering matches experiment and the values agree with the QM results ReaxFF was trained against (9.4 kcal/mol and 49.4 kcal/mol respectively).

3.2.2. Small Hydrocarbons Binding to Ni(100) and Ni(110)

To provide further evidence for the transferability of ReaxFF to systems not explicitly included in the training set we compare ReaxFF results for binding energies for five small hydrocarbons binding to Ni(100) and Ni(110) to results obtained from QM. The results are presented in Table 7, and show reasonable agreement between ReaxFF and QM, suggesting that although ReaxFF was trained primarily against data on hydrocarbon binding to Ni(111) that it is appropriate for applications to hydrocarbon chemistry on other nickel surfaces. These validation cases include C in a variety of chemical environments binding to several different types of nickel surface sites, again, highlighting the versatility and transferability of ReaxFF.

3.2.3. MD Simulations of Methyl Decomposition

To provide additional support for the validity of using ReaxFF for studying the decomposition of hydrocarbon molecules on nickel surfaces we performed NVT simulations of methyl decomposition on three nickel surfaces. Each simulation started with twelve methyl radicals (CH_3) bonded to either a Ni(100) surface, a Ni(111) surface or a Ni(111) surface with steps (one three-coordinate step and one four-coordinate step). The

initial temperature was set to 800 K and increased at a rate of 10 K/ps, so that the final temperature after 100 ps of dynamics was 1800 K. As seen from the results, 800 K was an appropriate starting temperature for our simulations, because at the timescale we studied methyl decomposition is not seen below 1000 K. Our ending temperature of 1800 K is also appropriate because there is significant melting of the nickel slabs above this temperature. During each simulation the populations of hydrocarbon species formed on the surface were monitored. They are presented in Figure 7 a, c, e.

On all three surfaces all or almost all of the CH_3 is converted to C and H by the end of the temperature ramp. As expected, CH_2 and CH are the key intermediates [26], with CH being more stable. On Ni(100) the reaction commences at about 900K, while on Ni(111) and stepped Ni(111) it commences at about 1000 K. In all three cases all CH_3 has decomposed by the time the temperature reaches 1300 K. The formation of CH_2 is quickly followed by further decomposition resulting in CH, so that there are never more than three or four CH_2 molecules on any surface at a given time. In contrast, CH is more stable, so that there exist simultaneously as many as ten molecules of CH on the Ni(111) slab and seven on Ni(100) and stepped Ni(111) slabs. The CH populations are largest when the temperature is between 1100 K and 1500 K. On Ni(100) all of the CH_3 is fully converted to C and H atoms by 1500 K, while a molecule or two of CH remain at 1600 K on the Ni(111) and stepped Ni(111) surfaces. Thus, Ni(100) is more efficient than Ni(111) at breaking the final C-H bond to convert CH to C and H.

The final structures of these simulations are shown in Figures 8-10. A visual analysis of the trajectories reveals the following processes. For the Ni(100) slab, breaking the final C-H bond to form C and H from CH is simultaneous with C going into the subsurface. Thus

the C atoms formed are not adsorbed on top of the surface, but have migrated into the bulk. There is a large barrier for this to take place, which is not overcome until the temperature reaches 1250 K, 44 ps into the simulation. When the all the CH has been converted to C and H at 90 ps (1550 K), all the C atoms produced are in the bulk of the nickel slab rather than sitting on the surface. By moving to the subsurface C is able to form four bond with Ni (instead of the limit of three to the surface due to geometric orbital constraints). Thus, both C and H are able to form an additional bond to Ni to compensate for the C-H bond being broken. While C prefers moving into the Ni subsurface, H prefers the surface; however, as the top surface of the slab fills up H easily diffuses through the slab and ends up on the bottom of the slab as well. Finally, after 95 ps the Ni(100) slab begins to melt.

For Ni(111), the slab spontaneously forms a step after 20 ps. This explains the strong similarities between the Ni(111) and stepped Ni(111) slab results. The decomposition process on the Ni(111) slabs is similar to the process on Ni(100) outlined above. The key differences are a slower reaction rate (i.e. higher temperatures are required for reactions to occur on Ni(111) than on Ni(100)), especially with respect to H and C moving into the subsurface. Again, CH does not like to break down into C and H until C is able to move into an energetically more stable subsurface position. The close-packed nature of the (111) surface requires higher temperatures for surface defects capable of introducing C into the subsurface to form. Thus, C first appears in the simulation on the (100) slab at 44 ps when the temperature is less than 1250 K, while it does not appear until 63 ps in the simulation on the (111) slab, which corresponds to a temperature of 1350 K. The stepped Ni(111) surface gives results somewhere in between because the original step encourages additional surface defects to form later on.

From these simulations it appears that surface defects play an important role in speeding up CH_3 decomposition. To test the role of surface defects we performed a second set of simulations, with two thermostats instead of one. To retain the crystalline surface structure of the slabs throughout the simulations, the temperature of the Ni atoms was maintained at 800 K, while the temperature of C and H atoms was ramped from 800 K to 1800 K. Results of this second set of simulations are presented in Figure 7 b, d, f. The initial and final structures can be seen in Figures 8-10. In all cases, methyl decomposition slows down significantly on the cool slabs. On the cool slabs it is much more evident that the Ni(100) surface is more reactive than the Ni(111) slab with or without steps. Of particular interest is the failure to break the final C-H bond to form C on the (111) surface and the difficulty of doing it on the (100) surface as evidenced in the small number (two) of C atoms formed. This supports the hypothesis that surface defects, particularly vacancies, provide an important low energy pathway for the final dehydrogenation step.

Another noticeable difference is the absence of H migration across the cooled slabs. A couple factors are likely involved in explaining this difference. First, the lack of defects in the Ni slab, makes it more difficult for H to find an energetically feasible pathway into the bulk. Second, a lone H in the bulk, or even on the surface, may have a difficult time maintaining its kinetic energy because it is in contact with heavier cool Ni atoms. The buildup of H on the upper surface may also be a factor in decreasing the reactivity of the cool slabs as higher surface coverage favors the formation—rather than breaking—of C-H bonds.

4. Summary

We find that the ReaxFF parameters developed by fitting to an extensive set of QM reaction surfaces and equations of state, lead to reactive energy surfaces for hydrocarbon decomposition, rearrangements, and reactions on nickel in good agreement with QM results. Here we have applied this ReaxFF description to explore the decomposition of methyl on Ni(100) and Ni(111) surfaces including the affect of surface defects, which we find play a substantial role in the rate of CH_3 decomposition and especially on the last step converting CH to C and H. These results are in plausible agreement with current experimental understanding of these systems, which sets the stage for using ReaxFF to study more complex reactions on nickel surfaces, as reported in Chapter 4 [71]. Finally, our results suggest that the ReaxFF strategy may prove useful in coupling between QM on small systems and the large complex systems representative of the operation of real catalysts, thus, allowing reactive dynamics simulations to become useful in designing new reaction systems.

Tables

Atom	r_o^σ	r_{vdW}	D_{ij}	α	γ_w
Ni	1.8201	1.9449	0.1880	12.1594	3.8387

Bond	D_e^σ ,kcal/mol	$p_{be,1}$	$p_{ovun,1}$	$p_{be,2}$	$p_{bo,1}$	$p_{bo,2}$
Ni-Ni	91.2220	-0.2538	0.2688	1.4651	-0.1435	4.3908

Table 1: Ni Parameters fitted to 78 point Ni training set. (r_o^σ and r_{vdW} in Å; D_{ij} and D_e^σ in kcal/mol)

Bond	D_e^σ	D_e^π	$p_{be,1}$	$p_{ovun,1}$	$p_{be,2}$	$p_{bo,3}$	$p_{bo,4}$	$p_{bo,1}$	$p_{bo,2}$
C-Ni	***83.5810***	***9.0383***	***0.2531***	***0.0529***	***1.4085***	***-0.1113***	***13.3900***	***-0.1436***	***4.5683***
H-Ni	***114.7566***	—	***-0.8939***	***0.1256***	***0.1054***	—	—	***-0.1196***	***5.0815***

Table 2: Bond Parameters fitted to 470 point C/H/Ni training set. (D_e^σ and D_e^π in kcal/mol, all other parameters are unitless)

Bond	D_{ij}	R_{vdW}	α	r_o^σ	r_o^π ,Å,
C-H	0.1188	1.4017	9.8545	1.1203	—
C-Ni	*0.0800*	*1.7085*	*10.0895*	*1.5504*	*1.4005*
H-Ni	*0.0366*	*1.7306*	*11.1019*	*1.2270*	—

Table 3: Off-diagonal Bond Parameters fit to 470 point C/H/Ni training set. (D_{ij} in kcal/mol, R_{vdW}, r_o^σ and r_o^π in Å, all other parameters are unitless).

Angle	Θ_o	$p_{val,1}$	$p_{val,2}$	$p_{val,7}$	$p_{val,4}$
C-Ni-C	***62.5000***	***16.6806***	***0.7981***	***0.9630***	***1.0711***
C-C-Ni	***87.6241***	***12.6504***	***1.8145***	***0.6154***	***1.5298***
Ni-C-Ni	***100.0000***	***40.4895***	***1.6455***	***0.0100***	***1.7667***
C-Ni-Ni	***5.0994***	***3.1824***	***0.7016***	***0.7465***	***2.2665***
H-H-Ni	0.0000	***26.3327***	***4.6867***	0.8177	***1.0404***
Ni-H-Ni	0.0000	***60.0000***	***1.8471***	***0.6331***	***1.8931***
H-Ni-Ni	***30.3748***	***1.0000***	***4.8528***	***0.1019***	***3.1660***
H-Ni-Ni	180.0000	***-27.2489***	***8.3752***	0.8112	***1.0004***
C-Ni-H	***97.5742***	***10.9373***	***2.5200***	***1.8558***	***1.0000***
C-H-Ni	0.0000	***0.2811***	***1.1741***	***0.9136***	***3.8138***
H-C-Ni	***84.0006***	***45.0000***	***0.6271***	***3.0000***	***1.0000***

Table 4: Selected Angle Parameters. Parameters in italics were fit to 470 point C/H/Ni training set. (Θ_o in degrees, all other parameters are unitless).

Torsion	V_2	V_3	$p_{tor,1}$
Ni-C-C-Ni	***44.3024***	***0.4000***	***-4.0000***
H-C-C-Ni	***21.7038***	***0.0100***	***-4.0000***
H-C-Ni-C	***5.2500***	***0.0100***	***-6.0000***

Table 5: Torsion parameters fitted to 470 point C/H/Ni training set. (V_2 in kcal/mol, all other parameters are unitless)

	Experiment	ReaxFF	DFT
ΔE for ½ $H_{2,gas}$ → H_{ad}	-11.5 kcal/mol [70]	-10.2 kcal/mol	-13.5 kcal/mol [26]
$\Delta E^{\ddagger}$ for ½ $H_{2,gas}$ → H_{ad}	17.7 kcal/mol [2]	18.4 kcal/mol	18.9 kcal/mol [26]
CH_3 low energy site & energy preference	μ_3 [24] —	μ_3 by 4.5 kcal/mol	μ_3 by 3.4 kcal/mol [26]
CH low energy site & energy preference	μ_3 [24] —	μ_3 by 10.7 kcal/mol	μ_3 by 9.4 kcal/mol [26]

Table 6: Comparison of Experimental, ReaxFF and QM results for binding H, CH_3, and CH to Ni(111)

	DFT	ReaxFF
Binding to Ni(100)		
CH_2 at bridge site	87.3	84.1
CH_2 at hollow site	95.7	74.2
CH_3 at top site	40.7	45.9
CC at adjacent top sites	124.0	84.9
CC at single hollow site	164.2	123.3
CC at adjacent hollow sites	153.4	130.5
CHCH at single hollow site	63.1	40.8
CHCH at adjacent hollow sites	46.7	47.2
CH_2CH_2 at hollow site	19.5	10.3
CH_2CH_2 at single top site	20.1	25.3
CH_2CH_2 at adjacent top sites	18.8	22.9
Binding to Ni(110)		
CH_2 at bridge site	86.4	86.0
CH_3 at top site	39.5	45.6
CC at single hollow site	162.8	153.6
CC at adjacent hollow sites	148.1	152.7
CHCH at single hollow site	47.3	67.8
CHCH at adjacent hollow sites	56.0	89.1
CH_2CH_2 at single top site	17.4	25.9
CH_2CH_2 at adjacent top sites	19.3	28.8

Table 7: ReaxFF validation for binding of small hydrocarbons to Ni(100) and Ni(110) surfaces. Binding energies are in kcal/mol.

Figures

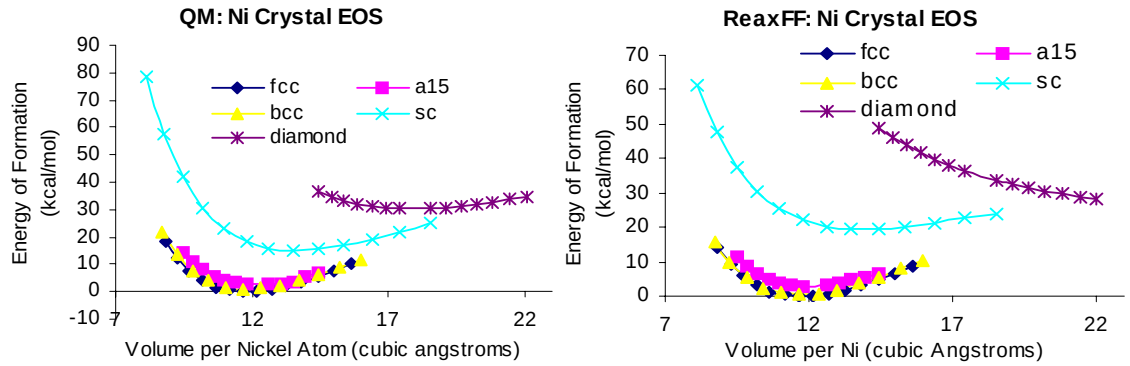

Figure 1: ReaxFF fit to equations of state (EOS) from QM calculations for a range pure nickel crystal structures.

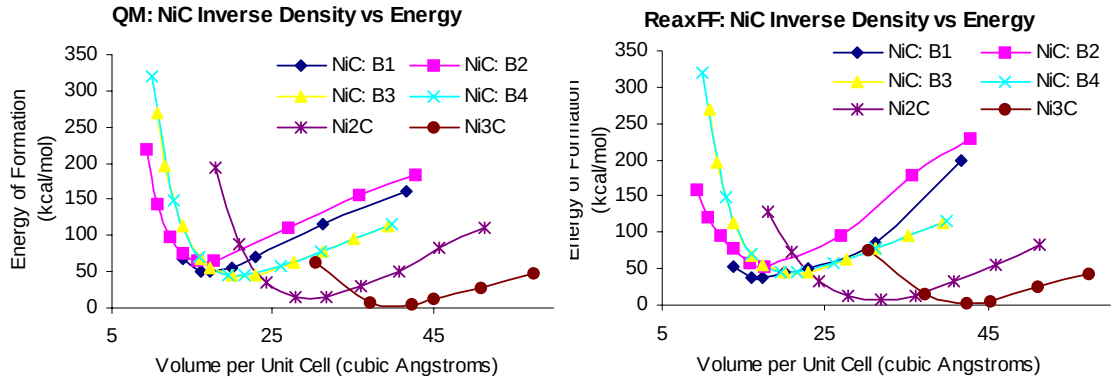

Figure 2: ReaxFF fit to equations of state (EOS) from QM calculations for various nickel carbide compositions and crystal structures.

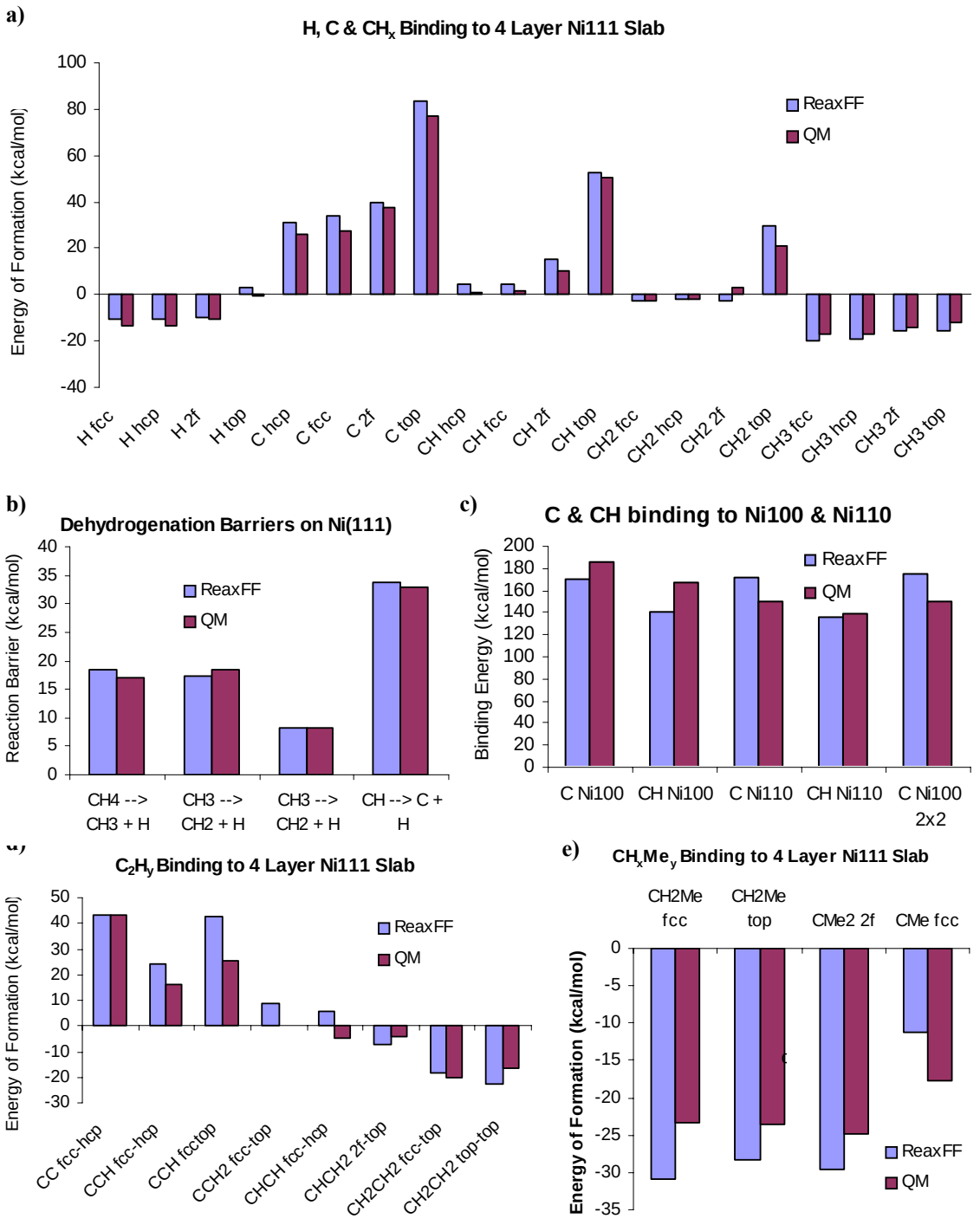

Figure 3: ReaxFF fits for **a)** H, C & CH_x binding at all Ni(111) surface sites, **b)** methane decomposition in Ni(111), **c)** C & CH binding to Ni(100) & Ni(110) surfaces, **d)** C_2H_y species binding to Ni(111), and **e)** methyl substituted CH_x species bonded to Ni(111).

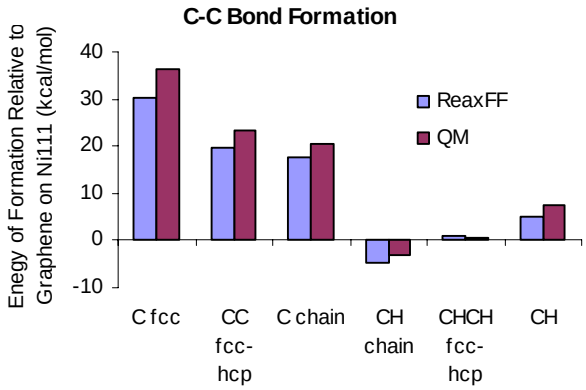

Figure 4: ReaxFF energy trends in formation of C-C bonds for extended carbon structures.

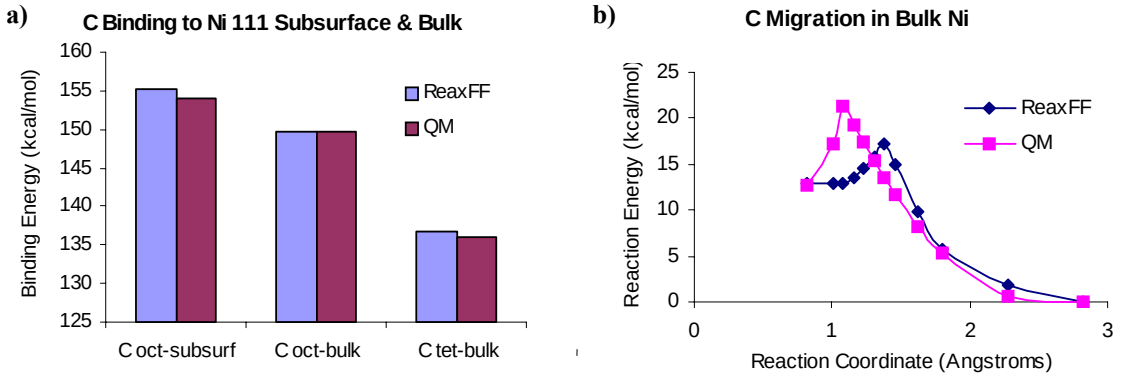

Figure 5: a) ReaxFF fit for C in Ni bulk and subsurface binding sites. **b)** ReaxFF fit to C migration between tetrahedral and octahedral interstitial sites in bulk Ni.

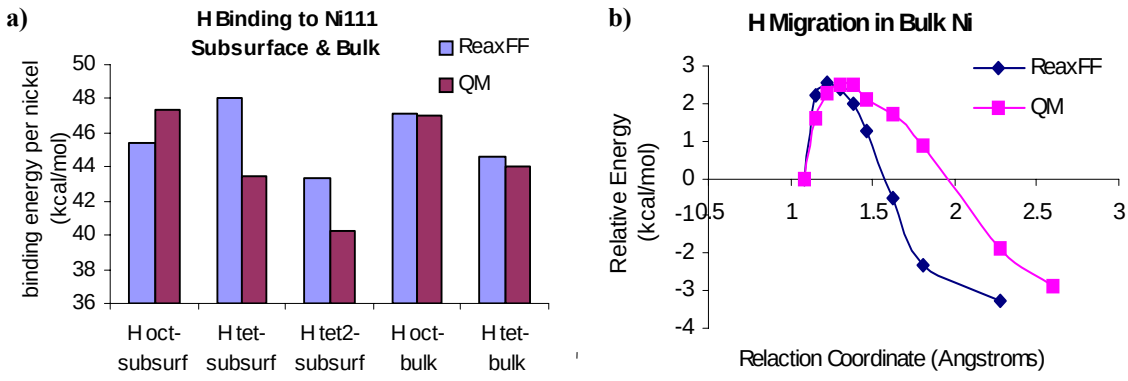

Figure 6: a) ReaxFF fit for H in Ni bulk and subsurface binding sites. **b)** ReaxFF fit to H migration between tetrahedral and octahedral interstitial sites in bulk Ni.

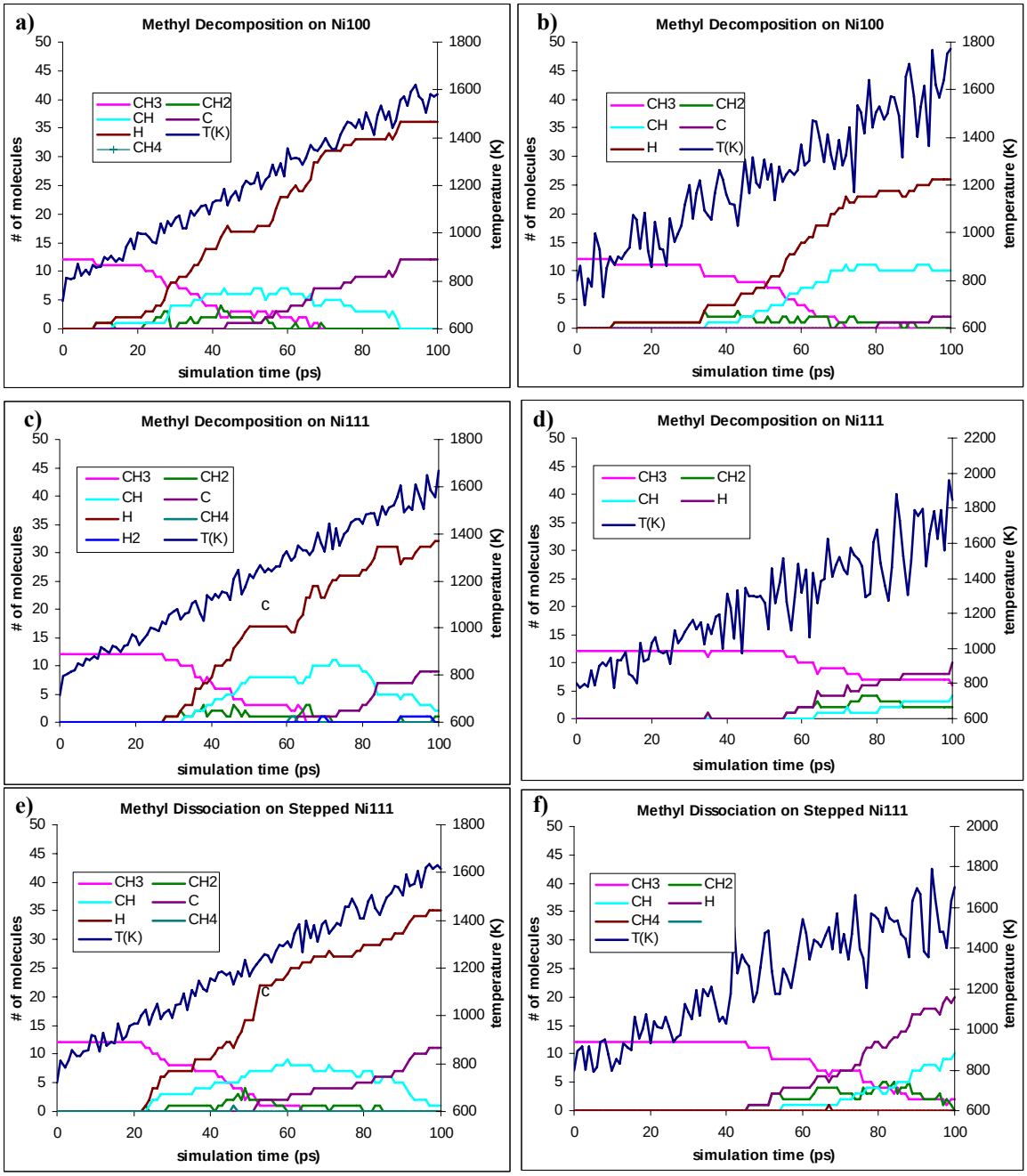

Figure 7: ReaxFF reactive MD simulations of methyl decomposition on nickel surface as the temperature is ramped from 800 K to 1800 K over 100 ps. In each case there were 12 CH_3 chemisorbed at the start. For the MD on the right the nickel slab was kept at 800 K. We consider three surfaces: top row: Ni(100), central row: Ni(111), bottom row: stepped Ni(111).

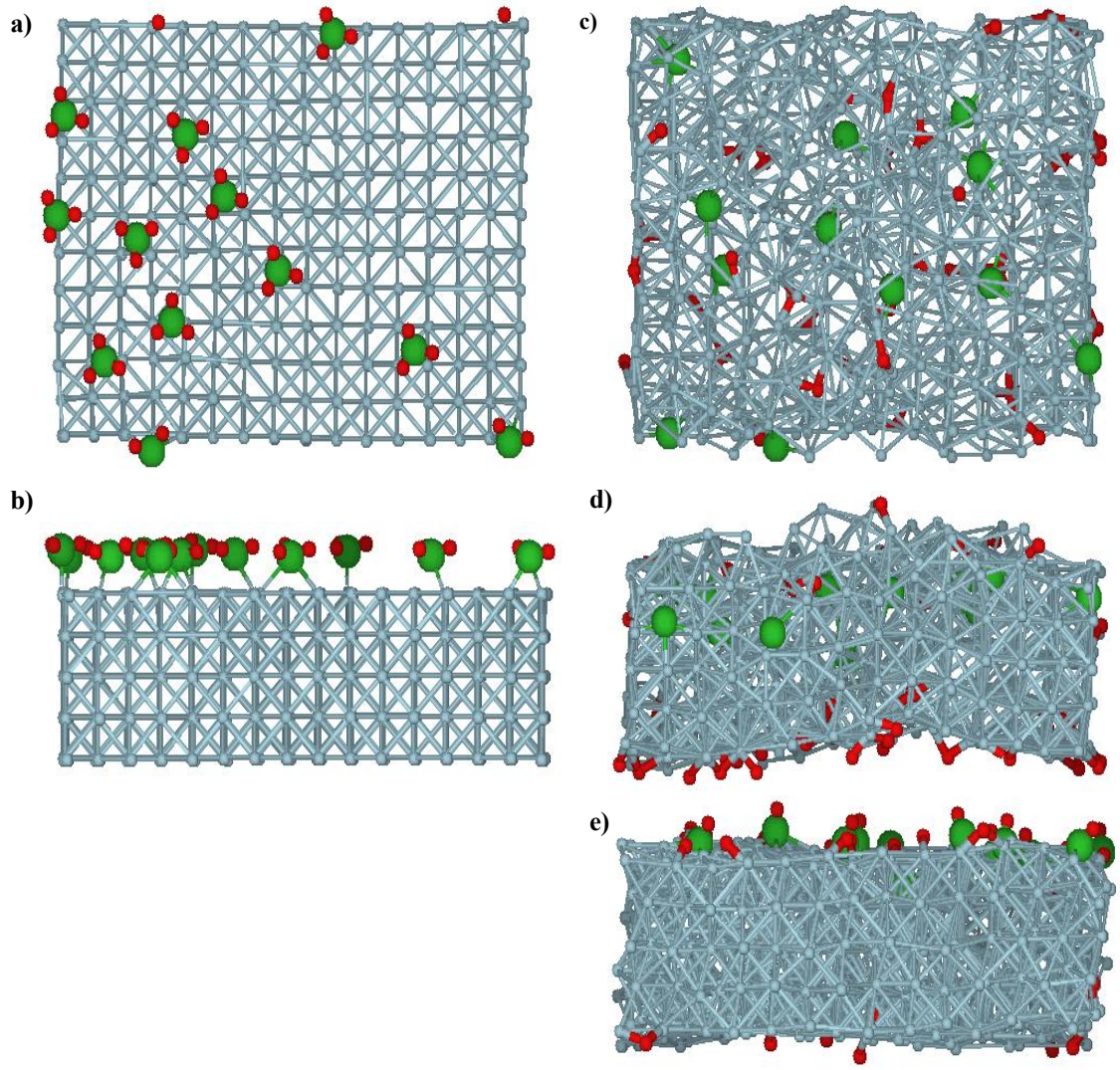

Figure 8: Snapshot of structures for ReaxFF NVT-MD simulations of methyl dissociation on Ni(100). Starting structure: **a)** top view, **b)** side view. Final structure (100 ps) with single thermostat: **c)** top view, **d)** side view. Final structure (100 ps) for simulation with nickel slab thermostat set at 800K: **e)** side view.

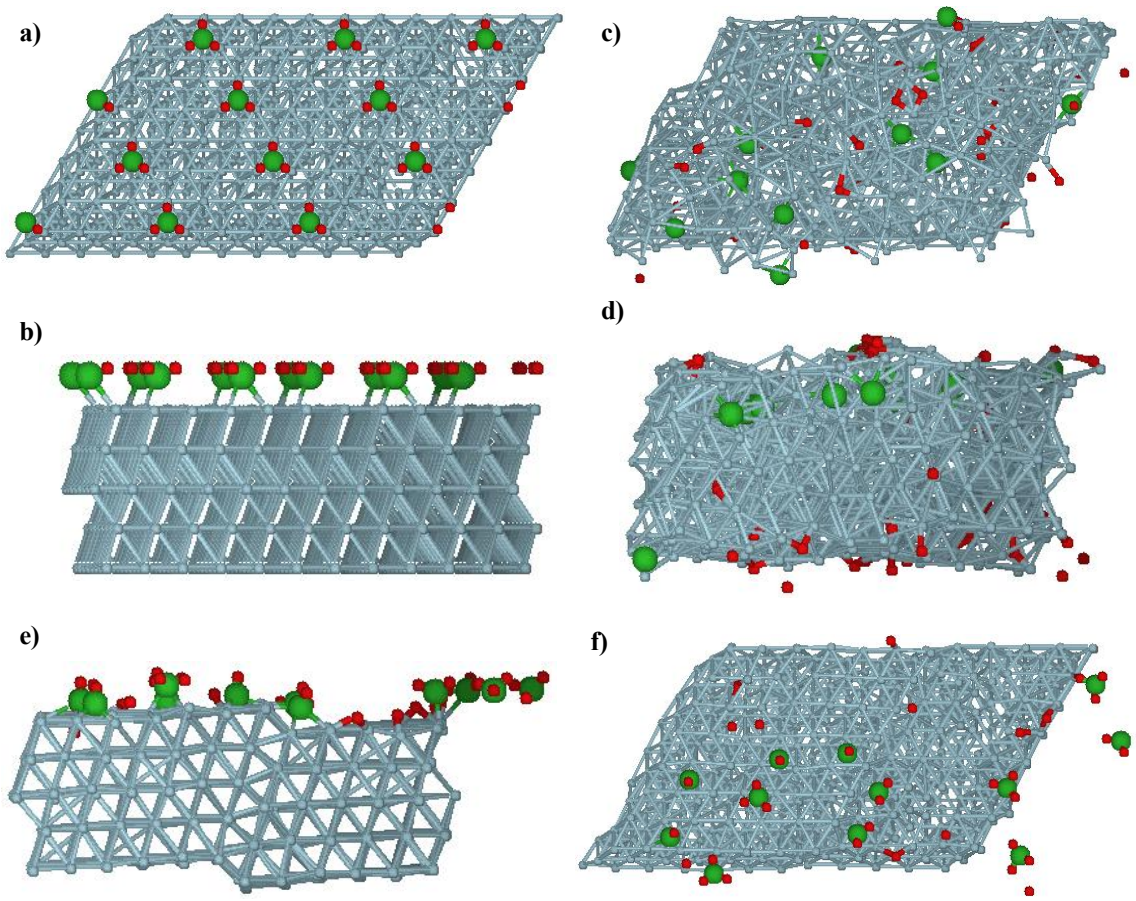

Figure 9: Snapshot of structures for ReaxFF NVT-MD simulations of methyl dissociation on Ni(111). Starting structure: **a)** top view, **b)** side view. Final structure (100 ps) with single thermostat: **c)** top view, **d)** side view. Final structure (100 ps) for simulation with nickel slab thermostat set at 800K: **e)** side view, **f)** top view.

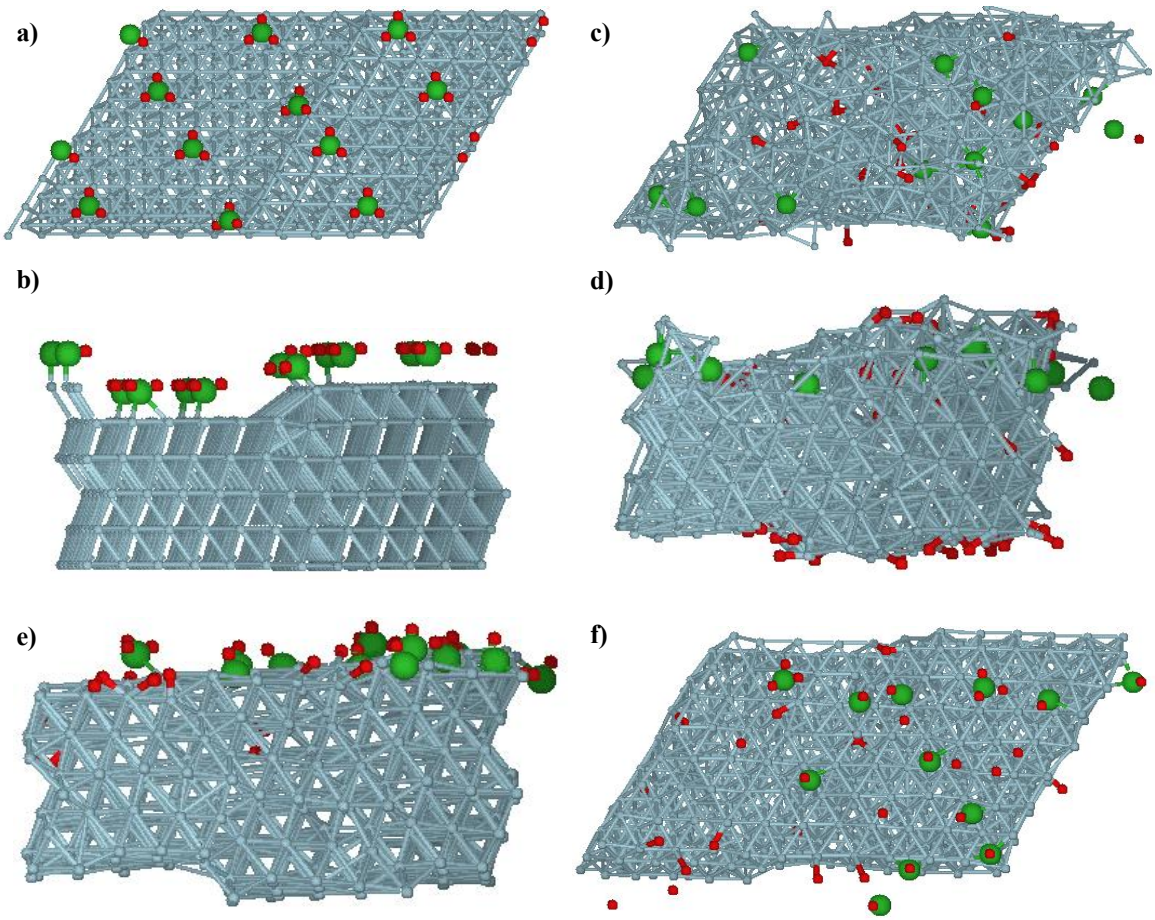

Figure 10: Snapshot of structures for ReaxFF NVT-MD simulations of methyl dissociation on stepped Ni(111). Starting structure: **a)** top view, **b)** side view. Final structure (100 ps) with single thermostat: **c)** top view, **d)** side view. Final structure (100 ps) for simulation with nickel slab thermostat set at 800K: **e)** side view, **f)** top view.

References

1. Rostrup-Nielsen, J. R. Catalytic Steam Reforming, in *Catalysis, Science and Technology*, J.R. Anderson and M. Boudar, Eds. 1984, Springer: Berlin; 1-117.
2. Egeberg, R. C.; Ullman, S.; Alstrup, I.; Mullins, C. B.; Chorkendorff, I. Dissociation of CH_4 on Ni(111) and Ru(0001). *Surf. Sci.* **2002**, *497* (1-3), 183-193.
3. Paillet, M.; Jourdain, V.; Phoncharal, P.; Sauvajol, J.-L.; Zahab, A. Versatile Synthesis of Individual Single-Walled Carbon Nanotubes from Nickel Nanoparticles for the Study of their Physical Properties. *J. Phys. Chem. B* **2004**, *108* (44), 17112-17118.
4. Beckerle, J.D.; Johnson, A.D.; Ceyer, S.T. Observation and Mechanism of Collision-Induced Desorption: CH_4 on Ni(111). *Phys. Rev. Lett.* **1989**, *62* (6), 685-688.
5. Beckerle, J.D.; Johnson, A.D.; Yang, Q. T.; Ceyer, S.T. Collision Induced Dissociative Chemisorption of CH_4 on Ni(111) by Inert Gas Atoms: The Mechanism for Chemistry with a Hammer. *J. Chem. Phys.* **1989**, *91* (9), 5756-5777.
6. Beckerle, J. D.; Yang, Q. T.; Johnson, A.D.; Ceyer, S.T Collision-Induced Dissociative Chemisorption of Adsorbates: Chemistry with a Hammer. *J. Chem. Phys.* **1987**, *86* (12), 7236-7237.
7. Ceyer, S.T. Dissociative Chemisorption: Dynamics and Mechanisms. *Annu. Rev. Phys. Chem.* **1988**, *39*, 479-510.
8. Lee, M. B.; Yang, Q. T.; Ceyer, S.T. Dynamics of the Activated Dissociative Chemisorption of CH_4 and Implication for the Pressure Gap in Catalysis: A Molecular Beam-High Resolution Electron Energy Loss Study. *J. Chem. Phys.* **1987**, *87* (1), 2724-2741.
9. Lee, M.B.; Yang, Q. Y.; Tang, S. L.; Ceyer, S. T. Activated Dissociative Chemisorption of CH_4 on Ni(111): Observation of a Methyl Radical and Implication for the Pressure Gap in Catalysis. *J. Chem. Phys.* **1986**, *85* (3), 1693-1694.
10. Burghgraef, H.; Jansen, A. P. J.; van Santen, R. A. Theoretical Investigation of CH_4 Decomposition on Ni: Electronic Structure Calculations and Dynamics. *Faraday Discuss.* **1993**, *96*, 337-347.
11. Henkelman, G.; Arnaldsson, A.; Jonsson, H. Theoretical Calculations of CH_4 and H_2 Associative Desorption from Ni(111): Could Subsurface Hydrogen Play an Important Role? *J. Chem. Phys.* **2006**, *124* (4), 044706.
12. Wonchoba, S.E.; Truhlar, D. G. Embedded Diatomics-in-Molecules Potential Energy Function for Methyl Radical and Methane on Nickel Surfaces. *J. Phys. Chem. B* **1998**, *102* (35), 6842-6860.
13. Yang, H.; Whitten, J.L. Ab initio Chemisorption Studies of CH_3 on Ni(111). *J. Am. Chem. Soc.* **1991**, *113* (17), 6442-6449.
14. Beebe, T. P.; Goodman, D. W.; Kay, B. D.; Yates, J. D. Kinetics of the Activated Dissociative Adsorption of Methane on the Low Index Planes of Nickel Single Crystal Surfaces. *J. Chem. Phys.* **1987**, *87* (4), 2305-2315.
15. Abbott, H. L.; Burkoski, A.; Kavulak, D. F.; Harrison, I. Dissociative Chemisorption of Methane on Ni(100): Threshold Energy from $CH_4(2\nu_3)$ Eigenstate-Resolved Sticking Measurements. J. Chem. Phys. **2003**, *119* (13), 6407-6410.

16. Bengaard, H. S.; Alstrup, I.; Chorkendorff, I.; Ullmann, S.; Rostrup-Nielsen, J. R.; Nørskov, J. K. Chemisorption of Methane on Ni(100) and Ni(111) Surfaces with Preadsorbed Potassium. *J. Catal.* **1999**, *187* (1), 238-244.
17. Lai, W. Z.; Xie, D.Q.; Zhang, D.H. First-Principles Study of Adsorption of Methyl, Coadsorption of Methyl and Hydrogen, and Methane Dissociation on Ni(100). *Surf. Sci.* **2005**, *594* (1-3), 83-92.
18. Abild-Pedersen, F.; Lytken, O.; Engbaek, J.; Nielsen, G.; Chorkendorff, I; Nørskov, J. K.; et al., *Methane activation on Ni(111): Effects of poisons and step defects.* Surface Science **2005**, *590* (2-3): p. 127-137.
19. Kratzer, P.; Hammer, B.; Nørskov, J. K. A Theoretical Study of CH_4 Dissociation on Pure and Gold-Alloyed Ni(111) Surfaces. *J. Chem. Phys.* **1996**, *105* (13), 5595-5604.
20. Bengaard, H. S.; Nørskov, J. K.; Sehested, J.; Clausen, B. S.; Nielsen, L. P.; Molenbroek, A. M.; Rostrup-Nielsen, J. R. Steam Reforming and Graphite Formation on Ni Catalysts. *J. Catal.* **2002**, *209* (2), 365-384.
21. Hofmann, S.; Sharma, R.; Ducati, C.; Du, G.; Mattevi, C.; Cepek, C.; Cantoro, M.; Pisana, S.; Parvez, A.; Cervantes-Sodi, F.; Ferrari, A. C.; Dunin-Borkowski, R.; Lizzit, S.; Petaccia, L.; Goldoni, A.; Robertson, J. In situ Observations of Catalyst Dynamics During Surface-Bound Carbon Nanotube Nucleation. *Nano Lett.* **2007**, *7* (3), 602-608.
22. Kaminsky, M. P. Winograd, N.; Geoffroy, G. L.; Vannice, M. A. Direct SIMS Observation of Methylidyne, Methylene, and Methyl Intermediates on a Ni(111) Methanation Catalyst. *J. Am. Chem. Soc.* **1986**, *108* (6), 1315-1316.
23. Yang, Q.Y.; Ceyer, S.T. The Stability and Chemistry of Methyl Radicals Adsorbed on Ni(111). *J. Vac. Sci. Technol. A* **1988**. *6* (3), 851-852.
24. Yang, Q.Y.; Maynard, K. J.; Johnson, A. D.; Ceyer, S. T. The Structure and Chemistry of CH_3 and CH Radicals Adsorbed on Ni(111). *J. Chem. Phys.* **1995**, *102* (19), 7734-7749.
25. Car, R.; Parrinello, M. Unified Approach for Molecular Dynamics and Density Functional Theory. *Phys. Rev. Lett.* **1985**, *55* (22), 2471-2474.
26. Mueller, J. E.; van Duin, A.C.T.; Goddard, W.A. Structures, Energetics, and Reaction Barriers for CH_x Bound to Ni(111) Surfaces. *J. Phys. Chem. C* **2009**, *113* (47), 20290-20306. (Chapter 1)
27. Amara, H.; Roussel, J.-M.; Bichara, C.; Gaspard, J.-P.; Ducastelle, F. Tight-Binding Potential for Atomistic Simulations of Carbon Interacting with Transition Metals: Application to the Ni-C System. *Phys. Rev. B* **2009**, *79* (1), 014109.
28. Brenner, D.W. Empirical Potential for Hydrocarbons for Use in Simulating the Chemical Vapor-Deposition of Diamond Films. *Phys. Rev. B* **1990**, *42* (15), 9458-9471.
29. Brenner, D.W.; Shenderova, O. A.; Harrison, J. A.; Stuart, S. J.; Ni, B. A Second-Generation Reactive Empirical Bond Order (REBO) Potential Energy Expression for Hydrocarbons. *J. Phys.: Condens. Matter* **2002**, *14* (4), 783-802.
30. Tersoff, J. Empirical Interatomic Potential for Carbon, with Applications to Amorphous-Carbon. *Phys. Rev. Lett.* **1988**, *61* (25), 2879-2882.

31. Ding, F.; Bolton, K.; Rosen, A. Nucleation and Growth of Single-Walled Carbon Nanotubes: A Molecular Dynamics Study. *J. Phys. Chem. B,* **2004**, *108* (45), 17369-17377.
32. Ding, F.; Rosen, A.; Bolton, K. Molecular Dynamics Study of the Catalyst Particle Size Dependence on Carbon Nanotube Growth. *J. Chem. Phys.* **2004**, *121* (6), 2775-2779.
33. Ding, F.; Rosen, A.; Bolton, K. The Role of the Catalytic Particle Temperature Gradient for SWNT Growth from Small Particles. *Chem. Phys. Lett.* **2004**, *393* (4-6), 309-313.
34. Maiti, A.; Brabec, C. J.; Bernholc, J. Kinetics of Metal-Catalyzed Growth of Single-Walled Carbon Nanotubes. *Phys. Rev. B*, **1997**, *55* (10), R6097-R6100.
35. Maiti, A.; Brabec, C. J.; Roland, C.; Bernholc, J. Theory of Carbon Nanotube Growth. *Phys. Rev. B* **1995**, *52* (20),14850-14858.
36. Shibuta, Y.; Maruyama, S. Molecular Dynamics Simulation of Formation Process of Single-Walled Carbon Nanotubes by CCVD Method. *Chem. Phys. Lett.* **2003**, *382* (3-4), 381-386.
37. Shibuta, Y.; Maruyama, S. Molecular Dynamics Simulation of Generation Process of SWNTs. *Physica B-Condensed Matter* **2002**, *323* (1-4), 187-189.
38. van Duin, A.C.T.; Dasgupta, S.; Lorant, F.; Goddard, W. A. ReaxFF: A Reactive Force Field for Hydrocarbons. *J. Phys. Chem. A*, **2001**, *105* (41), 9396-9409.
39. van Duin, A. C. T.; Strachan, A.; Stewman, S.; Zhang, Q.; Xu, X.; Goddard, W. A. $ReaxFF_{SiO}$ Reactive Force Field for Silicon and Silicon Oxide Systems. *J. Phys. Chem. A* **2003**, *107* (19), 3803-3811.
40. Zhang, Q.; Cagin, T.; van Duin, A. C. T.; Goddard, W. A.; Qi, Y.; Hector, L. G. Adhesion and Nonwetting-Wetting Transition in the Al/α-Al_2O_3 Interface. *Phys. Rev. B* **2004**, *69* (4), 045423.
41. Chenoweth, K.; van Duin, A. C. T.; Persson, P.; Cheng, M.-J.; Oxgaard, J.; Goddard, W. A. Development and Application of a ReaxFF Reactive Force Field for Oxidative Dehydrogenation on Vanadium Oxide Catalysts. *J. Phys. Chem. C*, **2008**, *112* (37), 14645-14654.
42. Cheung, S.; Deng, W.-Q.; van Duin, A. C. T.; Goddard, W. A. $ReaxFF_{MgH}$ Reactive Force Field for Magnesium Hydride Systems. *J. Phys. Chem. A* **2005**, *109* (5), 851-859.
43. Chenoweth, K.; Cheung, S.; van Duin, A. C. T.; Goddard, W. A.; Kober, E. M. Simulations on the Thermal Decomposition of a Poly(dimethylsiloxane) Polymer Using the ReaxFFReactive Force Field. *J. Am. Chem. Soc.* **2005**, *127* (19), 7192-7202.
44. Chenoweth, K.; van Duin, A. C. T.; Goddard, W. A. ReaxFF Reactive Force Field for Molecular Dynamics Simulations of Hydrocarbon Oxidation. *J. Phys. Chem. A* **2008**, *112* (5), 1040-1053.
45. van Duin, A.C.T.; Faina, Y. Z.; Dubnikova, F. Kosloff, R.; Goddard, W. A. Atomistic-Scale Simulations of the Initial Chemical Events in the Thermal Initiation of Triacetonetriperoxide. *J. Am. Chem. Soc.* **2005**, *127* (31), 11053-11062.
46. Nielson, K.D.; van Duin, A. C. T.; Oxgaard, J.; Deng, W.Q.; Goddard, W. A. Development of the ReaxFF Reactive Force Field for Describing Transition Metal

Catalyzed Reactions, with Application to the Initial Stages of the Catalytic Formation of Carbon Nanotubes. *J. Phys. Chem. A* **2005**, *109* (3), 493-499.

47. Schultz, P.A. *SeqQuest*, Sandia National Labs, Albuquerque, NM http://dft.sandia.gov/Quest/.
48. *Jaguar*. 2000, Schrodinger, Inc.: Portland, Oregon.
49. Goddard, W.A. New Foundation for Use of Pseudopotentials in Metals. *Phys. Rev.* **1968**, *174* (3), 659-662.
50. Hay, P. J.; Wadt, W.R. Ab initio Effective Core Potentials for Molecular Calculations: Potentials for K to Au Including the Outermost Core Orbitals. *J. Chem. Phys.* **1985**, *82* (1), 299-310.
51. Melius, C. F.; Olafson, B.D.; Goddard, W.A. Fe and Ni Ab initio Effective Potentials for Use in Molecular Calculations. *Chem. Phys. Lett.* **1974**, *28* (4), 457-462.
52. Francl, M. M.; Pietro, W. J.; Hehre, W. J.; Binkley, J. S.; Gordon, M. S.; Defrees, D. J.; Pople, J. A. Self-Consistent Molecular Orbital Methods. XXIII . A Polarization-Type Basis Set for Second-Row Elements. *J. Chem. Phys.* **1982**, *77* (7), 3654-3665.
53. Hariharan, P. C.; Pople, J. A. Effect of d-Functions on Molecular-Orbital Energies for Hydrocarbons. *Chem. Phys. Lett.* **1972**, *16* (2), 217-219.
54. Mortier, W. J.; Ghosh, S. K.; Shankar, S. Electronegativity Equalization Method for the Calculation of Atomic Charges in Molecules. *J. Am. Chem. Soc.* **1986**, *108* (15), 4315-4320.
55. van Duin, A. C. T.; Baas, J. M. A.; van de Graaf, B. Delft Molecular Mechanics: a New Approach to Hydrocarbon Force Fields. *J. Chem. Soc. Faraday Trans.* **1994**, *90* (19), 2881-2895.
56. Kittel, C. *Introduction to Solid State Physics*. 8th ed. 2005, New York: Wiley.
57. Massabki, T. B. ed. *Binary Alloy Phase Diagrams*. 1986, Metals Park, OH: ASM International.
58. Grigoriev, I. S. ed. *Handbook of Physical Quantities*. 1997, New York: CRC Press.
59. Birch, F. Finite Elastic Strain of Cubic Crystals. *Phys. Rev.* **1947,** *71* (11), 809-824.
60. Tyson, W. R.; Miller, W.A. Surface Free Energies of Solid Metals: Estimation from Liquid Surface-Tension Measurements. *Surf. Sci.* **1977**, *62* (1), 267-276.
61. de Boer, F. R.; Boom, R.; Matteris, W. C. M.; Miedema, A. R.; Niessen, A. K. *Cohesion in Metals*. 1988, Amersterdam: North-Holland.
62. Hong, S.; Shin, Y.-H.; Ihm, J. Crystal Shape of a Nickel Particle Related to Carbon Nanotube Growth *Jpn. J. Appl. Phys*. **2002**, *41***,** 6142.
63. Kalibaeva, G.; Vuilleumier, R.; Meloni, S.; Alavi, A.; Ciccotti, G.; Rosei, R. Ab Initio Simulation of Carbon Clustering on an Ni(111) Surface: A Model of the Poisoning of Nickel-Based Catalysts. *J. Phys. Chem. B* **2006**, *110* (8), 3638-3646.
64. Maiya, P.S.; Blakely, J. M. Surface Self-Diffusion and Surface Energy of Nickel. *J. Appl. Phys.* **1967**, *38* (2), 698-704.

65. Rodriguez-Manzo, J. A. Terrones, M.; Terrones, H.; Kroto, H. W.; Sun, L.; Banhart, F. In situ Nucleation of Carbon Nanotubes by the Injection of Carbon Atoms into Metal Particles. *Nature Nanotechnology* **2007**, *2* (5), 307-311.

66. Saito, Y. Nanoparticles and Filled Nanocapsules. *Carbon* **1995**, *33* (7), 979-988.

67. Wagner, R. S.; Ellis,W. C. Vapor-Liquid-Solid Mechanism of Single Crystal Growth. *Appl. Phys. Lett.* **1964**, *4* (5), 89-90.

68. Daley, S. P.; Utz, A. L.; Trautman, T. R.; Ceyer, S. T. Ethylene Hydrogenation on Ni(111) by Bulk Hydrogen. *J. Am. Chem. Soc.* **1994**, *116* (13), 6001-6002.

69. Johnson, A. D.; Daley, S. P.; Utz, A. L.; Ceyer, S. T. The Chemistry of Bulk Hydrogen: Reaction of Hydrogen Embedded in Nickel with Adsorbed CH_3. *Science* **1992**, *257* (5067), 223-225.

70. Christmann, K.; Behm, R. J.; Ertl, G.; van Hove, M. A.; Weinberg, W. H. Chemisorption Geometry of Hydrogen on Ni(111): Order and Disorder. *J. Chem. Phys.* **1979**, *70* (9), 4168-4184.

71. Mueller, J. E.; van Duin, A. C. T.; Goddard, W. A. "Application of the ReaxFF Reactive Force Field to Reactive Dynamics of Hydrocarbon Chemisorption and Decomposition" *J. Phys. Chem. C*, **2010**, *114* (12), 5675-5685. (Chapter 4)

Chapter 4

APPLICATION OF THE REAXFF REACTIVE FORCE FIELD TO REACTIVE DYNAMICS OF HYDROCARBON CHEMISORPTION AND DECOMPOSITION ON NICKEL NANOPARTICLES[1]

We report here reactive dynamics (RD) simulations of the adsorption and decomposition of a gas of 20 to 120 methane, acetylene, ethylene, benzene, cyclohexane or propylene molecules interacting with a 21Å diameter nickel nanoparticle (468 atoms). These RD simulations use the ReaxFF reactive force field developed in Chapter 1 [14] to describe decomposition, reactivity, and desorption of hydrocarbons as they interact with nickel surfaces.

We carried out 100 ps of RD as the temperature was ramped at a constant rate from 500K to 2500K (temperature programmed reactions). We find that all four unsaturated hydrocarbon species chemisorb to the catalyst particle with essentially no activation energy (attaching to the surface through π electrons) and then proceed to decompose by breaking C-H bonds to form partially dehydrogenated species prior to decomposition to lower order hydrocarbons. The eventual breaking of C-C bonds usually involves a surface Ni atom inserting into the C-C bond to produce an atomic C that simultaneously with C-C cleavage moves into the subsurface layer of the particle. The greater stability of this subsurface atomic C (forming up to four Ni-C bonds) over adatom C on the particle surface (forming at most three Ni-C bonds) is critical for favorable cleaving of C-C bonds.

---

[1] Reproduced with permission from Jonathan E. Mueller, Adri C. T. van Duin and William A. Goddard, III, "Application of the ReaxFF Reactive Force Field to Reactive Dynamics of Hydrocarbon Chemisorption and Decomposition" *J. Phys. Chem. C*, **2010**, *114* (12), 5675-5685. Copyright 2010 American Chemical Society.

For the two saturated hydrocarbon species (methane and cyclohexane), we observe an activation energy associated with dissociative chemisorption.

These results are consistent with available experimental reactivity data and quantum mechanics (QM) energy surfaces, validating the accuracy of ReaxFF for studying hydrocarbon decomposition on nickel clusters.

1. Introduction

Nickel is the primary catalyst in the steam reforming process [1] for converting methane and water into synthesis gas (carbon monoxide and hydrogen) which is then used in such important industrial processes as the Haber-Bosch synthesis of ammonia and the Fischer-Tropsch formation of higher hydrocarbons [2]. In addition, nickel catalysts are used in high temperature solid oxide fuel cells using hydrocarbon fuels, and more recently nickel has been used to catalyze the formation and growth of carbon nanotubes (CNTs) from hydrocarbons [3]. These applications have stimulated numerous studies of hydrocarbon rearrangements on nickel, resulting in a good understanding of the fundamental processes of simple hydrocarbon molecules reacting on low index surfaces of nickel [4-7]. Nevertheless, there remain many questions about the chemistry on the defect rich surfaces of nanoparticles, used, for example, as catalysts for growing CNTs.

During CNT growth, the nickel particle catalyst is responsible for catalyzing at least three processes: decomposition of the hydrocarbon feedstock, transport of the activated hydrocarbon species to the edge of the growing nanotube, and addition of the activated carbon species to the growing end of the nanotube. Each of these steps could play a rate limiting role depending on growth conditions; however, experimental evidence suggests

that feedstock decomposition is the limiting step for low temperature (350 Cº) CNT growth [8].

While the adsorption and decomposition of hydrocarbons on low index surfaces has been examined in many experiments [2, 4, 7, 9-12], there has been little in the way of application of these results to larger catalytic problems, such as the role of feedstock decomposition in CNT growth. Thus surface science studies of hydrocarbon chemisorption and decomposition on low index nickel surfaces try to limit the number of defects; whereas, a nickel catalyst particle used in CNT growth may have many surface defects not present on the perfect (111) surface. These defects likely play important roles in catalyzing reactions on the particle surface, but experimental studies of CNT growth typically cannot isolate just one part of the process (feedstock decomposition) from the subsequent rearrangements, making it difficult to obtain a detailed chemical mechanism including the key steps involved in feedstock decomposition. We show here that reactive dynamics (RD) simulations provide mechanistic information about these heterogeneous catalytic processes, which we expect to be useful for understanding more complex reactions, such as CNT growth.

Here we present RD simulations of six representative hydrocarbon species (methane, acetylene, ethylene, benzene, cyclohexane and propylene) as they chemisorb and decompose on a 468 atom nickel nanoparticle (21 Å diameter). These six examples were chosen to cover a variety of hydrocarbon types. Acetylene and ethylene allow us to compare reactivity for species with one or two π bonds. Propylene allows us to consider the effect of the weak allylic C-H bond. Benzene brings in effects of aromaticity and ring structures. For the saturated hydrocarbons methane and cyclohexane, we can examine the

initial CH bond cleavage for systems that do not chemisorb strongly. With the exception of propylene, the chemisorption and decomposition of each of these hydrocarbon species on nickel has been studied experimentally [2, 4, 7, 9-12]. The aim of this study is to gain insights into the preferred decomposition pathways for each hydrocarbon species on nickel, in order to help guide the choice of optimum hydrocarbon feedstock species for controlling CNT growth.

2. Theoretical Methods

Modern quantum mechanics (QM) methods have been most valuable in providing reaction surfaces for reactions of simple molecules on low index surfaces [13]. However, studies of the reaction dynamics at higher temperatures and pressures for realistic sizes of metal clusters require system sizes and time scales well beyond the current practical limits of QM calculations. For example, full-scale atomistic modeling of CNT growth on a nanoparticle catalyst requires the treatment of hundreds or even thousands or atoms for timescales on the order of at least nanoseconds, which are unattainable with typical QM calculations today. Nevertheless, potential energy surfaces for reactions on low index surfaces studied in typical QM studies and the comparison of these results to surface science experiments provide useful data for validating methods which are more suitable for larger scale studies of reaction pathways on nanoparticle surfaces. The ReaxFF reactive force field, which was trained to accurately describe hydrocarbon chemistry on Ni(111) is one such method and provides a tool for extending the first principles accuracy of QM to the study of hydrocarbon decomposition on nickel catalyst particles.

2.1. ReaxFF Reactive Dynamics

The ReaxFF reactive force field potential described in Chapter 3 [14, 15] was used for all simulations (energy minimization and RD) described here. Our temperature programmed RD simulations used the velocity Verlet integrator with a time step of 0.25 fs. The temperature was set to an initial temperature of 500 K and increased every time step at a constant rate of 20 K/ps, leading to a final system temperature of 2500 K after 100 ps. We used a Berendsen thermostat with a damping constant of 100 fs for temperature control. The temperature control achieved, as well as the stability of the simulations attests to the reasonableness of these parameters for treating these particular systems.

In order to observe chemical reactions within a computationally practical simulation time, we considered a temperature range extending beyond normal experimental conditions. We expect that these elevated temperatures may affect the observed reaction pathways in two ways. First, the form of the Arrhenius expression for the rates results in a higher proportion of high energy processes compared with low energy processes at elevated temperatures. Thus, while the same reaction pathways are preferred at both high and low temperatures, the preference for low energy pathways is enhanced at low temperatures.

Second, changes in the structure of the catalyst surface at high temperature may have additional effects on reaction barriers and rates. These effects are less predictable. Nevertheless, ReaxFF RD calculations comparing CH_3 dissociation on hot (single increasing thermostat for nickel slab and hydrocarbons) and cold (separate increasing thermostat for hydrocarbons and constant cold thermostat for nickel slab) nickel slabs

suggest that while the additional defects present on hot surfaces increase the reaction rates, there is no major change in which reaction pathways are preferred [14].

We constructed the 468 atom, 21 Å nickel nanoparticle by removing the corners of a 500 atom, fcc nickel cube and optimizing the structure (energy minimization). This particle diameter is within the range of catalyst particle dimensions responsible for synthesizing SWCNTs [16]. The hydrocarbon molecules were added at random positions in the 80 Å x 80 Å x 80 Å periodic cubic simulation cell, with at least 3.0 Å of separation from other atoms in the cell. Then the full system was minimized (to remove any residual bad contacts) to within 0.5 kcal/mol Å RMS force. The number of hydrocarbon molecules in the gas phase was chosen so that each simulation had 120 carbon atoms. Thus, the simulation of methane decomposition began with 120 methane molecules, while the simulation of benzene began with 20 benzene molecules.

Each RD simulation was initiated using a Boltzmann distribution of velocities at 500 K. During the RD, the molecules chemisorb on the surface, decompose, and sometimes desorb (e.g. H_2). To obtain information about these reactive processes, we analyzed the RD trajectory to identify the molecular species at each step (using a bond-order cut-off of 0.30 to determine connectivity). The population of each chemical species (both gas phase and surface populations) was monitored as a function of time, providing a measure of the evolution of each catalytic system. The initial and final structures for the case of propylene are illustrated in Figure 1.

The elementary chemical reactions were extracted from the RD to obtain a reaction network indicating the transformations of various intermediates over the course of the

simulation. The relative number of times that various reaction pathways are followed provides clues about the relative kinetics of various mechanistic steps.

To illustrate the importance of the catalytic activity of the nickel particle, consider the RD on 40 propylene molecules (one of the more reactive species studied here) in our simulation cell, without the nickel particle. The only reaction to take place was that one molecule of propylene (C_3H_6) lost an H_2 molecule to form a single propyne (C_3H_4) molecule. This reaction took place in the final quarter picosecond of the simulation as the temperature approached 2500 K. This provides strong confirmation of the important catalytic role played by the nickel particle.

2.2. Kinetic Model for Chemisorption.

To obtain a quantitative picture of the chemisorption rate we use kinetic theory to derive an expression for the number of molecules in the gas phase and then obtain effective chemisorption barriers by fitting the resulting kinetic expression to our data. We derive the appropriate rate expression for chemisorption as follows:

The change in the number of molecules (N) in the gas phase can be written in terms of the rates of adsorption (R_a) and desorption (R_d) from the particle surface:

$$\frac{dN}{dt} = -NR_a + (N_s)R_d \qquad \textbf{(1)}$$

where N_s is the number of molecules chemisorbed to the surface. If the rate of desorption is negligible we can ignore the second term so that:

$$\frac{dN}{dt} = -NR_a \qquad \textbf{(2)}$$

We expect the rate of chemisorption be proportional to the product of the collision rate with the surface (which is proportional to the average molecular velocity, $\bar{v}$, and hence to the

square root of the temperature, $\sqrt{\mathrm{T}}$), the probability of having enough energy to overcome the reaction barrier (which is proportional to the Boltzmann factor, $e^{-\frac{E_a}{k_B \mathrm{T}}}$), and the fraction of the surface sites which are unoccupied, and hence available for reaction (which is proportional to $M - N_s$, where M is the total number of surface sites occupied at monolayer coverage and N_s is the number of molecules already adsorbed to the surface). Writing $\mathrm{M} = M - N_0$, where N_0 is the initial number of gas phase molecules, the rate equation becomes:

$$\frac{dN}{dt} = -N(\mathrm{M} + N)\Lambda\sqrt{\mathrm{T}}e^{\frac{-E_a}{k_B \mathrm{T}}} \tag{3}$$

where the constant Λ includes all other factors. Assuming a constant rate of temperature increase and changing variables to $\tau = \frac{E_a}{k_B \mathrm{T}}$, separates the variables, leading to:

$$\frac{dN}{N(N + \mathrm{M})} = -A\tau^{-\frac{5}{2}}e^{-\tau}d\tau \tag{4}$$

where the pre-exponential factor is $A = \Lambda\left(\frac{dt}{d\mathrm{T}}\right)\left(\frac{1}{k_B^3 E_a^5}\right)^{\frac{1}{2}}$. Integrating both sides leads to:

$$\ln\left(\frac{N(\mathrm{M} + N_0)}{N_0(\mathrm{M} + N)}\right) = -\frac{3A\mathrm{M}}{4}\left\{\sqrt{\pi}erf\left(\sqrt{\frac{E_a}{k_B \mathrm{T}_0}}, \sqrt{\frac{E_a}{k_B \mathrm{T}}}\right) + e^{-\frac{E_a}{k_B \mathrm{T}}}\sqrt{\frac{k_B \mathrm{T}}{E_a}}\left(1 - \frac{2k_B \mathrm{T}_0}{E_a}\right) - e^{-\frac{E_a}{k_B \mathrm{T}_0}}\sqrt{\frac{k_B \mathrm{T}_0}{E_a}}\left(1 - \frac{2k_B \mathrm{T}_0}{E_a}\right)\right\} \tag{5}$$

where N is the instantaneous number of gas phase molecules and T is the instantaneous temperature T, (T_0 = 500 K is the initial T).

We estimate M as follows: The catalyst particle is approximately spherical with a radius of 11Å, leading to a surface area of 1521Å^2. An alternate estimate of the surface area

is the solvent accessible surface, which is 1750 $Å^2$ (using a probe radius of 4.0 Å). We assume that the particle surface is similar to the Ni(111) surface, which leads to 5.41$Å^2$ per three-fold site, indicating that the cluster has about 280 three-fold surface sites. As described sections 3.4.1 – 3.4.3, this information is used to estimate M for each species investigated. N as a function of time from RD simulations is used to calculate the left hand side of **(5)**. Then the A and E_a parameters are fit to the right hand side to the data (least squares fit using the solver in Microsoft Excel [17]).

3. Results and Discussion

3.1. Reactive Dynamics of Hydrocarbon Chemisorption and Decomposition

3.1.1. Methane (Figure 2)

Methane is the most studied hydrocarbon species for nickel catalyzed decomposition and reforming reactions. Chemisorption requires breaking a C-H bond, leading to CH_3 and H radical fragments that each chemisorb onto the surface. We first observe these chemisorption products at T_A = 1300 K (41 ps). Beyond this point, the rate of chemisorption increases super-linearly with increasing temperature, and the chemisorbed CH_3 begins to decompose.

One methane has chemisorbed onto the nickel particle as $CH_{3,ad}$ + H_{ad}, it can undergo further dehydrogenation with subsequent breaking of additional C-H bonds or it can produce higher order hydrocarbons by forming C-C bonds. We found two cases in which C-C bonds were formed in our RD. Near the end of the simulation (>93 ps and 2350 K) the reaction of two C atoms to form surface C_2 occurs twice; however, only one of the C_2 molecules produced survives to the end. Also, we find that two of the methyl groups react to form C_2H_6 (which immediately loses one H, to form C_2H_5) during the final 0.25 ps in the

simulation when the temperature is nearly 2500 K. Thus, under our simulation conditions, C-C bonds do not form readily from the products of methane gas chemisorption.

On the other hand, a significant number of chemisorbed H atoms are produced (100 at the end), some of which desorbed to form H_2 gas (19 at the end). Because chemisorption requires breaking a C-H bond, the initial appearance of atomic chemisorbed H is simultaneous with the chemisorption of the CH_3 fragment at $T_H = T_A = 1300K$. Once chemisorbed CH_3 is present on the surface (first appears at 41 ps), it easily loses an H atom to form chemisorbed CH_2 (first appears at 46 ps) and a second to form chemisorbed CH (first appears at 48 ps). The final H is more difficult to remove from chemisorbed CH, so that chemisorbed atomic C is not observed until the temperature reaches $T_C = 1850$ K (68 ps). A visual examination of the trajectory suggests that the energy for breaking the final C-H bond is stabilized by migration of the C atom produced into the nickel particle subsurface. Thus, atomic C is not formed until there is sufficient thermal energy for it to migrate into the nickel particle subsurface, where it is energetically more stable.

The final population has 44 of the 120 original methane molecules chemisorbed onto the particle. Of these 28 were completely dehydrogenated, two of which combine to form C_2. The remainder of the chemisorbed methane is accounted for in adsorbed intermediates (three molecules each of CH, CH_2, and CH_3) and gas phase radicals (five gas phase CH_3 radicals and one gas phase C_2H_5). The presence of all three CH_x intermediates highlights their similar stabilities on the surface, while the presence of the gas phase methyl radicals is an artifact of the high temperatures used in our RD simulations since they appear between 2000 K and 2500 K.

Several experimental [7, 10, 18] and theoretical [5-6, 19-20] studies have focused on the products and intermediates formed as methyl decomposes on nickel. Methylidyne (CH) is the energetically favored species on Ni(111), but CH_3 is also observed experimentally. Methylene (CH_2) readily decomposes to CH, and is not observed experimentally as an intermediate in the dehydrogenation process. Consistent with these observations, the population of CH is typically higher than the population of CH_2 in our RD, although our system is far from a perfect (111) surface.

Experimental studies also show that at moderate temperatures (between 250 K and 400 K) and high surface coverage, CH dimerizes to form acetylene or even four-, six- and eight-member rings. At higher temperatures (above 400 K) CH is reformed and eventually breaks up (by 700 K), with atomic C dissolving into the bulk. For our RD the temperature range is too high and the coverage too low for C-C bond formation to be favorable, so we do not see such combination processes.

3.1.2. Acetylene (Figure 3)

The two π bonds of acetylene (C_2H_2) can each be broken to form σ bonds as it chemisorbs to the nickel surface. Thus, acetylene is able to chemisorb onto the particle without fragmenting. Indeed, in our RD simulation it first adsorbs onto the nickel particle after 8 ps, when the temperature reaches T_A = 650 K.

Once adsorbed, acetylene does not begin to decompose for another 20 ps (28 ps, T_H = 1050 K), at which point the adsorbed C_2H_2 begins dehydrogenating to form C_2H. The population of C_2H builds for about 20 ps until it breaks down (46 ps, T_C = 1450 K) to form either CH and C, or C_2 and H. Above this temperature, there are typically only about two C_2H_2 molecules on the surface at any given time despite continued adsorption of additional

molecules from the gas phase. This indicates that above 1450 K the rate of decomposition is at least as fast as the rate of adsorption.

Similarly, the population of CH remains low indicating that the rate of CH formation from C_2H is slower than the rate for decomposing CH into C and H. In contrast, the population of C_2 is sustained between 50 and 75 ps (1500 K and 2000 K), before the rate for C_2 to decompose into atomic C exceeds the rate of C_2 formation. Both CH and C_2 decomposition produce subsurface atomic C, which shows a marked increase at 70 ps (1900 K). This corresponds to a breakdown in the structure of the nickel particle providing the newly formed C atoms easy opportunity to migrate into the subsurface of the particle.

Snapshots (Figure 4) from the simulation suggest that C_2 also migrates into the subsurface of the particle as it loses its final H, and that it is here where the C-C bond is finally broken. Thus, both C_2 and atomic C are stabilized by moving into the subsurface, making the stability of subsurface C an important factor in facilitating cleavage of C-C bonds. By the end of our simulation (at a temperature of 2500 K), the atomic C formed has migrated into the bulk of the particle as shown in Figure 5.

The RD leads to the reaction network in Figure 3 with three pathways from C_2H_2 to C, corresponding to the three C_2H_x species that can be broken up into single C fragments. The vast majority (27) dehydrogenate to form C_2H, while only 3 adsorbed C_2H_2 molecules break the C-C bond to form CH fragments. Similarly, while 5 of 27 C_2H molecules break down into C and CH, the majority (21) lose H to form C_2, which then breaks down into subsurface atomic C. Thus, there is a marked preference for dehydrogenation prior to breaking C-C bonds indicating that C-H bonds are easier to break on the nickel particle than C-C bonds.

Ethylene decomposition on nickel has been studied extensively experimentally [4, 21-28]. On the (111) surface each C of the ethylene forms a σ bond with adjacent three-fold sites. Thus one C-C π bond becomes two C-Ni σ bonds. As the temperature is increased above 300 K, this di-σ bonded C_2H_2 decomposes into two chemisorbed CH's before breaking down into atomic C and H at higher temperatures (450 K) [27]. Thus, on the flat surface the C-C bonds break before C-H bonds. However, the presence of steps on the Ni(111) surface lowers the activation barrier for C-H bond cleavage, accelerating the decomposition of C_2H_2 [4] to form chemisorbed C_2. Because our nanoparticle has many step-like defects, it is plausible that it behaves like the stepped surface, rather than the flat surface. Indeed, we observe C-H bonds breaking prior to C-C bonds.

Previous QM studies [29-31] agree with experiment [21] in showing that acetylene binds most strongly to a μ-bridge site on Ni(111), with the C atoms at adjacent three-fold positions. The close proximity of acetylene to the surface represented by this structure is in good agreement with the structures we observe in our RD.

3.1.3. Ethylene (Figure 6)

Ethylene (C_2H_4) behaves similarly to acetylene in both chemisorption and decomposition. Like acetylene, ethylene can break a C-C π bond to form two σ bonds to the nickel surface. We expect this process to have a low barrier, and indeed we observe ethylene chemisorbing onto the particle after 18 ps when the temperature reaches T_A = 800 K.

Only half as many ethylene molecules (17) chemisorbed onto the particle compared to acetylene molecules (32). Since both ethylene and acetylene have essentially no barrier to chemisorption (they both bind by breaking a C-C π bonds) and neither leads to significant

steric effects, our results suggest that ethylene has a pre-exponential factor twice as large as ethylene. This is plausible since the solid angle for which acetylene π orbitals can overlap the Ni surface atoms is about twice that for ethylene.

After adsorbing to the surface C_2H_4 is stable for another 27 ps, until the temperature reaches T_H = 1400 K (45 ps), at which point dehydrogenation begins, forming C_2H_3, C_2H_2, and C_2H intermediates on the way to C_2, which first appears at 64 ps (1750 K). At these temperatures the dehydrogenation process is fast keeping the concentration of these C_2H_x intermediates low. At 68 ps (T_C = 1850 K) C-C bonds begin to break. Here dehydrogenation is generally completed to form C_2 before the C-C bond breaks (we found only one case in which the C-C bond in C_2H is broken first). This preference is the same as observed for acetylene, which also usually dehydrogenates completely before breaking C-C bonds.

Ethylene has been studied extensively on nickel surfaces experimentally [4, 21-28]. On the (111) surface the C-C π bond is broken to form two σ bonds each to an on-top nickel site, with the C-C bond lying parallel to the surface. As the temperature is increased on the (111) surface C_2H_4 loses two H atoms between 200 K and 230 K to form C_2H_2. This resulting acetylene then decomposes according to the pathway outlined previously [27]. Again, the presence of steps on the Ni(111) surface accelerates the cleavage of C-H bonds in C_2H_4 [4]. The defect rich nature of the nanoparticle in our studies explains why we observe C-H bond breaking well in advance of C-C bond breaking.

QM calculations have been reported for ethylene chemisorption on Ni(111) [29-31]. In agreement with experiment [21], these calculations find that ethylene binds further away

from the surface with each C atom sitting directly above a Ni surface atom. This is consistent with the structures observed in our RD.

3.1.4. Benzene (Figure 7)

The RD simulations for benzene (C_6H_6) show benzene initially binding through the C-C π orbitals to the nickel particle, leading to a geometry parallel to the surface, while retaining its resonance stabilization (Fig. 8a). As a result, σ bonds between ethylene and the surface are not formed, leading to only weak bonding and making the adsorption of benzene onto the nickel particle reversible so that a half dozen benzene desorption events are observed over the course of the RD simulation.

While benzene begins adsorbing to the nickel particle near the beginning of the simulation (2 ps, T_A = 550 K), it does not begin to decompose until T_H = 900 K (19 ps) when we observe an adsorbed C_6H_6 losing H to form C_6H_5. As the temperature increases additional dehydrogenation occurs forming di-σ bonded C_6H_4 (45 ps, 1400 K), tri-σ bonded allylic C_6H_3, (49 ps, 1500K), and eventually 1,2,3,4-C_6H_2 (63 ps, 1750 K) with 4 bonds to the surface. After 64 ps, at T_C = 1750 K, C-C bonds begin to break as C_6H_3 is converted to C_5H_3, which is then able to further decompose by breaking either C-C or C-H bonds. Throughout the simulation we find that breaking C-C bonds usually involves breaking a single C or C_2 off of a longer hydrocarbon chain while bonding it into the subsurface. In other words, when the terminal C or terminal C_2 is denuded of C-H bonds the Ni nanoparticle acts like Pac-Man [32], gobbling up the terminal C or C_2, but stopping at C atoms that still have C-H bonds. Except for the buildup of C_2 near the end of the simulation, the populations of chains with less than six C atoms remain small, suggesting that the decomposition of C-C bonds occurs quickly once the first C has been removed

from the ring. The most abundant intermediates at each length are: C_5H_3, C_4H_2, C_3H, and C_2.

An examination of snapshots from the trajectory suggests why these species are formed along the preferred decomposition pathway (Figure 8). Benzene adsorbs initially with its ring parallel to the particle surface, bonding to the surface using its π electrons. Breaking one C-H bond frees up a C in the ring to form a σ bond to the surface, which distorts the planar nature of the ring. The addition of a second σ bond to the surface, following the loss of another H, results in a 1,2-benzyne which bonds to the surface with the ring standing up perpendicular to the surface. In this perpendicular orientation, only two of the four remaining H atoms are close enough to the surface to react. Thus, we do not observe any C_6H or C_6 in our simulation because the remaining H atoms in C_6H_2 are too far from the surface to react readily.

Now that C_6H_4 is perpendicular to the surface it loses one or two of the remaining H atoms close to the surface to form allylic C_6H_3 or 1,2,3,4-C_6H_2. With three or four σ bonds to the surface, Ni atoms are now able to insert into the dehydrogenated C-C bonds. This initial cleavage of a C-C bond breaks the ring structure, but not the molecule, so our current analysis does not detect it. On the other hand, breaking a second C-C bond results in the formation of two new species. Thus 9 out of 11 reactive events involve cleavage of a C-C bond in C_6H_3 or C_6H_2 to form atomic chemisorbed C. Thus, like Pac-Man, the Ni particle "swallows" each C atom by migrating it into the subsurface, leaving C_5H_3 or C_5H_2 behind on the surface. The C_5H_x species either remains stretched out as a chain, or (in at least one observed instance) reconnects to form a five-membered C_5H_3 ring.

The decomposition of C_5H_x species is typically initiated from C_5H_2, resulting in loss of either C or C_2 into the subsurface of the Ni particle. Cleaving a C-C bond to form two new species (rather than just breaking a ring) results in either C_2 or atomic C as one of the products formed (except for one instance of $C_6H_2 \rightarrow C_3H_2 + C_3$). Thus, the Ni particle catalyzes the cleavage of a C-C bond by inserting Ni atoms into the bond to introduce either C or C_2 into the subsurface. Even for C_5H_x species, one or two of the H atoms are often inaccessible to the surface, so that 6 of the 9 C_5H_x decomposition events that form lower order hydrocarbons initiate immediately from C_5H_2 or more highly saturated C_5H_x species.

As the cleavage of C-C bonds continues to shorten the hydrocarbon chain, the H atoms that were originally too far away from the surface to react with the Ni as part of the six-membered ring are drawn closer to the surface, allowing the cleavage of the remaining C-H bonds. As for acetylene and ethylene, there is a noticeable preference for breaking off C rather than CH_x species when cleaving C-C bonds. Thus we can think of the overall mechanism as proceeding roughly along the following lines. Because cleavage of C-C bonds is stabilized by introducing C or C_2 into the subsurface of the nickel particle, the part of the hydrocarbon chain where a C-C bond is going to be attacked must first be stripped of H so that Ni atoms are able to insert into the bond and surround the C atom being introduced into the particle subsurface. As the chain length is reduced, H atoms originally too far away from the surface to react are reeled in toward the surface where they are stripped away, allowing another C-C bond to be broken. Thus we might idealize the mechanism by considering it as proceeding iteratively: $C_6H_6 \rightarrow C_6H_5 \rightarrow C_6H_4 \rightarrow C_6H_3 \rightarrow C_5H_3 \rightarrow C_5H_2 \rightarrow C_4H_2 \rightarrow C_4H \rightarrow C_3H \rightarrow C_3 \rightarrow C_2 \rightarrow C$.

The interaction of benzene with nickel surfaces has been studied previously [4, 9, 11-12, 25, 33-38]. Benzene can be synthesized from methane on Ni(111), where it is stable up to 395 K, at which temperature it begins to desorb and dehydrogenate [12]. These experiments have been interpreted in terms of benzene forming π bonds to the surface with the carbon ring remaining flat [24] while the H atoms point slightly away from the surface [38]. This initial binding structure is in agreement with our findings.

3.1.5. Cyclohexane (Figure 9)

Like methane, cyclohexane (C_6H_{12}) requires a C-H bond to break in order to chemisorb onto the nanoparticle. Thus, we observe no chemisorption until the temperature reaches $T_A = T_H = 1650$ K (59 ps), at which point chemisorption results in H and C_6H_{11} each bonding to the surface. The RD simulations reveal both initial dissociation of axial C-H bonds and equatorial C-H bonds upon chemisorption of C_6H_{12}; with no obvious preference

Once chemisorption occurs, dehydrogenation follows quickly as the predominant process. The pathways followed are analogous to those observed for benzene. As a result, dehydrogenation is observed to proceed as far as C_6H_2. Unlike benzene, cyclohexane can lose H and subsequently desorb from the surface because π bonds are formed when adjacent H atoms are lost. Thus, we observe two C_6H_{10} molecules, one C_6H_9 molecule, and one C_6H_8 molecule in the gas phase. Three of these retain their original carbon ring structure, but C_6H_8 is a chain with three resonance stabilized double bonds.

Few C-C bonds are broken over the course of the simulation. The first such cleavage occurs after 88 ps at $T_C = 2250$ K, and produces C_4H_2 and C_2 from C_6H_2. The products further decompose into atomic C and H over the remainder of the simulation, following reaction pathways similar to those observed in the decomposition of other hydrocarbon

species. The only other C-C bond to break is the conversion of C_6H_7 into C_4H_4 and C_2H_3 in the final picosecond of the simulation. Thus, of the nine adsorbed molecules, only two convert into lower order hydrocarbons: one C_4H_3, one C_2H_3 and six C atoms. The remaining seven only undergo dehydrogenation. Of these, four return to the gas phase, as noted above, and three remain on the surface as two molecular fragments of C_6H_4 and one of C_6H_2.

Experiments show that cyclohexane physisorbs to Ni(111) at 150 K and desorbs above 170 K. In the presence of steps it dehydrogenates to form benzene [4]. Since our focus is primarily on chemisorption, and we start at 500K, there is no direct comparison with these experiments. However, the experimental observation that surface defects (particularly steps) play an important role in breaking C-H bonds, is consistent with our RD study.

3.1.6. Propylene (Figure 10)

Like acetylene and ethylene, propylene (H_2C=CH-CH_3) has a π bond allowing it to bond to the surface without breaking C-H bonds. Thus it begins to adsorb onto the particle after only 3 ps, when the temperature reaches T_A = 550 K.

Adsorbed propylene (C_3H_6) is a stable species similar to chemisorbed ethylene, except with a CH_3 group substituted for H. The population of H_2C=CH-CH_3 on the surface grows to nine molecules over the first 31 ps (T_H = 1150 K) before dehydrogenation begins. We find cases in the simulation where the first H is lost from each of the three C atoms in H_2C=CH-CH_3, to form HC_a-C_aH-CH_3, H_2C_a-C_a-CH_3, and H_2C_a-C_aH-C_aH_2, where the subscript a indicates which atoms are bonded to the surface. Note here that in the gas phase the allyl product would be dominant, because of resonance; however, on the surface the unpaired electrons bind to the Ni surface so that all species have similar energies. In all

cases, C_3H_5 further dehydrogenates to C_3H_4 before any C-C bonds break. Again, we observe all forms of C_3H_4 that can be obtained from propylene by breaking only C-H bonds. These are: HC_a-C_aH-C_aH_2, HC_a-C_a-CH_3, C_a-C_aH-CH_3, and H_2C_a-C_a-C_aH_2. Further, dehydrogenation of C_3H_4 is strongly preferred, leading through C_3H_3, C_3H_2, C_3H and finally to C_3 in 22 of 23 total reactions that start from C_3H_4. The one exception converts C_a-C_aH-CH_3 into atomic C at an interstitial subsurface site and the carbine, HC_a-CH_3, bonded to the Ni surface. As dehydrogenation continues the ratio of each C_3H_x species undergoing a C-C bond cleavage compared with further dehydrogenation increases. This is partially a function of there being fewer C-H bonds to break, and partially a function of the increased ease of breaking off C or C_2 compared to CH_x species. Of the 21 reactions converting C_3H_x species to C_2H_x and CH_x species, all but one result directly in the formation of either C_2 or atomic C at interstitial subsurface sites. This again emphasizes the importance of forming multiple C-Ni bonds in order to stabilize breaking C-C bonds by moving C or C_2 into the subsurface. Similar to ethylene and benzene, atomic C is not produced by breaking C-C bonds until the temperature reaches T_C = 1800 K.

3.2. Summary of RD Results

To compare the relative reactivities of various hydrocarbon species, it is useful to consider the temperature at which each species first adsorbs to the particle (T_A), the temperature at which H first appears signifying the first breaking of a C-H bond (T_H), and finally the temperature when atomic C is first produced corresponding to C-C bonds breaking and C moving into the bulk (T_C). These results are summarized in Table 1.

First, we consider chemisorption. At T_A = 550 K propylene and benzene are the first species to adsorb to the surface, (through their π bonds). Ethylene and acetylene also have π

bonds available for bonding to the surface, and begin sticking at T_A = 650 K and T_A = 800 K respectively. In contrast, methane and cyclohexane have no π bond electrons to form bonds with the surface, so chemisorption requires breaking a C-H σ bond, so that C can form a σ bond to the surface. This results in chemisorption being delayed until these systems reach higher temperatures: T_A = 1300 K and T_A = 1650 K respectively.

Once molecules chemisorb onto the surface, dehydrogenation (breaking C-H bonds) precedes the cleavage of C-C bonds in all cases studied. There are two important considerations in understanding the different temperatures at which we first observe C-H bonds breaking in the various species. First, the initial temperature of adsorption can be limiting, because breaking C-H bonds cannot be catalyzed by the particle until the hydrocarbon is adsorbed onto the particle surface. As a result T_H = 1300 K and T_H = 1650 K for methane and cyclohexane respectively, are identical to T_A for those species because chemisorption results in H formation.

Second, because breaking the C-H bonds is catalyzed by inserting a Ni atom into the C-H bond, it occurs more readily when the C-H bond is close to the surface. For example, adsorbed benzene with its ring structure parallel to the surface has the C-H bonds close to the surface and hence is vulnerable to dehydrogenation. Thus, we observe C-H bonds beginning to break at T_H = 900 K, the lowest temperature for any of the hydrocarbons we studied. The C-H bonds in ethylene are the next most reactive as they begin to break at T_H = 1050 K. Unlike benzene, where we expect the ring to sit well above the surface, acetylene binds to the surface with the C atoms in hollow sites. Thus, while the H atoms point away from the surface, the closer proximity of the C atoms to the surface enables Ni

atoms to more easily insert into the C-H bond to stabilize both the C and H atoms as the bond breaks.

In contrast, steric effects require propylene to sit further above the surface so that it requires a higher temperature, T_H = 1150 K, before C-H bonds first break, even though the C-H bond is weaker. Methane is the next most reactive, requiring a C-H bond to break in order for the initial chemisorption step start taking place at T_H = 1300 K. The C-H bonds in the CH_3 adsorbates begin to break at 1400 K, the same temperature as the C-H bonds in ethylene begin breaking (T_H = 1400 K). Finally, atomic H is not produced from cyclohexane until chemisorption begins at T_H = 1650 K. In this final case the initiation of dehydrogenation is clearly limited by the commencement of the chemisorption process.

Finally, we consider the cleavage of C-C bonds. The most common mechanism we observe for C-C bond cleavage is the Pac-Man mechanism which requires a bare C at the end of a hydrocarbon chain. In the Pac-Man mechanism a Ni atom inserts into the C-C bond, and the C atom at the end of the hydrocarbon chain is drawn into the catalyst particle subsurface where it is stabilized by forming four bonds to Ni, rather than the three it is limited to when sitting on top of the surface. Thus, subsurface atomic C formation is the product in the vast majority of reactions involving C-C bond cleavage that we observe. As a result, we can use the temperature at which atomic C first appears as a convenient indicator of when C-C bond cleavage is initiated, allowing us to include the decomposition of methane in our comparison. In this context, the decomposition processes studied here provides the following particular insights.

The C-C bonds in ethylene begin to break at T_C = 1450K to form C and CH. The low temperature for this process relative to the other species studied is likely due to the

dimensions of the molecule, which allow it to fit deeply into adjacent hollow sites on the surface. In this position, the Ni-C bonding is readily able to compensate for the C-C bond energy being lost. Furthermore, acetylene can undergo at most two dehydrogenation reactions, before the only remaining bond to break is a C-C bond, so that C_2 first appears soon after the temperature reaches 1400 K. Four of the other species begin to produce C near 1800K: acetylene at T_C = 1750K, propylene at T_C = 1800K, and ethylene and methane at T_C = 1850K. This temperature corresponds to the melting point of bulk nickel. Such a partially melted, amorphous particle surface makes it easier to introduce C atoms into the particle subsurface, where they are stabilized energetically to facilitate breaking a C-C bond. Cyclohexane is more difficult to decompose and does not produce C atoms (or any other species with less than six C atoms) until the temperature reaches T_C = 2250 K.

3.3. Relevance to CNT Growth

3.3.1. Implications for CNT Growth

The findings of our RD study have at least three implications for understanding feedstock selection for CNT growth. First, barriers for chemisorption for saturated hydrocarbon species are significantly higher than barriers for unsaturated species. Thus, at appropriate temperatures and pressures it should be possible to reduce the hydrocarbon population on the catalyst surface by using saturated hydrocarbon feedstock. There may be growth conditions under which a less than saturated concentration of hydrocarbon in the surface would be advantageous; however, surface (and possibly subsurface or bulk) saturation is generally believed to be a requirement for CNT growth. Thus, the low chemisorption barriers of unsaturated hydrocarbon species may provide an important advantage in pursuing low temperature growth.

Second, we find that C-H bonds break far more readily than C-C bonds. The orbital arguments underlying this were explained in Low and Goddard [39]. Thus, there may be conditions under which CNT growth occurs via the addition of short carbon chains rather than individual atoms. In particular, we observe C_2 as a stable intermediate in most of the decomposition pathways studied here. Preliminary ReaxFF simulations suggest that the addition of C_2 to the edge of a growing CNT may have a lower activation barrier than the addition of atomic C. If this is the case, there may be advantages to using hydrocarbon feedstock that easily breaks down into units of C_2.

Finally, the energetic favorability of subsurface C has been highlighted by the important role it plays in stabilizing breaking C-C bonds. There are models of CNT growth (particularly the VLS model) in which a nickel carbide phase is an important thermodynamic driving force for growth [40-42]. In this case, there may be advantages in selecting hydrocarbon feedstock that more easily decompose to form the carbide phase. On the other hand, there is evidence that some growth conditions depends on surface, rather than bulk, migration of the activated hydrocarbon species [43]. Under such growth conditions the formation of nickel carbide, may not be advantageous. Here also, the choice of feedstock may play a role in determining the extent of carbide formation and its subsequent effect on the CNT growth process.

3.3.2. Comparison with Other Theoretical Studies of CNT Growth

Other reactive force fields have been developed for nickel (or other similar transition metals such as iron) and carbon in order to study carbon nanotube growth [44-50], however, none of these studies treat hydrocarbon species. Thus, previous reactive force field studies of nanotube growth have been limited to migration and addition of the

activated carbon species to the growing nanotube edge as well as nucleation steps from the activated carbon species. Because extensive QM studies of feedstock decomposition (taking into account all the complexities of a real nanoparticle surface) are not computationally feasible with current technology there are no previous, systematic, computational studies of hydrocarbon feedstock decomposition on catalyst nanoparticles.

Nevertheless, a variety of tight-binding, reactive dynamics and density functional theory studies have noted the greater stability of subsurface C over atomic C on nickel surfaces [49, 51-52]. Thus, they conclude that saturating the nickel bulk (or at least the subsurface layer) may play an important role in adjusting the chemical potential of C to an appropriate level for CNT growth.

3.4. Analysis of Chemisorption Rates

To analyze the chemisorption rates from our RD simulations quantitatively, we utilized the kinetic model developed in section 2.2. Because this model assumes that desorption is negligible, it is not appropriate to apply it to the simulations on ethylene, propylene, and benzene. Thus we will apply our kinetic model to methane, cyclohexane and acetylene chemisorption and then use other means to compare ethylene, propylene and benzene with them.

3.4.1. Methane (Figure 11a)

To apply our kinetic model to methane chemisorption we first must estimate M. To do this we assume that either H or CH_3 occupies alternate three-fold site, (leaving half the three-fold sites empty) leading to $M = 70$. Since $N_0 = 120$ methane molecules, we use $\mathrm{M} = M - N_0 = -50$.

Using values of N from our RD simulation we plot the LHS of **(5)** in Figure 11a and fit the RHS of **(5)** to these values by optimizing the A and E_a parameters**.** This leads to an apparent activation energy for chemisorption of E_a = 41 kcal/mol. This result is incompatible with the calculated activation energies on Ni(111), where ReaxFF leads to 18.4 kcal/mol [14], in good agreement the experimental value of 17.7 kcal/mol [2] and the QM activation energy of 18.9 kcal/mol [19]. This discrepancy invalidates the simplifying assumptions in our kinetic model, because we expect a lower barrier on a defect rich surface, similar to those observed at steps [53, 54].

3.4.2. Cyclohexane (Figure 11b)

The application of our kinetic model to cyclohexane chemisorption yields similar results. Assuming that each chemisorbed molecule in a complete monolayer on Ni(111) occupies eight three-fold sites results in an activation energy of E_a = 31.3 kcal/mol. This is also higher than expected, since cyclohexane chemisorption should have a similar to barrier to methane chemisorption.

3.4.3. Acetylene (Figure 11c)

In contrast to the cases of methane and cyclohexane, breaking a C-H bond is not required for acetylene to chemisorb onto the nickel particle. Instead the C sp orbitals rehybridize with p orbitals from one of the π bonds to form sp^2 orbital on each C that can form σ bonds to the surface. Assuming each acetylene molecule in a complete monolayer on Ni(111) occupies 4 three-fold sites, our kinetic model leads to an activation energy of 1.9 kcal/mol (Figure 11c). Because acetylene binds strongly to Ni(111) (57 kcal/mol), and has electron density in a π bond readily able to do so, we expect a negligible barrier for

chemisorption. This is consistent with the analysis of a kinetic model, with the nearly constant adsorption rate observed in our RD.

3.4.4. Ethylene, Propylene, and Benzene (Figure 12)

Like acetylene, we expect ethylene, propylene and benzene to have small chemisorption barriers. However, because they bind more weakly to the particle surface than acetylene, we observe a significant number of desorption events as the temperature increases, making application of our simple chemisorption kinetic model inappropriate. Nevertheless we can gain insight into these chemisorption processes by comparing their relative rates during the first 25 ps of RD before desorption is observed.

Assuming that chemisorption barriers are negligible, the rate of chemisorption is equal to the rate of collision times the sticking co-efficient. The collision frequency per molecule should be the same for each species except for the $1/\sqrt{m}$ factor from the Boltzmann velocity distribution. Thus Figure 12 compares the relative sticking coefficients of each species. Acetylene and ethylene have similar molecule weights and sticking coefficients (examining the entire duration of the dynamics suggests that the rate of acetylene chemisorption is twice the rate of acetylene adsorption as noted earlier). Despite propylene's higher molecule weight it has a higher chemisorption rate than either acetylene or ethylene, showing that it has a higher sticking coefficient, which is even higher for benzene. This is expected from the larger number of low frequency modes that can absorb some of the collision energy to better trap the molecule on the surface.

4. Summary

Using the ReaxFF reactive force field with the parameters for C/H/Ni developed in Chapter 3 [14], we studied the adsorption and decomposition of six hydrocarbon species

(acetylene, benzene, cyclohexane, ethylene, methane and propylene) on a 468 atom nickel nanoparticle. We find that unsaturated hydrocarbons (molecules with π bonds) adsorb and decompose far more readily than saturated hydrocarbons (molecules with only σ bonds), because they chemisorb readily onto the surface. This difference is evident in the temperature at which chemisorption is initiated in our simulations (T_A = 800K or lower for unsaturated species and T_A = 1300K or higher for saturated species). The difference may be an important factor in selecting feedstock species for low temperature CNT growth.

Once the species are chemisorbed to the particle, dehydrogenation usually precedes decomposition into lower order hydrocarbons. The C-C bonds typically do not break until one of the C is denuded of H at which point it can insert into the subsurface of Ni, where the C atom is stabilized. This Pac-Man mechanism can chomp away on the longer hydrocarbon chains as subsequent C's are denude of their H's. In some cases a C_2 fragment can be chomped off, once it has been dehydrogenated. These observations suggest that there may be choices of precursor species that would provide optimal C-H and C-C bond breaking rates relative to the surface diffusion rates of adsorbed species in order to manipulate the CNT growth process. Additionally, the selection of the feedstock precursor might control the extent of carbide formation to take advantage of the role nickel carbide may play in a variety of CNT growth mechanisms.

Tables

	Acetylene	Benzene	Cyclohexane	Ethylene	Methane	Propylene
T_A	650 K	550 K	1650 K	800 K	1300 K	550 K
T_H	1050 K	900 K	1650 K	1400 K	1300 K	1150 K
T_C	1450 K	1750 K	2250 K	1850 K	1850 K	1800 K

Table 1: Results from ReaxFF RD simulations of hydrocarbons adsorbing and decomposing on a 468 atom nickel particle. The temperature was ramped from 500K to 2500K at a rate 20K/ps.

T_A : temperature at which the first molecule adsorbs onto the nickel nanoparticle.

T_H, : temperature at which the first C-H bond is broken to produce atomic H on the nickel nanoparticle.

T_C : temperature at which a C-C bond is broken to first produce atomic C on the nickel nanoparticle.

Figures

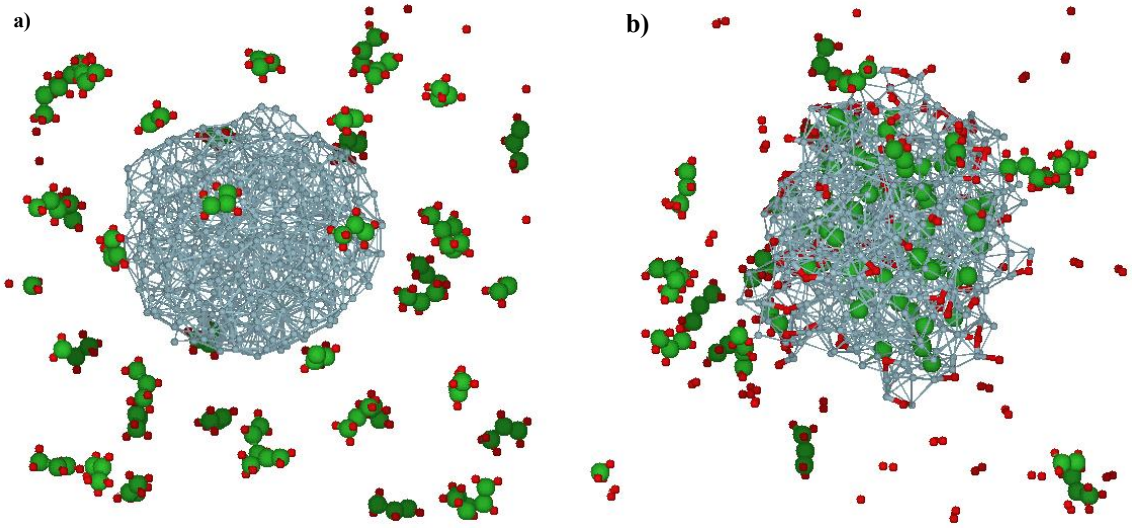

Figure 1: **a)** Initial and **b)** final structures for ReaxFF RD simulations of propene adsorption and decomposition on a nickel particle.

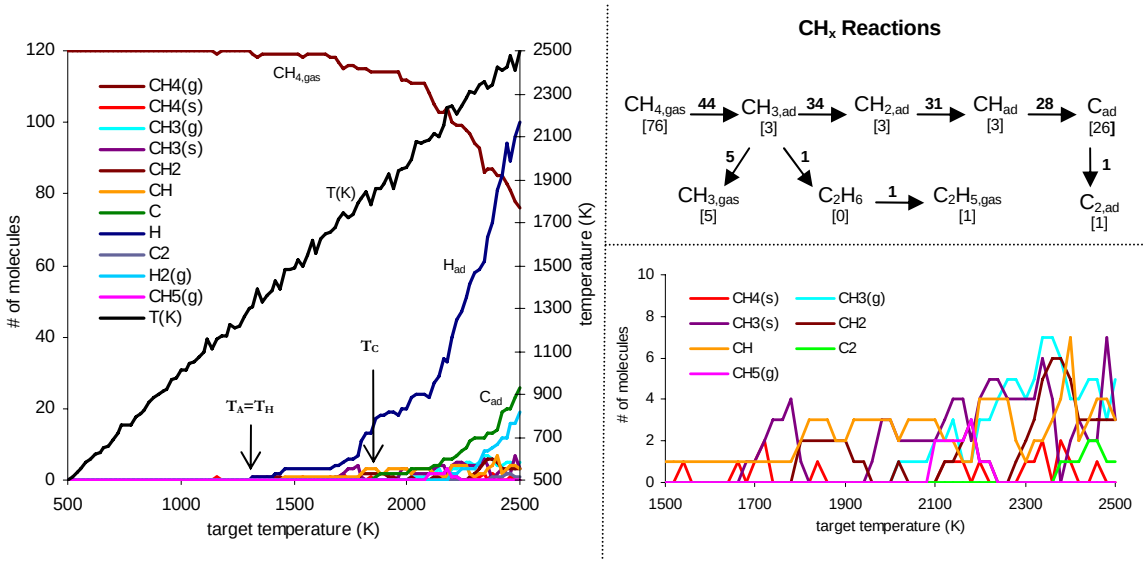

Figure 2: Population analysis and reaction network for methane chemisorption and decomposition on nickel. The numbers in brackets in the reaction network are the final populations of each species, the number on each reaction arrow is the total number of times the reaction took place. The simulation started with 120 CH_4 gas phase molecules, and no other HC species.

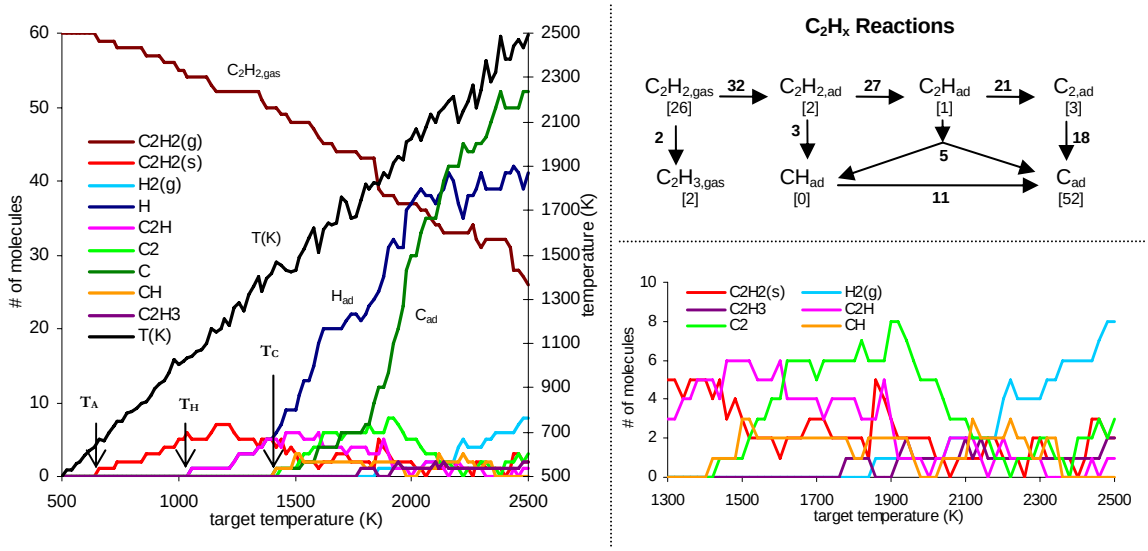

Figure 3: Population analysis and reaction network for ethylene chemisorption and decomposition on nickel. The numbers in brackets of the reaction network are the final populations of each species. The number on each reaction arrow is the total number of times the specific reaction took place. The simulation started with 60 C_2H_2 gas phase molecules, and no other HC species.

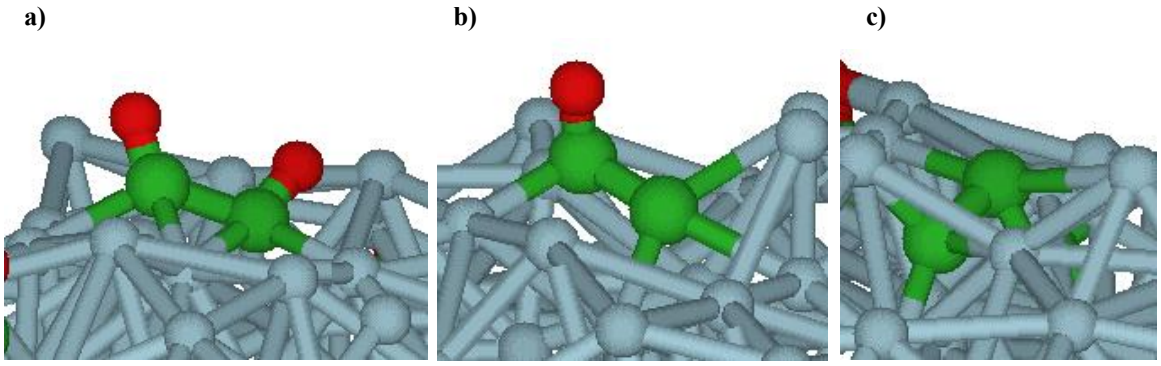

Figure 4: Snapshots of structures observed during ethyne decomposition on the nickel nanoparticle: **a)** C_2H_2 chemisorbed to the particle surface; **b)** C_2H on particle surface; **c)** C_2 in the subsurface region, where the C-C bond is more readily broken.

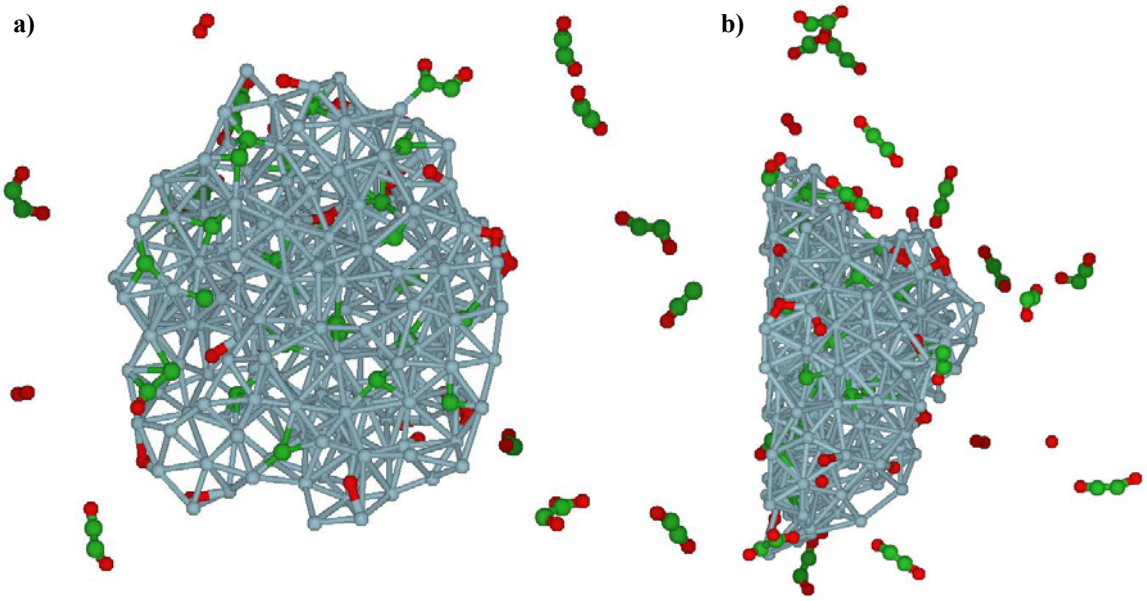

Figure 5: Cross-section (particle and simulation cell sliced in half) of final structure from acetylene simulation showing the migration of atomic C into the interior of the catalyst particle: **a)** head-on view; **b)** side view.

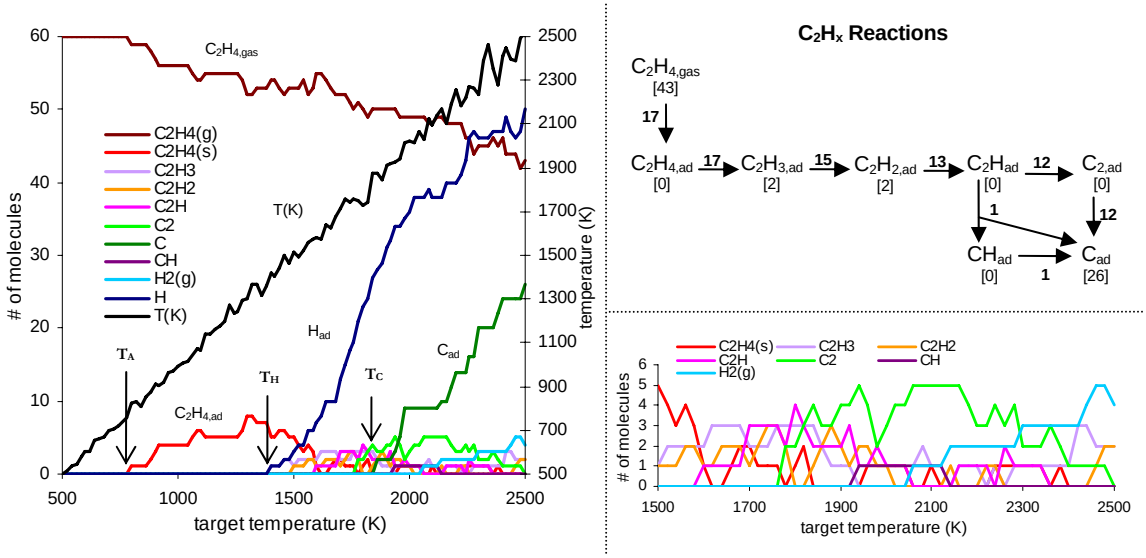

Figure 6: Population analysis and reaction network for ethene chemisorption and decomposition on nickel. The numbers in brackets of the reaction network are the final populations of each species, the number on each reaction arrow is the overall number of times the reaction took place. The simulation started with 60 C_2H_4 gas phase molecules, and no other HC species.

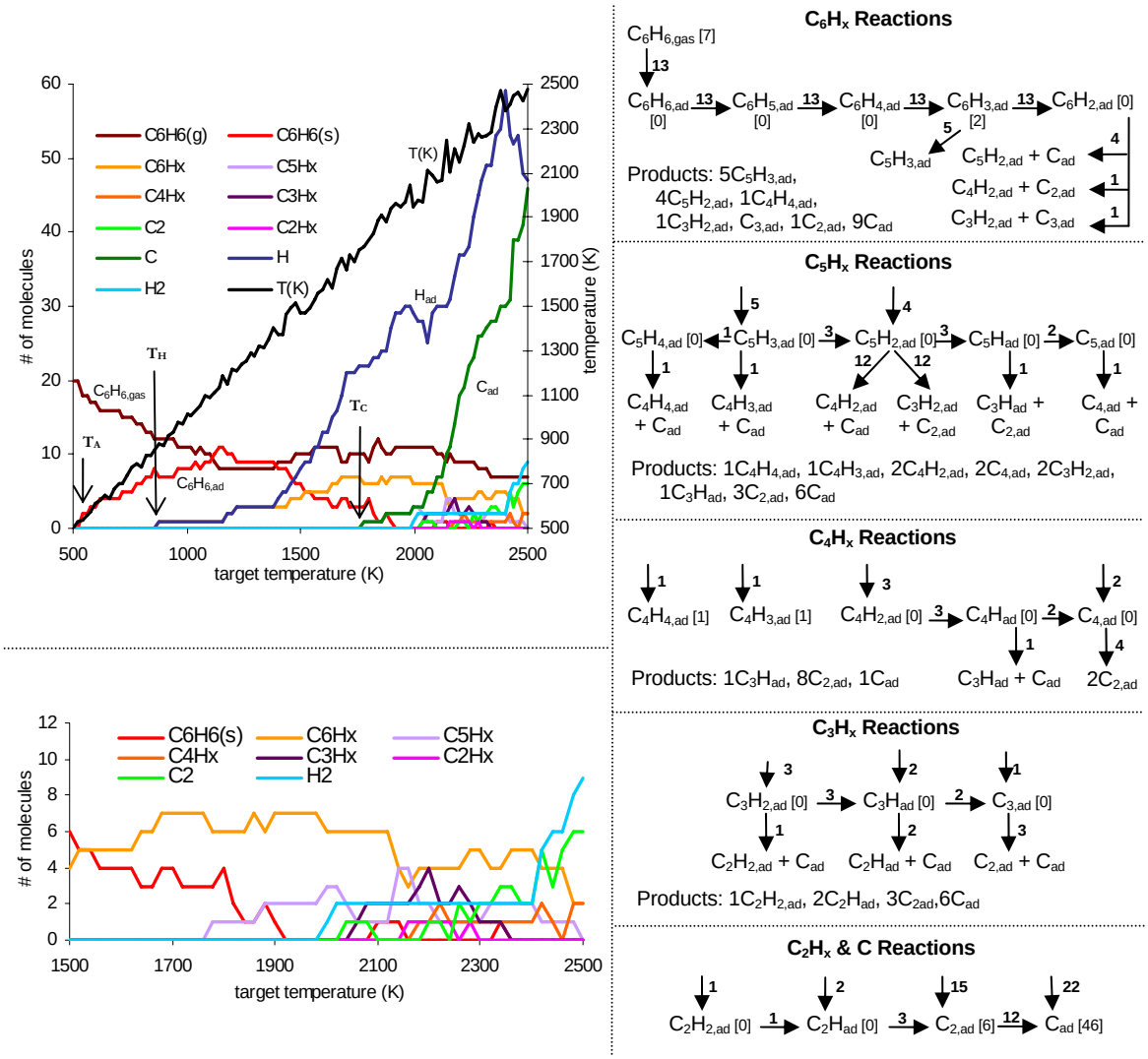

Figure 7: Population analysis and reaction network for benzene chemisorption and decomposition on nickel. The numbers in brackets of the reaction network are the final populations of each species, the number on each reaction arrow is the overall number of times the reaction took place. The simulation started with 20 C_6H_6 gas phase molecules, and no other hydrocarbon species.

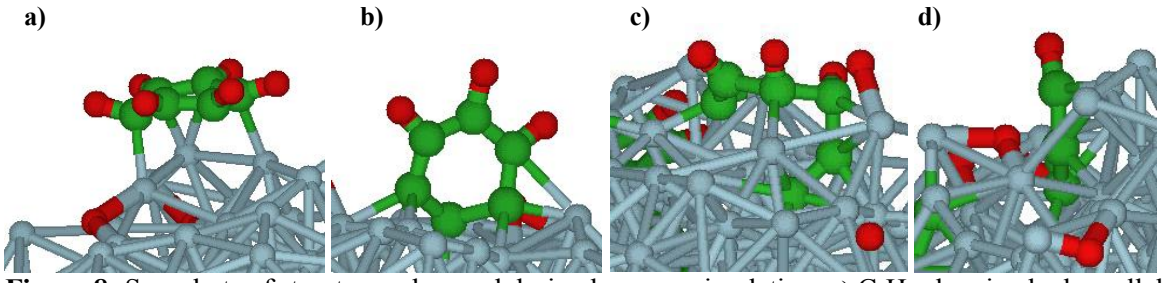

Figure 8: Snapshots of structures observed during benzene simulation: **a)** C_6H_6 chemisorbed parallel to the particle surface; **b)** C_6H_3 ring standing perpendicular to the surface; **c)** C_6H_3 chain on particle surface with dehydrogenated tail in subsurface; **d)** C_3H showing the preference of bare C atoms (no H) for the subsurface and hydrogenated C atoms for the surface.

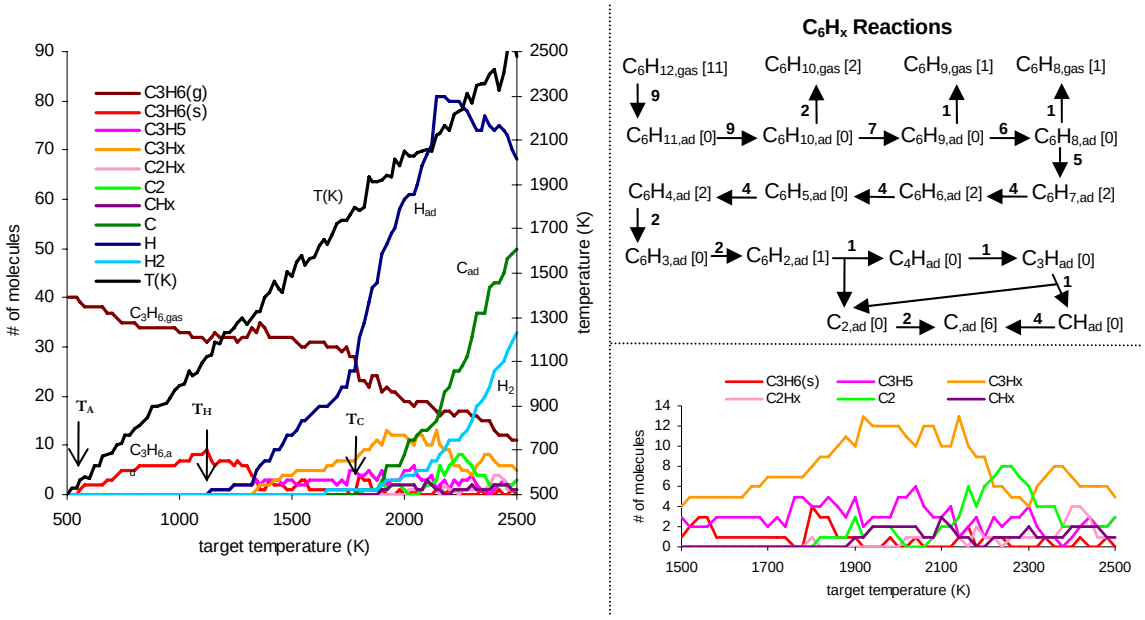

Figure 9: Population analysis and reaction network for cyclohexane chemisorption and decomposition on nickel. The numbers in brackets of the reaction network are the final populations of each species, the number on each reaction arrow is the overall number of times the reaction took place. The simulation started with 20 C_6H_{10} gas phase molecules, and no other hydrocarbon species.

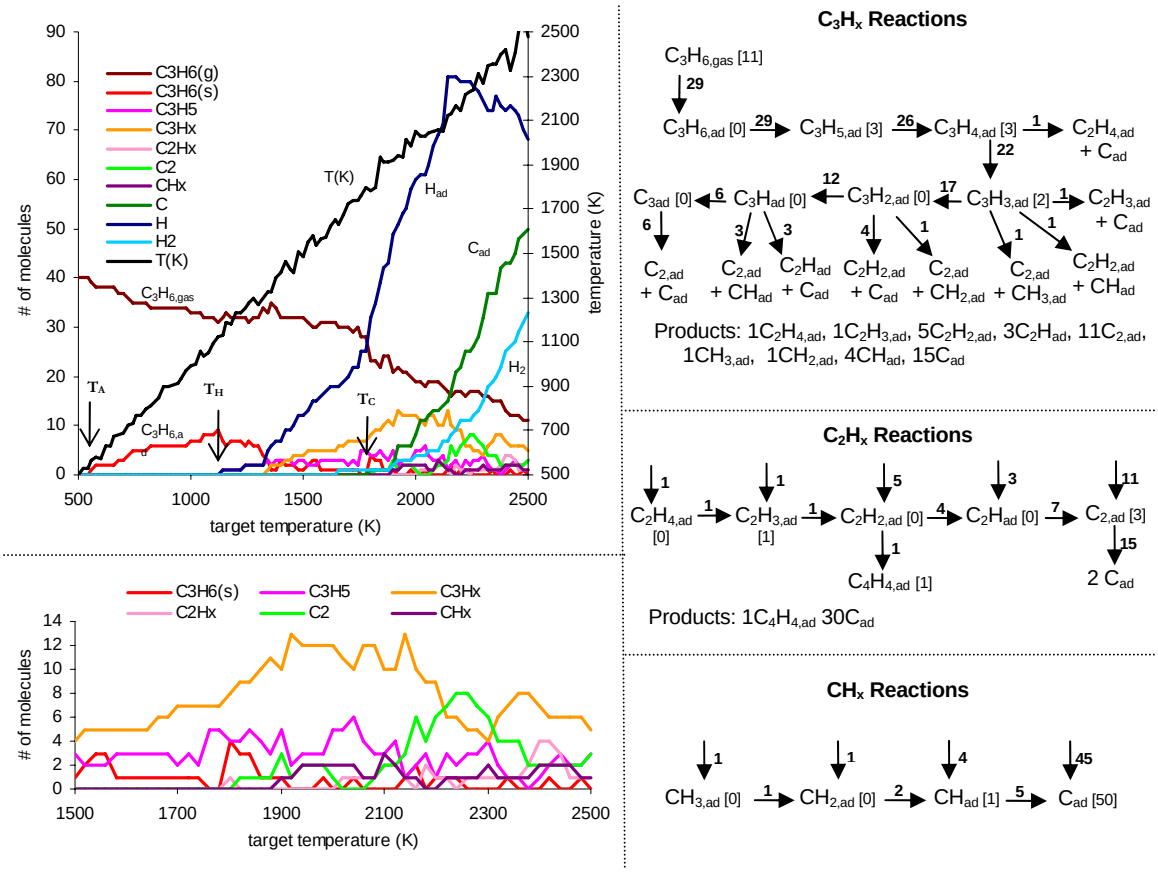

Figure 10: Population analysis and reaction network for propene chemisorption and decomposition on nickel nanoparticle. The numbers in brackets in the reaction network are the final populations of each species, the number on each reaction arrow is the overall number of times the reaction took place. The simulation started with 40 C_3H_6 gas phase molecules, and no other hydrocarbon species.

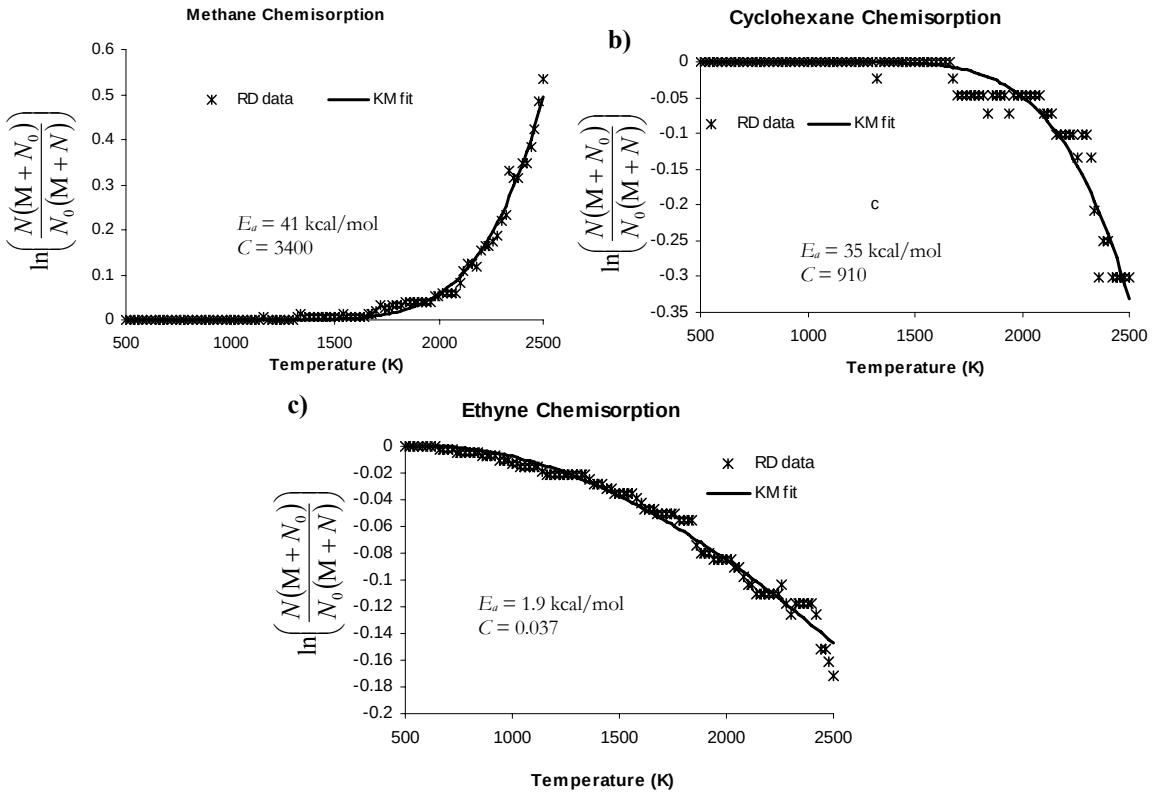

d) KM fit—equation **(5)**:

$$\ln\left(\frac{N(\mathrm{M}+N_0)}{N_0(\mathrm{M}+N)}\right) = C\left\{\sqrt{\pi}erf\left(\sqrt{\frac{E_a}{k_B\mathrm{T}_0}},\sqrt{\frac{E_a}{k_B\mathrm{T}}}\right)+e^{-\frac{E_a}{k_B\mathrm{T}}}\sqrt{\frac{k_B\mathrm{T}}{E_a}}\left(1-\frac{2k_B\mathrm{T}_0}{E_a}\right)-e^{-\frac{E_a}{k_B\mathrm{T}_0}}\sqrt{\frac{k_B\mathrm{T}_0}{E_a}}\left(1-\frac{2k_B\mathrm{T}_0}{E_a}\right)\right\}$$

Figure 11: The kinetics of chemisorption of **a)** methane, **b)** cyclohexane, and **c)** ethyne on the Ni_{468} nanoparticle from ReaxFF RD compared to the rate expression from **d)** kinetic model (KM) for chemisorption—equation **(5)**.

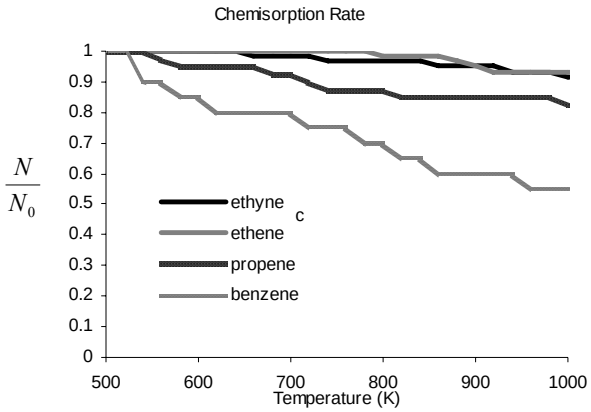

Figure 12: Relative **r**ates of chemisorption for unsaturated hydrocarbons during first 25 ps of RD, before desorption is noticeable.

References

1. Rostrup-Nielsen, J. R. Catalytic Steam Reforming, in *Catalysis, Science and Technology*, J.R. Anderson and M. Boudar, Eds. 1984, Springer: Berlin; 1-117.
2. Egeberg, R. C.; Ullman, S.; Alstrup, I.; Mullins, C. B.; Chorkendorff, I. Dissociation of CH_4 on Ni(111) and Ru(0001). *Surf. Sci.* **2002**, *497* (1-3), 183-193.
3. Paillet, M.; Jourdain, V.; Phoncharal, P.; Sauvajol, J.-L.; Zahab, A. Versatile Synthesis of Individual Single-Walled Carbon Nanotubes from Nickel Nanoparticles for the Study of their Physical Properties. *J. Phys. Chem. B* **2004**, *108* (44), 17112-17118.
4. Lehwald S.; Ibach, H. Decomposition of Hydrocarbons on Flat and Stepped Ni(111) Surfaces. *Surf. Sci.* **1979**, *89* (1-3), 425-445.
5. Mueller, J. E.; van Duin, A.C.T.; Goddard, W.A. Structures, Energetics, and Reaction Barriers for CH_x Bound to Ni(111) Surfaces. *J. Phys. Chem. C* **2009**, *113* (47), 20290-20306.
6. Watwe, R. M.; Bengaard, H. S.; Rostrup-Nielsen, J. R.; Dumesic,J. A.; Norskov, J. K. Theoretical Studies of Stability and Reactivity of CH_x species on Ni(111). *J. Catal.* **2000**, *189* (1) 16-30.
7. Yang, Q.Y.; Maynard, K. J.; Johnson, A. D.; Ceyer, S. T. The Structure and Chemistry of CH_3 and CH Radicals Adsorbed on Ni(111). *J. Chem. Phys.* **1995**, *102* (19), 7734-7749.
8. Mora, E.; Pigos, J. M.; Ding, F.; Yakobson, B. I.; Harutyunyan, A. R. Low-Temperature Single-Wall Carbon Nanotubes Synthesis: Feedstock Decomposition Limited Growth. *J. Am. Chem. Soc.* **2008**, *130* (36), 11840-11841.
9. Demuth, J.E. Conversion of Ethylene to Acetylene on Ni(111). *Surf. Sci.* **1978**, *76* (2), L603-L608.
10. Kaminsky, M. P.; Winograd, N.;Geoffroy, G. L. Direct SIMS Observation of Methylidyne, Methylene, and Methyl Intermediates on a Ni(111) Methanation Catalyst. *J. Am. Chem. Soc.* **1986**, *108* (6), 1315-1316.
11. Lehwald, S.; Ibach, H.; Demuth, J. E. Vibration Spectroscopy of Benzene Adsorbed on Pt(111) and Ni(111). *Surf. Sci.* **1978**, *78* (3), 577-590.
12. Yang, Q.Y.; Johnson, A. D.; Maynard, K. J.; Ceyer, S. T. Synthesis of Benzene from Methane over a Ni(111) Catalyst. *J. Am. Chem. Soc.* **1989**, *111* (23), 8748-8749.
13. Car R.; Parrinello, M. Unified Approach for Molecular-Dynamics and Density-Functional Theory. *Phys. Rev. Lett.* **1985**, *55* (22), 2471-2474.
14. Mueller, J. E.; van Duin, A. C. T.; Goddard, W. A. Development and Validation of ReaxFF Reactive Force Field for Hydrocarbon Chemistry Catalyzed by Nickel. *J. Phys. Chem. C* **2010**, *114* (11), 4939-4949. (Chapter 1)
15. Nielson, K.D.; van Duin, A. C. T.; Oxgaard, J.; Deng, W.Q.; Goddard, W. A. Development of the ReaxFF Reactive Force Field for Describing Transition Metal Catalyzed Reactions, with Application to the Initial Stages of the Catalytic Formation of Carbon Nanotubes. *J. Phys. Chem. A* **2005**, *109* (3), 493-499.

16. Dai, H.J.; Rinzler, A. G.; Nikolaev, P.; Thess, A.; Colbert, D. T.; Smalley, R. E. Single-Wall Nanotubes Produced by Metal-Catalyzed Disproportionation of Carbon Monoxide. *Chem. Phys. Lett.* **1996**, *260* (3-4), 471-475.

17. Flystra, D.; Lasdon, L.; Watson, J.; Waren, A. *Design and Use of the Microsoft Excel Solver. Interfaces* **1998**, *28* (5), 29-55.

18. Yang, Q. Y.; Ceyer, S. T. The Stability and Chemistry of Methyl Radicals Adsorbed on Ni(111).*J. Vac. Sci. Technol. A* **1988**, *6* (3), 851-852.

19. Henkelman, G.; Arnaldsson, A.; Jonsson, H. Theoretical Calculations of CH_4 and H_2 Associative Desorption from Ni(111): Could Subsurface Hydrogen Play an Important Role? *J. Chem. Phys.* **2006**, 124 (4), 044706.

20. Michaelides, A.; Hu, P. A First Principles Study of CH_3 Dehydrogenation on Ni(111). *J. Chem. Phys.* **2000**, *112* (18), 8120-8125.

21. Bao, S.; Hofmann, Ph.; Schindler, K.-M.; Fritzsche, V.; Bradshaw, A. M.; Woodruff, D. P.; Casado, C.; Asenio, M. C. The Local Geometry of Reactant and Product in a Surface Reaction: the Dehydrogenation of Adsorbed Ethylene on Ni(111). *Surf. Sci.* **1995**, *323* (1-2), 19-29.

22. Demuth, J. E. Molecular Geometries of Acetylene and Ethylene Chemisorbed on Cu, Ni, Pd, and Pt Surfaces. *IBM Journal of Research and Development* **1978**, *22* (3), 265-276.

23. Demuth, J. E.; Eastman, D. E. Determination of State of Hybridization of Unsaturated-Hydrocarbons Chemisorbed on Nickel. *Phys. Rev. B* **1976**, *13* (4), 1523-1527.

24. Demuth, J. E.; Eastman, D. E. Photoemission Observations of π-d Bonding and Surface Reactions of Adsorbed Hydrocarbons on Ni(111). *Phys. Rev. Lett.* **1974**, *32* (20), 1123-1127.

25. Demuth, J. E.; Ibach, H.; Lehwald, S. CH Vibration Softening and Dehydrogenation of Hydrocarbon Molecules on Ni(111) and Pt(111). *Phys. Rev. Lett.* **1978**, *40* (15), 1044-1047.

26. Sham, T. K.; Carr, R. G. Carbon Near Edge X-Ray Absorption Fine-Structure (NEXAFS) Studies of Ethylene Adsorption on Ni(111) and Ni(110) Surfaces: Implication for Surface-Morphology Insensitive Reactions. *J. Chem. Phys.* **1986**, *84* (7), 4091-4095.

27. Zhu, X. Y.; Castro, S.; Akhter, S.; White, J. M.; Houston, J. E. Static Secondary Ion Mass-Spectroscopy Study of Ethylene and Acetylene on Ni: Coverage Dependence. *J. Vac. Sci. Technol. A* **1989**, ***7*** (3), 1991-1995.

28. Zhu, X. Y.; White, J. M. Interaction of Ethylene and Acetylene with Ni(111): A SSIMS Study. *Surf. Sci.* **1989**, *214* (1-2), 240-256.

29. Anderson, A. B. Structural and Orbital Analysis of Ethylene and Acetylene on Ni(111) Surfaces. *J. Chem. Phys.* **1976,** *65* (5), 1729-1734.

30. Fahmi, A.; van Santen, R. A. Density Functional Study of Acetylene and Ethylene Adsorption on Ni(111). *Surf. Sci.* **1997**, *371* (1), 53-62.

31. Medlin, J. W.; Allendorf, M. D. Theoretical Study of the Adsorption of Acetylene on the (111) Surfaces of Pd, Pt, Ni, and Rh. *J. Phys. Chem. B* **2003,** *107* (1), 217-223.

32. Pac-Man is a character in the Pac-Man arcade game first produced by Namco in 1980. Pac-Man is represented as a yellow circle (or sphere) with a wedged shaped mouth that continually opens and closes as he moves through a maze eating Pac-dots one at a time. In an analogous manner, the Ni particle breaks C-C bonds by "eating up" the C atoms one at a time in what we call the Pac-Man mechanism.
33. Bertolini, J. C.; Rousseau, J. C_2H_4 Adsorption on the Ni(111) Face at Room-Temperature: Vibrations of Surface Complexes Studied by Electron-Energy Loss Spectroscopy. *Surf. Sci.* **1979**, *83* (2), 531-544.
34. Demuth, J. E. Interaction of Acetylene with Ni(111), Chemisorbed Oxygen on Ni(111), and NiO(111): Formation of CH Species on Chemically Modified Ni(111) Surfaces. *Surf. Sci*. **1977,** *69* (2), 365-384.
35. Demuth, J. E. Structure of Chemisorbed Acetylene and Ethylene on Ni, Pd and Pt Surfaces. *Surf. Sci.* **1979**, *84* (2), 315-328.
36. Demuth J. E.; Ibach, H. Experimental Study of the Vibrations of Acetylene Chemisorbed on Ni(111). *Surf. Sci.* **1979**, *85* (2), 365-378.
37. Demuth, J. E.; Ibach, H. Identification of CH Species on Ni(111) by High-Resolution Electron-Energy Loss Spectroscopy. *Surf. Sci.* **1978**, *78* (1), L238-L244.
38. Mittendorfer, F.; Hafner, J. Density-Functional Study of the Adsorption of Benzene on the (111), (100) and (110) Surfaces of Nickel. *Surf. Sci.* **2001**, *472* (1-2), 133-153.
39. Goddard, W. A.; Carter, E. A.; Guo, Y.; Peters, J. C.; Donnelly, R. E.; Low, J. J. Chemisorbed Intermediates on Metal and Semiconductor Surfaces. *Abstracts of Papers of the American Chemical Society* **1987**, *194*, 85-Phys.
40. Rodriguez-Manzo, J. A. Terrones, M.; Terrones, H.; Kroto, H. W.; Sun, L.; Banhart, F. In situ Nucleation of Carbon Nanotubes by the Injection of Carbon Atoms into Metal Particles. *Nature Nanotechnology* **2007**, *2* (5), 307-311.
41. Saito, Y. Nanoparticles and Filled Nanocapsules. *Carbon* **1995**, *33* (7), 979-988.
42. Wagner, R. S.; Ellis, W.C. Vapor-Liquid-Solid Mechanism of Single Crystal Growth. *Appl. Phys. Lett.* **1964**, *4* (5), 89-90.
43. Hofmann, S.; Csanyi, G.; Ferrari, A. C.; Payne, M. C.; Robertson, J. Surface Diffusion: The Low Activation Energy Path for Nanotube Growth. Phys. Rev. Lett. **2005**, *95* (3), 036101.
44. Ding, F.; Bolton, K.; Rosen, A. Nucleation and Growth of Single-Walled Carbon Nanotubes: A Molecular Dynamics Study. *J. Phys. Chem. B,* **2004**, *108* (45), 17369-17377.
45. Ding, F.; Rosen, A.; Bolton, K. Molecular Dynamics Study of the Catalyst Particle Size Dependence on Carbon Nanotube Growth. *J. Chem. Phys.* **2004**, *121* (6), 2775-2779.
46. Ding, F.; Rosen, A.; Bolton, K. The Role of the Catalytic Particle Temperature Gradient for SWNT Growth from Small Particles. *Chem. Phys. Lett.* **2004**, *393* (4-6), 309-313.
47. Maiti, A.; Brabec, C. J.; Bernholc, J. Kinetics of Metal-Catalyzed Growth of Single-Walled Carbon Nanotubes. *Phys. Rev. B*, **1997**, *55* (10), R6097-R6100.

48. Maiti, A.; Brabec, C. J.; Roland, C.; Bernholc, J. Theory of Carbon Nanotube Growth. *Phys. Rev. B* **1995**, *52* (20),14850-14858.

49. Shibuta, Y.; Maruyama, S. Molecular Dynamics Simulation of Formation Process of Single-Walled Carbon Nanotubes by CCVD Method. *Chem. Phys. Lett.* **2003**, *382* (3-4), 381-386.

50. Shibuta, Y.; Maruyama, S. Molecular Dynamics Simulation of Generation Process of SWNTs. *Physica B-Condensed Matter* **2002**, *323* (1-4), 187-189.

51. Abild-Pedersen, F.; Norskov, J. K.; Rostrup-Nielsen, J. R.; Sehested, J.; Helveg, S. Mechanisms for Catalytic Carbon Nanofiber Growth Studied by ab initio Density Functional Theory Calculations. *Phys. Rev. B* **2006**, *73* (11), 115419.

52. Amara, H.; Bichara, C.; Ducastelle, F. Understanding the Nucleation Mechanisms of Carbon Nanotubes in Catalytic Chemical Vapor Deposition. *Phys. Rev. Lett.* **2008**, *100* (5), 056105.

53. Bengaard, H. S. Norskov, J. K.; Sehested, J.; Causen, B. S.; Nielsen, L. P.; Molenbroek, A. M.; Rostrup-Nielsen, J. R. Steam Reforming and Graphite Formation on Ni Catalysts. *J. Catal.* **2002**, *209* (2), 365-384.

54. Hofmann, S.; Sharma, R.; Ducati, C.; Du, G.; Mattevi, C.; Cepek, C.; Cantoro, M.; Pisana, S.; Parvez, A.; Cervantes-Sodi, F.; Ferrari, A. C.; Dunin-Borkowski, R.; Lizzit, S.; Petaccia, L.; Goldoni, A.; Robertson, J. In situ Observations of Catalyst Dynamics During Surface-Bound Carbon Nanotube Nucleation. *Nano Lett.* **2007**, *7* (3), 602-608.

Outlook

An important motivation for our work on hydrocarbon chemistry on nickel has been the goal of studying carbon nanotube growth. Describing a reactive system as complex as a carbon nanotube growing on a nickel catalyst particle necessitates the use of a tool like ReaxFF. While we have performed numerous preliminary studies of carbon nanotube growth using the current ReaxFF description and its precursors, much work remains in the way of fully utilizing the capabilities of ReaxFF in the study carbon nanotube growth. In this closing section I will briefly sketch work we are currently performing along these lines as well as what I believe would be the most profitable directions for future work to take.

The synthesis of carbon nanotubes can be broken down into three or four distinct stages. The first stage is feedstock decomposition, which was the subject of Chapter 4. Under low temperature growth conditions, experiments suggest that feedstock decomposition is the rate limiting step [1]. Thus our analysis of hydrocarbon decomposition pathways on nickel nanoparticles shows how the selection of different hydrocarbon species for the feedstock influences the chemisorption rate, surface coverage and extent of carbide formation during the nanotube growth process.

Following feedstock decomposition is the carbon transport stage, in which a hydrocarbon or carbon species is either transported along the catalyst surface or else diffuses through the catalyst bulk as carbide. Because a constant supply of carbon is needed for both nucleation and growth, carbon transport likely occurs during both the nucleation and growth stages and so is most naturally treated as a part of each of these stages taken separately. It is also possible that a partially decomposed species migrates to the nucleation or growth site where it further decomposes into the activated species. In any case,

experiments indicate that there are growth conditions under which surface diffusion is the rate limiting step [2].

It is believed that nucleation occurs when enough carbon material accumulates on the surface for the formation of surface ring structures. The ring structures develop into a graphene island on the particle which, when it becomes large enough, lifts its center off the particle surface in the experimentally observed Yarmulke mechanism [3,4]. Previous ReaxFF simulations and previously published MD studies [5] suggest that nucleation may take place in time scales as short as 10 nanoseconds. Currently we are performing ReaxFF RD simulations to study carbon nanotube nucleation following acetylene decomposition on a nickel nanoparticle catalyst, and observe carbon ring structures involving more than one hundred carbon atoms, within the first couple nanoseconds of RD. A careful analysis of these simulation trajectories is expected to yield a detailed, atomistic understanding of the nucleation process.

Following nucleation is the nanotube growth stage in which carbon is added to the end of the growing nanotube. This stage likely lasts significantly longer than the previous stages, which means that ReaxFF RD simulations of the entire growth stage are probably not computationally feasible at present. Nevertheless, a couple different strategies are available for overcoming this difficulty. The first, is to use an already growing nanotube as the initial structure for ReaxFF RD simulations, and study just a part of the growth process. This approach assumes that the nanotube growth mechanism is essentially unchanged over the duration of the growth, so that the whole process can be understood by characterizing a limited part of it. The key to performing these simulations successfully will be setting up a realistic starting structure.

The second option for circumventing the time limitations on ReaxFF RD is the use of a kinetic Monte Carlo procedure to bypass long periods of quasi-equilibrium dynamics between reaction events using principles from statistical mechanics and transition state theory. Because traditional kinetic Monte Carlo methods require predefined reactions and make the lattice approximation, they are not directly applicable to a complex process such as carbon nanotube growth. Nevertheless, alternative schemes have been proposed for circumventing the lattice approximation by calculating reaction barriers on the fly [6]. The bond order/ bond distance relationship already present in ReaxFF would provide a natural tool for the development of an automated reaction search procedure, enabling kinetic Monte Carlo simulations within the ReaxFF framework. Such simulations would be capable of looking at carbon nanotube growth over a significantly longer time scale than ReaxFF RD.

References

1. Mora, E.; Pigos, J. M.; Ding, F.; Yakobson, B. I.; Harutyunyan, A. R. Low-Temperature Single-Wall Carbon Nanotubes Synthesis: Feedstock Decomposition Limited Growth. *J. Am. Chem. Soc.* **2008**, *130* (36), 11840-11841.
2. Hofmann, S.; Csanyi, G.; Ferrari, A. C.; Payne, M. C.; Robertson, J. Surface Diffusion: The Low Activation Energy Path for Nanotube Growth. Phys. Rev. Lett. **2005**, *95* (3), 036101.
3. Hofmann, S.; Sharma, R.; Ducati, C.; Du, G.; Mattevi, C.; Cepek, C.; Cantoro, M.; Pisana, S.; Parvez, A.; Cervantes-Sodi, F.; Ferrari, A. C.; Dunin-Borkowski, R.; Lizzit, S.; Petaccia, L.; Goldoni, A.; Robertson, J. In situ Observations of Catalyst Dynamics During Surface-Bound Carbon Nanotube Nucleation. *Nano Lett.* **2007**, *7* (3), 602-608.
4. Heleg, S.; Lopez-Cartes, C.; Sehested, H; Hansen, P. L.; Clausen, B. S.; Rostrup-Nielsen, J. R.; Ablid-Pedersen, P.; Norsekove, J. K. Atomic-Scale Imaging of Carbon Nanofibre Growth. *Nature* **2004**, *427*, 426-429.
5. Ding, F.; Rosen, A.; Bolton, K. Molecular Dynamics Study of the Catalyst Particle Size Dependence on Carbon Nanotube Growth. *J. Chem. Phys.* **2004**, *121* (6), 2775-2779.
6. Henkelman, G.; Jonsson, H. Long Time Scale Kinetic Monte Carlo Simulations without Lattice Approximation and Predefined Event Table. *J. Chem. Phys.* **2001**, *115*, 9657-9666.

A p p e n d i x A

ReaxFF Potential Function Used in C/H/Ni Force Field[4]

This document contains all the general ReaxFF-potential functions. In the current ReaxFF code all the energy contributions in this document are calculated regardless of system composition. All parameters that do not bear a direct physical meaning are named after the partial energy contribution that they appear in. For example, p_{val1} and p_{val2} are parameters in the valence angle potential function. Parameters with a more direct physical meaning, like the torsional rotational barriers (V_1, V_2, V_3) bear their more recognizable names.

1. Overall system energy

Equation (1) describes the ReaxFF overall system energy as a sum of the partial energies of associated with several different energy types.

$$E_{system} = E_{bond} + E_{lp} + E_{over} + E_{under} + E_{val} + E_{pen} + E_{coa} + E_{C2} + E_{triple} + E_{tors} + E_{conj} + E_{H-bond} + E_{vdWaals} + E_{Coulomb} \quad (1)$$

A description and expression for calculating each of the partial energy types introduced in equation (1) follows.

2. Bond Order and Bond Energy

A fundamental assumption of ReaxFF is that the bond order BO'_{ij} between a pair of atoms can be obtained directly from the interatomic distance r_{ij} as given in Equation (2). In calculating the bond orders, ReaxFF distinguishes between contributions from sigma

[4] Courtesy of Adri C. T. van Duin.

bonds, pi-bonds and double pi bonds. Thus the total bond order for a pair of atoms can be written as follows:

$$BO'_{ij} = BO^{\sigma}_{ij} + BO^{\pi}_{ij} + BO^{\pi\pi}_{ij} = \exp\left[p_{bo1}\cdot\left(\frac{r_{ij}}{r^{\sigma}_{o}}\right)^{p_{bo2}}\right] + \exp\left[p_{bo3}\cdot\left(\frac{r_{ij}}{r^{\pi}_{o}}\right)^{p_{bo4}}\right] + \exp\left[p_{bo5}\cdot\left(\frac{r_{ij}}{r^{\pi\pi}_{o}}\right)^{p_{bo6}}\right] \quad (2)$$

Based on the uncorrected bond orders (BO') derived from Equation 1, an uncorrected overcoordination Δ' can be defined for the atoms as the difference between the total bond order around the atom and the number of its bonding electrons *Val*.

$$\Delta'_i = -Val_i + \sum_{j=1}^{neighbours(i)} BO'_{ij} \quad (3a)$$

ReaxFF then uses these uncorrected overcoordination definitions to correct the bond orders BO'_{ij} using the scheme described in Equations (4a-f). To soften the correction for atoms bearing lone electron pairs a second overcoordination definition Δ'^{boc} (equation 3b) is used in equations 4e and 4f. This allows atoms like nitrogen and oxygen, which bear lone electron pairs after filling their valence, to break up these electron pairs and involve them in bonding without obtaining a full bond order correction.

$$\Delta'^{boc}_i = -Val^{boc}_i + \sum_{j=1}^{neighbours(i)} BO'_{ij} \quad (3b)$$

$$\begin{aligned}
BO^{\sigma}_{ij} &= BO'^{\sigma}_{ij}\cdot f_1(\Delta'_i,\Delta'_j)\cdot f_4(\Delta'_i,BO'_{ij})\cdot f_5(\Delta'_j,BO'_{ij}) \\
BO^{\pi}_{ij} &= BO'^{\pi}_{ij}\cdot f_1(\Delta'_i,\Delta'_j)\cdot f_1(\Delta'_i,\Delta'_j)\cdot f_4(\Delta'_i,BO'_{ij})\cdot f_5(\Delta'_j,BO'_{ij}) \\
BO^{\pi\pi}_{ij} &= BO'^{\pi\pi}_{ij}\cdot f_1(\Delta'_i,\Delta'_j)\cdot f_1(\Delta'_i,\Delta'_j)\cdot f_4(\Delta'_i,BO'_{ij})\cdot f_5(\Delta'_j,BO'_{ij}) \\
BO_{ij} &= BO^{\sigma}_{ij} + BO^{\pi}_{ij} + BO^{\pi\pi}_{ij}
\end{aligned} \quad (4a)$$

$$f_1(\Delta_i,\Delta_j)=\frac{1}{2}\cdot\left(\frac{Val_i+f_2(\Delta'_i,\Delta'_j)}{Val_i+f_2(\Delta'_i,\Delta'_j)+f_3(\Delta'_i,\Delta'_j)}+\frac{Val_j+f_2(\Delta'_i,\Delta'_j)}{Val_j+f_2(\Delta'_i,\Delta'_j)+f_3(\Delta'_i,\Delta'_j)}\right) \quad (4b)$$

$$f_2(\Delta'_i,\Delta'_j)=\exp(-p_{boc1}\cdot\Delta'_i)+\exp(-p_{boc1}\cdot\Delta'_j) \quad (4c)$$

$$f_3(\Delta'_i,\Delta'_j)=-\frac{1}{p_{boc2}}\cdot\ln\left\{\frac{1}{2}\cdot\left[\exp\left(-p_{boc2}\cdot\Delta'_i\right)+\exp\left(-p_{boc2}\cdot\Delta'_j\right)\right]\right\} \quad (4d)$$

$$f_4(\Delta'_i,BO'_{ij})=\frac{1}{1+\exp(-p_{boc3}\cdot(p_{boc4}\cdot BO'_{ij}\cdot BO'_{ij}-\Delta'^{boc}_i)+p_{boc5})} \quad (4e)$$

$$f_5(\Delta'_j,BO'_{ij})=\frac{1}{1+\exp(-p_{boc3}\cdot(p_{boc4}\cdot BO'_{ij}\cdot BO'_{ij}-\Delta'^{boc}_j)+p_{boc5})} \quad (4f)$$

A corrected overcoordination Δ_i can then be derived from the corrected bond orders using equation (5).

$$\Delta_i=-Val_i+\sum_{j=1}^{neighbours(i)}BO_{ij} \quad (5)$$

From these corrected bond orders (BO_{ij}) the bond energies are calculated from equation (6).

$$E_{bond}=-D_e^{\sigma}\cdot BO_{ij}^{\sigma}\cdot\exp\left[p_{be1}\left(1-\left(BO_{ij}^{\sigma}\right)^{p_{be2}}\right)\right]-D_e^{\pi}\cdot BO_{ij}^{\pi}-D_e^{\pi\pi}\cdot BO_{ij}^{\pi\pi} \quad (6)$$

3. Lone pair energy

Equation (8) is used to determine the number of lone pairs around an atom. Δ_i^e is determined in Equation (7) and describes the difference between the total number of outer shell electrons (6 for oxygen, 4 for silicon, 1 for hydrogen) and the sum of bond orders around an atomic center.

$$\Delta_i^e = -Val_i^e + \sum_{j=1}^{neighbours(i)} BO_{ij} \tag{7}$$

$$n_{lp,i} = \mathrm{int}\left(\frac{\Delta_i^e}{2}\right) + \exp\left[-p_{lp1}\cdot\left(2+\Delta_i^e - 2\cdot\mathrm{int}\left\{\frac{\Delta_i^e}{2}\right\}\right)^2\right] \tag{8}$$

For oxygen with normal coordination (total bond order=2, Δ_i^e=4), equation (8) leads to 2 lone pairs. As the total bond order associated with a particular O starts to exceed 2, equation (8) causes a lone pair to gradually break up, causing a deviation Δ_i^{lp}, defined in equation (9), from the optimal number of lone pairs $n_{lp,opt}$ (e.g. 2 for oxygen, 0 for silicon and hydrogen).

$$\Delta_i^{lp} = n_{lp,opt} - n_{lp,i} \tag{9}$$

This is accompanied by an energy penalty, as calculated by equation (10).

$$E_{lp} = \frac{p_{lp2}\cdot\Delta_i^{lp}}{1+\exp\left(-75\cdot\Delta_i^{lp}\right)} \tag{10}$$

4. Overcoordination

For an overcoordinated atom (Δ_i>0), equations (11a-b) impose an energy penalty on the system. The degree of overcoordination Δ is decreased if the atom contains a broken-up lone electron pair. This is done by calculating a corrected overcoordination (equation 11b), taking the deviation from the optimal number of lone pairs, as calculated in equation (9), into account.

$$E_{over} = \frac{\sum_{j=1}^{nbond} p_{ovun1}\cdot D_e^{\sigma}\cdot BO_{ij}}{\Delta_i^{lpcorr} + Val_i}\cdot\Delta_i^{lpcorr}\cdot\left[\frac{1}{1+\exp\left(p_{ovun2}\cdot\Delta_i^{lpcorr}\right)}\right] \tag{11a}$$

$$\Delta_i^{lpcorr} = \Delta_i - \frac{\Delta_i^{lp}}{1 + p_{ovun3} \cdot \exp\left(p_{ovun4} \cdot \left\{ \sum_{j=1}^{neighbours(i)} \left(\Delta_j - \Delta_j^{lp}\right) \cdot \left(BO_{ij}^{\pi} + BO_{ij}^{\pi\pi}\right) \right\} \right)} \qquad (11b)$$

5. Undercoordination

For an undercoordinated atom (Δ_i<0), we want to take into account the energy contribution for the resonance of the π-electron between attached under-coordinated atomic centers. This is done by equations 12 where E_{under} is only important if the bonds between under-coordinated atom *i* and its under-coordinated neighbors *j* partly have π-bond character.

$$E_{under} = \frac{-p_{ovun5} \cdot \dfrac{1 - \exp\left(p_{ovun6} \cdot \Delta_i^{lpcor}\right)}{1 + \exp(-p_{ovun2} \cdot \Delta_i^{lpcor})}}{1 + p_{ovun7} \cdot \exp\left[p_{ovun8} \cdot \left\{ \sum_{j=1}^{neighbours(i)} \left(\Delta_j - \Delta_j^{lp}\right) \cdot \left(BO_{ij}^{\pi} + BO_{ij}^{\pi\pi}\right) \right\} \right]} \qquad (12)$$

6. Valence Angle Terms

6.1 Angle energy. Just as for bond terms, it is important that the energy contribution from valence angle terms goes to zero as the bond orders in the valence angle goes to zero. Equations (13a-g) are used to calculate the valence angle energy contribution. The equilibrium angle Θ_o for Θ_{ijk} depends on the sum of π-bond orders (*SBO*) around the central atom *j* as described in Equation (13d). Thus, the equilibrium angle changes from around 109.47 for sp^3 hybridization (π-bond=0) to 120 for sp^2 (π-bond=1) to 180 for sp (π-bond=2) based on the geometry of the central atom j and its neighbors. In addition to including the effects of π-bonds on the central atom j, Equation (13d) also takes into account the effects of over- and under-coordination in central atom j, as determined by equation (13e), on the equilibrium valency angle, including the influence of a lone electron

pair. Val^{angle} is the valency of the atom used in the valency and torsion angle evaluation. Val^{angle} is the same as Val^{boc} used in equation (3c) for non-metals. The functional form of Equation (13f) is designed to avoid singularities when SBO=0 and SBO=2. The angles in Equations (13a)-(13g) are in radians.

$$E_{val} = f_7(BO_{ij}) \cdot f_7(BO_{jk}) \cdot f_8(\Delta_j) \cdot \left\{ p_{val1} - p_{val1} \exp\left[-p_{val2} \left(\Theta_o(BO) - \Theta_{ijk} \right)^2 \right] \right\} \quad (13a)$$

$$f_7(BO_{ij}) = 1 - \exp\left(-p_{val3} \cdot BO_{ij}^{p_{val4}} \right) \quad (13b)$$

$$f_8(\Delta_j) = p_{val5} - (p_{val5} - 1) \cdot \frac{2 + \exp\left(p_{val6} \cdot \Delta_j^{angle} \right)}{1 + \exp\left(p_{val6} \cdot \Delta_j^{angle} \right) + \exp\left(-p_{val7} \cdot \Delta_j^{angle} \right)} \quad (13c)$$

$$SBO = \sum_{n=1}^{neighbors(j)} \left(BO_{jn}^{\pi} + BO_{jn}^{\pi\pi} \right) + \left[1 - \prod_{n=1}^{neighbours(j)} \exp\left(-BO_{jn}^{8} \right) \right] \cdot \left(-\Delta_j^{angle} - p_{val8} \cdot n_{lp,j} \right) \quad (13d)$$

$$\Delta_j^{angle} = -Val_j^{angle} + \sum_{n=1}^{neighbours(j)} BO_{jn} \quad (13e)$$

$$\begin{aligned} &SBO2 = 0 \text{ if } SBO \le 0 \\ &SBO2 = SBO^{p_{val9}} \text{ if } 0 < SBO < 1 \\ &SBO2 = 2 - (2 - SBO)^{p_{val9}} \text{ if } 1 < SBO < 2 \\ &SBO2 = 2 \text{ if } SBO > 2 \end{aligned} \quad (13f)$$

$$\Theta_0(BO) = \pi - \Theta_{0,0} \cdot \left\{ 1 - \exp\left[-p_{val10} \cdot (2 - SBO2) \right] \right\} \quad (13g)$$

6.2 Penalty energy. To reproduce the stability of systems with two double bonds sharing an atom in a valency angle, like allene, an additional energy penalty, as described in Equations (14a) and (14b), is imposed for such systems. Equation (9b) deals with the effects of over/undercoordination in central atom *j* on the penalty energy.

$$E_{pen} = p_{pen1} \cdot f_9(\Delta_j) \cdot \exp\left[-p_{pen2} \cdot \left(BO_{ij} - 2 \right)^2 \right] \exp\left[-p_{pen2} \cdot \left(BO_{jk} - 2 \right)^2 \right] \quad (14a)$$

$$f_9(\Delta_j) = \frac{2 + \exp\left(-p_{pen3} \cdot \Delta_j \right)}{1 + \exp\left(-p_{pen3} \cdot \Delta_j \right) + \exp\left(p_{pen4} \cdot \Delta_j \right)} \quad (14b)$$

6.3 Three-body conjugation term. The hydrocarbon ReaxFF potential contained only a four-body conjugation term (see section 7.2), which was sufficient to describe most conjugated hydrocarbon systems. However, this term failed to describe the stability obtained from conjugation by the $-NO_2$-group. To describe the stability of such groups a three-body conjugation term is included (equation 15).

$$E_{coa} = \frac{p_{coa1}}{1+\exp\left(p_{coa2}\cdot\Delta_j^{val}\right)}\cdot\exp\left[-p_{coa3}\cdot\left(-BO_{ij}+\sum_{n=1}^{neighbours(i)}BO_{in}\right)^2\right]\cdot \exp\left[-p_{coa3}\cdot\left(-BO_{jk}+\sum_{n=1}^{neighbours(i)}BO_{kn}\right)^2\right]\cdot \exp\left[-p_{coa4}\cdot\left(BO_{ij}-1.5\right)^2\right]\cdot\exp\left[-p_{coa4}\cdot\left(BO_{jk}-1.5\right)^2\right] \quad (15)$$

7. Torsion angle terms

7.1 Torsion rotation barriers. Just as with angle terms we need to ensure that dependence of the energy of torsion angle ω_{ijkl} accounts properly for BO $\rightarrow$ 0 and for BO greater than 1. This is done by Equations (16a)-(16c).

$$E_{tors} = f_{10}(BO_{ij},BO_{jk},BO_{kl})\cdot\sin\Theta_{ijk}\cdot\sin\Theta_{jkl}\cdot \left[\frac{1}{2}V_1\cdot\left(1+\cos\omega_{ijkl}\right)+\frac{1}{2}V_2\cdot\exp\left\{p_{tor1}\cdot\left(BO_{jk}^{\pi}-1+f_{11}(\Delta_j,\Delta_k)\right)^2\right\}\cdot \left(1-\cos2\omega_{ijkl}\right)+\frac{1}{2}V_3\cdot\left(1+\cos3\omega_{ijkl}\right)\right] \quad (16a)$$

$$f_{10}(BO_{ij},BO_{jk},BO_{kl}) = \left[1-\exp\left(-p_{tor2}\cdot BO_{ij}\right)\right]\cdot\left[1-\exp\left(-p_{tor2}\cdot BO_{jk}\right)\right]\cdot \left[1-\exp\left(-p_{tor2}\cdot BO_{kl}\right)\right] \quad (16b)$$

$$f_{11}(\Delta_j,\Delta_k) = \frac{2+\exp\left[-p_{tor3}\cdot\left(\Delta_j^{angle}+\Delta_k^{angle}\right)\right]}{1+\exp\left[-p_{tor3}\cdot\left(\Delta_j^{angle}+\Delta_k^{angle}\right)\right]+\exp\left[p_{tor4}\cdot\left(\Delta_j^{angle}+\Delta_k^{angle}\right)\right]} \quad (16c)$$

7.2 Four body conjugation term. Equations (17a-b) describe the contribution of conjugation effects to the molecular energy. A maximum contribution of conjugation

energy is obtained when successive bonds have bond order values of 1.5 as in benzene and other aromatics.

$$E_{conj} = f_{12}(BO_{ij}, BO_{jk}, BO_{kl}) \cdot p_{\cot 1} \cdot \left[1 + \left(\cos^2 \omega_{ijkl} - 1\right) \cdot \sin\Theta_{ijk} \cdot \sin\Theta_{jkl}\right] \tag{17a}$$

$$f_{12}(BO_{ij}, BO_{jk}, BO_{kl}) = \exp\left[-p_{\cot 2} \cdot \left(BO_{ij} - 1\frac{1}{2}\right)^2\right] \cdot \exp\left[-p_{\cot 2} \cdot \left(BO_{jk} - 1\frac{1}{2}\right)^2\right] \cdot \exp\left[-p_{\cot 2} \cdot \left(BO_{kl} - 1\frac{1}{2}\right)^2\right] \tag{17b}$$

8. Hydrogen bond interactions

Equation (18) described the bond-order dependent hydrogen bond term for a X-H—Z system as incorporated in ReaxFF.

$$E_{Hbond} = p_{hb1} \cdot \left[1 - \exp\left(p_{hb2} \cdot BO_{XH}\right)\right] \cdot \exp\left[p_{hb3}\left(\frac{r_{hb}^o}{r_{HZ}} + \frac{r_{HZ}}{r_{hb}^o} - 2\right)\right] \cdot \sin^8\left(\frac{\Theta_{XHZ}}{2}\right) \tag{18}$$

9. Correction for C_2

ReaxFF erroneously predicts that two carbons in the C_2-molecule form a very strong (triple) bond, while in fact the triple bond would get de-stabilized by terminal radical electrons, and for that reason the carbon-carbon bond is not any stronger than a double bond. To capture the stability of C_2 we introduced a new partial energy contribution (E_{C2}). Equation (19) shows the potential function used to de-stabilize the C_2 molecule:

$$\begin{aligned} E_{C2} &= k_{c2} \cdot \left(BO_{ij} - \Delta_i - 0.04 \cdot \Delta_i^4 - 3\right)^2 \quad \text{if } BO_{ij} - \Delta_i - 0.04 \cdot \Delta_i^4 > 3 \\ E_{C2} &= 0 \qquad\qquad\qquad\qquad\qquad\qquad\quad \text{if } BO_{ij} - \Delta_i - 0.04 \cdot \Delta_i^4 \le 3 \end{aligned} \tag{19}$$

where Δ_i is the level of under/overcoordination on atom i as obtained from subtracting the valency of the atom (4 for carbon) from the sum of the bond orders around that atom and k_{c2} the force field parameter associated with this partial energy contribution.

11. Triple bond energy correction.

To describe the triple bond in carbon monoxide a triple bond stabilization energy is used, making CO both stable and inert. This energy term only affects C-O bonded pairs. Equation (20) shows the energy function used to describe the triple bond stabilization energy.

$$E_{trip} = p_{trip1} \exp\left[-p_{trip2}\left(BO_{ij} - 2.5\right)^2\right] \cdot \frac{\exp\left[-p_{trip4} \cdot \left(\sum_{k=1}^{neighbours(i)} BO_{ik} - BO_{ij}\right)\right] + \exp\left[-p_{trip4} \cdot \left(\sum_{k=1}^{neighbours(j)} BO_{jk} - BO_{ij}\right)\right]}{1 + 25 \cdot \exp\left[p_{trip3}\left(\Delta_i + \Delta_j\right)\right]} \quad (20)$$

12. Nonbonded interactions

In addition to valence interactions which depend on overlap, there are repulsive interactions at short interatomic distances due to Pauli principle orthogonalization and attraction energies at long distances due to dispersion. These interactions, comprised of van der Waals and Coulomb forces, are included for *all* atom pairs, thus avoiding awkward alterations in the energy description during bond dissociation.

12.1 Taper correction. To avoid energy discontinuities when charged species move in and out of the non-bonded cutoff radius ReaxFF employs a Taper correction, as developed by de Vos Burchart (1995). Each nonbonded energy and derivative is multiplied by a Taper-term, which is taken from a distance-dependent 7th order polynomial shown in equation 21.

$$Tap = Tap_7 \cdot r_{ij}^7 + Tap_6 \cdot r_{ij}^6 + Tap_5 \cdot r_{ij}^5 + Tap_4 \cdot r_{ij}^4 + Tap_3 \cdot r_{ij}^3 + Tap_2 \cdot r_{ij}^2 + Tap_1 \cdot r_{ij} + Tap_0 \quad (21)$$

The terms in this polynomal are chosen to ensure that all 1st, 2nd and 3rd derivatives of the non-bonded interactions to the distance are continuous and go to zero at the cutoff boundary. To that end, the terms Tap_0 to Tap_7 in equation (21) are calculated by the scheme in equation (22), where R_{cut} is the non-bonded cutoff radius.

$$\begin{aligned} Tap_7 &= 20/R_{cut}^7 \\ Tap_6 &= -70/R_{cut}^6 \\ Tap_5 &= 84/R_{cut}^5 \\ Tap_4 &= -35/R_{cut}^4 \\ Tap_3 &= 0 \\ Tap_2 &= 0 \\ Tap_1 &= 0 \\ Tap_0 &= 1 \end{aligned} \tag{22}$$

12.2 van der Waals interactions. To account for the van der Waals interactions we use a distance-corrected Morse-potential (Equations. 23a-b). By including a shielded interaction (Equation 23b) excessively high repulsions between bonded atoms (1-2 interactions) and atoms sharing a valence angle (1-3 interactions) are avoided.

$$E_{vdWaals} = Tap \cdot D_{ij} \cdot \left\{ \exp\left[\alpha_{ij} \cdot \left(1 - \frac{f_{13}(r_{ij})}{r_{vdW}} \right) \right] - 2 \cdot \exp\left[\frac{1}{2} \cdot \alpha_{ij} \cdot \left(1 - \frac{f_{13}(r_{ij})}{r_{vdW}} \right) \right] \right\} \tag{23a}$$

$$f_{13}(r_{ij}) = \left[r_{ij}^{p_{vdW1}} + \left(\frac{1}{\gamma_w} \right)^{p_{vdW1}} \right]^{\frac{1}{p_{vdW1}}} \tag{23b}$$

12.3 Coulomb Interactions. As with the van der Waals-interactions, Coulomb interactions are taken into account between *all* atom pairs. To adjust for orbital overlap between atoms at close distances a shielded Coulomb-potential is used (Equation 24).

$$E_{coulomb} = Tap \cdot C \cdot \frac{q_i \cdot q_j}{\left[r_{ij}^3 + \left(1/\gamma_{ij} \right)^3 \right]^{1/3}} \tag{24}$$

Atomic charges are calculated using the Electron Equilibration Method (EEM)-approach. The EEM charge derivation method is similar to the QEq-scheme; the only differences, apart from parameter definitions, are that EEM does not use an iterative scheme for hydrogen charges (as in QEq) and that QEq uses a more rigorous Slater orbital approach to account for charge overlap.

A p p e n d i x B

Completer Parameters for ReaxFF Reactive Force Field for C/H/Ni

Parameters in bold/italics were trained against the training set presented in Chapter 3.

General Parameters

parameter	unit	value	parameter	unit	value
$p_{boc,1}$	-	50.0000	$p_{pen,2}$	-	6.9290
$p_{boc,2}$	-	9.5469	$p_{pen,3}$	-	0.3842
$p_{coa,2}$	-	26.5405	$p_{pen,4}$	-	2.9294
$p_{trip,4}$	-	1.7224	$p_{tor,2}$	-	5.7796
$p_{trip,3}$	-	6.8702	$p_{tor,3}$	-	10.0000
kc_2	kcal/mol	60.4850	$p_{tor,4}$	-	1.9487
$p_{ovun,6}$	-	1.0588	$p_{cot,2}$	-	2.1645
$p_{trip,2}$	-	4.6000	$p_{vdW,1}$	-	1.5591
$p_{ovun,7}$	-	12.1176	*B.O. Cutoff*	-	0.0010
$p_{ovun,8}$	-	13.3056	$p_{coa,4}$	-	2.1365
$p_{trip,1}$	kcal/mol	-70.5044	$p_{ovun,4}$	-	0.6991
$p_{val,7}$	-	33.8667	$p_{ovun,3}$	-	50.0000
$p_{lp,1}$	-	6.0891	$p_{val,8}$	-	1.8512
$p_{val,9}$	-	1.0563	$p_{coa,3}$	-	2.6962
$p_{val,10}$	-	2.0384			

Atom Parameters

	r_o^{σ}	Val_i	m	r_{vdW}	D_{ij},	γ	r_o^{π}	Val_i^e	α	γ_w	Val_i^{angle}	p_{ovun5}	χ
	Å	-	amu	Å	kcal/mol	Å^{-1}	Å	-	-	Å^{-1}	-	kcal/mol	eV
C	1.3831	4.0000	12.0000	1.8814	0.1923	0.9000	1.1363	4.0000	9.7821	2.1317	4.0000	30.0000	5.9666
H	0.8873	1.0000	1.0080	1.5420	0.0598	0.6883	-0.1000	1.0000	8.1910	30.9706	1.0000	0.0000	3.5768
Ni	1.8201	2.0000	58.6900	1.9449	0.1880	0.8218	0.1000	2.0000	12.1594	3.8387	2.0000	0.0000	4.8038

	η	$r_o^{\pi\pi}$	p_{lp2},	I	p_{boc4}	p_{boc3}	p_{boc5}	p_{ovun2}	p_{val3}	Val_i^{boc}	p_{val5}
	eV	Å	kcal/mol	kcal/mol	—	—	—	—	—	—	—
C	7.0000	1.2071	0.0000	186.1720	9.0068	34.9357	13.5366	-2.8983	2.5675	4.0000	2.9663
H	10.5896	-0.1000	0.0000	54.0596	1.3986	2.1457	0.0003	-15.7683	2.1488	1.0000	2.8793
Ni	7.3852	-1.0000	0.0000	95.6300	50.6786	0.6762	0.0981	-3.7733	3.6035	2.0000	2.5791

Bond Parameters

	D_e^{σ}	D_e^{π}	$D_e^{\pi\pi}$	$p_{be,1}$	$p_{bo,5}$	13*corr*	$p_{bo,6}$	$p_{ovun,1}$	$p_{be,2}$	$p_{bo,3}$	$p_{bo,4}$	$p_{bo,1}$	$p_{bo,2}$
	kcal/mol	kcal/mol	kcal/mol	—	—	—	—	—	—	—	—	—	—
C-C	143.3883	96.3926	76.4404	-0.7767	-0.4710	1.000	34.9900	0.5108	0.4271	-0.1116	9.0638	-0.0840	6.7452
C-H	181.9084	0.0000	0.0000	-0.4768	0.0000	1.000	6.0000	0.7499	12.8085	1.0000	0.0000	-0.0608	6.9928
H-H	168.2342	0.0000	0.0000	-0.2191	0.0000	1.000	6.0000	1.0062	6.1152	1.0000	0.0000	-0.0889	6.0000
C-Ni	***83.5810***	***9.0383***	0.0000	***0.2531***	-0.200	1.000	16.0000	***0.0529***	***1.4085***	***-0.1113***	***13.3900***	***-0.1436***	***4.5683***
H-Ni	***114.7566***	0.0000	0.0000	***-0.8939***	0.0000	1.000	6.0000	***0.1256***	***0.1054***	1.0000	0.0000	***-0.1196***	***5.0815***
Ni-Ni	91.2220	0.0000	0.0000	-0.2538	-0.2000	0.000	16.0000	0.2688	1.4651	-0.2000	15.0000	-0.1435	4.3908

Off Diagonal Parameters

	D_{ij}	R_{vdW}	α	r_o^{σ}	r_o^{π}	$r_o^{\pi\pi}$
	kcal/mol	Å	—	Å	Å	Å
C-H	0.1188	1.4017	9.8545	1.1203	-1.0000	-1.0000
C-Ni	***0.0800***	***1.7085***	***10.0895***	***1.5504***	***1.4005***	-1.0000
H-Ni	***0.0366***	***1.7306***	***11.1019***	***1.2270***	-1.0000	-1.0000

Angle Parameters

	Θ_o	$p_{val,1}$	$p_{val,2}$	$p_{coa,1}$	$p_{val,7}$	$p_{pen,1}$	$p_{val,4}$
	degrees	kcal/mol	-	kcal/mol	-	-	-
C-C-C	72.7917	38.5829	0.7209	0.0000	0.1409	17.4509	1.0670
C-C-H	72.1533	14.2108	6.2512	0.0000	0.0100	0.0000	1.1022
H-C-H	73.2608	24.9703	3.7807	0.0000	0.1335	0.0000	3.0461
C-H-H	0.0000	0.0000	6.0000	0.0000	0.0000	0.0000	1.0400
C-H-C	0.0000	7.5000	5.0000	0.0000	0.0000	0.0000	1.0400
H-H-H	0.0000	27.9213	5.8635	0.0000	0.0000	0.0000	1.0400
C-Ni-C	***62.5000***	***16.6806***	***0.7981***	0.0000	***0.9630***	0.0000	***1.0711***
C-C-Ni	***87.6241***	***12.6504***	***1.8145***	0.0000	***0.6154***	0.0000	***1.5298***
Ni-C-Ni	***100.0000***	***40.4895***	***1.6455***	0.0000	***0.0100***	0.0000	***1.7667***
C-Ni-Ni	***5.0994***	***3.1824***	***0.7016***	0.0000	***0.7465***	0.0000	***2.2665***
H-Ni-H	106.3969	30.0000	0.9614	0.0000	1.9664	0.0000	2.2693
H-H-Ni	0.0000	***26.3327***	***4.6867***	0.0000	0.8177	0.0000	***1.0404***
Ni-H-Ni	0.0000	***60.0000***	***1.8471***	0.0000	***0.6331***	0.0000	***1.8931***
H-Ni-Ni	***30.3748***	***1.0000***	***4.8528***	0.0000	***0.1019***	0.0000	***3.1660***
H-Ni-Ni	180.0000	***-27.2489***	***8.3752***	0.0000	0.8112	0.0000	***1.0004***
C-Ni-H	***97.5742***	***10.9373***	***2.5200***	0.0000	***1.8558***	0.0000	***1.0000***
C-H-Ni	0.0000	***0.2811***	***1.1741***	0.0000	***0.9136***	0.0000	***3.8138***
H-C-Ni	***84.0006***	***45.0000***	***0.6271***	0.0000	***3.0000***	0.0000	***1.0000***

Torsion Parameters

	V_1	V_2	V_3	$p_{tor,1}$	$p_{\cot,1}$
	kcal/mol	kcal/mol	kcal/mol	-	kcal/mol
C-C-C-C	-0.5000	53.0886	-0.1335	-6.2875	-1.9524
C-C-C-H	-0.4614	29.0459	0.2551	-4.8555	-2.7007
H-C-C-H	-0.2833	31.2867	0.2965	-4.8828	-2.4652
X-C-H-X	0.0000	0.0000	0.0000	0.0000	0.0000
X-H-H-X	0.0000	0.0000	0.0000	0.0000	0.0000
X-C-C-X	0.0000	50.0000	0.3000	-4.0000	-2.0000
C-C-C-Ni	0.0000	5.0000	0.4000	-6.0000	0.0000
Ni-C-C-Ni	0.0000	***44.3024***	***0.4000***	***-4.0000***	0.0000
H-C-C-Ni	0.0000	***21.7038***	***0.0100***	***-4.0000***	0.0000
H-C-Ni-C	0.0000	***5.2500***	***0.0100***	***-6.0000***	0.0000
C-C-Ni-C	0.0000	5.1676	0.0100	-5.9539	0.0000
C-C-Ni-H	0.0000	5.1676	0.0100	-5.9539	0.0000